

**Search for Excited Randall-Sundrum
Gravitons with Semi-Leptonic Diboson Final
States in 4.7 fb^{-1} of pp Collisions using the
ATLAS Detector at the Large Hadron Collider**

Eric Lloyd Williams

Submitted in partial fulfillment of the
requirements for the degree
of Doctor of Philosophy
in the Graduate School of Arts and Sciences

COLUMBIA UNIVERSITY

2012

©2012

Eric Lloyd Williams

All Rights Reserved

ABSTRACT

Search for Excited Randall-Sundrum Gravitons with Semi-Leptonic Diboson Final States in 4.7 fb^{-1} of pp Collisions using the ATLAS Detector at the Large Hadron Collider

Eric Lloyd Williams

This dissertation describes a search for resonant WW and WZ production in the $\ell\nu jj$ decay channel using 4.701 fb^{-1} of $\sqrt{\hat{s}} = 7 \text{ TeV}$ LHC collision data collected by the ATLAS detector. Events with a single charged lepton, at least two jets and missing transverse energy are analyzed and no significant deviation from the Standard Model prediction is observed.

Upper limits on the production cross section are interpreted as lower limits on the mass of a resonance and are derived assuming two warped extra-dimension production modes: the original Randall-Sundrum (RS1) model and the more recent “bulk” Randal-Sundrum (Bulk RS) model. The mass range for both models is excluded at 95% CL with a lower mass limit for an RS1 graviton of **936** GeV and **714** GeV for the Bulk RS graviton.

Table of Contents

1	Introduction	1
1.1	The Standard Model	1
1.1.1	Fundamental Particles and Forces	2
1.1.2	Symmetry and Conservation Laws	4
1.1.3	Quantum Electrodynamics	4
1.1.4	Electroweak Theory	5
1.1.5	Spontaneous Symmetry Breaking	7
1.2	Limitations of the Standard Model	9
2	Extra Dimensions and Warped Geometries	12
2.1	Previous Searches	18
3	The LHC and the ATLAS Detector	20
3.1	The Large Hadron Collider	21
3.2	The ATLAS Detector	27
3.3	Coordinate System and Physics Variables	28
3.4	Inner Detector	30
3.5	Calorimeters	33
3.5.1	Electromagnetic Calorimeter	34
3.5.2	Hadronic Calorimeter	36
3.6	Muon Spectrometer	38
3.7	Trigger System and Data Acquisition	42

4 Physics Object Reconstruction and Selection	45
4.1 Reconstruction and Identification of Electrons	46
4.1.1 Electron Reconstruction	46
4.1.2 Electron Identification	47
4.1.3 Electron Energy and Efficiency Corrections	48
4.2 Reconstruction of Muons	51
4.2.1 Muon Momentum and Efficiency Corrections	52
4.3 Reconstruction of Jets	53
4.3.1 The Anti- k_T Jet Reconstruction Algorithm	53
4.3.2 Jet Calibration	55
4.3.3 Jet Vertex Fraction and Quality Criteria	56
4.4 Missing E_T	58
4.4.1 Calculation of the E_T^{miss} calorimeter term	59
4.4.2 Calculation of the E_T^{miss} muon term	61
5 Data and Simulated Monte-Carlo Samples	62
5.1 Data Samples	62
5.2 Monte-Carlo Samples	64
5.2.1 Pile-up Reweighting	75
5.2.2 Signal Templates for $G^* \rightarrow WW \rightarrow \ell\nu jj$	76
6 Event Selection	84
6.1 Analysis Overview	84
6.2 Preselection Criteria	86
6.3 Signal Region Definition	89
7 Background Estimation and Control Regions	93
7.1 ALPGEN $W+jets$ Reweighting	93
7.2 QCD Multijet Modeling and Normalization	102
7.3 Preselection Yields and Distributions	104
7.4 $t\bar{t}$ Modeling and Control Region	110

7.5	Signal Control Region and $W/Z+jets$ Normalization	112
8	Signal Selection	122
8.1	Signal Region Yields and Distributions	122
9	Sources of Systematic Uncertainty	126
9.1	Trigger Efficiency	127
9.2	Electron Energy Scale, Energy Resolution and Reconstruction Efficiency	128
9.3	Muon Momentum Resolution and Reconstruction Efficiency	130
9.4	Jet Energy Scale and Energy Resolution	131
9.5	E_T^{miss} Uncertainties from Pile-Up and Low- p_T Jets	134
9.6	Multijet Background	135
9.7	Jet p_T Threshold in LAr Hole Removal	136
9.8	ALPGEN $W+jets$ re-weighting	136
9.9	$W/Z+jets$ Normalisation and Shape	137
9.10	Luminosity Uncertainty	141
9.11	Selection Check Using the Debug Stream	141
9.12	PDF Signal Uncertainty	141
9.13	Initial and Final State Radiation Signal Uncertainty	145
9.14	$t\bar{t}$ Modeling	145
9.15	Theoretical Cross Section Uncertainty	147
9.16	Summary of Systematic Uncertainties	148
9.16.1	Systematic Uncertainties for the $WW \rightarrow \ell\nu jj$ Analysis	148
10	Signal Significance Calculation	152
10.1	Log Likelihood Ratio	153
10.2	Pseudo Experiments	154
10.3	Confidence Level Determination	156
10.3.1	CL_s Method	158

11 Results	160
11.1 Limits on Excited Gravitons	160
11.2 Summary and Conclusions	165
12 Appendices	167
A Comparison of Signal Monte Carlo Events	168
B Additional Preselection Plots	175
B.1 Electron Channel	175
B.2 Muon Channel	177
C Additional Signal Region Plots	179
C.1 Electron Channel	179
C.2 Muon Channel	181

List of Figures

1.1	Particle content of the SM	3
2.1	Gravity as depicted in the RS1 model	14
2.2	Standard Model profiles in fifth dimension	16
3.1	The LHC superconducting dipole magnet	22
3.2	The CERN Accelerator Complex	23
3.3	The proton source	24
3.4	The ATLAS detector and subsystems	28
3.5	Cross section of the ATLAS inner detector	31
3.6	A cut away view of the ATLAS inner detector	32
3.7	A cut away view of the ATLAS calorimeters	33
3.8	A cut away view of the LAr calorimeter geometry	35
3.9	The LAr calorimeter geometry	36
3.10	Diagram of a tile calorimeter module	37
3.11	A cut away view of the ATLAS muon system	39
3.12	Schematic views of an MDT and CSC chamber	40
3.13	Schematic view of the muon system	41
4.1	Jet Vertex Fraction (JVF)	57
4.2	JVF distribution and effect on jet multiplicity	58
5.1	Event yield per pb^{-1} after basic event selection	64
5.2	Average number of interactions in data and MC	75

5.3	Crystal Ball fits for G^* samples in the $e\nu jj$ channel	78
5.4	Crystal Ball fits for G^* samples in the $\mu\nu jj$ channel	79
5.5	Fits of Crystal Ball paramters in the $e\nu jj$ channel	80
5.6	Fits of Crystal Ball parameters in the $\mu\nu jj$ channel	81
5.7	Landau fit to signal acceptances in the $e\nu jj$ channel	82
6.1	Preselection MC distributions of η and p_T in the $e\nu jj$ channel	87
6.2	Preselection MC distributions of η and p_T in the $\mu\nu jj$ channel	88
6.3	Examples of the “triangle cuts” applied in the $e\nu jj$ channel	89
6.4	Signal region MC distributions in the $\mu\nu jj$ channel	91
6.5	Signal region MC distributions in the $e\nu jj$ channel	92
7.1	Boson p_T distributions after $\ell\nu jj$ preselection	94
7.2	Electron and muon p_T data/MC distributions after $\ell\nu jj$ preselection	94
7.3	E_T^{miss} distributions after $\ell\nu jj$ preselection	95
7.4	ALPGEN/SHERPA boson p_T distributions	96
7.5	ALPGEN/SHERPA lepton p_T distributions	96
7.6	ALPGEN/SHERPA E_T^{miss} distributions	97
7.7	ALPGEN/SHERPA truth W -boson p_T distributions	97
7.8	ALPGEN/SHERPA truth lepton p_T distributions	98
7.9	ALPGEN/SHERPA truth E_T^{miss} distributions	98
7.10	Boson p_T distributions after $W/Z+jets$ reweighting	99
7.11	Lepton p_T distributions after $W/Z+jets$ reweighting	100
7.12	E_T^{miss} distributions after $W/Z+jets$ reweighting	101
7.13	QCD $M_T(\ell, E_T^{miss})$ distribution with $W+jets$ contamination estimation	103
7.14	QCD $M_T(\ell, E_T^{miss})$ before and after $W+jets$ contamination subtraction	103
7.15	$M_T(\ell, E_T^{miss})$ before/after QCD estimation	104
7.16	$e\nu jj$ preselection plots	106
7.17	$\mu\nu jj$ preselection plots	107
7.18	$\ell\nu jj$ distributions in $t\bar{t}$ control region	112
7.19	$M(jj)$ distribution for data/MC in signal control region	113

7.20	$M(jj)$ distribution in the signal control region	115
7.21	$M(\ell\nu jj)$ distributions in the $M(jj)$ sidebands	116
7.22	$M(\ell\nu jj)$ distributions after applying $W/Z+jets$ scale factor	117
7.23	Data/MC plots for $e\nu jj$ events in the signal control region	118
7.24	Data/MC plots for $e\nu jj$ events in the signal control region	119
7.25	Data/MC plots for $\mu\nu jj$ events in the signal control region	120
7.26	Data/MC plots for $\mu\nu jj$ events in the signal control region	121
8.1	$M(jj)$ distribution in the signal region	124
8.2	$\ell\nu jj$ invariant mass distribution in the signal region	125
9.1	Effect of the electron energy resolution uncertainty	129
9.2	Effect of the electron energy scale uncertainty	129
9.3	Effect of the electron reconstruction efficiency scale factor uncertainty	130
9.4	Effect of the muon momentum resolution uncertainty	131
9.5	Effect of the muon reconstruction efficiency scale factor uncertainty .	131
9.6	Fractional JES uncertainty	132
9.7	Effect of JES uncertainty	132
9.8	Fractional JER uncertainty	133
9.9	Effect of JER uncertainty	134
9.10	$W/Z+jets$ scale factor as a function of $M(\ell\nu jj)$	138
9.11	Effect of $W/Z+jets$ scale factor uncertainty	139
9.12	Effect of JES on $M(jj)$ distribution	140
9.13	Effect of JER on $M(jj)$ distribution	140
9.14	Lepton distributions for various parton distribution functions	143
9.15	Lepton distributions for various parton distribution functions	144
9.16	Effect of top mass and ISR/FSR uncertainties	146
9.17	Effect of $t\bar{t}$ modeling uncertainties	147
10.1	NLLR distributions for H0 and H1 hypotheses	156
11.1	$M(\ell\nu jj)$ distributions in signal region	161

11.2	RS1 graviton cross section limits for the combined $\ell\nu jj$ channel	163
11.3	Bulk RS graviton cross section limits for the combined $\ell\nu jj$ channel	164
A.1	Jet p_T and mass distributions for 500 GeV signal samples	169
A.2	Jet p_T and mass distributions for 1000 GeV signal samples	169
A.3	Jet p_T and mass distributions for 1500 GeV signal samples	170
B.1	Data/MC distributions after $e\nu jj$ preselection	175
B.2	Data/MC distributions after $e\nu jj$ preselection	176
B.3	Data/MC distributions after $\mu\nu jj$ preselection	177
B.4	Data/MC distributions after $\mu\nu jj$ preselection	178
C.1	Data/MC distributions after $e\nu jj$ signal region selection	179
C.2	Data/MC distributions after $e\nu jj$ signal region selection	180
C.3	Data/MC distributions after $\mu\nu jj$ signal region selection	181

List of Tables

1.1	Properties of the four fundamental forces	3
3.1	LHC operating parameters	26
3.2	Granularity of LAr Hadronic Calorimeter	38
4.1	Variables used for electron identification cuts	50
5.1	Data sample luminosity and trigger information	63
5.2	Event generators and cross sections used	69
5.3	ALPGEN $W+jets$ Monte Carlo samples	70
5.4	ALPGEN Z/γ^*+jets Monte Carlo samples	71
5.5	SHERPA $W+jets$ Monte Carlo samples	72
5.6	MC@NLO single-top and $t\bar{t}$ Monte Carlo samples	72
5.7	HERWIG diboson Monte Carlo samples	72
5.8	PYTHIA Randall-Sundrum (RS1) graviton Monte Carlo samples	73
5.9	CALCHEP ‘bulk’ Randall-Sundrum (RS) graviton Monte Carlo samples	74
5.10	Summary of signal template acceptances	83
7.1	QCD multi-jet scaling factor	104
7.2	$\ell\nu jj$ preselection yields	105
7.3	RS1 and ‘bulk’ RS graviton $e\nu jj$ preselection yields	108
7.4	RS1 and ‘bulk’ RS graviton $\mu\nu jj$ preselection yields	109
7.5	$t\bar{t}$ control region yields	111
7.6	$M(jj)$ sideband scale factors	114

8.1	Signal region yields and acceptances	123
9.1	QCD scale factors from fits with various template variables	135
9.2	$W/Z+jets$ scale factors with and without $W+jets$ re-weighting	136
9.3	$W/Z+jets$ signal region yields with and without $W+jets$ re-weighting	137
9.4	Systematic uncertainty from $W/Z+jets$ scale factor	138
9.5	PYTHIA parameter settings used in the ISR/FSR varied samples . .	147
9.6	Effects of theoretical cross section uncertainties	148
9.7	Summary of $e\nu jj$ channel systematic uncertainties	150
9.8	Summary of $\mu\nu jj$ channel systematic uncertainties	151
11.1	Signal region yields with statistical and systematic uncertainties . .	162
11.2	Lower mass limits for signal templates	163
11.3	Lower mass limits for fully simulated signal samples	164
11.4	Signal region p -values	165
A.1	$e\nu jj$ cut flow for three 500 GeV signals	171
A.2	$e\nu jj$ cut flow for three 500 GeV signals	172
A.3	$e\nu jj$ channel cut flow for three 1500 GeV signals	173
A.4	$\mu\nu jj$ channel cut flow for three 1500 GeV signals	174

Acknowledgments

There are many people to whom I am heavily indebted, the first of which is my advisor Michael Tuts. Without his guidance, patience and support none of this would have been possible. I have also benefited greatly from the advice and encouragement of many other faculty and staff of the Columbia physics department. I want to thank John Parsons for his continual interest in my progress and Gustaaf Brooijmans for always challenging me. Additionally, I am grateful to the decades of scientists and staff at CERN whose enormous efforts made an experiment like this possible.

I was blessed to be surrounded by so many talented ATLAS colleagues. Thomas Gadfort has guided me in this process from the beginning. From my introduction to ROOT at Nevis, to suggesting to me, and conducting with me, this search for diboson resonances, perhaps no one else was more fundamental to my high energy physics education. I am grateful for my fellow Columbia classmates and postdocs for the numerous enlightening discussions. In particular, I want to thank Alex Penson, Dustin Urbaniec and Evan Wulf with whom I've shared my time, and many adventures, in both New York and Switzerland. Additionally, I received much guidance and wisdom from current and former Columbia scientists: Tim Andeen, Seth Caughron, Mark Cooke, Kathy Copic, Zachary Marshall, David Lopez Mateos, Nikiforos Nikiforou, Francesco Spano, Emily Thompson, Feng Tien, Ning Zhou and Lidija Zivkovic. While writing this thesis, I've also benefited from the examples and help provided by many others, namely Doctors Doglioni, Caputo, Dobson, Jen-La Plante, Miller, Ohm, Terashi and Wooden.

Throughout my education I have also been very fortunate to come into contact with many mentors that have helped to motivate and guide me through this process.

Starting with my high school instructor, Dave Thuleen, who first showed me how fascinating and challenging physics can be and is someone that I very much look up to and respect. At Berkeley, Dmitry Budker and Alex Sushkov gave me my first glimpse of rigorous scientific research and I am very grateful for the opportunities they provided to me. I am also indebted to Thomas Murphy at UCSD who offered me the chance to shoot the moon and to Adam Orin and Eric Michelson who helped with the “lunar laser rearranging” and always kept it fun.

Additionally, I want to thank all of my friends from Achilles International of Geneva who provided me with more joy, support and inspiration than I can express. In particular, thanks to Najet Abdouli, Laetitia Ferrandini, David Gomez, Alexa Intrator, Pascale Perrottet, Jean-Yves Poupin, Rania Python, Kim Panther, Lucia Ramon, Gowri Sundaram, and Paola Villa. Special thanks are in order to Elena Gaia for her friendship, wisdom and always sound advice. Additionally, thanks to Pamela Balmuth for all that magic.

Finally, ‘thank you’ is not enough to describe the appreciation I have to my parents, their countless unacknowledged sacrifices and relentless support are the sole reasons I am where I am today. Likewise, I am grateful to the love and support of my sisters. Thank you to my older sister Holly for giving me something to chase and to Lori for being such a great little sister. To Alia, whose constant day-by-day encouragement, inspiration, entertainment, support, food, and love, unquestionably carried me through, thank you. Lastly, I want to thank my grandmother Gladys Lorenzen, to whom this thesis is dedicated, a true inspiration and role model and whose strength I can only hope to live up to.

for Gladys

*“There is in every atom a hidden sun,
If once every atom opens its mouth
The earth and galaxies will split apart
Before a hiding sun again comes out.”*

- Rumi

Chapter 1

Introduction

Our current understanding of particle physics phenomena, as expressed through the formalism of the Standard Model (SM) of particle physics, represents an astonishingly successful theoretical framework describing the fundamental constituents of nature and their interactions [1; 2; 3; 4]. This theory has been experimentally confirmed to remarkable accuracy over the forty years since its inception. Despite this, it is known that the model remains incomplete and unsatisfactory, and deviations from SM predictions (new physics) are expected as higher energy limits are explored. The Large Hadron Collider (LHC) was designed to search for these deviations and is currently colliding protons at the highest energies ever achieved. With these new energy regimes come hopes of exposing phenomena beyond the scope of the SM. This chapter will give a quick overview of the SM and the spectrum of elementary particles it provides, as well as its shortcomings and the motivations for the exotic physics searched for in this thesis.

1.1 The Standard Model

At its core, the Standard Model of particle physics is a relativistic quantum field theory (QFT) moored to elegant symmetries of nature. The SM provides a framework for the elementary particles in the universe, as well as a description of the interactions between them. It describes three of the four fundamental forces that

mediate interactions between all the known particles, the exception being gravity. Of these fundamental particles there are two types: fermions and bosons. The half-integer spin fermions constitute the matter particles while the integer spin bosons are the force mediators. These particles and their properties are addressed in Section 1.1.1. The forces in the Standard Model are described in terms of gauge fields as determined by their symmetries, this will be described further in Section 1.1.2. The theoretical underpinnings of Quantum Electrodynamics (QED) and the unified Electroweak Theory will be discussed in Section 1.1.3 and Section 1.1.4, respectively. Finally, this chapter will conclude with a review of the limitations of the SM and some prospective theories of new physics, motivated to address these limitations.

1.1.1 Fundamental Particles and Forces

The half-integer spin fermions are the quarks (d, u, s, c, b, t), the charged leptons (e, μ, τ) and the neutral leptons (ν_e, ν_μ, ν_τ). These quarks and leptons are divided into three generations, stratified by mass, each generation containing a charged and a neutral lepton and an up-type (charge $+2/3$) and down-type (charge $-1/3$) quark. Furthermore, the quarks carry an additional property called color charge, for which there are three types. As quark color is not observed in nature, quarks are always found confined in colorless doublets (mesons) or combined in triplets (baryons), collectively known as the hadrons.

In the SM, these fermions exert forces on each other through the exchange of interaction particles, or force carriers. These are the gauge bosons, each with integer-spin of $s = 1$. The electromagnetic force arises from the exchange of the massless photon γ , the massive W^\pm and Z bosons mediate the weak force and the quanta of the strong force are the eight massless gluons, g_k ($k = 1 \dots 8$). Properties of the gauge bosons, as well as the fermions, are shown in Figure 1.1. The charged leptons couple to both the electromagnetic and weak forces, while the neutral leptons only couple to the weak force. The quarks couple to all three forces, however, their interactions are usually dominated by the strong force due to the fact that, as its name suggests, the strong force coupling constant is many orders of magnitude larger

than the others. See Table 1.1 for the relative strengths of the four fundamental forces.

Three Generations of Matter (Fermions)			
	I	II	III
mass →	2.4 MeV	1.27 GeV	171.2 GeV
charge →	$\frac{2}{3}$	$\frac{2}{3}$	$\frac{2}{3}$
spin →	$\frac{1}{2}$	$\frac{1}{2}$	$\frac{1}{2}$
name →	u up	c charm	t top
Quarks			
mass →	4.8 MeV	104 MeV	4.2 GeV
charge →	$-\frac{1}{3}$	$-\frac{1}{3}$	$-\frac{1}{3}$
spin →	$\frac{1}{2}$	$\frac{1}{2}$	$\frac{1}{2}$
name →	d down	s strange	b bottom
Leptons			
mass →	<2.2 eV	<0.17 MeV	<15.5 MeV
charge →	0	0	0
spin →	$\frac{1}{2}$	$\frac{1}{2}$	$\frac{1}{2}$
name →	e electron neutrino	ν_μ muon neutrino	ν_τ tau neutrino
Bosons (Forces)			
mass →	0.511 MeV	105.7 MeV	1.777 GeV
charge →	-1	-1	-1
spin →	$\frac{1}{2}$	$\frac{1}{2}$	$\frac{1}{2}$
name →	e electron	μ muon	τ tau
Bosons (Forces)			
mass →	80.4 GeV	91.2 GeV	0
charge →	± 1	0	0
spin →	$\frac{1}{2}$	1	1
name →	W^\pm weak force	Z weak force	

Figure 1.1: The matter content of the SM consists of three generations of spin- $1/2$ fermions, while forces are mediated by spin-1 bosons. The electromagnetic, weak and strong forces are mediated by the photon, W^\pm and Z bosons and gluons respectively.

Interaction	Theory	Mediators	Relative Strength	Range (m)
Strong	Quantum chromodynamics	gluons	$\alpha_s = 1$	10^{-15}
Electromagnetic	Quantum electrodynamics	photons	$\alpha = 1/137$	∞
Weak	Electroweak Theory	W and Z bosons	$\alpha_W = 10^{-6}$	10^{-18}
Gravitational	General Relativity (GR)	gravitons (hypothetical)	$\alpha_g = 10^{-39}$	∞

Table 1.1: Properties of the four fundamental forces

1.1.2 Symmetry and Conservation Laws

As previously stated, the Standard Model is a quantum field theory based on the fundamental property of gauge invariance. Gauge invariance requires that the dynamics of the system, characterized by the Lagrangian, are invariant under local transformations that belong to the symmetry or gauge group of the theory. In the Standard Model, the quanta of the gauge invariant fields are identified with the twelve gauge bosons: the force mediators already described, corresponding to the strong, weak and electromagnetic forces.

Specifically, electromagnetism is represented by the Unitary group $U(1)$, and is described by Quantum Electrodynamics (QED). This group is combined with the Special Unitary group $SU(2)$ through the description of the weak force in the Glashow-Weinberg-Salam (GWS) formalism. Finally, the strong force is governed by Quantum Chromodynamics (QCD) which operates within the framework of the $SU(3)$ group. In total, the full Standard Model can then be characterized as a theory invariant under the symmetry group:

$$SU(3)_C \times SU(2)_L \times U(1)_Y. \quad (1.1)$$

Noether's theorem states that any differentiable symmetry of the action of a physical system has a corresponding conservation law [5]. Thus, each group contains an underlying conserved symmetry of the theory; color charge C , weak hypercharge Y , and the left-handed component of weak isospin L .

1.1.3 Quantum Electrodynamics

The theory of quantum electrodynamics is a quantum gauge theory invariant under the symmetry group $U(1)$. Given a particle field, $\psi(x)$, a local gauge transformation takes the form of,

$$\psi(x) \rightarrow \psi'(x) \equiv e^{i\alpha(x)}\psi(x), \quad (1.2)$$

where $\alpha(x)$ is an arbitrary function of space and time. Therefore, the generic Lagrangian of a Lorentz scalar given by,

$$\mathcal{L} = \bar{\psi}(x)(i\gamma^\mu\partial_\mu - m)\psi(x), \quad (1.3)$$

is not invariant under a local gauge transformation due to the fact that the derivative will bring about an additional term from the spatial dependence of the phase rotation α :

$$\partial_\mu \psi \rightarrow e^{i\alpha(x)} \partial_\mu \psi + ie^{i\alpha(x)} \psi \partial_\mu \alpha. \quad (1.4)$$

To impose local gauge invariance on such a Lagrangian, the derivative is replaced by the covariant derivative, \mathcal{D}_μ , expressed as,

$$\mathcal{D}_\mu \equiv \partial_\mu + ieA_\mu(x), \quad (1.5)$$

where e is an arbitrary constant and $A_\mu(x)$ is a vector field corresponding to the photon that is required to transform under local phase transformations as,

$$A_\mu(x) \rightarrow A'_\mu(x) \equiv A_\mu(x) - \frac{1}{e}\partial\alpha(x). \quad (1.6)$$

If A_μ is the gauge field corresponding to the physical photon field, there must also be a term which corresponds to its kinetic energy. Since it too must be invariant when transformed as the gauge field, it can only involve the gauge invariant field strength tensor:

$$F_{\mu\nu} = \partial_\mu A_\nu - \partial_\nu A_\mu. \quad (1.7)$$

Substituting these into the generic Lagrangian of Equation 1.3 produces,

$$\mathcal{L}_{QED} = \bar{\psi}(i\gamma^\mu \partial_\mu - m)\psi + e\bar{\psi}\gamma^\mu A_\mu\psi - \frac{1}{4}F_{\mu\nu}F^{\mu\nu} \quad (1.8)$$

which is the Lagrangian describing quantum electrodynamics. In this way, the Lagrangian of QED possesses the desired local gauge invariance and additionally contains the expected interaction term between the fermion field and a necessarily massless gauge field.

1.1.4 Electroweak Theory

In the Standard Model, the electromagnetic and weak interactions are unified under the “electroweak” gauge theory with symmetry $SU(2)_L \times U(1)_Y$ [6; 7; 8]. While QED arises as a natural evolution of a gauge invariant quantum field theory, the weak interactions must account for what is observed in nature. Specifically, the

inherent violation of parity conservation by the weak coupling as well as the masses of the weak gauge bosons.

In the last section, it was observed that the gauge invariance of QED is associated with an infinite set of wave-function phase transformations which are elements of the group $U(1)$ and can be written,

$$\psi \rightarrow \exp(i\frac{1}{2}g'\alpha(x))\psi. \quad (1.9)$$

These transformations change an electron state into a new electron state, for example $e^- \rightarrow e^-$. Applying gauge invariance then leads to the interaction $e^- \rightarrow e^-\gamma$ in which a gauge boson, the photon, is admitted or absorbed.

Similarly, the transformations associated with the $SU(2)$ symmetry group are of the form,

$$\psi \rightarrow \exp(i\frac{1}{2}gT^a\alpha^a(x))\psi, \quad (1.10)$$

where T^a ($a = 1, 2, 3$) are the three 2×2 Pauli $SU(2)$ generator matrices and g is the weak coupling constant. From these generators arise a triplet of gauge bosons belonging to the $SU(2)_L$ gauge group: (W^\pm, W^0) . These bosons are the weak isospin analogies of the photon in QED and are produced or absorbed in interactions such as,

$$e^- \rightarrow \nu_e W^-, \quad \nu_e \rightarrow e^- W^+, \quad e^- \rightarrow e^- W^0, \quad \nu_e \rightarrow \nu_e W^0. \quad (1.11)$$

Here arises an obvious problem, besides the lack of boson masses, the neutral current processes accompanied with the emission or absorption of a W^0 boson are not observed in nature.

The solution is found in the combination of the $SU(2)$ and $U(1)$ symmetries in the unified electroweak $SU(2)_L \times U(1)_Y$ representation. The gauge transformation for this symmetry group is then,

$$\psi \rightarrow e^{igT^a\alpha^a(x)/2}e^{ig'\alpha(x)/2}\psi \quad (1.12)$$

and again, the requirement of local gauge invariance on the Lagrangian leads to a covariant derivative of the form,

$$D_\mu\psi = (\partial_\mu - i\frac{1}{2}gW_\mu^a T^a - i\frac{1}{2}g'B_\mu^0)\psi. \quad (1.13)$$

Here, the W_μ^a ($a = 1, 2, 3$) and B_μ^0 are massless $SU(2)$ and $U(1)$ gauge bosons, respectively. It is then the neutral component W^3 which mixes with the B^0 boson to form the photon A_μ (γ) and the neutral Z_μ^0 boson. The previously mentioned W^\pm bosons arise from the charged W^1 and W^2 components. Thus the physical gauge bosons are linear combinations of the gauge fields, and are written as:

$$W_\mu^\pm = \frac{1}{\sqrt{2}}(W_\mu^1 \mp iW_\mu^2), \quad (1.14)$$

$$A_\mu = \frac{1}{\sqrt{g^2 + g'^2}}(g'W_\mu^3 + gB_\mu^0) \equiv \sin \theta_w W_\mu^3 + \cos \theta_w B_\mu^0, \quad (1.15)$$

$$Z_\mu^0 = \frac{1}{\sqrt{g^2 + g'^2}}(gW_\mu^3 - g'B_\mu^0) \equiv \cos \theta_w W_\mu^3 - \sin \theta_w B_\mu^0, \quad (1.16)$$

where the parameter θ_w is called the Weinberg angle or weak mixing angle. This angle is not specified in the model, however as A_μ is identified with the photon coupling to the electromagnetic current with strength g_e , the $SU(2)_L$ coupling strength g and the $U(1)_Y$ coupling strength g' must be related to g_e by

$$g_e = g \sin \theta_w = g' \cos \theta_w. \quad (1.17)$$

The electromagnetic current is therefore interpreted as a combination of the neutral weak isospin current and the weak hypercharge current, arising from a unified, gauge invariant, theory of electroweak interactions.

Although the theory has predicted the four force mediating bosons, local gauge invariance still requires massless fields, which conflicts with the massive W and Z bosons experimentally observed. Additionally, the problem is not isolated to the bosonic sector, as adding a mass term to the fermionic Lagrangian would result in spoiling the separation of chiralities. The resolution requires a process referred to as spontaneous symmetry breaking, which is discussed in the following section.

1.1.5 Spontaneous Symmetry Breaking

The solution to the problem of massless bosons arises through the introduction of a neutral scalar particle which ‘breaks’ the symmetry of the vacuum state while retaining the gauge symmetry of the full Lagrangian. The symmetry of a physical

system is ‘broken’, as referred to here, if the interactions governing the dynamics of the system possess a symmetry in which the ground state of the system does not [9]. This phenomenon, in general, is referred to as spontaneous symmetry breaking and in the case of electroweak theory is also referred to as the Higgs mechanism [10; 11; 12; 13].

To facilitate this type of symmetry breaking, a doublet of complex scalar fields,

$$\Phi(x) = \frac{1}{\sqrt{2}} \begin{pmatrix} \phi_1(x) + i\phi_2(x) \\ \phi_3(x) + i\phi_4(x) \end{pmatrix} \quad (1.18)$$

with $\phi_i = \phi_i^\dagger$ and with Lagrangian,

$$\mathcal{L}_\Phi = \partial_\mu \Phi^\dagger \partial^\mu \Phi - m_\Phi^2 \Phi^\dagger \Phi - \frac{1}{2} \lambda^2 (\Phi^\dagger \Phi)^2 \quad (1.19)$$

$$= \frac{1}{2} \partial_\mu \phi_i \partial^\mu \phi_i - \frac{1}{2} m_\Phi^2 \phi_i \phi_i - \frac{1}{8} \lambda^2 (\phi_i \phi_i)^2 \quad (1.20)$$

is added to the electroweak Lagrangian. In the above equation for \mathcal{L}_Φ , a summation over i is understood and a requirement that $m_\Phi^2 < 0$ and $\lambda > 0$ ensures a stable ground state with non-zero expectation value for the scalar field. The interaction of the complex scalar field with itself is described by the last two terms in \mathcal{L}_Φ , and therefore the minimum of this potential implies:

$$|\langle \phi_i \rangle| = \sqrt{-\frac{m_\phi^2}{2\lambda}} \equiv \frac{\nu}{\sqrt{2}}, \quad (1.21)$$

where ν is the vacuum expectation value, $\nu = (\sqrt{2}G_F)^{-\frac{1}{2}} = 246$ GeV with G_F being the Fermi coupling constant.

If $\Phi(x)$ is assumed to transform non-trivially under $SU(2) \times U(1)$ gauge transformations, one can reparameterize by expanding around the vacuum state in a way that eliminates $\phi_1(x)$, $\phi_2(x)$, and $\phi_4(x)$ leaving:

$$\phi(x) = \frac{1}{\sqrt{2}} \begin{pmatrix} 0 \\ \nu + H(x) \end{pmatrix}, \quad (1.22)$$

where $H(x)$ is a real field.

If we apply this representation to the $SU(2)_L \times U(1)_Y$ gauge theory and substitute it into the Lagrangian, the bilinear terms are:

$$(\mathcal{D}_\mu \phi)^\dagger \mathcal{D}^\mu \rightarrow \frac{1}{2} \partial_\mu H \partial^\mu H + (\nu + H)^2 \left[\frac{g^2}{4} W_\mu^\dagger W^\mu + \frac{g^2}{8 \cos \theta_W^2} Z_\mu Z^\mu \right]. \quad (1.23)$$

From this term we achieve the anticipated W_μ^\pm and Z_μ^0 of Equation 1.14, now provided with mass terms produced through the Higgs mechanism, respectively:

$$M_W = \frac{1}{2} g \nu, \quad M_Z = \frac{1}{2} \sqrt{g^2 + g'^2} \nu, \quad (1.24)$$

suggesting,

$$\frac{M_W}{M_Z} = \cos \theta_W, \quad (1.25)$$

while the photon remains conveniently massless. The scalar field H also persists and acquires a mass term and it is this that is referred to as the Higgs boson: the neutral scalar field that has escaped experimental detection thus far.

The addition of an extra scalar field to the gauge theory is the simplest implementation of the Higgs mechanism. The spontaneous symmetry breaking of the underlying local symmetry allows interactions of the Higgs field with other fields in the theory, so as to produce mass terms for the gauge bosons.

1.2 Limitations of the Standard Model

The SM is a powerfully predictive theory of the strong, weak and electromagnetic interactions. However, until experimental confirmation of the neutral spin-0 Higgs boson, it remains incomplete¹. Furthermore, even with the discovery of a Higgs boson, the SM will not represent a complete theory of particle interactions, since there are many problems that it cannot resolve on its own. Perhaps most obvious is the exclusion of the gravitational force within the SM framework. The theory additionally predicts only massless, left-handed neutrinos, a prediction which is

¹It should be noted that as of two days after the successful defense of this thesis, physicists at CERN announced the “observation of a new particle with the properties consistent with a Higgs Boson”. This new particle has appeared as an excess in data at the level of 5σ , with a mass near 125.3 GeV.

contradicted by experimental results. The SM also has nothing to offer toward explanations of cosmological mysteries such as dark matter, dark energy, or the large matter-antimatter asymmetry of the Universe. Another peculiarity of the SM is that it contains 19 arbitrary parameters (including fermion masses); their values not specified and often chosen to fit the data. These problems suggest that perhaps the Standard Model is only a limiting case of a larger theoretical framework and thus motivates the search for new physics.

Another issue arises when one considers the dramatic difference between the electroweak symmetry breaking scale (~ 1 TeV) and the Planck scale ($\sim 10^{19}$ GeV). Both of these scales are related to fundamental constants of nature, Fermi's constant G_F and Newton's constant G_N , respectively. The ratio of these two constants (G_F/G_N) is roughly 10^{32} and the SM gives no insight into why nature has chosen such vastly disparate mass scales, this is referred to as the “hierarchy problem”.

Another way to frame this issue is in terms of the Higgs boson mass scale. From measurements of the top quark and W boson mass, the Higgs mass is expected to be $\mathcal{O}(100 \text{ GeV})$ [14; 15]. In quantum field theory, theoretical computations of the mass of a scalar particle include quadratic radiative corrections through loop diagrams to the order of the cut off scale for the Standard Model. Thus, one would expect that the large quantum corrections to the square of the Higgs boson mass would inevitably result in a predicted mass value comparable to the scale at which new physics appears ($\sim 2 \times 10^{16}$ TeV if the cutoff scale is taken as the Planck scale). To avoid this, the theory needs precise cancellation between the radiative corrections and the bare mass. These corrections are referred to as fine-tuning. The current formalism of the SM implies a cancellation of the corrections from the loop diagrams to the $\mathcal{O}(10^{31})$ which many argue to be an unnatural level of fine-tuning to impose on nature [16].

This ‘unnaturalness’ thus motivates the search for some new mechanism close to the electroweak scale which can stabilize the Higgs boson mass or resolve the hierarchy problem. For example, super-symmetry removes the power-law divergences of the quantum corrections by postulating “super-partners” for all the SM particles

which have contributions with opposite sign to that from their SM partners. Additional theories put forth to resolve the SM hierarchy problem include models that predict the existence of additional space-time dimensions. Of particular interest to this thesis is the warped extra-dimensional model originally proposed by Randall and Sundrum. The phenomenology of this model as well its solutions to the current limitations of the Standard Model are described in the following chapter.

Chapter 2

Extra Dimensions and Warped Geometries

It appears, at first glance, that we live in a universe composed of three infinitely sized spatial dimensions and a single time dimension. This four-dimensional universe hypothesis is confirmed experimentally on large scales via cosmological measurements which confirm the $1/r^2$ scaling of the gravitational force. This functional form, reinforced with the geometrical description of space-time provided by Einstein (general theory of relativity), precisely describes the force of gravity at very large distances. At short distances, however, the picture is not so clear. The theoretical formulation of the general theory of relativity is incompatible with quantum mechanics and the Standard Model as they stand. Experimental tests of gravity at short distances are extremely challenging due to its weakness as compared to the electromagnetic force. Currently, the $1/r^2$ form of the force of gravity has been confirmed down to the order of 10 microns [17; 18; 19]. This is the lower-limit of exclusion of the size of additional dimensions in our universe, under the assumption that only gravity extends into hypothesized small extra dimensions [20; 21; 22] (electromagnetism's $1/r^2$ form conforms exceedingly well to the 4D description of space time down to the spatial dimensions probed at the LHC $\sim 10^{-16}$ mm).

In addition to the possibilities of hidden, smaller dimensions, Randall and Sun-

drum have proposed that it is also possible for gravity to be localized in a “warped” extra-dimension [23; 24]. That is, a dimension with a non-factorizable metric, thus relaxing the constraint on its spatial extent. This suggestion follows two assumptions about the structure of the extra dimensions: first, that matter and forces can be confined to them and second, the extra-dimensions contain energy. These extra-dimensional structures are referred to as “branes” in string theory (short from “membranes”), and can be thought of as lower dimensional objects floating in higher dimensional spaces (e.g. one surface of a cube is a 2-D brane of the 3-D object). Because matter can be confined to a brane, we can imagine ourselves in a universe where the standard model particles and forces are confined to our (3+1)-D brane, while gravity is allowed to propagate into the 5th dimensional “bulk”. If branes are allowed to carry energy, and if we are residing in an energetic four-dimensional flat brane in a larger five-dimensional space-time, it turns out that the geometry of the extending dimensions are not flat but warped, the strength of which is determined by their distance from the flat brane.

Specifically, the solution to Einstein’s equations assigns this bulk space with negative vacuum energy (negative curvature), and is referred to as anti-de Sitter (AdS) space [25]. The curved (orbifold structure) fifth dimension resides on a line segment (ds) where distance scales are measured with the non-factorizable metric given by,

$$ds^2 = e^{-2ky} \eta_{\mu\nu} dx^\mu dx^\nu + dy^2 \quad (2.1)$$

where $\eta_{\mu\nu}$ is the Minkowski metric $\text{diag}(-+++)$, x^μ are the four dimensions of space-time ($\mu = 0, 1, 2, 3$), with $x^0 = t$, and k is the AdS curvature scale and is on the order of the Planck scale. The fifth dimension y , is bounded by $0 \leq y \leq \pi R$, where R is the extent of the fifth dimension. This describes a bulk of five-dimensional space (AdS_5) separating two four-dimensional boundaries (branes) as shown in Figure 2.1 and is the basis for the RS1 model as proposed by Randall and Sundrum [23; 26].

The RS1 theory suggests that each of the two branes spanning the AdS_5 space carry tension; one positive and one negative. In the original RS1 formulation, all the Standard Model particles and forces are trapped on a single brane, referred to as the

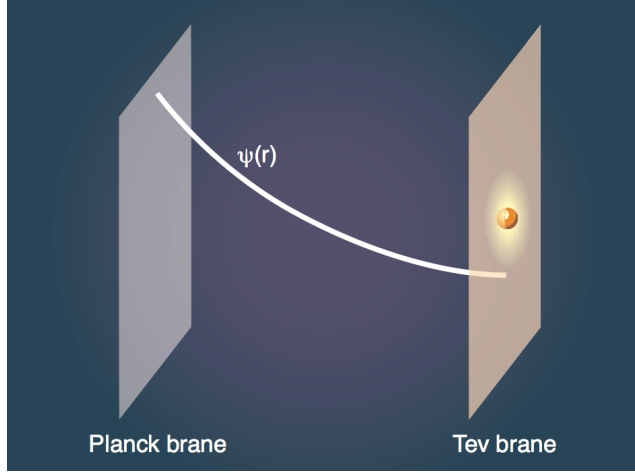


Figure 2.1: The exponential shape of the gravitational wave function, $\Psi(r)$, spanning the bulk between two four-dimensional branes.

TeV- or IR-brane. Separated from this brane is the second, the Planck- or UV-brane, on which gravity is concentrated and space ends. It was further postulated that only gravity can propagate through the bulk, the five-dimensional volume separating the branes, and that the strength of gravity decreases exponentially with distance from the Planck brane. Therefore the 10^{16} orders of magnitude that separate the Planck scale from the Electroweak symmetry breaking scale arise naturally from the fact that the gravitational coupling changes so rapidly over the distance between the branes.

In this way, the RS1 warped extra-dimensional theory can address the hierarchy problem. Previously, most theoretical attempts at solving the hierarchy problem, sought out additional structures to the electroweak sector to explain why the two mass scales are so different. In this approach, it is possible to connect the fundamental gravitational and weak interaction mass scales due to the fact that the 4-D physical masses on the TeV brane acquire an exponential rescaling by e^{-2ky} [27; 28], a function of location in the 5-D bulk. Thus the scale of physical phenomena on the TeV-brane ($y = \pi R_c$), with gravity located on the Planck-brane ($y = 0$), is then given by $\Lambda_\pi = M_{Pl} e^{-2\pi k R_c}$. This factor thereby offers a source of the hierarchy discrepancy between the electroweak scale of order TeV and the Planck scale which

is approximately 10^{16} times bigger. This large scale difference is then accounted for by the geometrical exponential factor with modest values of kR_c , namely $kR_c \sim 11$, leading to the energy scale of gravity on the IR-brane to be on the order of a TeV, as required to address the hierarchy problem.

Additionally the 4-D Planck scale is given by,

$$M_{Pl}^2 = \frac{M_{5d}^3}{k}(1 - e^{-2ky}), \quad (2.2)$$

where M_{5d} is the 5-D Planck mass, the fundamental scale in the theory. The fact that M_{Pl} depends only weakly on y suggests that $M_{Pl} \sim M_{5d} \sim k$ and hence no new hierarchies are introduced through this formalism.

Technically, this proposal does not solve the hierarchy problem but reframes it into a problem of explaining, or ‘stabilizing’, the size of the extra dimension. It was originally shown by Goldberger and Wise [29; 30] that this stabilization is possible through the minimization of the potential of the modulus field, the radion, which describes the relative motion between the two branes [31]. The energy of this scalar field is characterized by the warp factor at the distant brane, even if it resides in the whole bulk. The resulting size of the stabilized extra dimension is on the correct order to solve the hierarchy problem, without the fine tuning of parameters. Additionally, because the RS1 theory proposes that the TeV scale is not the highest energy scale accessible to the full higher-dimensional theory, the unification of couplings at a high energy scale can be readily incorporated [32; 33].

Although this formulation is attractive due to its elegant solution to the hierarchy problem, among other things, it leads to problems with proton decay [34], and FCNC effects [35; 36] through the introduction of higher-dimensional operators that were previously sufficiently suppressed in the Standard Model [37; 38]. Specifically, these features stem from the fact that as originally presented, the RS1 model assumes that all the SM particles are localized on the TeV brane. In fact, it is only the Higgs field that needs to be localized on this brane to address the hierarchy problem while the SM gauge bosons and fermions are not restricted from propagating into the bulk [39; 40; 41; 42]

Allowing Standard Model fermions into the bulk has the consequence of naturally explaining the fermion mass hierarchy. Since fermion masses are determined by their Yukawa couplings to the Higgs boson, the spectrum of fermion masses can be understood as a result of the separation of fermionic and Higgs wave functions in the orbifold bulk. The SM fermions have exponential probability density distributions (profiles) describing their extensions into this 5th dimension. Assuming a uniform fermionic bare mass for all the SM particles, the magnitude of the coupling constants, as observed on our (3+1)-D brane, depends on the overlap of the particle's bulk wave functions at the surface of our TeV brane. In other words, the location of the concentration of these distributions, either near the TeV brane or near the Planck brane, determine its coupling strength to the Higgs (which resides on or near the TeV brane). For example, the electron, being the lightest fermion as observed from our brane, has its zero mode profile (ground state) localized furthest from the TeV brane (and the Higgs) in the bulk, while the top, being the heaviest fermion, has a zero mode closest to the TeV brane. This is illustrated in Figure 2.2.

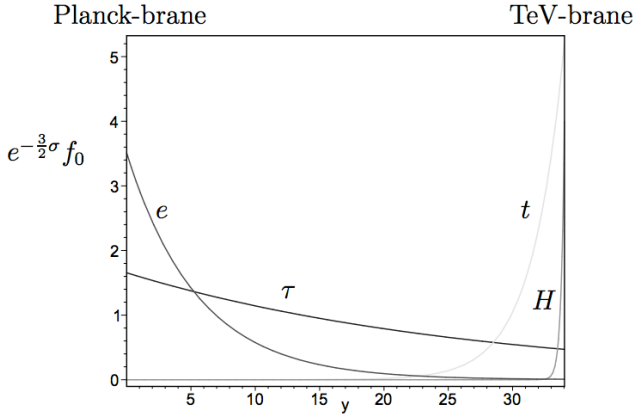


Figure 2.2: Profiles of the electron (e), tau (τ), top quark (t) and Higgs (H) zero modes in the fifth dimension. [34]

It is presumed, that confirmation of an extra dimension, such as that described above, will arise with the appearance of Kaluza-Klein (KK) excitation modes of these particles (KK graviton, KK gauge bosons, or KK fermions) [43; 44; 45; 46]. As might be expected, the KK graviton couplings to light fermions are highly suppressed due

to the fact that the KK gravitons are localized near the TeV brane while the profiles of the light particles reside mostly near the Planck brane. Similarly, couplings of the highly localized graviton KK modes to gauge fields, such as the photon, are suppressed due to the flat profiles of SM gauge bosons in the bulk. For the same reason, the decay of warped gravitons to transverse¹ W and Z bosons are suppressed by a volume factor. The production via gluon fusion followed by decays to heavier resonances such as $t\bar{t}$, $W_L W_L$ and $Z_L Z_L$ may then be preferred and left as observable evidence of a KK graviton at the LHC [47; 48; 49].

Under this framework, the dominant KK graviton production mode at the LHC is via gluon-gluon fusion with decay to $t\bar{t}$ pairs [50; 51]. This channel is experimentally challenging due to backgrounds generated both by Standard Model $t\bar{t}$ production as well as the efficiency for top identification, made increasingly difficult due to the collimated decay products of the highly boosted tops. The next dominant decay mode of the gravitons is to the manifestations of the IR-localized Higgs sector Goldstone modes (nonphysical Higgses): the longitudinal Z_L and W_L^\pm gauge bosons. The “golden mode”, $Z_L Z_L \rightarrow \ell^\pm \ell^\pm$, where $\ell^\pm = e^\pm, \mu^\pm$, is a promising channel that provides a clean final state with little SM background [52; 53].

Of particular interest to this thesis is the $W_L^+ W_L^-$ final state. The KK graviton branching fraction into W_L^\pm is twice that for the $Z_L Z_L$ final state. With the additional benefit that the subsequent branching fraction of the W_L^\pm into a leptonic final state ($\text{Br}(W \rightarrow \ell\nu)$) is about 11% compared to 3% for the Z ($\text{BR}(Z \rightarrow \ell^+ \ell^-)$) [54].

The following chapters describe the search methods and analysis techniques employed to find such a decay signature in the ATLAS detector at the LHC. The ultimate goal of this search is to either obtain experimental evidence of a resonance that might suggest a universe as described by the Randal-Sundrum warped extra-dimensional model or, if no evidence of graviton production is observed, to

¹Massive spin-1 bosons can exists in three polarization states: two longitudinally polarized states with the spin aligned or anti-aligned with the direction of boson motion, and one transverse state aligned orthogonal to the direction of motion.

set exclusion limits on the bulk KK graviton production as proposed from such a description.

2.1 Previous Searches

The phenomenology of the KK graviton in the original RS model can be described by the graviton mass and the ratio k/M_{Pl} . In experimental searches $k/M_{Pl} \leq 1$ is usually assumed, and the RS1 model with $k/M_{Pl} = 0.1$ is used as a benchmark model to compare results between different decay channels and different colliders.

The best direct limits on the original RS1 model are currently imposed by a search done at the ATLAS experiment using a total integrated luminosity of 4.9 fb^{-1} . From this search, a RS1 KK graviton decaying via two leptons with coupling $k/M_{Pl} = 0.1$ (0.01) has been experimentally excluded at the 95% CL up to 2.16 (0.91) TeV [55]. Comparable results have been published by the CMS Collaboration searching for extra-dimensional signatures in the diphoton channel. In this analysis, lower limits were set on the mass of the first graviton excitation in the RS1 model of 1.84 (0.86) TeV for a value of the coupling parameter of 0.1 (0.01), using an integrated luminosity of 2.2 fb^{-1} [56].

Searches in the diboson final state are important to cover the possibility that the graviton coupling to leptons in the RS1 model may be lower than the value predicted by the SM and therefore not seen in the dilepton searches. A resonant WW/WZ search at D0 using 5.4 fb^{-1} of integrated luminosity from Run II of the Fermilab Tevatron Collider and combining the results from $\ell\nu jj$, $\ell\ell jj$ and $\ell\nu\ell\ell$ channels, has excluded the mass range of a resonance in this channel between $300 - 754 \text{ GeV}$ [57; 58].

A recent search conducted at ATLAS of $G_{RS1}^* \rightarrow ZZ$, using 1.04 fb^{-1} of integrated luminosity, combines the $\ell\ell\ell\ell$ and $\ell\ell jj$ final states to expand this exclusion range at 95% CL up to 845 GeV [59]. However, the most stringent current limit for RS1 graviton production via diboson final states will be presented in context of the work done in this thesis.

Additionally, as described above, the warped extra-dimensional formulation of the RS graviton model predicts natural suppression of both the dilepton and diphoton couplings of the KK graviton due to volume suppression of the overlap of particle profiles in the 5-D bulk. This further motivates searches of WW/WZ resonances. This thesis will additionally present the results of the first direct search for bulk warped extra-dimension RS KK graviton decays in the diboson final state at ATLAS.

Chapter 3

The LHC and the ATLAS Detector

The Large Hadron Collider (LHC) [60; 61] is currently the highest energy hadron accelerator and collider facility in the world, providing proton-proton collisions at a center-of-mass energy of $\sqrt{s} = 7$ TeV throughout the 2011 running period. The LHC accelerates bunches of protons to 99.999999% the speed of light and brings them to collision at the centers of four detectors (experiments): ATLAS [62], CMS [63], LHCb [64] and ALICE [65]. These detectors are designed to reconstruct the kinematics of the collisions produced within them and are optimized to search for a wide range of particle signatures.

ATLAS (A Toroidal LHC ApparatuS) and CMS (Compact Muon Solenoid) are general purpose detectors designed to search for physics of and beyond the Standard Model. LHCb (Large Hadron Collider Beauty Experiment) and ALICE (A Large Ion Collider Experiment) are smaller, more specialized experiments. LHCb is searching for new physics in rare bottom quark decays as well as conducting precision measurements of CP violation (important for a better understanding of the matter-antimatter asymmetry of the universe). At times, typically one month per year, the LHC accelerates and collides lead nuclei instead of protons. Both ATLAS and CMS study these types of collisions, however the ALICE detector is specially

designed to measure heavy ion collisions and to study the postulated quark-gluon plasma, thought to have existed a few millionths of a second after the big bang.

This chapter outlines the basic parameters of the LHC as well as the ATLAS detector and the technologies employed that made the analysis presented in this thesis possible.

3.1 The Large Hadron Collider

The Large Hadron Collider is a proton-proton collider located at the CERN (European Organization for Nuclear Research) laboratory near Geneva, Switzerland. The LHC is located in a 26.7 km circumference tunnel lying beneath the ground at a varying depth between 45 to 170 m, and intersecting the winding Franco-Swiss border at four points [66].

Using superconducting NbTi cables cooled to approximately 1.9 K by super-fluid He, 1,232 main dipole magnets produce a magnetic field of up to 8.33 T to curve the trajectory of the particles circulating inside the accelerator. Additionally, there are 392 main quadrupole magnets, also cooled by the helium bath to an operating temperature of 2.2 K, which are used for beam corrections and focusing at the interaction points. Because the LHC collides two separate beams of protons, each needs its own beam pipe for clockwise and anti-clockwise acceleration. The magnets were thus designed based on a two-in-one dipole magnet, shown in the cross section of the LHC beam pipe in Figure 3.1. In this configuration the same magnet provides fields in opposite directions in order to bend the two counter-rotating beams of positively charged particles.

The LHC makes use of existing accelerator complexes still present from past CERN experiments to provide the initial acceleration and injection. Figure 3.2 details the layout of these initial-stage accelerators through which the proton beams pass before being injected into the main LHC ring. The protons begin their journey simply enough as hydrogen nuclei in a canister of H₂ gas, shown in Figure 3.3. From these humble beginnings, their orbiting electrons are stripped and the protons

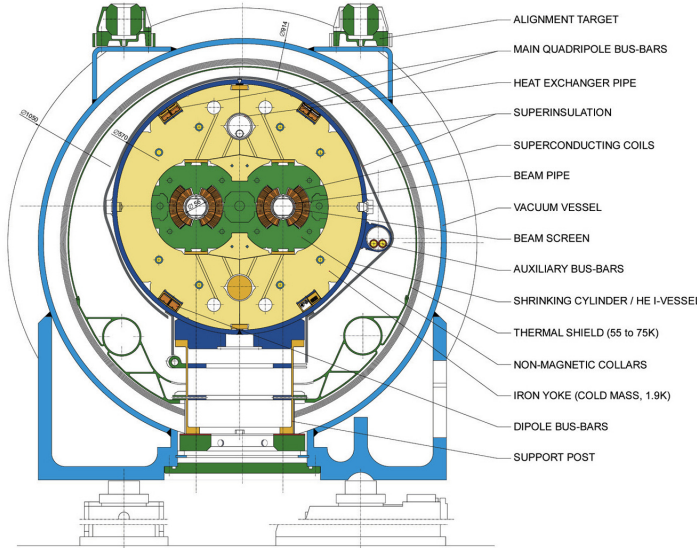


Figure 3.1: A cross section of the LHC superconducting dipole magnet [67].

are accelerated to ~ 50 MeV by the LINAC 2 linear accelerator. These hydrogen nuclei (protons) are then injected into the first of three synchrotrons, the Proton Synchotron Booster (BOOSTER) [68]. The BOOSTER, originally constructed in 1968, accelerates the protons up to an energy of 1.4 GeV. From there, the beam is directed to the Proton Synchrotron (PS) [69] which uses its 277 electromagnets to further increases the beam energy to 26 GeV. The last step before injection into the main LHC ring is done in the 7 km long Super Proton Synchrotron (SPS) [70] where protons reach 450 GeV: the minimum energy at which the LHC can maintain a stable beam.

During the acceleration phases in the PS and the SPS, the protons are divided into bunches, each bunch containing on the order of 10^{11} protons. Protons are injected into the SPS from the PS in 3 to 4 batches consisting of 72 bunches which are then passed to the LHC ring after acceleration in the SPS. The LHC ring was designed to hold up to 2,808 of these bunches, each in what is referred to as an ‘RF bucket’. Each bucket was designed to be separated in time by 25 ns providing the possibility of bunch crossings (collisions) at the rate of 40 million per second. Upon injection, the bunches are distributed onto the LHC ring in ‘bunch trains’: groups

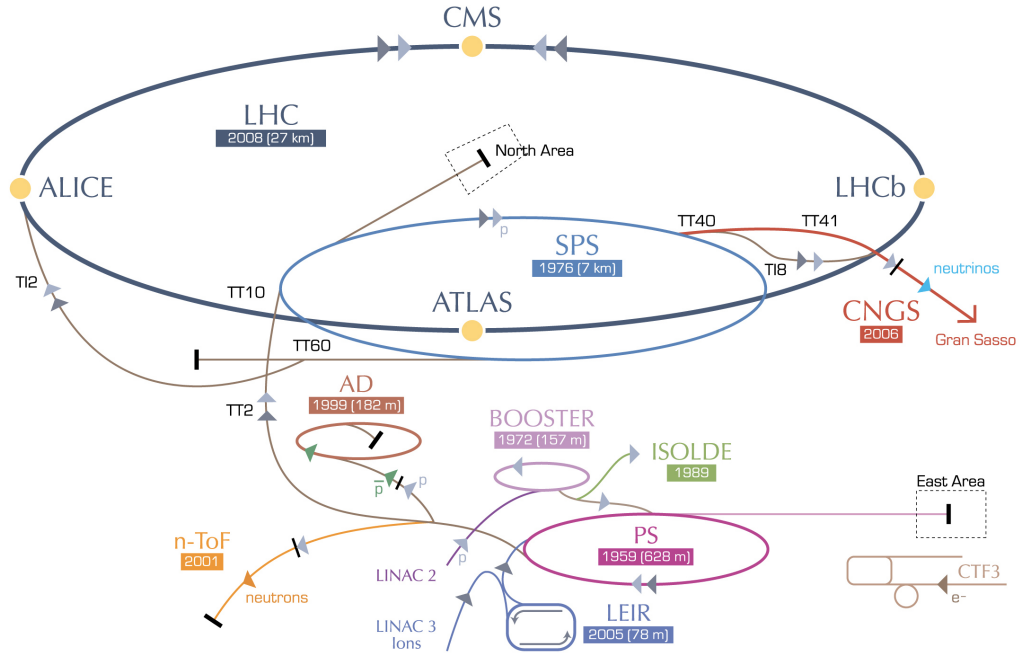


Figure 3.2: The CERN Accelerator Complex [71].

of 72 bunches separated by 12 empty bunches. Once inside the two beam pipes of the LHC, the protons are incrementally accelerated each time they pass through the Radio Frequency (RF) cavities which use a standing wave electric field with a frequency corresponding to the bunch spacing (e.g. 40 MHz). The beam energy is increased by the RF cavities from the injection energy of 450 GeV until they reach their final energy of 3.5 TeV, resulting in a center-of-mass energy of 7 TeV.

The main goal of the LHC is discovery physics. To achieve this, it is necessary to not only maximize the total energy of the collisions, but the total number of collisions as well. For any given process (e.g. Randall-Sundrum graviton production) the rate of production, R_{proc} , is not only dependent on the number of bunches in the machine and the number of protons in those bunches, but also on properties of the beam itself as well as the cross section¹ of the process σ . The beam dependent contributions to

¹In high energy physics, the cross section refers to the effective area which governs the particle interaction probability. Cross sections are measured in units of barns ($1 \text{ barn} = 10^{-28} \text{ m}^2$), however this unit is rather large in terms of processes observed at the LHC so picobarns ($1 \text{ pb} = 10^{-12} \text{ barns}$)



Figure 3.3: Where it all begins, the tank of H₂ gas at the base of LINAC 2. [72]

the rate of production is referred to as the instantaneous luminosity, \mathcal{L} [73]. The rate is then given by:

$$R_{\text{proc}} = \sigma_{\text{proc}} \mathcal{L} \quad (3.1)$$

where σ_{proc} is the cross section for a given process, at the center of mass energy of the collision. Thus, to maximize the number of events produced per second of a given type, it is necessary to maximize the instantaneous luminosity of the LHC. In terms of beam parameters, the instantaneous luminosity is given by:

$$\mathcal{L} = \frac{N_b^2 f k_b}{4\pi\sigma_x\sigma_y} \quad (3.2)$$

where:

- N_b is the number of protons per bunch,
- f is the frequency of revolution of the bunches,

are typically used.

- k_b is the number of bunches in the beam and
- $\sigma_x \sigma_y$ characterize the transverse profile of the beams.

In practice, the beam performance parameters that are used in the instantaneous luminosity calculation are ϵ_n , the nominal transverse emittance of the beam, and β^* , the amplitude function at the interaction point. The transverse emittance quantifies the position and momentum phase space occupied by the particles in the beam and the amplitude function is a measure of the magnet configuration and beam spread.

These terms are related by the function,

$$\epsilon = \frac{\pi \sigma_x \sigma_y}{\beta^*} \quad (3.3)$$

and the instantaneous luminosity can then be expressed as:

$$\mathcal{L} = \frac{N_b^2 f k_b}{4 \epsilon_n \beta^*} F, \quad (3.4)$$

where the F is a geometric factor to account for the fact that the two proton beams do not approach each other exactly head on². Thus, in order to achieve high instantaneous luminosity, the LHC should collide beams containing large numbers of protons with minimized transverse spread (low emittance), at high frequency, in a region where the amplitude is as low as possible. The total integrated luminosity \mathcal{L}_{tot} , is used as a measure of the total amount of data recorded and is measured in units of pb^{-1} . The total number of events N for a process with a given cross section σ is then expressed by,

$$N = \sigma \mathcal{L}_{tot}, \text{ where } \mathcal{L}_{tot} = \int \mathcal{L} dt. \quad (3.5)$$

Table 3.1 lists the nominal parameters for the pp collisions during the 2011 data taking period.

Between April 14th and October 30th, 2011 the LHC collided protons at a center-of-mass energy of $\sqrt{s} = 7 \text{ TeV}$. The 2,808 available ‘RF buckets’ were quickly filled

²At the point where the colliding protons meet, the incoming beams cross at a slight angle (300 microradians) relative to each other. This angle is called the ‘crossing angle’.

as the data taking progressed, starting with 214 colliding bunches and reaching a maximum value of 1,380 by July. Bunch crossings proceeded at 20 Mhz, corresponding to a bunch spacing of 50 ns; each bunch containing on the order of 10^{11} protons. Beam optics improved over the year as well with β^* dropping from 1.5 m to 1 m for most of the recorded luminosity. Similarly, the beam emittance performed well despite an unexplained 20 – 30 % ‘blow-up’ in value upon beam extraction from SPS to LHC [74; 75]. The average value of ϵ_n was $\sim 2.5 \mu\text{m}$ with a minimum of $1.89 \mu\text{m}$. These beam parameters, combined with the large number of colliding protons, lead to a peak instantaneous luminosity of $3.69 \times 10^{33} \text{ cm}^{-2}\text{s}^{-1}$ and a total delivered integrated luminosity of 5417.4 pb^{-1} in 2011 [76; 77].

Parameter	Design	2011 runs
Beam energy [TeV]	7	3.5
Number of bunches per beam	2808	1380
Number of protons	1.5×10^{11}	1.1×10^{11}
β^* [m]	0.55	~ 1
Transverse Emittance ϵ_n [μm]	3.75	2.5
Revolution frequency	11.2×10^3	11.2×10^3
Geometric crossing factor (F)	0.836	~ 1
Bunch spacing [ns]	25	50
Peak instantaneous luminosity [$\text{cm}^{-2}\text{s}^{-1}$]	10^{34}	3.69×10^{33}
Average interactions per crossing	23	~ 9

Table 3.1: LHC beam parameters for the nominal design and during 2011 pp collisions.

3.2 The ATLAS Detector

The ATLAS (A Toroidal LHC ApparatuS) detector [78; 79], located at ‘Point 1’³ of the LHC ring, is designed to be a general-purpose experiment capable of supporting a broad range of physics analyses. Its detection capabilities must be flexible enough to accommodate a range of experimental signatures that might be left by processes predicted by theories such as supersymmetry, extra-dimensions, new gauge bosons, excited or heavy fermions, technicolor models, lepto-quarks, and black holes to name a few. At the same time, the detector must retain the precision and sensitivity needed for Standard Model measurements as well as the much anticipated hunt for the elusive Higgs boson. To accomplish all of this, ATLAS must provide accurate, reliable measurements of physics objects such as electrons (e), photons (γ), muons (μ), jets, and missing transverse energy⁴ (E_T^{miss}).

The detector is a composite of three main subsystems:

1. The inner detector (ID): used for tracking charged particles within the pseudo-rapidity⁵ range $|\eta| < 2.5$. It is composed of a silicon pixel detector, a silicon micro-strip detector (SCT) and a transition radiation tracker (TRT) for $|\eta| < 2.0$.
2. The calorimetry system: used for measuring the energies of electrons, photons and hadrons. Divided by function, the inner calorimeter is a high-granularity lead/liquid-argon (LAr) sampling electromagnetic calorimeter covering $|\eta| < 3.2$. Surrounding the EM calorimeter is an iron/scintillator-tile sampling calorimeter providing hadronic coverage in the range $|\eta| < 1.7$ and extended to $|\eta| < 3.2$ with LAr technology in the end-caps. Both EM

³There are eight possible proton crossing points along the LHC labeled Points 1-8. The four experiments: ATLAS, ALICE, CMS and LHCb are located at Point 1, Point 2, Point 5 and Point 8, respectively.

⁴Defined in detail in Section 4.4, missing transverse energy refers to energy which is not detected in a collision but is expected due to the laws of conservation of energy and conservation of momentum.

⁵See section 3.3 for definition of physics variables such as η , referred to here.

and hadronic calorimeters have LAr based ‘forward’ detectors reaching up to $|\eta| < 4.9$.

3. The muon spectrometer (MS): used for identifying muons and measuring their properties. Surrounding the calorimeters, the muon system consists of three large air-core superconducting toroid systems, precision tracking chambers for muon track reconstruction up to $|\eta| = 2.7$ and fast trigger chambers for muon event triggering in the region $|\eta| < 2.4$.

These subsystems as well as the trigger and data acquisition system, used to select interesting events and store detector measurements, are discussed in this chapter.

The ATLAS detector layout is shown in Figure 3.4.

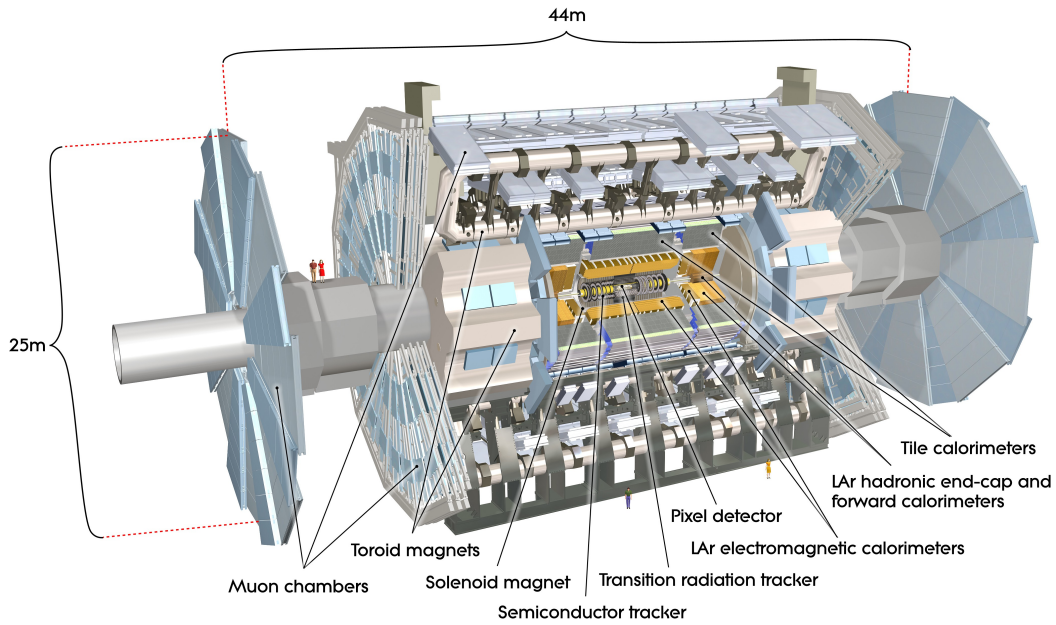


Figure 3.4: A cut away view of the ATLAS detector and subsystems [80].

3.3 Coordinate System and Physics Variables

The ATLAS coordinate system is described here and used throughout the rest of this thesis. The origin is defined as the nominal interaction point (IP). The x -axis

points toward the center of the LHC ring and the y -axis is defined to be pointing upwards toward the surface. The z -axis is aligned co-linear with the beam line with the orientation as defined by a right-hand coordinate system. The detector is symmetric along the z direction and the two halves are referred to as A side (positive z) and C side (negative z). The azimuthal angle ϕ is measured in the $x - y$ plane around the z -axis and the polar angle θ measures the angular separation from the positive z -axis. Measurements are often made in terms of the $R - \phi$ plane, where R is the perpendicular distance from the beam line to the point of interest.

There are many variables that will be used in this thesis that are particular to experimental particle physics. In any collision, the incoming partons⁶ have essentially zero momentum in the $x - y$ plane. Conservation of energy and momentum dictate that the vector sums of energy and momentum of the outgoing particles in the $x - y$ plane must then also be zero. Therefore, it is often convenient to make measurements in terms of transverse variables such as transverse energy, written as E_T , transverse momentum, written as p_T and transverse missing energy, written as E_T^{miss} . All transverse objects are defined as the projection of the given quantity on the $x - y$ plane.

For directional measurements, instead of using the polar angle θ , it is often more useful to speak in terms of a particle's pseudo-rapidity, η . The difference in the pseudo-rapidity of two particles, unlike the same difference in θ , is an invariant under boosts along the beamline (e.g. a transformation of coordinates from the collision center-of-mass frame to the laboratory frame). The pseudo-rapidity is defined as,

$$\eta = -\ln(\tan \theta/2). \quad (3.6)$$

One can also define the rapidity (often used in the case of massive objects such as jets),

$$y = \frac{1}{2} \ln[(E + p_z)/(E - p_z)]. \quad (3.7)$$

Finally, the ‘distance’ between two particles in the pseudo-rapidity-azimuthal angle

⁶The term ‘parton’ refers to the point-like constituents of the proton, namely quarks and gluons

space is defined as,

$$\Delta R = \sqrt{\Delta\eta^2 + \Delta\phi^2}, \quad (3.8)$$

where $\Delta\eta$ and $\Delta\phi$ are the respective η and ϕ distances between the particles. This measure is useful in defining overlaps between objects in the detector.

3.4 Inner Detector

The ATLAS inner tracking system, or inner detector (ID), is designed to track the paths of charged particles produced from a collision at the interaction point. At design luminosity, the inner detector would see on the order of 1,000 charged particle tracks for each beam crossing [81]. To handle such a large particle density while simultaneously achieving high accuracy in momentum and vertex resolution measurements, the inner tracker is divided into three main components. Closest to the interaction point lies the high-resolution semi-conductor pixel detector, followed by the SemiConductor Tracker (SCT) and finally the Transition Radiation Tracker (TRT). A schematic of the active components of the three subsystems is shown in Figure 3.5. The inner detector is split into a barrel region, where the detectors are arranged in concentric cylinders around the beam axis, and two end-cap regions, where detector layers are positioned in planes of constant z , perpendicular to the beam pipe. This configuration can be seen in Figure 3.6.

The entire inner detector system is located within a 2 T magnetic field, which bends the trajectory of the charged particles, enabling a measurement of momentum using the ‘hits’, or measured energy, the particles leave behind while traversing the components. The TRT exchanges precision for volume of hits while covering the region $|\eta| < 2.5$. The pixel and SCT subsystems provide high precision track measurements within $|\eta| < 2.0$ [80].

Within ATLAS, the highest granularity and precision in measurement is achieved by the inner detector’s pixel detector. It is composed of three concentric cylindrical layers, parallel to the beam axis, in the central (barrel) region and three disks, perpendicular to the beam axis, in the forward (end-cap) region. The innermost

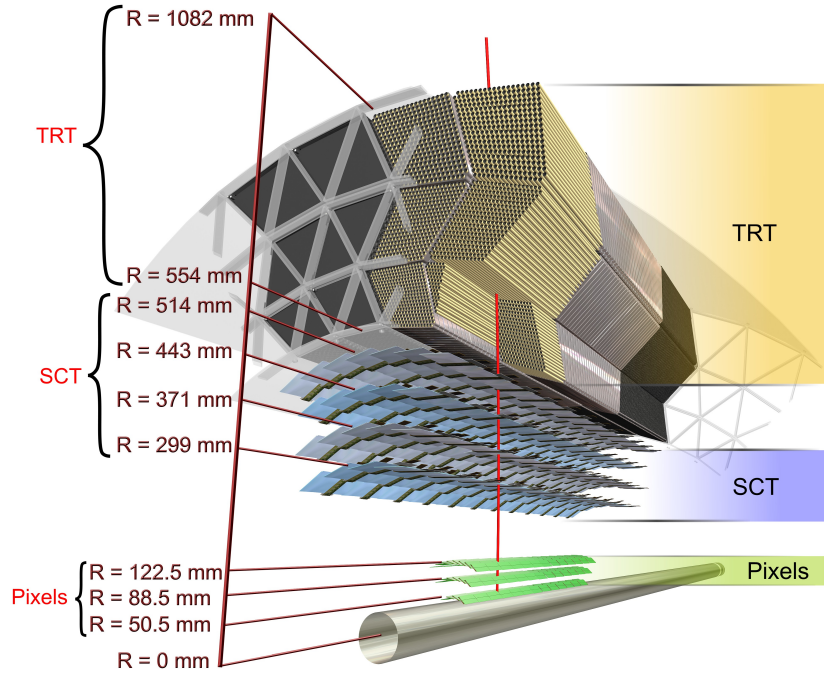


Figure 3.5: A cross section of the ATLAS inner detector [80]

cylindrical layer is the closest active detector element to the IP, called the “vertexing layer”, at a radius of only 50.5 mm. The pixels are doped silicon detectors with a bias voltage of 150 V. Charged particles passing through the semi-conductor generate electron-hole pairs through impact ionization, inducing a measurable current which can be amplified and compared to a given threshold. In total, the pixel detector is comprised of 1,744 pixel modules, each consisting of 47,232 individual pixels, which results in over 80 million readout channels.

The next layer of the inner detector is the Semi-Conductor Tracker (SCT) and its purpose, similar to the pixel detector, is to provide spatial measurements of the charged particles passing through the ID. The SCT is arranged in four concentric cylinders of double strip layers in the barrel and nine disks in the end-cap regions. Each layer consists of a pair of stereo strips, at a pitch of $80 \mu\text{m}$, which provide

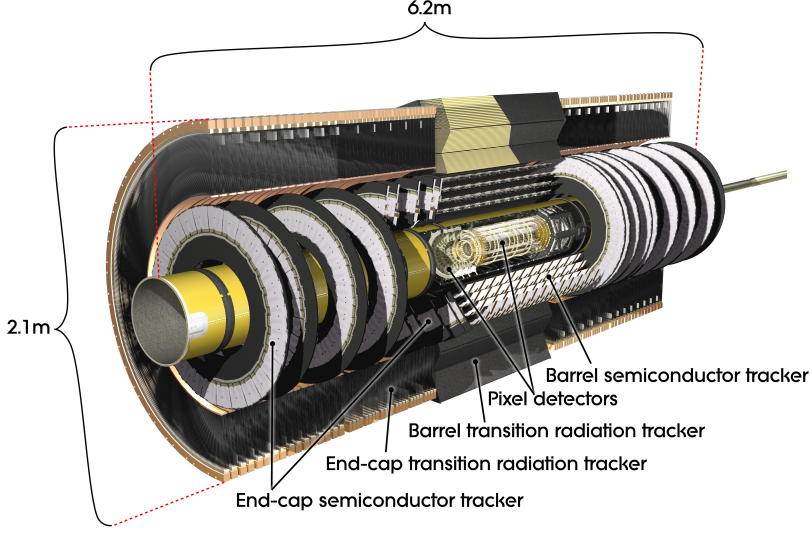


Figure 3.6: A cut away view of the ATLAS inner detector [80]

measurement in the direction around the circumference of the beamline ($R - \phi$). Each strip pair is rotated by 40 mrad with respect to the other to also obtain measurement along the z -direction. This configuration allows the measurement of four space-points for each measured track.

Surrounding the SCT is the final component of the inner detector, the Transition Radiation Tracker (TRT). The TRT measures up to 36 hits for each charged particle passing through its collection of 4 mm diameter, 144 cm long, straw tubes. The tubes cover a range of $|\eta| < 2.0$, placed parallel to the beam in the barrel region and arranged radially as wheels in the end-cap region ($0.8 < |\eta| < 2.0$). Each tube is filled with a gaseous mixture (70% Xe, 27% CO₂ and 3% O₂) which ionizes when traversed by a charged particle. By estimating the time needed for the drift electrons to reach the central anode wire, a drift circle radius is measured for each hit providing a measurement in the $R - \phi$ plane, with an intrinsic precision of 130 μm per track. Additionally, the TRT system takes advantage of the transition radiation (TR) produced by the relativistic particles as they pass through the polypropylene fibers that surround the tubes. These radiated photons are produced with a probability proportional to the Lorentz factor $\gamma = E/m$ [82], which allows the TRT to

be particularly useful in identification and discrimination between electromagnetic and hadronic deposits (e.g. electrons and pions).

3.5 Calorimeters

The ATLAS calorimeters span the range $|\eta| < 4.9$, provide roughly 196,000 readout channels, and must contain and measure both electromagnetic and hadronic showers. They are situated outside of the 2 T solenoidal magnet surrounding the inner detector. The calorimetry system is composed of an electromagnetic calorimeter for electron and photon reconstruction surrounded by a hadronic calorimeter to provide the measurement of jets and missing E_T . To ensure accurate measurements of missing E_T , the calorimeters must not only provide good hermeticity but also must prevent electron and hadron energy from reaching the muon system. The structure of the calorimeter system is shown in Figure 3.7.

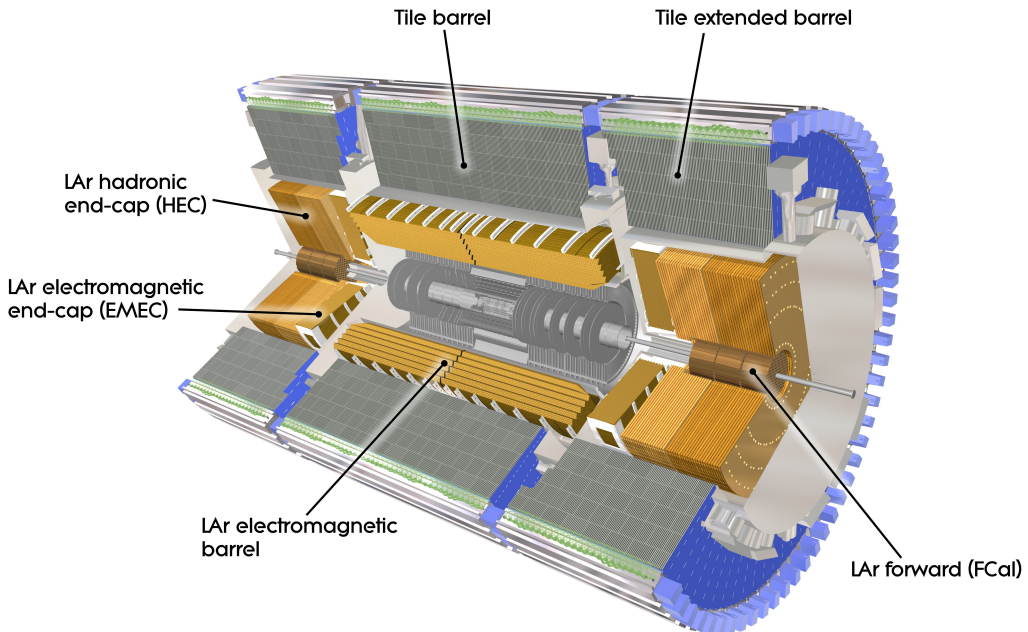


Figure 3.7: A cut away view of the ATLAS calorimeters [62]

Both the electromagnetic and hadronic calorimeters are sampling calorimeters

in which the material that produces the particle shower is distinct from the material that measures it. By absorbing energy in high-density regions while periodically sampling the energy of the particle shower, the energy of the original particle is inferred. By this method, only a fraction of the true shower energy is recorded in the active material, thus accurate calibration of the calorimeters is necessary.

3.5.1 Electromagnetic Calorimeter

The liquid-argon (LAr) electromagnetic (EM) calorimeter is designed to accurately measure the energy of electrons and photons with energies ranging from 5 GeV to 5 TeV [81]. As particles traverse the calorimeter, interactions within the lead absorbers begin the particle shower cascade due to the short radiation length⁷ of lead. The secondary electrons create ionization in the narrow gaps filled with liquid argon. These ionized charge deposits drift in the presence of the electric field and are collected by the copper electrodes.

The EM calorimeter is divided into three overlapping regions: the electromagnetic barrel section (EMB) covering $|\eta| < 1.475$, the electromagnetic end-cap section (EMEC) covering $1.375 < |\eta| < 3.2$ and the forward section (FCal) which covers the range $3.1 < |\eta| < 4.9$. The arrangement of these sub-calorimeters can be seen in Figure 3.8. The calorimeter barrel has an accordion-like geometry with lead absorbing plates between the LAr active material. This geometry was chosen as it facilitates full ϕ symmetry as well as fast read out in the front and rear of the kapton electrodes, mounted on the plates. A segment of the accordion shaped LAr calorimeter at $|\eta| = 0$ can be seen in Figure 3.9.

Liquid-argon was chosen as the active material due to its intrinsic radiation ‘hardness’ as well as its linear behavior and stable response over time. Cryostats keep the argon in liquid phase by cooling it to about 87 K. Due to the fact that variations on the liquid argon temperature have a direct impact on drift velocity,

⁷Radiation length X_0 , is a measure of the mean distance an electron travels through a material until it loses all but $\frac{1}{e}$ of its original energy through bremsstrahlung interactions. It is used as the scale length for describing high-energy electromagnetic cascades.

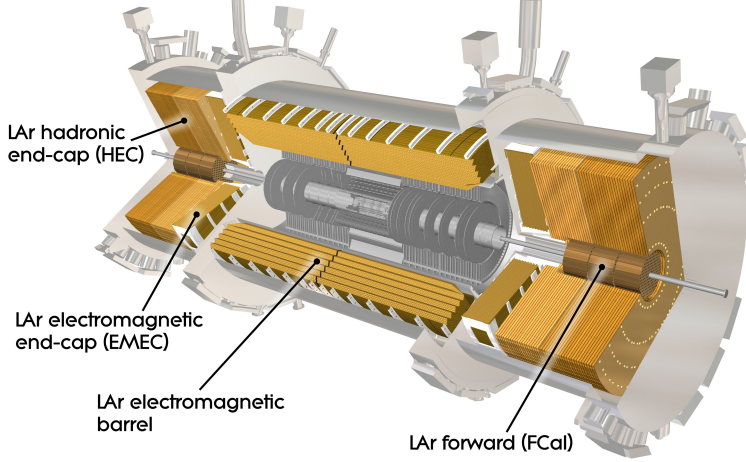


Figure 3.8: A cut away view of the LAr calorimeter geometry

and consequently the readout signal and energy scale, a temperature uniformity of better than 100 mK is required [83]. Additionally, variations in the gaps between the 1,024 accordion absorbers in the end-caps must be compensated for by varying the applied high voltage in order to obtain a calorimeter response independent of pseudo-rapidity.

Over the region devoted to precision physics ($|\eta| < 2.5$), the EM calorimeter is segmented in depth by three sections. As seen in Figure 3.9, the first layer has high granularity $\Delta\eta \times \Delta\phi = 0.0031 \times 0.0245$ and is used to precisely measure the η position of the shower. Additionally, the first layer is approximately 6 radiation lengths (X_0) thick (including the presampler and dead material), which provides the potential for differentiating between π^0 and electron/photon shower shapes as previously mentioned. The second sample absorbs most of the energy of the shower as it is the thickest layer, spanning roughly $16X_0$ in the barrel and $20X_0$ in the end-caps. The third layer records only the tails of electromagnetic showers, however it can help discriminate between electromagnetic and hadronic showers as hadronic particles are more likely to reach the hadronic calorimeter.

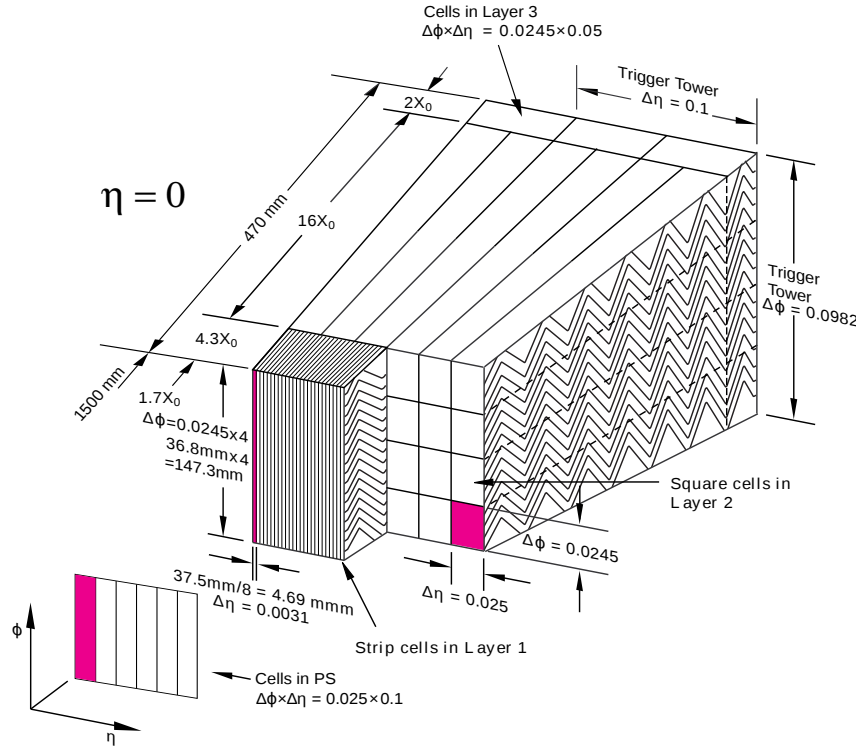


Figure 3.9: The LAr calorimeter geometry

3.5.2 Hadronic Calorimeter

Directly outside of the EM calorimeter are the hadronic calorimeters. They are designed to reconstruct the energies of hadrons produced in the interaction as well as provide reliable missing E_T (see Section 4.4) measurements. The hadronic calorimeter is subdivided into a scintillator tile calorimeter in the barrel region, and LAr calorimeters in the forward direction and end-caps.

The tile calorimeter [84] comprises the largest part of the hadronic calorimeter, composed of the barrel section, with a central component spanning $|\eta| < 1.0$, and two extended barrels covering the range $0.8 < |\eta| < 1.7$. The cylindrical structure has an inner radius of 2280 mm, an outer radius of 4230 mm and is split into the 5640 mm long central barrel with the two 2910 mm extended barrels on each side. The tile calorimeter is a sampling calorimeter, like the EM calorimeter, however it uses steel as the absorber and scintillating tiles as the active material instead of

Pb-LAr. Also, similar to the EM calorimeter, it is composed of three longitudinal sampling layers, approximately 1.5, 4.1 and 1.8 radiation lengths (X_0) thick in the barrel and 1.5, 2.6 and 3.3 X_0 in the extended barrels. In the first two samplings, the $\Delta\eta \times \Delta\phi$ granularity is 0.1×0.1 and 0.2×0.1 for the third. The 3 mm thick scintillating tiles are placed perpendicular to the colliding beams and staggered in depth such that particles emerging from the IP will cross the tiles perpendicularly, in a longitudinal direction. This design allows for a fine segmentation in the z -plane allowing accurate determination of the shower shape. The two sides of the scintillating tiles are read out by wavelength shifting fibers coupled to photomultipliers which transform the output into a signal proportional to the energy sampled. A diagram of a tile calorimeter module is shown in Figure 3.10

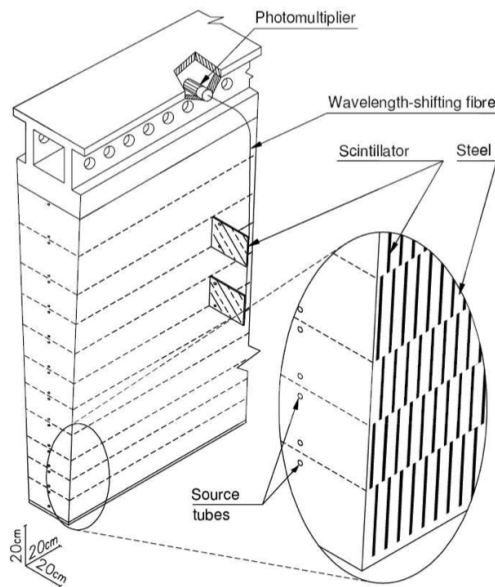


Figure 3.10: Diagram of a tile calorimeter module. Particles enter from below.

The LAr hadronic end-cap calorimeters (HEC) extend the hadronic coverage to higher η , spanning $1.5 < |\eta| < 3.2$. These calorimeters use copper absorbers and liquid-argon as the active medium [85]. It is necessary to change the active medium from the scintillating tiles to LAr for $|\eta| > 1.5$ because the level of radiation and

expected particle flux becomes critical for scintillators at this point⁸. The HEC is comprised of two independent copper wheels per side, located directly behind the EM end-cap calorimeter and sharing the same cryostats. Each wheel has 32 modules (divided in ϕ) with outer radius 2.03 m and is divided into two segments in depth, providing four layers per end-cap. The inner wheel uses 25 mm thick copper plates interleaved with 8.5 mm LAr gaps, while the outer wheel has 50 mm thick copper plates. Detailed information about the granularity of the hadronic end-cap is given in Table 3.2.

	Inner Wheel	Outer Wheel
$ \eta < 2.5$	0.1×0.1	0.1×0.1
$ \eta < 3.1$	0.2×0.2	0.2×0.2

Table 3.2: Granularity of LAr Hadronic Calorimeter in $\Delta\eta \times \Delta\phi$

The final hadronic calorimeter is the LAr forward calorimeter (FCAL), covering the range $3.1 < |\eta| < 4.9$ and composed of three subsystems, all enclosed in the end-cap cryostats. Due to the high particle flux in the forward region, three segments each 45 cm long are employed to minimize long latency times as a result of positive ion build up and saturation. All three segments of the FCAL add up to approximately $1X_0$. The first module, made with copper absorbing plates and 12,000 rods and tubes, is optimized for electromagnetic measurements. The second and third modules are made of tungsten plates with 10,000 rods and tubes each and predominately measure the energy of hadronic interactions.

3.6 Muon Spectrometer

The ATLAS muon spectrometer (MS) surrounds the calorimeters and measures the trajectories of muons, recording their direction, electric charge and momentum. This

⁸During the testing of the calorimeter, LHC particle fluxes were estimated and components were tested under a high-intensity beam provided by the CERN SPS. Saturation and failure of the scintillator system was observed at a beam flux of 10^8 particles/cm²/s [86].

measurement is made possible by the magnetic deflection of the muon tracks by the large superconducting air-core toroid magnets. Within $|\eta| \leq 1.4$, the muons are bent by a large, eight coil, barrel magnet surrounding the tile calorimeter. Between $1.6 \leq |\eta| \leq 2.7$ magnetic bending is provided by two smaller end-cap toroidal magnets situated inside both ends of the barrel toroid. In the transition region $1.4 \leq |\eta| \leq 1.6$, magnetic deflection is provided by a combination of barrel and end-cap fields. The air-core design minimizes multiple scattering of the muons in the material and allows a relatively precise ‘stand-alone’ measurement of the muon properties, even after passing through the inner detector and calorimeters. In the barrel region, tracks are measured in chambers arranged in three cylindrical layers around the beam axis at radial distances from the IP of 5, 7, and 10 m. In the end-caps, four wheels are located at $|z| = 7$ m, $|z| = 10$ m, $|z| = 14$ m, and $|z| = 21–23$ m perpendicular to the beam axis, as shown in Figure 3.11.

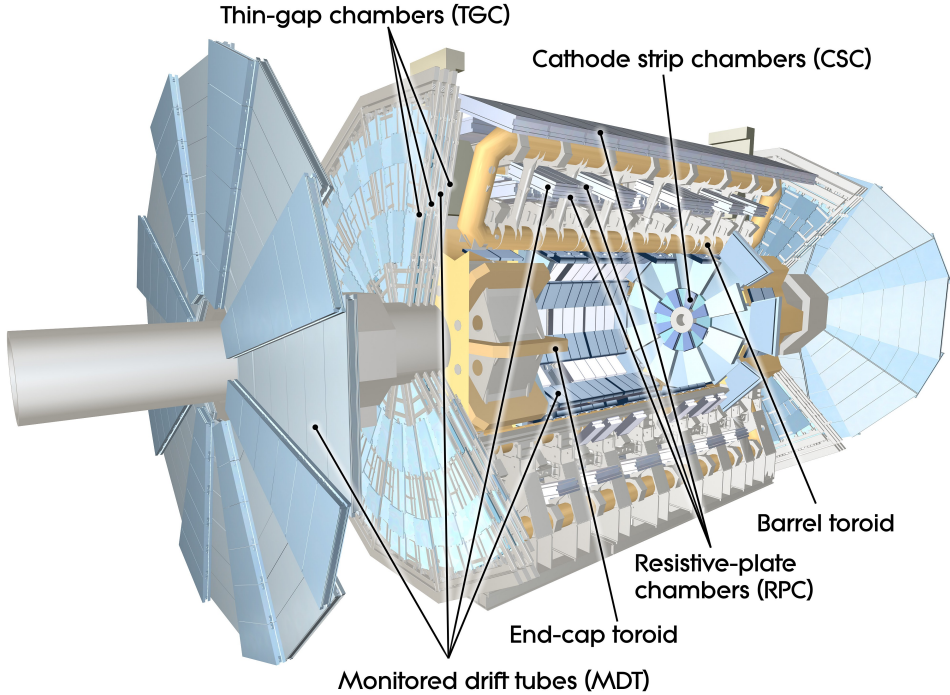


Figure 3.11: A cut away view of the ATLAS muon system [62]

The muon spectrometer has four distinct type of chambers, two designed for the

detection and measurement of muons and two for precise triggering of muons [87]. The two chambers designed for the tracking of muons, collectively referred to as precision chambers, are the monitored drift tubes (MDT) [88] and cathode strip chambers (CSC) [89]. Schematics of an MDT module and a CSC module are shown in Figure 3.12(a) and Figure 3.12(b) respectively. The two chambers designed for trigger purposes, referred to as the fast trigger chambers, are the resistive plate chambers (RPC) [90] in the barrel and thin gap chambers (TGC) [91] in the wheels. The chambers are arranged such that any muon originating at the IP passes through at least three chambers around the beam axis. The arrangement of these chambers within the muon system is shown in Figure 3.13.

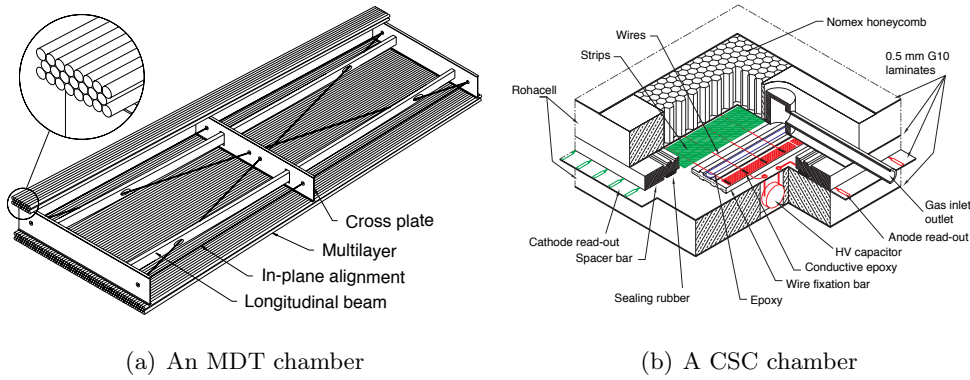


Figure 3.12: Schematic views of the two types of precision muon chambers used for muon measurement.

Monitored drift tube (MDT) chambers comprise a large fraction of all muon chambers and provide a precision measurement of the track coordinates in the principal bending direction. They are deployed over the three layers, extending to $|\eta| < 2$ in the innermost layer and $|\eta| < 2.7$ in the second and third layers. Each MDT contains between 3 to 8 cylindrical aluminum drift tubes of 3 cm diameter, filled with a gas mixture (93% Ar and 7% C) at 3 bar. Measurements from these chambers result in an average resolution of $80 \mu\text{m}$ perpendicular to the wire direction ($r - z$ plane), or $35 \mu\text{m}$ per chamber.

The second type of precision chambers are the cathode strip chambers (CSC).

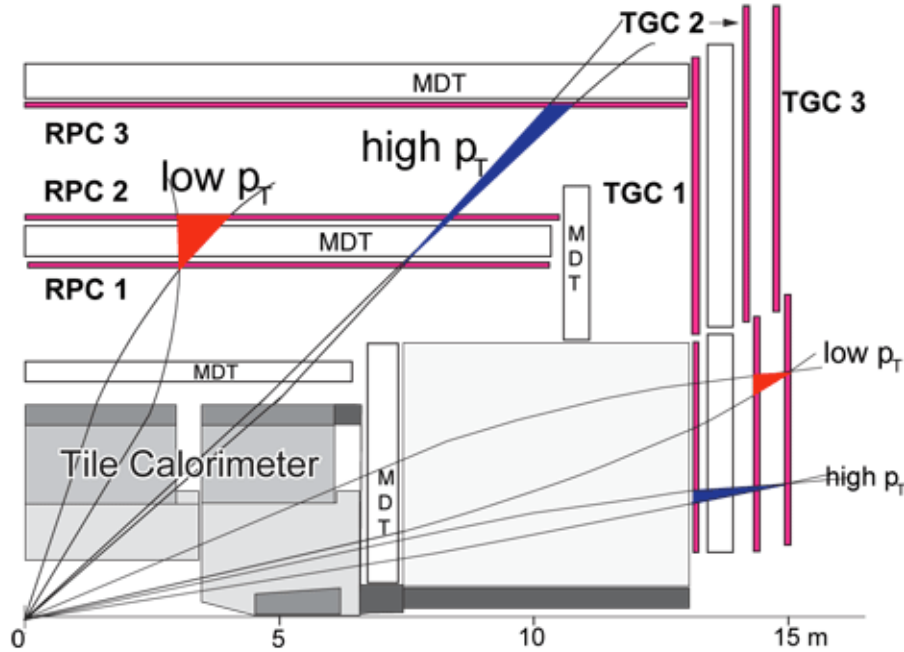


Figure 3.13: A schematic view of muon chambers within the muon system. The curved lines represent possible muon trajectories with opposite inflections indicating opposite charges and the amount of bending signifying the magnitude of the muon momentum (as labeled low/high p_T).

The CSCs are multi-wire proportional chambers with cathodes split into strips with higher granularity. They provide $40 \mu\text{m}$ resolution per station in the bending plane and 5 mm in the transverse. Designed to withstand a demanding rate and background condition, they are deployed in the innermost layer at high pseudo-rapidity ($2.0 < |\eta| < 2.7$).

The muon trigger system identifies bunch crossings that produce muons of interest with well defined p_T thresholds, in addition to providing an orthogonal coordinate measurement to that determined by the precision chamber measurements. Resistive plate chambers accomplish this for events with muons in the barrel region ($|\eta| < 1.05$). These muon chambers are arranged in three concentric shells around the beam axis at a radii of approximately 5, 7, and 10 m. Each RPC is constructed with two parallel, insulated resistive plates which are separated by a 2 mm gap filled

with a gas mixture comprised of 94.7% C₂H₂F₄, 5% C₄H₁₀ and 0.3% SF₆. A total of 380,000 channels are deployed in the central region yielding a 1.5 ns time resolution and spatial resolution of $\Delta\eta = 30$ mm and $\Delta\phi = 3$ cm.

At higher pseudo-rapidities ($1.05 < |\eta| < 2.7$), the thin-gap chambers (TGC) provide the trigger measurement. Because the muon momentum corresponding to a particular p_T increases strongly with η , the TPCs must deliver finer granularity compared to the RPCs in order to withstand higher rates with the same p_T resolution as in the barrel. Similar to the CSCs, TGCs are multiwire proportional chambers, however they are operated in saturation mode to guarantee quick response. The chamber is filled with a highly-quenching gas mixture of 55% CO₂ and 45% n-pentane (C₅H₁₂). Accordingly, the TGCs are able to deliver signals within 25 ns (the duration between bunch crossings) with 4 ns resolution, in addition to providing azimuthal information and the radial coordinate in bending direction.

3.7 Trigger System and Data Acquisition

The challenge of the ATLAS trigger system is to intelligently and efficiently, without any redundancies, reduce the LHC’s design 40 MHz bunch-crossing rate, to a manageable 200 Hz; a reduction factor of 10^7 (at 23 events per bunch-crossing). Due to the low cross sections of interesting physics processes, it is necessary that the LHC run at the highest instantaneous luminosity possible. It would be impractical to record every event as most of these interactions will produce uninteresting “minimum bias” events⁹. The high interaction rate, and the large number of channels of the ATLAS detector, means that the full trigger decision must be accomplished in stages. Therefore, event triggering at ATLAS is based on a three tier approach. Each trigger level refines the decisions made at the previous level and, where necessary, applies additional selection criteria [92].

The first level (L1) is based on limited hardware information from the muon

⁹“Minimum bias” events refer to bunch crossings in which the protons have at least minimal interaction at the IP. These glancing blows, where the proton itself may or may not fragment, often result in a diffuse, ϕ -symmetric distribution of low p_T particles.

trigger chambers as well as coarse readouts from all calorimeter components (electromagnetic and hadronic; barrel, end-cap and forward). This trigger must reduce the event rate to ~ 75 kHz, a rejection factor of nearly 500, and thus has a window of operation of just $2.5\ \mu\text{s}$ to decide whether to accept or reject the event [81]. For events with electromagnetic clusters, the E_T is measured at L1 by trigger towers in a region of 0.1×0.1 in $\Delta\eta \times \Delta\phi$. The RPCs and TGCs provide the first level trigger for muons. The L1 muon and calorimeter triggers are processed by the Central Trigger Processor (CTP) that additionally implements a trigger “menu”, a configurable combination of trigger selections used to optimize the use of available bandwidth as luminosity and background conditions change. If an event is selected by the L1 trigger, all of the data for the selected bunch crossing is read out from the front-end electronics systems of the detectors into readout buffers (ROBs) and held until a L2 decision is made.

The High Level Trigger (HLT) consists of the Level 2 (L2) and the Event Filter (EF) trigger. The L2 trigger makes use of region-of-interest (ROI) information provided by the L1 trigger. The L1 trigger will always define at least one ROI corresponding to a region of the detector in $\eta - \phi$ where the trigger has identified interesting features (e.g. high- p_T muons, electrons/photons, hadrons/taus, etc.). Along with direction information, ROIs include a p_T range of candidate objects and energy sums (missing E_T vector and scalar E_T value). At L2, fast software algorithms are run on the ROIs with, if necessary, full detector granularity and precision and within 40 ms provide an accept/reject decision. At this level, the acceptance rate drops by a factor of ~ 40 , and events are passed to the EF at the rate of around a few kHz.

Events passed from the L2 to the EF trigger, which is responsible to bring the final reduction in rate required to lower it to $\sim 200\text{Hz}$, have an average event processing time on the order of a few seconds. The process of moving data from the ROBs to the EF and assembling all the information associated with a given bunch crossing is called event building. At this stage, a full offline analysis of the event, typically the same as those used in offline event reconstruction, is used to accurately

select events containing the physics objects of interest. If an event is accepted by the EF, it is written to mass storage as Raw Data Output (RDO) ready to be used for full ATLAS physics reconstruction.

Chapter 4

Physics Object Reconstruction and Selection

It is the task of the ATLAS event reconstruction software to use the RDOs, provided by the various detector subsystems after the event selection (as described in Section 3.7), to build up a view of the events in terms of physical final state objects including vertices, tracks, particles, jets and missing E_T . These objects can then be used in physics analyses to understand the properties of the collisions and decay products.

The final state studied in this analysis consists of leptons, E_T^{miss} and jets. Identifying and precisely measuring diboson decays from a high mass resonance requires reliable reconstruction of all of these objects. Electrons are reconstructed by the combined information from the inner detector and the EM calorimeter and are described in Section 4.1. The decay products of quarks and gluons, measured as a shower of hadronic energy in the detector, are referred to as “jets” and deposit the majority of their energy in the hadronic calorimeters. A brief description of the algorithm used to reconstruct jets in an event is described in Section 4.3. A distinctive muon track is reconstructed from a combination of tracks in both the inner detector and muon spectrometer. The specific muon reconstruction package used in this analysis is outlined in Section 4.2. Finally, the E_T^{miss} calculation is done using

the information from all the reconstructed objects in the event and is described in Section 4.4.

4.1 Reconstruction and Identification of Electrons

4.1.1 Electron Reconstruction

The ATLAS electron reconstruction procedure is based on clusters of energy recorded in the central region ($|\eta| < 2.47$) of the electromagnetic calorimeter, which are then associated to tracks of charged particles in the inner detector.

Reconstruction of the EM clusters begins by creating a preliminary set of seed clusters. The sliding-window algorithm [93] identifies seed clusters with $E_T > 2.5$ GeV located in the second layer of the LAr EM calorimeter. The search window size is 3×5 in $\Delta\eta \times \Delta\phi$ cell units, corresponding to the granularity of the calorimeter middle layer (0.025×0.025) [94]. The name “sliding-window” refers to the algorithm’s strategy of adjusting the position of this window so that the contained transverse energy is a local maximum. To avoid double counting, after the first pass of seed cluster finding, duplicates are removed if two clusters have positions within $\Delta\eta < 2.0$ and $\Delta\phi < 2.0$; only the cluster with the larger E_T is kept.

In the tracking volume of $|\eta| < 2.5$, an electron is defined by the existence of one or more reconstructed tracks matched to a seed cluster. Inner detector tracks with $p_T > 0.5$ GeV are extrapolated from their last measurement point to the second EM calorimeter layer. An extrapolated track must match the cluster’s barycenter within a window of $\Delta\eta \times \Delta\phi = 0.05 \times 0.1$, and thus the track-to-cluster matching forms the central part of the electron reconstruction.

The electromagnetic showers corresponding to the seed clusters matched to inner detector tracks are then considered electron candidates [95]. The energy deposited by the candidates depends on the location of the seed, thus the clusters are rebuilt using 3×7 longitudinal towers of cells if the electron is in the barrel and 5×5 towers if in the end-caps. Corrections to the reconstructed cluster energy are then applied to account for various effects such as the finite granularity of the cells, the

ϕ -dependence of the absorber material traversed and the possibility that the shower is not entirely contained within the cluster window (see Section 4.1.3).

Finally, the electron four-momentum is computed using information from both the cluster and best track matched to the original seed cluster. The energy is taken as a weighted average between the cluster energy and the track momentum. The ϕ and η directions are taken from the corresponding track parameters at the vertex. However, if the electron track has less than four silicon hits then the track η measurement is not used since it would have very poor resolution. In this case, the calorimeter η , based on the directional information provided by the cluster, is used instead.

4.1.2 Electron Identification

Electron identification is based on a set of cuts using discriminating variables that provide good separation between isolated electrons and jets that may ‘look’ like electrons. These variables include information from the calorimeter and the inner detector. By independently applying these variables, the ATLAS reconstruction algorithm defines three sets of reference cuts with increasing background rejection power: `loose++`, `medium++` and `tight++`¹. The expected jet rejection factors for these cuts, based on MC simulation, are about 500, 5,000 and 50,000, respectively. These three categories of electrons are defined below:

- `loose++`: the basic selection; hadronic leakage and shower shape variables in the second layer of the EM LAr calorimeter are evaluated. Additionally, track quality hits in the pixel and silicon layers along with loose ($|\Delta\eta| < 0.015$) track cluster-matching are required. This level has the highest efficiency but the lowest background rejection.
- `medium++`: this selection adds tighter track quality and cluster matching variables on top of the `loose++` requirements, as well as additional hadronic re-

¹The “++” refers to the fact that these quality definitions are 2011 improvements on similar requirements originally implemented for electrons in 2010

jection using shape information on energy deposition in the first layer of EM calorimeter. Requirements are also made on the total shower width, the shower width over three strips around the maximum energy deposit and the fraction of energy deposited outside these three central strips.

- **tight++**: optimized for rejection, the **tight++** selection adds to the **medium++** requirements: cluster energy divided by momentum² (E/p), the particle identification potential of the TRT and b-layer hit requirements³ to further reject photon conversions and information about reconstructed conversion vertices. Track cluster-matching requirements are futher tightened as well as cuts on shower shape variables.

A complete list of the variables that define the three categories is given in Table 4.1. These cuts are optimized in 10 bins of cluster η (based on calorimeter topology) and 11 bins of cluster E_T (from 5 to above 80 GeV).

4.1.3 Electron Energy and Efficiency Corrections

Several corrections are applied to a calorimeter cluster that has been identified as an electron. Some of these corrections have been derived from residual, in-situ, studies using $Z \rightarrow ee$ and $J/\psi \rightarrow ee$ events and their well known distribution shapes [96], however most corrections are derived from test beam experiments [97; 98]. Such corrections include compensation for:

- η and ϕ modulations of the calorimeter response;
- lateral energy leakage outside of the cluster window as well as longitudinal leakage outside of the calorimeter;
- energy losses from electrons propagating through the ‘crack regions’ ($|\eta| \sim 1.5$) where reconstruction efficiency suffers;

²The E/p ratio is used to reject electrons with large amounts of bremsstrahlung radiation, which are less efficiently reconstructed.

³The b-layer is the innermost part of the Pixel detector; it is used to optimize the impact parameter resolution.

- sampling fraction variation as a function of shower depth;
- energy lost upstream of the calorimeter.

The energy of Monte Carlo electrons is also smeared to reproduce the resolution measured in W and Z boson events in data. The electron energy is smeared before the p_T threshold cuts are applied since the electron p_T depends both on the electron energy and η .

Furthermore, electrons in the Monte Carlo simulated events do not fully reproduce the reconstruction and identification efficiencies measured in the data. A correction factor (commonly called a scale factor) is applied to each electron in the Monte Carlo events that satisfy the selection criteria described in Chapter 6. This factor is defined as the ratio of the reconstruction or identification efficiencies for data and Monte Carlo events as measured using $Z \rightarrow ee$ events.

Correction factors are measured by a dedicated group⁴ for the **tight++** electrons and provided in 20, E_T dependent, bins of η from -2.47 to 2.47 . The reconstruction and **tight++** identification scale factors are found to be between 0.98 and 1.13 depending on the position of the electron cluster in the calorimeter.

The systematic uncertainties due to the electron energy scale, energy resolution, reconstruction efficiency and identification efficiency corrections are presented in Chapter 9.

⁴The ATLAS e/γ performance group.

Type	Description	Name
loose++ selection		
Acceptance	$ \eta < 2.47$	-
Hadronic leakage	Ratio of E_T in the first layer of the hadronic calorimeter to the E_T of the EM cluster (for $ \eta < 0.8$ and $ \eta > 1.37$)	R_{had1}
	Ratio of E_T in the hadronic calorimeter to the E_T of the EM cluster (for $ \eta > 0.8$ and $ \eta < 1.37$)	R_{had}
Middle layer of EM calorimeter	Ratio in η of cell energies in 3×7 versus 7×7 cells.	R_η
	Lateral width of shower.	w_2
medium++ selection (includes loose++)		
Strip layer of EM calorimeter	Total shower width	w_{stot}
	Ratio of the energy difference between the largest and second largest and energy deposits in the cluster over the sum of these energies	E_{ratio}
Track quality	Number of hits in the pixel detector (≥ 1)	n_{pixel}
	Number of total hits in the pixel and SCT detectors (≥ 7)	n_{Si}
	Transverse impact parameter ($ d_0 < 5$ mm)	d_0
Track-cluster matching	$\Delta\eta$ between the cluster position in the strip layer and the extrapolated track ($ \Delta\eta < 0.01$)	$\Delta\eta$
tight++ selection (includes medium++)		
Track-cluster matching	$\Delta\phi$ between the cluster position in the middle layer and the extrapolated track ($ \Delta\phi < 0.015$)	$\Delta\phi$
	Ratio of the cluster energy to the track momentum	E/p
	Tighter $\Delta\eta$ requirement ($ \Delta\eta < 0.005$)	$\Delta\eta$
Track quality	Tighter transverse impact parameter requirement ($ d_0 < 1$ mm)	d_0
TRT	Total number of hits in the TRT	n_{TRT}
	Ratio of the number of high-threshold hits to the total number of hits in the TRT	f_{HT}
Conversions	Number of hits in the b-layer (≥ 1)	n_{BL}
	Veto electron candidates matched to reconstructed photon conversions	-

Table 4.1: Definition of variables used for **loose++**, **medium++** and **tight++** electron identification cuts for the central region of the detector ($|\eta| < 2.47$) [96]

4.2 Reconstruction of Muons

Muons are produced in a broad spectrum of final states from the collisions within the ATLAS detector and it is the purpose of the muon reconstruction software to identify and measure their properties with high precision. To accomplish this, all three of the ATLAS detector systems are put to use; muon candidates are reconstructed from the combination of tracks from the inner detector as well as tracks from the muon spectrometer, while also accounting for multiple scattering and energy loss from the minimum ionizing signature left as the muon traverses the calorimeter.

Muon track reconstruction from the hits solely recorded in the Muon Spectrometer (see Section 3.6), referred to as stand-alone muons, is performed by the MUONBOY [99] software package. The vast span of the MS (44 m length and 22 m diameter), in addition to the magnetic field inhomogeneities from the open air-core toroid, make this reconstruction particularly challenging. The MUONBOY algorithm follows a four step procedure:

- (i) identification of drift-circles or clusters in the precision and fast trigger chambers;
- (ii) formation of ‘local straight track segments’ within muon stations;
- (iii) combination of track segments between stations to form track muon candidates;
- (iv) final track-fitting procedure performed while taking into account energy loss in material traversed as well as magnetic field inhomogeneities along the muon trajectory.

The tracks are then extrapolated back to the beam line to calculate the initial momentum and energy of the muon. Bremsstrahlung (dE/dx) energy loss in the calorimeter is taken as measured only if it exceeds significantly the estimated most probable energy loss.

By combining the stand-alone tracks reconstructed in the MS with the tracks from the inner detector, considerable improvements in the momentum resolution for tracks with momenta below 100 GeV can be achieved [100]. Additionally, this

combination helps to suppress backgrounds from in flight π/K decays as well as pions that “punch-through” the calorimeter system, depositing energy in the MS. The combination is done by the STACO [101] statistical software package, which uses a χ^2 match between the stand-alone and inner detector muon candidate’s reconstructed tracks and covariance matrices. The pair of tracks with the best combined χ^2 is accepted and defined as a “combined” muon.

4.2.1 Muon Momentum and Efficiency Corrections

Muon momentum resolution, $\sigma(p)/p$, as measured by the muon system is parametrized, for a given value of η , by the equation,

$$\frac{\sigma(p)}{p} = \frac{C_0}{p_T} \oplus C_1 \oplus C_2 \cdot p_T \quad (4.1)$$

where C_0 is the coefficient corresponding to energy lost in the calorimeter, C_1 corresponds to multiple scattering and C_2 is related to the intrinsic precision on the sagitta [102].

However, the agreement of this momentum resolution between data and the MC is not in full agreement without corrections. For this reason, smearing factors are derived from $Z \rightarrow \mu\mu$ events in 2011 data [103] and provided to be applied to muons in the MC to compensate for this discrepancy⁵. Both the muon spectrometer and inner detector track are smeared and the result is propagated to the combined muon p_T measurement.

Muons in the Monte Carlo simulated events also do not fully reproduce the reconstruction efficiency measured in the data. Similar to electrons, a correction factor is applied to each Monte Carlo muon that satisfies the criteria described in the previous section. Using $Z \rightarrow \mu\mu$ events, the overall muon data/MC efficiency scale factor is found to be close to 1 with an uncertainty of 1-2% [104].

The systematic uncertainties associated with the muon momentum resolution and reconstruction efficiency corrections are presented in Chapter 9.

⁵Smearing factors are provided by the dedicated ATLAS Muon Combined Performance working group

4.3 Reconstruction of Jets

Jets are the experimental signature of quarks and gluons (partons) produced from proton-proton scattering in particle colliders. Due to postulated color confinement, free partons do not exist independently; thus as they pull away from the interaction point additional colored particles (quarks and gluons) are generated from the vacuum which combine to form colorless hadrons. This process of hadronization produces a spray of particles, usually confined to a small solid angle, with direction and energy correlated to the original parton. This tight cone of particles created by the hadronization process is what is measurable in particle detectors and is what is referred to as a jet [105; 106].

4.3.1 The Anti- k_T Jet Reconstruction Algorithm

The goal of jet reconstruction is to reconnect the energy deposited in the calorimeter to the kinematics of the partons that generated the jet. Many jet reconstruction algorithms are available in the ATLAS offline software, in this thesis, only the anti- k_T jet algorithm [107] is used.

A jet algorithm is required to be well behaved when confronted with possible QCD divergences such as infrared and collinear emissions. Infrared safety refers to the fact that perturbative calculations diverge to infinity in the limit of infinitely soft radiation. Therefore, for a jet algorithm to be infrared safe, the presence or absence of additional infinitely soft particles radiated by the primary partons should not modify the result of jet finding (e.g. the number of jets). Collinear safety refers to the fact that calculations also diverge if an outgoing parton splits into two partons traveling in parallel. Thus, jet finding should not be sensitive to particles radiated at very small angles with respect to the original parton.

The anti- k_T algorithm belongs to a class of “sequential recombination” algorithms [108] and is an example of a jet algorithm that satisfies both infrared and collinear safety requirements. In calorimeter jet finding, the algorithm begins with a list of energy clusters measured in the calorimeter. Three-dimensional energy depo-

sitions in the calorimeters are represented as topological cell clusters or “topoclusters”. These objects are built in an attempt to capture the shower of a particle while suppressing calorimeter noise. Topological clusters are groups of calorimeter cells clustered into three-dimensional energy deposits, exploiting the longitudinal and transverse calorimeter segmentation. The topocluster formation algorithm proceeds along the following steps:

- A seed cell is identified if it has a significant signal-to-noise (electronics plus pile-up) ratio above a given threshold. Specifically, it is required that $|E_{\text{cell}}| > 4 \times \sigma_{\text{noise}}$.
- All neighboring cells with $|E_{\text{cell}}| > 2 \times \sigma_{\text{noise}}$ are then added to the cluster.
- Any remaining continuous cells are added, with no energy threshold imposed.

The algorithm then defines a distance parameter between the topoclusters and a distance parameter between the clusters and beam axis,

$$d_{i,j} = \min(p_{T,i}^{-2}, p_{T,j}^{-2}) \times \frac{\Delta R}{R} \quad (4.2)$$

and

$$d_{i,\text{beam}} = p_{T,i}^{-2} \quad (4.3)$$

where p_T is the transverse momentum of the cluster considered, ΔR is the spatial distance between two clusters in $\eta - \phi$ and R is the size parameter of the algorithm: the larger R , the wider the jets. If the minimum between all $d_{i,j}$ and $d_{i,\text{beam}}$ is a $d_{i,j}$, topoclusters i and j will be recombined into a new cluster, which then replaces i and j in the list of topoclusters to be combined. Otherwise, object i is identified as a jet and not considered in the next iteration. Thus soft radiation is first clustered nearby the harder core of the process. This is repeated until none of the original clusters remain unassigned. The resulting anti- k_T jets show a regular, conical shape, experimentally desirable as it allows for a well defined jet area that can be used for pile-up subtraction [109].

4.3.2 Jet Calibration

The topoclusters used to build the jet collection have an energy that corresponds to the “electromagnetic scale”. This means that the calorimeter signals are calibrated to properly reproduce the energy lost in the calorimeter by an electron or photon. This scale has been determined by test-beam measurements for electrons and muons in the electromagnetic calorimeters [110] and more recently with $Z \rightarrow ee$ data [111]. The ATLAS calorimeter, however, is a non-compensating calorimetry system, meaning the electromagnetic response is not equivalent to the hadronic response. Due to this, the energy of hadronic jets reconstructed with topoclusters at the EM scale is $\sim 30\%$ lower than the true energy deposited. Additionally, the EM scale does not account for other detector related effects including:

- energy losses from particles crossing inactive regions of the detector (dead material),
- particles escaping the active region of the calorimeter (leakage),
- particles not included in the reconstructed jet that are part of the true jet energy (out-of-cone),
- inefficiencies in calorimeter clustering and jet reconstruction.

Therefore, an explicit additional calibration, a jet energy scale (JES), must be applied to jets reconstructed in the calorimeter to determine the original parton energy [112]. The calibration scheme applied to jets in this thesis is referred to as EM+JES calibration. The EM+JES calibration scheme is divided in four steps of corrections, each based on cluster energy, shape variables and cluster pseudo-rapidity.

- (i) A pile-up correction is applied to the EM scale clusters. This correction was extracted from 2011 data using a fit to the distribution of jet energies as a function of the number of average interactions (μ) and the number of primary vertices with at least two associated tracks (N_{pv}) [113].

- (ii) The jet position, and therefore its p_T , is shifted to correspond to the chosen primary vertex in the event. This correction does not change the jet energy.
- (iii) A calibration composed of multiple corrections is applied, affecting both the energy and direction, to correct the jet four-momentum to the particle level scale. This calibration is obtained using reconstructed calorimeter jets matched to MC particle truth jets⁶, with the simulation validated using test-beam and collision data [114]. Included is a correction for the non-compensating calorimeter response, losses due to dead regions as well as energy losses due to high energy particles punching through the calorimeter.
- (iv) A final calibration is applied only to jets reconstructed in data from in-situ measurements of the jet energy scale [115; 116]

4.3.3 Jet Vertex Fraction and Quality Criteria

The jet vertex fraction (JVF) [117; 118] is a combined variable used to reduce the influence of pile-up jets (those not originating from the primary vertex) on jet selection. The JVF quantifies the amount of pile-up energy deposited in a given jet and represents the probability that a jet came from a primary vertex. More specifically, in an event with l reconstructed tracks and n reconstructed vertices, the JVF is given by:

$$JVF(jet_i, vtx_j) = \frac{\sum_k p_T(trk_k^{jet_i}, vtx_j)}{\sum_n \sum_l p_T(trk_l^{jet_i}, vtx_n)}, \quad (4.4)$$

where for each jet i , the JVF is the track p_T fraction from vertex j . This is graphically illustrated in Figure 4.1.

Typically, a JVF is calculated with respect to the vertex with the highest sum of track transverse momenta is used, referred to as the leading primary vertex (PV). A distribution of possible JVF values is shown in Figure 4.2(a). A JVF value of

⁶The term ‘truth jets’ refers to the outgoing parton level particles generated by the Monte Carlo. This information can be used to compare with the fully reconstructed objects in the MC, after parton showering, digitization and detector simulation is applied

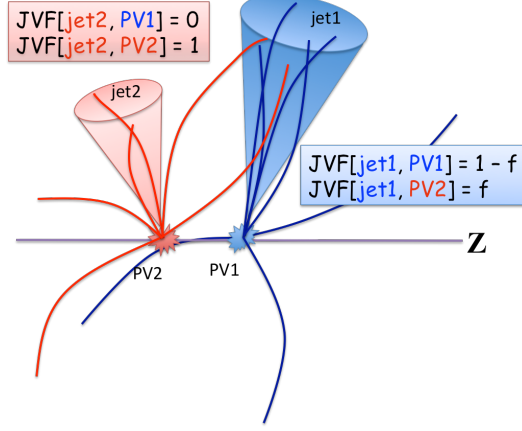


Figure 4.1: Illustration of the Jet Vertex Fraction (JVF). JVF = 1 corresponds to a jet associated only with tracks from the primary vertex.

one implies that the jet has little or no contribution from pile-up jets in the form of charged tracks. Values less than one suggest contamination of jet energy from additional tracks not associated with the selected hard-scattering interaction. Jets without matched tracks, or beyond the tracking acceptance ($|\eta| > 2.5$) have a JVF of negative one and are accepted.

Without any requirements on the JVF, the average number of jets in an event increases with the amount of reconstructed vertices (which corresponds to the amount of pile-up), as can be seen in Figure 4.2(b) (black points). A flat jet multiplicity spectrum is achieved for a requirement of $|JVF| > 0.75$. This cut is applied to all jets in this analysis, insuring a sample of jets minimally contaminated by extraneous pile-up energy.

Additional jet quality criteria are designed and imposed to reject jets that may have been poorly reconstructed due to a variety of reasons [119]. This may be the case if the jet was measured in an area of the detector with inactive regions (such as the end-cap transition) or a region with dead cells. One of these regions is referred to as the “LAr hole”⁷ and is discussed further in Chapter 9. Quality requirements are

⁷The LAr Hole is an inactive region (starting from run 180614) in the LAr electromagnetic calorimeter ($-0.1 < \eta < 1.5$ and $-0.9 < \phi < -0.5$) that not only affects the reconstruction of jets but any object that overlaps the area.

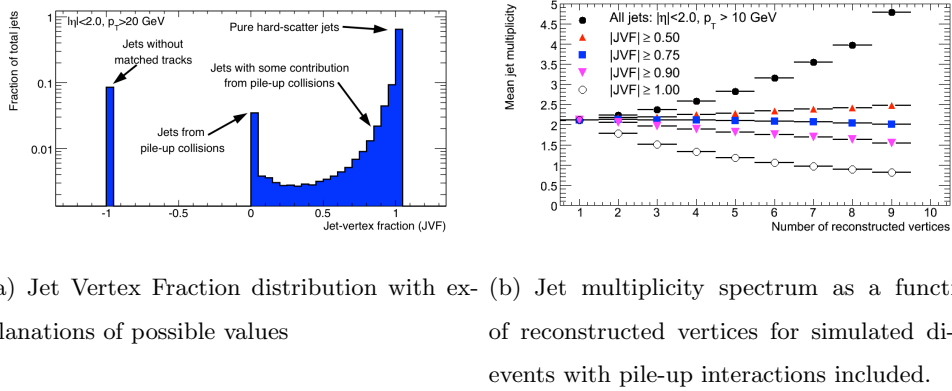


Figure 4.2: JVF distribution and effect on jet multiplicity.

also placed on the time and pulse shape measured by the calorimeter which helps prevent signal distortions. Pulse shape quality criteria reduce mismeasurements from coherent noise in the calorimeters while timing cuts help discriminate signals not associated with the bunch crossing of interest.

4.4 Missing E_T

At the LHC, the colliding proton beams have very little (effectively zero) momentum in the xy -plane at the interaction point, thus the total vector sum of the transverse momenta of all the particles produced in the collisions at the LHC is expected to be zero due to momentum conservation. However, an imbalance in the measured total E_T may signal the presence of unseen, or non-interacting, particles such as neutrinos. Thus, if the total transverse momentum of the system is summed to be non-zero, the event's missing E_T (E_T^{miss}) is defined to be equal and opposite to the measured system p_T such that the total p_T is zero with the E_T^{miss} included.

At ATLAS, and used in this thesis, the official E_T^{miss} algorithm, referred to as “refined-final” (MET_RefFinal) [120; 121; 122], is calculated from the energy deposits in calorimeter cells within $|\eta| < 4.9$ that survive a noise suppression procedure and from muons reconstructed in the muon spectrometer. The two components are calculated as:

$$E_{x(y)}^{\text{miss}} = E_{x(y)}^{\text{miss,calo}} + E_{x(y)}^{\text{miss,}\mu}. \quad (4.5)$$

4.4.1 Calculation of the E_T^{miss} calorimeter term

Calorimeter cells used in the E_T^{miss} calculation are calibrated individually according to the fully reconstructed physics object to which they are associated. This strategy allows the E_T^{miss} calculation to benefit from the high accuracy of calibrations applied to these objects, as opposed to generic calibrations of individual cells, where there is no knowledge of the source of the energy deposit. Cells that are not associated with any reconstructed and identified high- p_T object are also taken into account ($E_T^{\text{miss,CellOut-Eflow}}$). Through this classification, the E_T^{miss} calorimeter term can be written:

$$\begin{aligned} E_{x(y)}^{\text{miss,Calo}} = & E_{x(y)}^{\text{miss},e} + E_{x(y)}^{\text{miss},\gamma} + E_{x(y)}^{\text{miss},\tau} + E_{x(y)}^{\text{miss,Jets}} + \\ & E_{x(y)}^{\text{miss,SoftJets}} + E_{x(y)}^{\text{miss,Calo},\mu} + E_{x(y)}^{\text{miss,CellOut-Eflow}} \end{aligned} \quad (4.6)$$

Each term is the negative sum of the calorimeter cells associated with the parent physics object,

$$\begin{aligned} E_x^{\text{miss},j} &= - \sum_{i=1}^{N_{\text{cell}}^j} E_i \sin \theta_i \cos \phi_i, \\ E_y^{\text{miss},j} &= - \sum_{i=1}^{N_{\text{cell}}^j} E_i \sin \theta_i \sin \phi_i, \\ E_T^{\text{miss},j} &= \sqrt{(E_x^{\text{miss},j})^2 + (E_y^{\text{miss},j})^2}, \end{aligned} \quad (4.7)$$

where the index j refers to a given E_T^{miss} term (e.g. $E_T^{\text{miss},e}$, $E_T^{\text{miss,Calo}}$, $E_T^{\text{miss},\tau}$, etc.) and the variables E_i , θ_i and ϕ_i are the cell's calibrated energy, polar angle and azimuthal angle, respectively.

To account for electronic noise in the calorimeter, which can lead to mismeasurement of the E_T^{miss} , cells used in this calculation are required to be a constituent of a 3-dimensional topological cluster (as described in Section 4.3.1) which is associated with the parent object. The topocluster seed threshold values, referred to as 4/2/0, are optimized to suppress electronics noise as well as pile-up from minimum bias events [81].

If a cell used in the calculation is to be associated with a high- p_T object, it should only be associated with one object to avoid double counting. For this reason, the

cell-object association map is done in a specific order, namely: electrons, photons, hadronically decaying τ -leptons, jets and finally muons. If a cell is associated with multiple reconstructed objects, only the first association is used and thus overlap removal is accomplished at the cell level. The definitions and calibrations of the various terms in Equation 4.6 are outlined here:

- $E_{x(y)}^{miss,e}$ is reconstructed from cells in clusters associated to electrons passing the `medium++` identification requirements, with $p_T > 10$ GeV calibrated with the default “RefCalib” electron calibration [123];
- $E_{x(y)}^{miss,\gamma}$ is reconstructed from cells in clusters associated to photons that satisfy the “tight” photon quality requirement [95] and have $p_T > 10$ GeV at the EM scale;
- $E_{x(y)}^{miss,\tau}$ is from local-hadronic calibrated (LCW) [124] τ -jets with $p_T > 10$ GeV, required to satisfy “tight” τ identification [125];
- $E_{x(y)}^{miss,Jets}$ is reconstructed from cells in clusters associated with topo anti- k_T R=0.4 jets that have $p_T > 20$ GeV with the LCW and jet energy scale (JES) calibration factor applied;
- $E_{x(y)}^{miss,SoftJets}$ is reconstructed from cells in clusters associated to topo anti-kT R=0.4 jets that have $5 < p_T < 20$ GeV and LCW calibration applied;
- $E_{x(y)}^{miss,Calo,\mu}$ is the contribution to E_T^{miss} from energy lost by muons as they traverse the calorimeter; usage of this term in the calculation depends on ‘isolation’ of muons, discussed in Section 4.4.2;
- $E_{x(y)}^{miss,\text{CellOut-Eflow}}$ is calculated from the cells in LCW calibrated topoclusters which are not included in the reconstructed objects. Cluster/track matching is performed and, if a better resolution is expected, the cells in the matched cluster are removed and replaced with the track energy.

4.4.2 Calculation of the E_T^{miss} muon term

The E_T^{miss} muon term is calculated from the momenta of muon tracks reconstructed with $|\eta| < 2.7$:

$$E_{x(y)}^{\text{miss},\mu} = - \sum_{\text{muons}} E_{x(y)}^\mu \quad (4.8)$$

Combined STACO muons are used for $|\eta| < 2.5$, however only the momentum calculated by the muon spectrometer (MS) is used to avoid double counting due to energy deposited in the calorimeter.

The treatment of muon energy lost in the calorimeters depends on the isolation of the selected muon. If a muon is close to a reconstructed jet, its energy lost in the calorimeter cannot be resolved from the calorimetric energy depositions of the particles in the jet. To account for this the reconstruction algorithm treats ‘isolated’⁸ muons separately from ‘non-isolated’ muons.

- *Isolated muons:* In this case, the contribution to $E_T^{\text{miss},\mu}$ is calculated from the combined measurement of the muon spectrometer and inner detector. In this way, the term $E_T^{\text{miss,Calo},\mu}$ is not added to Equation 4.6 to avoid double counting.
- *Non-isolated muons:* If the muon is close to a jet, the momentum of the muon as calculated from the muon spectrometer only (after the energy loss in the calorimeter) is used in the $E_T^{\text{miss},\mu}$ term while $E_T^{\text{miss,Calo},\mu}$ is also included in the calorimeter E_T^{miss} term.

In the region $2.5 < |\eta| < 2.7$, where there is no matched track requirement because the inner detector measurement is not available, only the muon momentum as calculated from the muon spectrometer is used for both isolated and non-isolated cases.

⁸Isolated muons are those that have $\Delta R = \sqrt{\Delta\eta^2 + \Delta\phi^2} > 0.3$ of the nearest jet

Chapter 5

Data and Simulated Monte-Carlo Samples

5.1 Data Samples

This analysis uses data collected during the proton-proton collisions at $\sqrt{s} = 7$ TeV recorded during the 2011 LHC run. The data is divided up into data periods, such that each period defines a range of runs with a coherent configuration of the detector and trigger. Any significant changes, from run to run, to either the detector configuration, calibration, or to the trigger, is indicated by the definition of a new period.

Independent data samples are used for the electron and muon channels, referred to as the $e\nu jj$ and $\mu\nu jj$ channels, respectively. Single lepton triggers are used to record the data for these channels. In order to maximize the acceptance, the trigger chain with the lowest p_T threshold is chosen out of the triggers that are not prescaled¹. A list of the triggers employed in this analysis along with the integrated luminosity collected by the triggers after a data quality selection is applied is shown in Table 5.1. The trigger nomenclature is such that, for example, `EF_e20_medium` corresponds to an event filter (EF) trigger with an electron (`e`) p_T threshold of

¹If a trigger is ‘prescaled’, only a designated fraction of the events that pass are recorded.

20 GeV (20) and an approximation of the medium level quality criteria (`medium`) that uses the hadronic leakage and shower shapes of calorimeter clusters.

Data Period	Run Range	Luminosity Recorded [pb ⁻¹]	Electron Trigger	Muon Trigger
D-J	179710 → 186755	1679.25	EF_e20_medium	EF_mu18_MG
K	186873 → 187815	590.36	EF_e22_medium	EF_mu18_MG_medium
L-M	188902 → 191933	2431.74	EF_e22vh_medium	EF_mu18_MG_medium
Total	179710 → 191933	4701.35		

Table 5.1: The luminosity for each data sample used for this analysis [126]. The ‘vh’ trigger applies an additional cut on the hadronic core isolation (≤ 1 GeV) at L1.

Duplicate events in the electron and muon channels are avoided at the trigger selection level. For an event to be considered a muon channel event, it must trigger the corresponding muon trigger as shown in Table 5.1, with no requirement on the electron trigger. Similarly, electron channel events are required to have an electron trigger fired, however these events are also required to not have a muon trigger fired. This preserves orthogonality between the $e\nu jj$ and $\mu\nu jj$ channels without losing any efficiency, and allows for easily combining the channels during the statistical analysis.

This data quality selection is implemented through a centrally produced “good runs list” (GRL) which contains a standard set of standardized requirements for each detector subsystem to ensure good data quality [119]. Additionally the GRL requires that runs were delivered when the LHC was in a condition of stable beams: each with an energy greater than $\sqrt{s} = 3.4$ TeV. Good data quality flags are required for all detector systems critical to muon, electron and jet identification, and E_T^{miss} determination. Periods A and B are removed due to the longer bunch spacing than the rest of the data periods (75 vs 50 ns) and are negligible due to their small contribution to the total luminosity ($\sim 0.48\%$). Period C was removed due to bad data quality during data taking. This results in a full integrated luminosity of 4701.37 ± 174.02 pb⁻¹ proton-proton collisions recorded by ATLAS at the LHC during 2011.

Shown in Figure 5.1 is the event yield per pb^{-1} after basic event selection (described in Section 6.2). From this plot you can see the data period groups versus run number and an overall constant event yield.

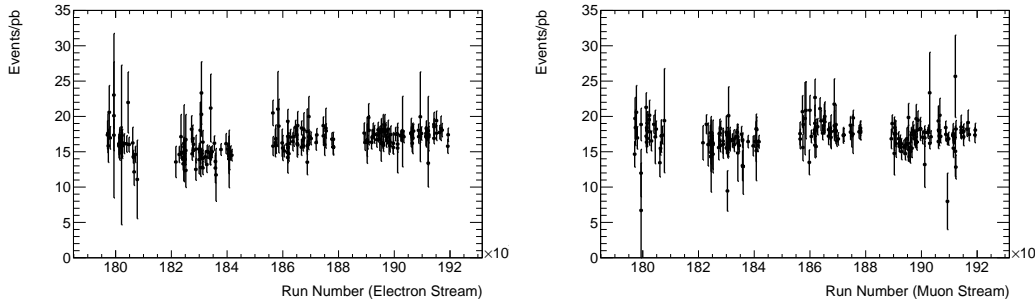


Figure 5.1: Event yield per pb^{-1} after basic event selection. Electron (left) and muon (right) channels shown.

5.2 Monte-Carlo Samples

Monte Carlo simulated events are employed to examine how certain physics processes are observed with the ATLAS detector. Simulation of proton-proton collisions is done in several steps [127]. The first of which is generating the hard process. In effect, the event generator samples the phase space of the proposed interaction. In other words, final state probabilities are calculated in a multi-dimensional hypercube which spans all of the events degrees of freedom, by evaluating the theoretical matrix element for the process. Each sample leads to a differential cross section $d\sigma$ and consequently many samples will produce an estimate of the measured total cross section. By using the relevant Feynman diagrams, a tree level matrix element generator, such as ALPGEN [128] can simulate events in this way, restricting the matrix element with a fixed number of outgoing partons.

To obtain a physically sensible description of the production process, the output of such an event generator, bare quarks and gluons, is then passed to a program such as PYTHIA [129] or HERWIG [130] to handle the resulting showering and hadroniza-

tion. By incorporating higher order effects, these simulators allow the initial partons to split and hadronize and evolve into colorless states². The MC@NLO [131] program is another package used in this analysis and is an example of a matrix element generator that also calculates the next-to-leading order corrections.

The next step is to propagate the particles through the detector while simulating the particle response to interactions with the material. This is done with the GEANT4 [132] program which takes into account the detector geometry as well as magnetic fields. GEANT4 records hits, corresponding to volumes of the detector that a generated particle passes through. It is with these hits that normal event reconstruction can be performed, however the simulated (truth) particle information is preserved for performance studies as well. Details on how reconstruction is performed on specific physics objects at ATLAS are described in Chapter 4. All the Monte Carlo samples used in this analysis, with the exception of the bulk graviton samples (discussed below), are produced with ATLAS approved event generator settings and simulated for the ATLAS detector and trigger based on GEANT4.

Standard Model background processes for this diboson resonance search include $W/Z + \text{jets}$, $t\bar{t}$, single top, and diboson (WZ , ZZ and WW) production. These processes must be produced via Monte Carlo generation and, after many corrections and cross-checks, used as predictions of what is expected to be observed by the ATLAS detector, assuming a background only (SM) hypothesis.

The samples for $Z \rightarrow ee + np$, $Z \rightarrow \mu\mu + np$ and $Z \rightarrow \tau\tau + np$, as well as for $W \rightarrow e\nu + np$, $W \rightarrow \mu\nu + np$ and $W \rightarrow \tau\nu + np$, where np refers to the number of associated partons, are produced using ALPGEN, the leading-order (LO) perturbative QCD matrix element generator. ALPGEN generates W and Z bosons with up to five additional partons in the final state ($n = 0-5$). The HERWIG package is then used for the parton showering and cluster hadronization, while JIMMY [133] is used for simulating the underlying events.

²PYTHIA and HERWIG also have the ability to calculate leading order (LO) matrix elements (ME) using perturbative QCD. They both then match the highest p_T emission from the parton shower (PS) with the ME calculation for one additional parton.

For comparative studies, inclusive samples of $W \rightarrow e\nu$, $W \rightarrow \mu\nu$, $Z \rightarrow ee$ and $Z \rightarrow \mu\mu$ events with up to five jets are simulated using SHERPA [134] event generator. SHERPA uses its own implementation of parton showers and hadronization. ALPGEN and SHERPA also employ different algorithms to match the ME generated partons to the PS after splitting. The MLM matching algorithm [135; 136] is used by ALPGEN and the CKKW [137; 138] algorithm is used by SHERPA. Observing the differences between the two samples therefore provides a useful cross-check for these background predictions.

Background samples for $t\bar{t}$ and single-top (tb , tqb , tW) production processes are generated with the MC@NLO package interfaced to JIMMY for simulation of the underlying events. A generator-level filter of at least one lepton with $p_T > 1$ GeV is applied to the $t\bar{t}$ sample to select events with at least one W -boson decaying leptonically.

Standard Model diboson backgrounds of WZ , ZZ and WW processes are simulated with HERWIG program. For each diboson process, all the possible decay channels (fully-leptonic, semi-leptonic, fully-hadronic) are generated.

Signal samples for RS1 graviton are produced with PYTHIA, which implements LO matrix elements for $2 \rightarrow 2$ processes and p_T -ordered parton showers calculated in a leading-logarithmic approximation. Multiple parton interactions are used for underlying events and the Lund string fragmentation model for hadronization. The $G_{RS1}^* \rightarrow WW \rightarrow \ell\nu jj$ graviton samples are generated for graviton masses of 500, 750, 1000, 1250 and 1500 GeV with a coupling constant of $k/\overline{M}_{pl} = 0.1$.

Signal samples for the bulk RS graviton are produced with the CALCHEP [139; 140] package which is used for the calculation of Feynman diagrams and integration over multi-particle phase space. CALCHEP implements the full $2 \rightarrow 4$ production and decay of the graviton from the WW diboson intermediate state to the $\ell\nu jj$ final state. LO events produced by CALCHEP are then processed by PYTHIA for parton showering and hadronization.

CALCHEP is used rather than PYTHIA for the parton level generation due to the fact that it retains all spin information for the graviton and W boson decays [141].

Due to the fact that the bulk RS model predicts that both W bosons will be polarized along the longitudinal direction, the net effect is higher p_T decay products compared to the unpolarized W bosons produced by PYTHIA. This leads to an expected increase in acceptance of the bulk RS model samples as compared to the RS1 model samples for low masses (e.g. $M(G^*) = 500$ GeV). However, at higher masses the acceptance of the bulk RS model drops relative to the RS1 model due to an increased jet merging rate. This effect is discussed further in Appendix A. Additionally, the production cross section for the graviton in the bulk RS model is lower than in the RS1 model as a result of the suppression of $qq \rightarrow G^*$ production mechanism; it also falls slightly faster in the bulk model as a function of graviton mass. The cross-section times branching ratios for $G^* \rightarrow \ell\nu jj$ for the original RS1 graviton as well as the bulk RS graviton are shown later in Tables 5.8 and 5.9, respectively.

As mentioned above, the simulation of the detector for these samples is not computed with the GEANT4 package like the rest of the MC, but with the fast detector simulation package, ATLFast II [142]. The ATLFast II simulation package includes only the basic information of the detector geometry, such as the sub-detector acceptance regions in η and ϕ along with the detection efficiency and resolution in those regions. The detector simulation is done by parametrizations of particle momentum and energy resolution, the actual values taken as inputs of four-momentum vectors from event generators, as well as magnetic field effects on jet reconstruction. These parametrizations are implemented as Gaussian smearing functions, as obtained from full simulation distributions.

Due to a large demand placed on ATLAS computing resources in the winter of early 2012, only a small subset of the bulk RS graviton samples were generated with full simulation, while the rest were simulated with ATLFast II to conserve available grid resources. The acceptances of the corresponding ATLFast II samples were cross-checked with the acceptances of the fully simulated samples and observed to agree within statistical uncertainty.

The bulk RS graviton $G^* \rightarrow WW \rightarrow \ell\nu jj$ signal samples were generated for graviton masses between 500 and 1500 GeV in 100 GeV steps. To bridge the po-

tential signal gaps between the generated mass points for both the RS1 and the bulk RS graviton samples, template signal samples are constructed which span the same mass range, however do so in steps of 50 GeV rather than 100 GeV. The details of the generation of these template samples is described in further detail in Section 5.2.2.

All Monte Carlo events are given the event weight accounting for the data luminosity, defined as:

$$w_i = \frac{\sigma \times B \times \varepsilon_{\text{filter}} \times \mathcal{L}_{\text{int}}}{N'_{\text{gen}}} \quad (5.1)$$

where:

- σ is the production cross section including the k -factor from LO to (N)NLO
- B is the decay branching fraction,
- $\varepsilon_{\text{filter}}$ is the Monte Carlo filter efficiency,
- \mathcal{L}_{int} is the integrated luminosity shown in Table 5.1 and
- N'_{gen} is the sum of generated event weights.

The MC@NLO generator simulates events with weights w_m equal to $\pm 1^3$ and only the sum of these weights over generated events, $N'_{\text{gen}} = \sum^{N_{\text{gen}}} w_m$, results in the expected behavior where N_{gen} is the number of generated events. The SHERPA samples used have weights between 0.1 – 1 distributed as a function of parton multiplicity to correct for event filtering at the generation stage. All other event generators simulate events with weights equal to 1, i.e, $N'_{\text{gen}} = N_{\text{gen}}$. The production cross sections for each sample are taken from the most recent and precise result available. Table 5.2 summarizes the generator used for each physics process and provides references for the quoted cross sections.

Tables 5.3-5.9 show the Monte Carlo samples used for this analysis. For each sample, the most recent production cross section multiplied by the branching ratio

³Negative weight is a unique feature of the MC@NLO generator, which arises from interference in the amplitude calculation [143].

Process	Generator	Cross Section and Reference
$W + \text{jets}$	ALPGEN [128], SHERPA [134]	14060 pb [144]
$Z + \text{jets}$	ALPGEN [128], SHERPA [134]	1070 pb [144]
$t\bar{t}$	MC@NLO [131]	164 pb [145]
Single Top ($tb + tqb + tW$)	MC@NLO [131]	4.23, 64.1, 15.6 pb [146; 147; 148]
Dibosons (WW, WZ, ZZ)	HERWIG [132]	44.9, 18.5, 5.96 pb [149; 150; 151]
RS1 Graviton (G_{RS1}^*)	PYTHIA [129]	Mass-dependent [152; 153; 23]
‘Bulk’ RS Graviton (G_{RS}^*)	CALCHEP [141]	Mass-dependent [47; 54]

Table 5.2: Short summary of the event generator employed and cross section of each physics processes

and the generator filter efficiency is shown along with the number of generated events.

Process	Cross Section (σ)	Generated
	$\times B \times \varepsilon_{\text{filter}}$ [pb]	Events (N_{gen})
$W \rightarrow e\nu + 0p$	8288.88	6952874
$W \rightarrow e\nu + 1p$	1561.14	4998487
$W \rightarrow e\nu + 2p$	452.24	3768632
$W \rightarrow e\nu + 3p$	121.82	1008947
$W \rightarrow e\nu + 4p$	30.71	250000
$W \rightarrow e\nu + 5p$	8.36	69999
$W \rightarrow \mu\nu + 0p$	8284.22	6962239
$W \rightarrow \mu\nu + 1p$	1560.55	2498593
$W \rightarrow \mu\nu + 2p$	451.79	3768737
$W \rightarrow \mu\nu + 3p$	121.71	1008446
$W \rightarrow \mu\nu + 4p$	30.74	254950
$W \rightarrow \mu\nu + 5p$	8.37	70000
$W \rightarrow \tau\nu + 0p$	8283.50	3418296
$W \rightarrow \tau\nu + 1p$	1559.36	2499194
$W \rightarrow \tau\nu + 2p$	451.63	3750986
$W \rightarrow \tau\nu + 3p$	121.84	1009946
$W \rightarrow \tau\nu + 4p$	30.72	249998
$W \rightarrow \tau\nu + 5p$	8.37	65000

Table 5.3: ALPGEN W+jets Monte Carlo samples. In the ‘Process’ column, the notation Np denotes the number of partons associated with the boson production.

Process	Cross Section (σ)	Generated
	$\times B \times \varepsilon_{\text{filter}}$ [pb]	Events (N_{gen})
$Z \rightarrow ee + 0p$	835.40	6618284
$Z \rightarrow ee + 1p$	167.95	1334897
$Z \rightarrow ee + 2p$	50.67	2004195
$Z \rightarrow ee + 3p$	13.95	549949
$Z \rightarrow ee + 4p$	3.60	149948
$Z \rightarrow ee + 5p$	1.04	50000
$Z \rightarrow \mu\mu + 0p$	835.85	6615230
$Z \rightarrow \mu\mu + 1p$	167.67	1334296
$Z \rightarrow \mu\mu + 2p$	50.41	1999941
$Z \rightarrow \mu\mu + 3p$	13.99	549896
$Z \rightarrow \mu\mu + 4p$	3.44	150000
$Z \rightarrow \mu\mu + 5p$	0.96	50000
$Z \rightarrow \tau\tau + 0p$	835.50	10613179
$Z \rightarrow \tau\tau + 1p$	168.51	3334137
$Z \rightarrow \tau\tau + 2p$	50.45	1004847
$Z \rightarrow \tau\tau + 3p$	14.06	509847
$Z \rightarrow \tau\tau + 4p$	3.49	144999
$Z \rightarrow \tau\tau + 5p$	0.96	45000

Table 5.4: ALPGEN $Z/\gamma^* + \text{jets}$ ($40 < M(ll) < 2000$ GeV) Monte Carlo samples. In the ‘Process’ column, the notation Np denotes the number of partons associated with the boson production.

Process	Cross Section (σ)	Generated
	$\times B \times \varepsilon_{\text{filter}}$ [pb]	Events (N_{gen})
$W \rightarrow e\nu$	10460.00	1699846
$W \rightarrow \mu\nu$	10460.00	1699694
$W \rightarrow \tau\nu$	10460.00	1699496

Table 5.5: SHERPA W+jets Monte Carlo samples.

Process	Cross Section (σ) \times	Generated
	$B \times \varepsilon_{\text{filter}}$ [pb]	Events (N_{gen})
$tb \rightarrow e\nu$	0.50	299948
$tb \rightarrow \mu\nu$	0.50	299998
$tb \rightarrow \tau\nu$	0.50	299899
$tqb \rightarrow e\nu$	6.97	299998
$tqb \rightarrow \mu\nu$	6.97	299999
$tqb \rightarrow \tau\nu$	6.97	299999
$tW \rightarrow \ell + X$	15.74	899694
$t\bar{t} \rightarrow \ell + X$	90.55	14943835

Table 5.6: MC@NLO single-top and $t\bar{t}$ Monte Carlo samples.

Process	Cross Section (σ)	Generated
	$\times B \times \varepsilon_{\text{filter}}$ [pb]	Events (N_{gen})
$WW \rightarrow \ell + X$	17.02	2489244
$WZ \rightarrow \ell + X$	5.54	999896
$ZZ \rightarrow \ell + X$	1.26	249999

Table 5.7: HERWIG diboson Monte Carlo samples.

Process	Cross Section (σ) $\times B \times \varepsilon_{\text{filter}}$ [pb]	Generated Events (N_{gen})
$G^* \rightarrow WW \rightarrow \ell\nu jj$ ($M = 500$ GeV; $k/\bar{M}_{\text{pl}} = 0.1$)	5.59	30000
$G^* \rightarrow WW \rightarrow \ell\nu jj$ ($M = 750$ GeV; $k/\bar{M}_{\text{pl}} = 0.1$)	0.61	30000
$G^* \rightarrow WW \rightarrow \ell\nu jj$ ($M = 1000$ GeV; $k/\bar{M}_{\text{pl}} = 0.1$)	0.13	30000
$G^* \rightarrow WW \rightarrow \ell\nu jj$ ($M = 1250$ GeV; $k/\bar{M}_{\text{pl}} = 0.1$)	0.034	30000
$G^* \rightarrow WW \rightarrow \ell\nu jj$ ($M = 1500$ GeV; $k/\bar{M}_{\text{pl}} = 0.1$)	0.008	30000

Table 5.8: PYTHIA Randall-Sundrum (RS1) graviton $G^* \rightarrow WW$ Monte Carlo samples.

Process	Cross Section (σ)	Generated
	$\times B \times \varepsilon_{\text{filter}} [\text{pb}]$	Events (N_{gen})
$G_{\text{bulk}}^* \rightarrow WW \rightarrow \ell\nu jj$ ($M = 500 \text{ GeV}$)	1.241	15000
$G_{\text{bulk}}^* \rightarrow WW \rightarrow \ell\nu jj$ ($M = 600 \text{ GeV}$)	0.37723	15000
$G_{\text{bulk}}^* \rightarrow WW \rightarrow \ell\nu jj$ ($M = 700 \text{ GeV}$)	0.14048	15000
$G_{\text{bulk}}^* \rightarrow WW \rightarrow \ell\nu jj$ ($M = 800 \text{ GeV}$)	0.06012	15000
$G_{\text{bulk}}^* \rightarrow WW \rightarrow \ell\nu jj$ ($M = 900 \text{ GeV}$)	0.02769	15000
$G_{\text{bulk}}^* \rightarrow WW \rightarrow \ell\nu jj$ ($M = 1000 \text{ GeV}$)	0.01389	15000
$G_{\text{bulk}}^* \rightarrow WW \rightarrow \ell\nu jj$ ($M = 1100 \text{ GeV}$)	0.00712	15000
$G_{\text{bulk}}^* \rightarrow WW \rightarrow \ell\nu jj$ ($M = 1200 \text{ GeV}$)	0.00385	15000
$G_{\text{bulk}}^* \rightarrow WW \rightarrow \ell\nu jj$ ($M = 1300 \text{ GeV}$)	0.00215	15000
$G_{\text{bulk}}^* \rightarrow WW \rightarrow \ell\nu jj$ ($M = 1400 \text{ GeV}$)	0.00123	15000
$G_{\text{bulk}}^* \rightarrow WW \rightarrow \ell\nu jj$ ($M = 1500 \text{ GeV}$)	0.00073	15000

Table 5.9: CALCHEP ‘bulk’ Randall-Sundrum (RS) graviton $G_{\text{bulk}}^* \rightarrow WW$ Monte Carlo samples with ATLFast II simulation.

5.2.1 Pile-up Reweighting

In 2011, the LHC bunch structure led to numerous interactions per bunch crossing, known as “pile-up”. Because of these additional interactions, more charged particles traverse the tracking detectors and more energy is deposited in the calorimeter. To account for this, the Monte Carlo hard-scatter events include a number of additional minimum bias, or pile-up, pp interactions to simulate the same effect in the data.

The number of these pile-up interactions per bunch crossing (Bx) is governed by Poisson statistics with a mean value of $\langle \mu \rangle$ that is proportional to the instantaneous luminosity of the colliding proton bunches. The four conditional setups, as described in Section 5.2, also simulate different pile-up conditions, using different $\langle \mu \rangle$ values as measured for the corresponding periods. A centrally produced pile-up reweighting tool is used to adjust the distribution of the Monte Carlo $\langle \mu \rangle$ values to those for the data. The average number of interactions for the four different setups as simulated in the Monte Carlo samples as well as the measured values in the data for the periods B–K and L–M are shown in Fig. 5.2.

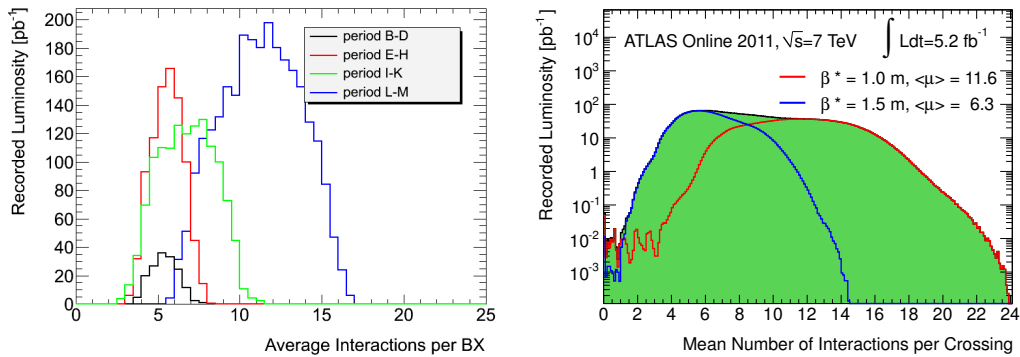


Figure 5.2: Average number of interactions for the four different setups in the Monte Carlo simulations (left) and measurement in the data divided in periods B–K and L–M (right).

5.2.2 Signal Templates for $G^* \rightarrow WW \rightarrow \ell\nu jj$

As previously mentioned, fully simulated RS1 G^* samples were only available for five mass points: $M(G^*) = 500, 750, 1000, 1250, 1500$ GeV. If just these mass points were used to extract a final result, it is possible that a real signal in data, with an intermediate value of mass, might be hidden from this calculation and thus missed. To account for this, a set of signal templates with masses in between the fully simulated mass points, in steps of 50 GeV, are created. The method described in this section is used to create signal templates for the bulk RS G^* as well.

To obtain these templates, the reconstructed $\ell\nu jj$ mass from each available fully simulated signal sample was fitted to a Crystal Ball function [154]. This Crystal Ball function is implemented in RooFit [155] and has 4 parameters along with its absolute normalization N. The function is described as

$$CB(x; a, n, \bar{x}, \sigma) = N \cdot \begin{cases} \exp\left(-\frac{(x-\bar{x})^2}{2\sigma^2}\right), & \text{for } \frac{x-\bar{x}}{\sigma} > -a \\ A \cdot (B - \frac{x-\bar{x}}{\sigma})^{-n}, & \text{for } \frac{x-\bar{x}}{\sigma} \leq -a \end{cases} \quad (5.2)$$

where

$$A = \left(\frac{n}{|a|}\right)^n \cdot \exp\left(-\frac{|a|^2}{2}\right) \quad (5.3)$$

and

$$B = \frac{n}{|a|} - |a|. \quad (5.4)$$

For the fitting, the n parameter was arbitrarily set and fixed to 2 because the shape of the tail of the Crystal Ball function can be appropriately controlled solely by varying the a parameter. The a parameter, or ‘join parameter’, determines the transition between the gaussian component of the Crystal Ball function and its exponential tail.

Once the fits are performed on the available fully simulated samples, the mean \bar{x} , the width σ and the a parameter are then extracted from the fully simulated distributions and their trend, as a function of M_{G^*} , are fitted to simple functions: the mean of the distribution is fitted linearly with $f(x) = p_0 + p_1x$, the width is also fitted with a linear function, $f(x) = p_0 + p_1x$, and finally the tail parameter a is

fitted to the function $f(x) = \frac{p_0}{p_1 x^2} + p_2 x$. Figure 5.3 and Figure 5.4 show the Crystal Ball fits to the fully simulated samples in the $e\nu jj$ and $\mu\nu jj$ channels respectively and likewise, Figure 5.5 and Figure 5.6 show the fits to the Crystal Ball parameters across the mass range for each channel. Good agreement has been observed for 500, 750, 1000, 1250, and 1500 GeV mass points. These parameter fits are then used to extrapolate the form of the signal for mass points between 500 and 1500 GeV in steps of 50 GeV.

To mirror the statistical uncertainties found in the available fully simulated samples, a substitute statistical uncertainty was constructed for each template under the assumption that it had been obtained with a 30,000 event dataset (15,000 events for the bulk RS graviton templates). This is chosen to match the number of events in the fully simulated samples.

As for the systematic uncertainties, each upward and downward systematic fluctuation, sometimes referred to as ‘positive’ and ‘negative’ modulations, was fitted and normalized independently. In other words, the above extrapolation procedure was reproduced for each systematic uncertainty separately, thus reproducing all possible shape uncertainties across all extrapolated mass points.

The template acceptances were extrapolated from a fit to the acceptances of the fully simulated samples channel-by-channel, using a Landau distribution; chosen due to its empirical fit of the acceptance shape (a Gaussian with an exponential tail is used for the bulk RS templates). Figure 5.7 shows the fit and acceptance values obtained in the $e\nu jj$ channel as an example, whereas Table 5.10 shows the signal cross-section and extrapolated acceptances used for all channels. The acceptance drop starting from above the 750 GeV mass point results from the falling signal cross-section at higher masses in conjunction with the merging of the two jets into one unresolvable jet.

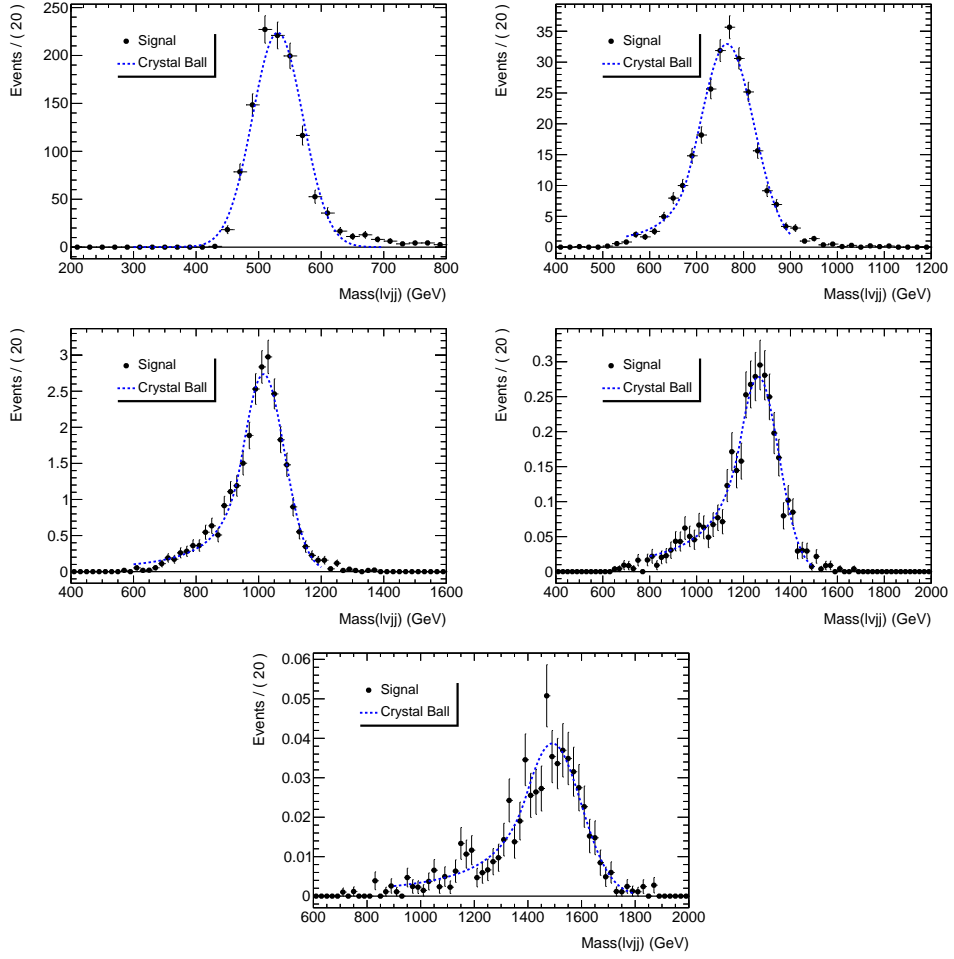


Figure 5.3: Full-simulated G^* samples ($e\nu jj$) with Crystal Ball functional fit for masses 500 GeV (upper-left), 750 GeV (upper-right), 1000 GeV (middle-left), 1250 GeV (middle-right) and 1500 GeV (bottom row). Crystal Ball parameters obtained by interpolating the full-simulated sample distributions as explained in the text.

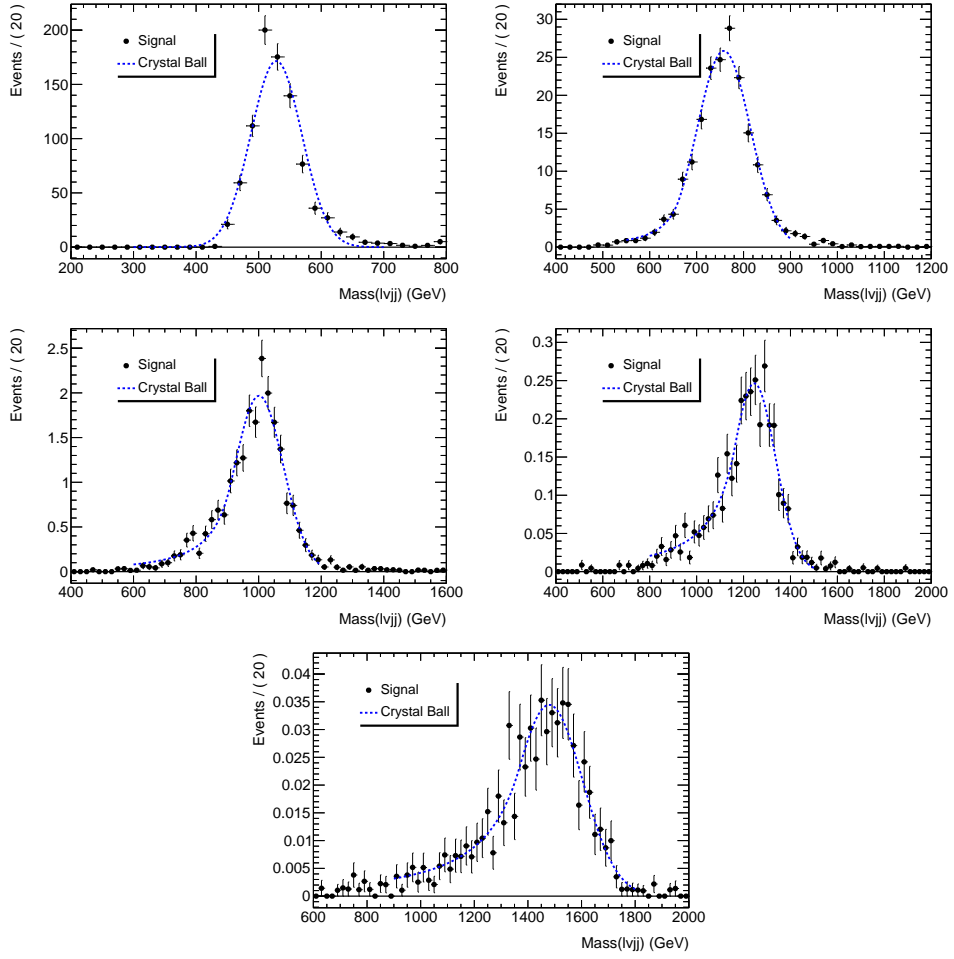


Figure 5.4: Full-simulated G^* samples ($\mu\nu jj$) with Crystal Ball functional fit for masses 500 GeV (upper-left), 750 GeV (upper-right), 1000 GeV (middle-left), 1250 GeV (middle-right) and 1500 GeV (bottom row). Crystal Ball parameters obtained by interpolating the full-simulated sample distributions as explained in the text.

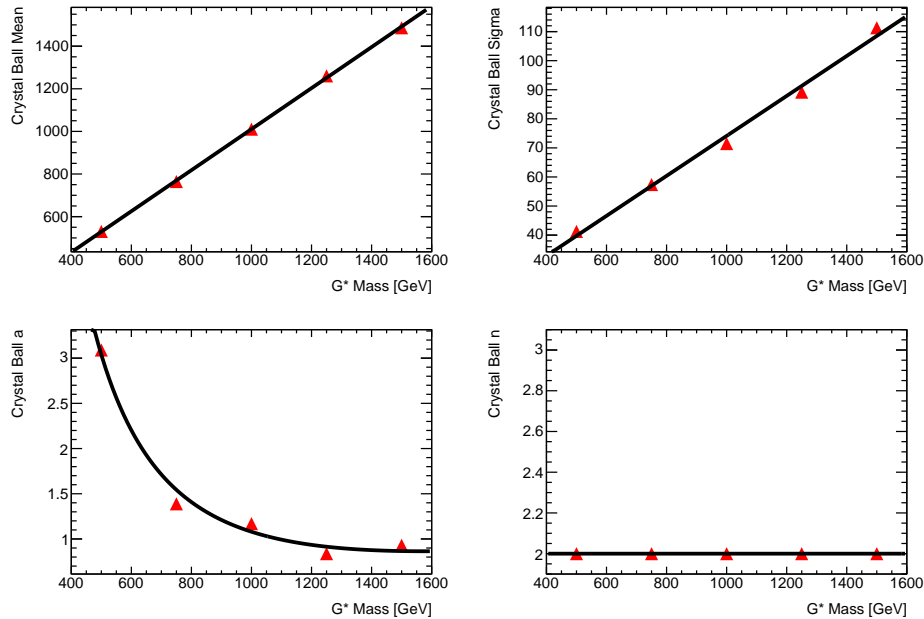


Figure 5.5: Fits of Crystal Ball parameters across full-simulated $G^* \rightarrow e\nu jj$ shown vs $M(G^*)$ shown. From left to right and top to bottom are the obtained fits for the mean, the width σ , the a , and the n of the Crystal Ball shown in Figure 5.3. Again, the parameter n was fixed to 2, hence no actual fit was performed.

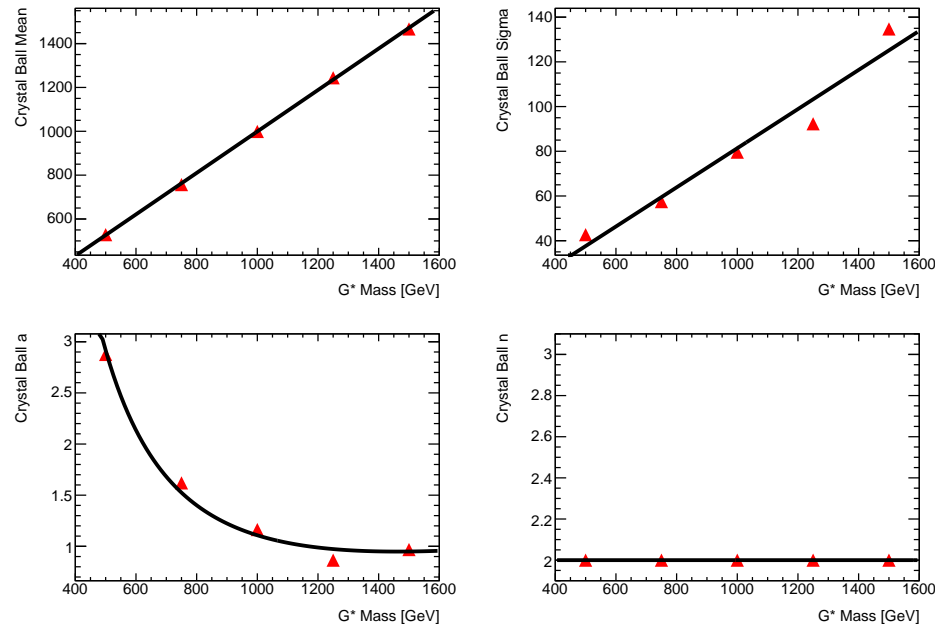


Figure 5.6: Fits of Crystal Ball parameters across full-simulated $G^* \rightarrow \mu\nu jj$ vs $M(G^*)$ shown. From left to right and top to bottom are the obtained fits for the mean, the width σ , the a , and the n of the Crystal Ball shown in Figure 5.4. Again, the parameter n was fixed to 2, hence no actual fit was performed.

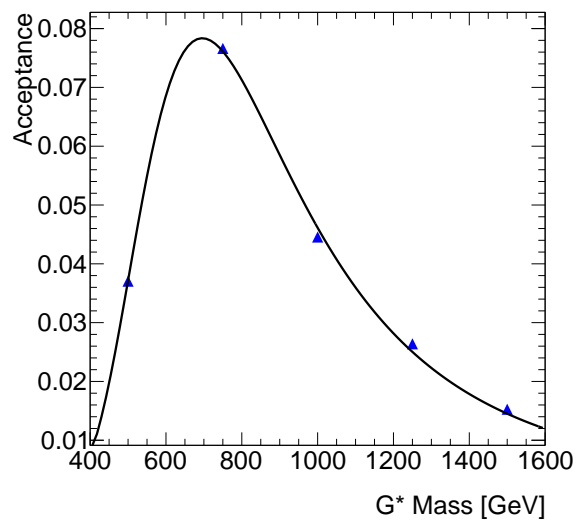


Figure 5.7: Landau functional fit (in black) to the acceptances in the $e\nu jj$ channel using to the full-simulated G^* samples (in blue) with masses 500, 750, 1000, and 1500 GeV. Acceptances of template signal distributions were extrapolated from fit.

Table 5.10: Summary of cross-sections times branching ratio and acceptances per channel used to derive cross section limits at intermediate M_{G^*} mass values, where fully simulated samples were non available.

G^* Mass [GeV]	$\sigma \times B$ [pb]	Acceptance		
		$e\nu jj$	$\mu\nu jj$	Average
500	5.593	0.045	0.034	0.040
550	4.597	0.065	0.048	0.057
600	3.601	0.081	0.058	0.070
650	2.643	0.089	0.065	0.077
700	1.648	0.091	0.067	0.079
750	0.614	0.089	0.068	0.079
800	0.514	0.082	0.064	0.073
850	0.413	0.075	0.059	0.067
900	0.313	0.067	0.054	0.061
950	0.212	0.060	0.049	0.055
1000	0.127	0.051	0.041	0.046
1050	0.095	0.047	0.040	0.044
1100	0.078	0.041	0.036	0.039
1150	0.061	0.036	0.032	0.034
1200	0.044	0.032	0.029	0.031
1250	0.034	0.030	0.027	0.029
1300	0.023	0.026	0.023	0.025
1350	0.019	0.023	0.021	0.022
1400	0.015	0.021	0.019	0.020
1450	0.012	0.018	0.017	0.018
1500	0.008	0.018	0.018	0.018

Chapter 6

Event Selection

This chapter presents the general methodology behind the search for a high-mass WW resonance decaying to the $\ell\nu jj$ final state. An overview of the analysis steps is given in Section 6.1. Following the review, the event preselection criteria are outlined in Section 6.2 and the analysis signal region is defined in Section 6.3.

6.1 Analysis Overview

Diboson resonance events with a mass greater than 500 GeV are characterized by a pair of highly boosted vector bosons. To separate this final state signature from background, this analysis searches for such pairs of W bosons, one of which decays leptonically ($\ell\nu$) while the other decays hadronically (jj). Since the graviton is expected to have high mass, both of the decay bosons are likely to have high transverse momentum. This leads to the minimally distinguishing characteristic of a high- p_T resonance in the lepton-neutrino system ($W \rightarrow \ell\nu$) and at least two high- p_T jets. The analysis proceeds according to the following steps:

1. Select events with at least one high p_T lepton, large E_T^{miss} , and at least two jets in both the data and Monte Carlo. The quality requirements on these objects have been discussed in Chapter 4 while the analysis specific threshold and geometric requirements are outlined in Section 6.2.

2. Reject QCD dijet-like events with the application of a set of two “triangle cuts”, as described in Section 6.2.
3. Reweight ALPGEN W +jets sample to match generator level $p_T(W)$ distribution from SHERPA W +jets sample. Motivation and details are given in Section 7.1.
4. Estimate multi-jet background by determining the fraction of fake lepton events in the data. Events which pass a loose lepton quality cut, but do not pass the lepton quality cut for this analysis are used to model the fake background. The normalization is determined by fitting the Monte Carlo-based backgrounds and the fake background to the data in a signal free region as described in Section 7.2.
5. Define a set of cuts that efficiently select a signal ($M > 500$ GeV) with a $\ell\nu jj$ final state. These ‘signal region’ cuts are defined in Section 6.3
6. Compare the data with the background for several important differential distributions after $\ell\nu jj$ preselection cuts to determine if the background model correctly reproduces the data. These preselection yields and distributions can be found in Section 7.3.
7. A $t\bar{t}$ control region is defined in Section 7.4. This control region is used to determine the level of agreement between the data and the $t\bar{t}$ model to gain confidence in the Monte-Carlo background prediction.
8. W/Z +jets Monte Carlo-based backgrounds are normalized to the data using sidebands in the dijet mass distribution in a signal control region, as described in Section 7.5.
9. The data and background model are compared after applying the signal selection cuts presented in Section 6.3. The compatibility of the background model with the data in the signal region is presented in Section 8.1 followed by a discussion of the systematic uncertainties in Chapter 9.

10. Finally, the methodology of the statistical analysis of the search results is outlined in Chapter 10, before presenting the final results in terms of graviton cross section and mass exclusion limits in Chapter 11.

6.2 Preselection Criteria

This analysis selects a final state with a single high p_T lepton (electron or muon) and two high p_T jets. The p_T thresholds and object quality criteria are the following:

- One isolated **tight++** electron with $p_T > 30$ GeV (known as the $e\nu jj$ channel)
or
- One isolated **combined** muon with $p_T > 30$ GeV (known as the $\mu\nu jj$ channel).
- At least two jets with the leading jet $p_T > 100$ GeV and the second leading jet $p_T > 40$ GeV. Both jets are required to be central with $0 < |\eta| < 2.8$.
- The $e\nu jj$ channel rejects events with two or more electrons with $p_T > 20$ GeV that satisfy both **medium++** and *b*-layer requirements, or any isolated muons with $p_T > 20$ GeV.
- The $\mu\nu jj$ channel vetos events with additional isolated muons with $p_T > 20$ GeV or one or more electrons with $p_T > 20$ GeV satisfying both **medium++** with *b*-layer requirements.
- Both channels require $E_T^{\text{miss}} > 40$ GeV.

Examples of Monte Carlo lepton and leading jet distributions after the application of these selection criteria are shown in Figure 6.1 and Figure 6.2 for the electron and muon channels respectively.

Additionally, a “triangle-cut” is applied at this stage to reduce the QCD multi-jet background; details of this background are further discussed in Section 7.2. An example of this cut is shown in Figure 6.3. An event is rejected if it is found to lie within a triangle defined by the difference between the lepton ϕ and the ϕ of

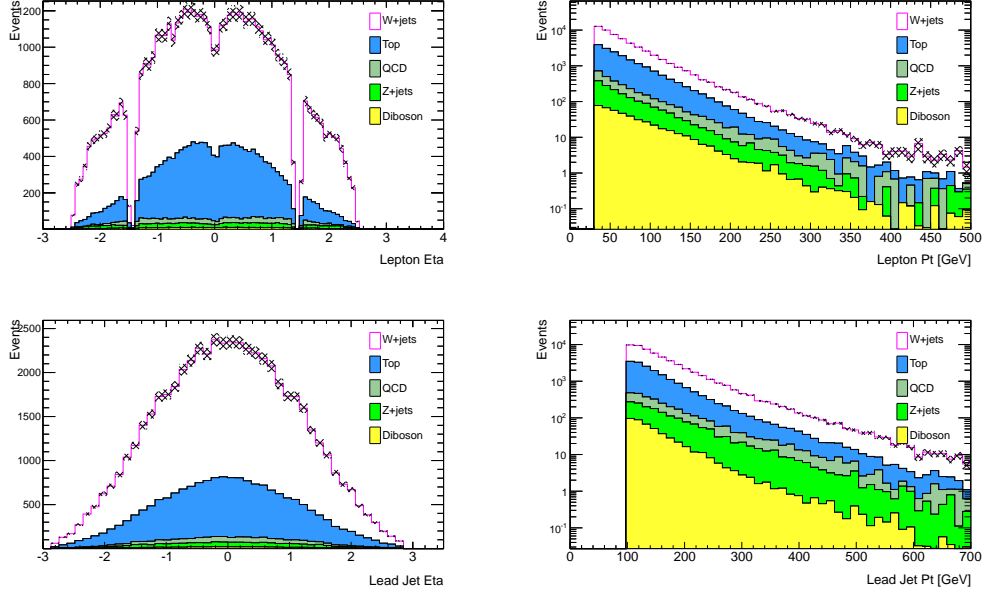


Figure 6.1: Preselection MC distributions of η (left) and p_T (right) in the $e\nu jj$ channel. Electron distributions are shown on the top row while the same distributions are shown for the leading jet in the event on the bottom row. The black hatched area is the MC statistical and luminosity uncertainty.

the E_T^{miss} on one axis and the E_T^{miss} on the other axis. The z -axis represents the number of events, however the overall value shown in the plots is arbitrary as they are presented for illustrative purposes only. The areas in which an event is vetoed are labelled ‘REJECT’ in the figures. Specifically, a ‘lower’ triangle is defined by a line that intersects the the $\Delta\Phi_{\text{lepton}} - E_T^{\text{miss}}$ (y) axis at 1.5 and the E_T^{miss} (x) axis at 75 GeV. Events that lie ‘below’ this boundary are removed. Similarly, an ‘upper’ triangle is defined by a line intersecting the y axis at 2 and has an x value of 75 GeV when y is π . Events that fall ‘above’ this axis are also removed. Both ‘upper’ and ‘lower’ triangle cuts are applied to the $e\nu jj$ channel however only the ‘lower’ cut is applied to the $\mu\nu jj$ channel. It is clear from these distributions that little signal is lost by this requirement, an example cut-flow for RS1 G^* and bulk RS G^* -boson signal efficiency, including this triangle cut, are shown in Tables 7.3 and 7.4 .

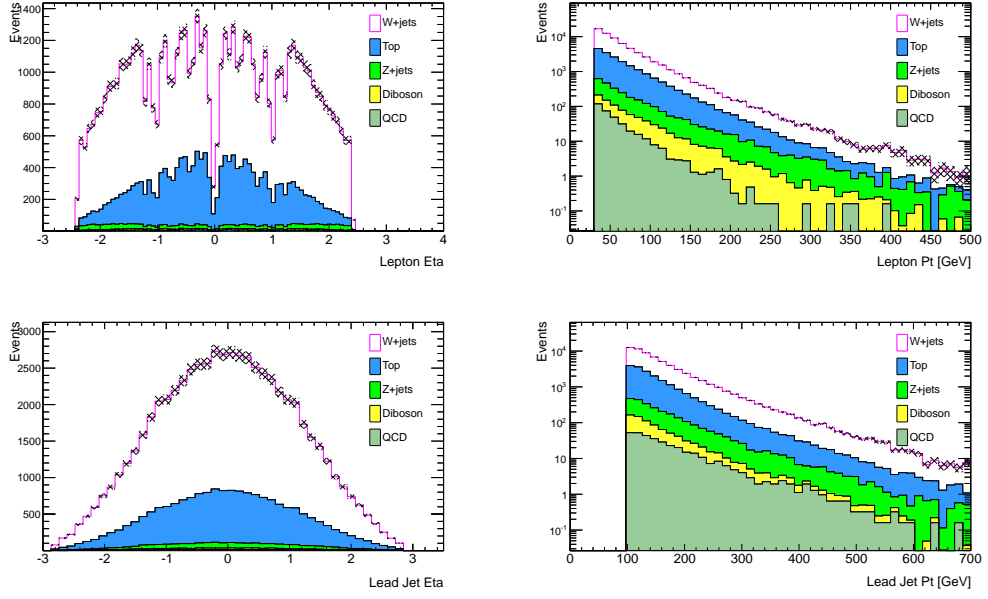


Figure 6.2: Preselection MC distributions of η (left) and p_T (right) in the $\mu\nu jj$ channel. Muon distributions are shown on the top row while the same distributions are shown for the leading jet in the event on the bottom row. The black hatched area is the MC statistical and luminosity uncertainty.

Using these selection cuts, the dominant backgrounds to this analysis are $W + \text{jets}$ and $t\bar{t}$ production with $Z + \text{jets}$, QCD multijet, single top (tb , tqb , tW), and diboson (WW , WZ , ZZ) production as subdominant backgrounds. All backgrounds except multijets are modeled using Monte Carlo events. Details of the production of these MC backgrounds including the generators used as well as the cross section to which the samples are normalized, have been described in Chapter 5.

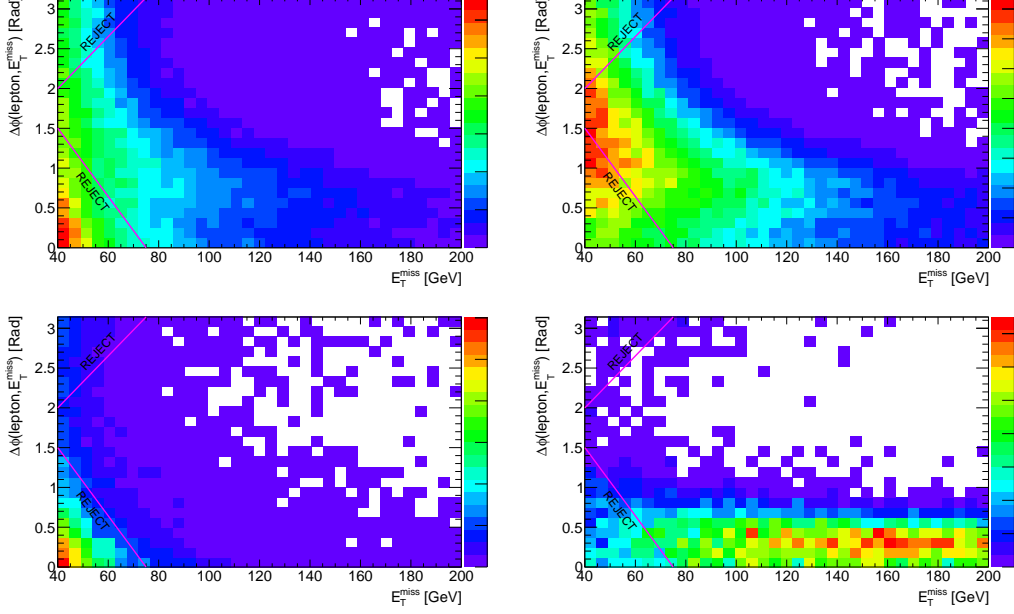


Figure 6.3: Examples of the “triangle cuts” applied in the $e\nu jj$ channel. The top left figure shows the plane defined by the difference between the lepton ϕ and the ϕ of the E_T^{miss} on one axis and the E_T^{miss} on the other axis for the preselected data. The top right plot shows the same distribution for $W + \text{jets}$ Monte Carlo events. The bottom left and bottom right plots show the same for the data-driven QCD multijet background estimation and G^* signal, respectively.

6.3 Signal Region Definition

The diboson resonance signal is characterized by two highly boosted bosons (WW or WZ), with one W boson decaying leptonically ($\ell\nu$), and the other W boson decaying to hadrons (jj). Thus, cuts on the p_T of the preselected leptonic W is made as well as a cut on the p_T of the hadronic W . Additionally, the invariant mass of the dijet system ($M(jj)$) is used as a discriminating variable to separate signal from background due to the fact that the mass distribution from two jets which are products of a heavy boson decay is likely to be peaked at the mass of the boson, while the same distribution from the proposed background processes have no such

shape¹. Thus the signal region is defined with the following criteria:

- **Signal Region:**

- $p_T(jj) \geq 200$ GeV
- $p_T(\ell\nu) \geq 200$ GeV
- $65 \leq M(jj) \leq 115$ GeV

Monte Carlo distributions of these variables, which define the signal region for signal masses of $M > 500$ GeV, are shown below in Figures 6.4 and 6.5.

As a final step, the data is compared with the background expectation in this region using the diboson invariant mass. To calculate the invariant mass of the system, the z -component of the decay neutrino must be solved for. This is done by requiring the invariant mass of the lepton and neutrino equal that of the W boson. If the solution to the resulting quadratic equation for the neutrino p_z is imaginary, the real part is taken. If there is more than one solution, the result with the smallest absolute value of neutrino p_z is used.

¹The values used for the dijet mass window cut are based on a broader analysis, of which the results presented by this thesis are a subset. This analysis included both WW/WZ as possible final states and thus set limits on an additional charged heavy vector boson resonances, namely $W'_{SSM+Egm} \rightarrow W^\pm Z$ [156].

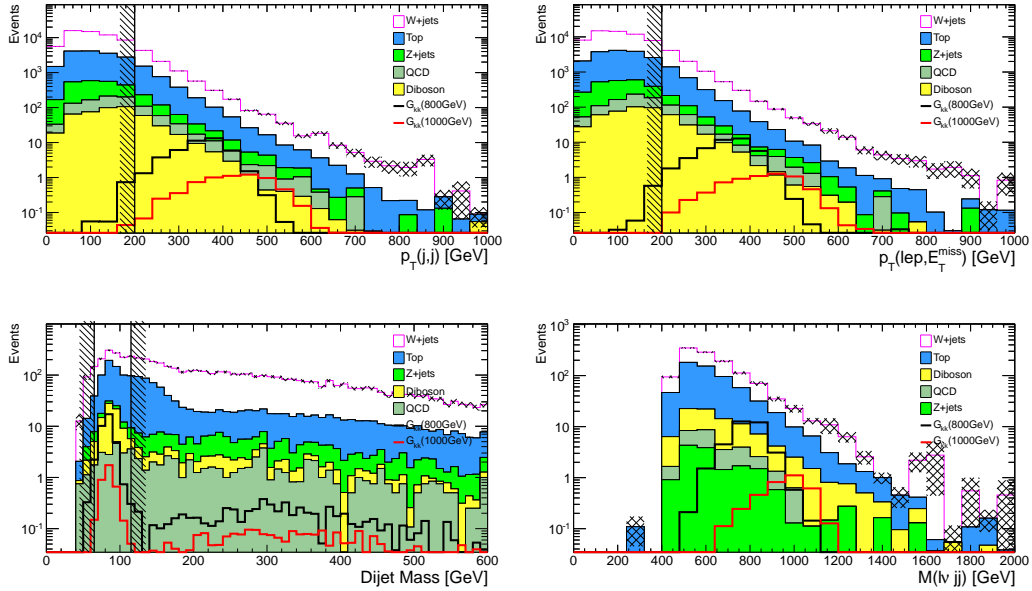


Figure 6.4: Signal region MC distributions in the $\mu\nu jj$ channel with cuts shown as hatched lines. Distributions of the dijet p_T (top left) and the lepton- E_T^{miss} p_T (top right) after preselection cuts are shown. The dijet mass (bottom left) and invariant mass of the $\ell\nu jj$ system (bottom right) after cuts are also shown. Distributions for two bulk RS Graviton signals ($M_{G^*} = 800$ GeV and $M_{G^*} = 1000$ GeV) are included.

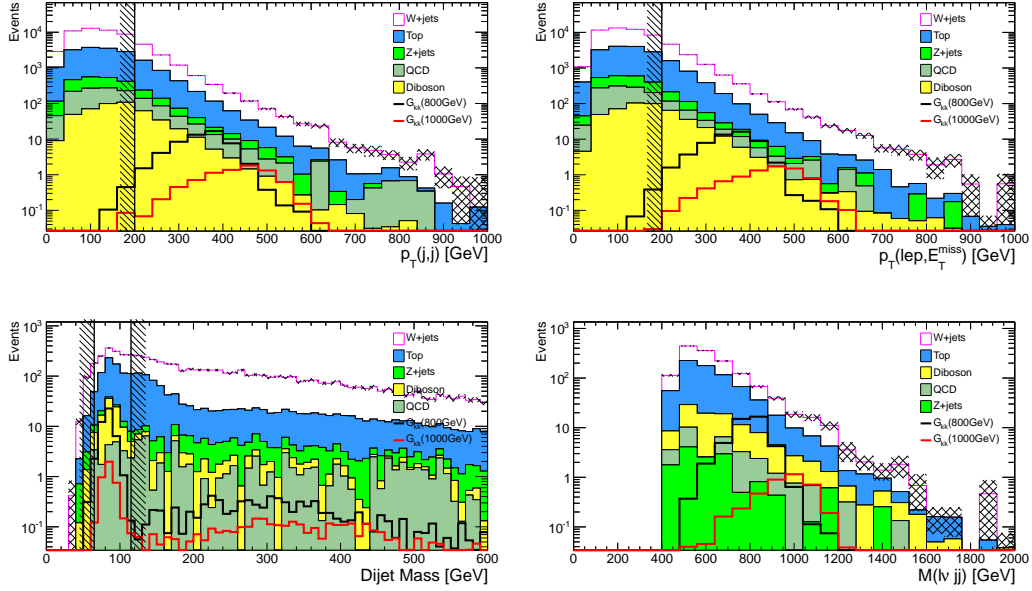


Figure 6.5: Signal region MC distributions in the $evjj$ channel with cuts shown as hatched lines. Distributions of the dijet p_T (top left) and the lepton- E_T^{miss} p_T (top right) after preselection cuts are shown. The dijet mass (bottom left) and invariant mass of the $\ell\nu jj$ system (bottom right) after cuts are also shown. Distributions for two bulk RS Graviton signals ($M_{G^*} = 800$ GeV and $M_{G^*} = 1000$ GeV) are included.

Chapter 7

Background Estimation and Control Regions

The following sections describe the modeling of background processes that were used in this analysis. In particular, a procedure to reweight ALPGEN W +jets Monte Carlo events due to mis-modeling at high W boson p_T is described in Section 7.1. Next, the data driven multijet background modeling and normalization procedure is described in Section 7.2. After these corrections are implemented, the agreement between data and Monte Carlo is presented in Section 7.3 after applying the analysis preselection criteria to the events. Before the data is surveyed in regions of phase space with high signal-to-background ratios, two background-dominated control regions are created to show the level of agreement between the data and the particular background. These control regions are described in Section 7.4, and Section 7.5. Finally, the sidebands of the signal control region are used to derive a correction factor to be applied to the W +jets background estimation in the signal region.

7.1 ALPGEN W +jets Reweighting

After the single-lepton plus two jet and missing transverse momentum selections are made, a large discrepancy between data and the predicted MC background is observed in many distributions. This discrepancy is most predominant at high

p_T and is clearly seen in the ‘sloping’ (data-MC)/MC ratio plot in the dijet p_T and lepton + E_T^{miss} p_T distributions (see Figure 7.1). It is also apparent in the lepton transverse momentum, shown in Figure 7.2, and in the missing transverse momentum distributions, shown in Figure 7.3.

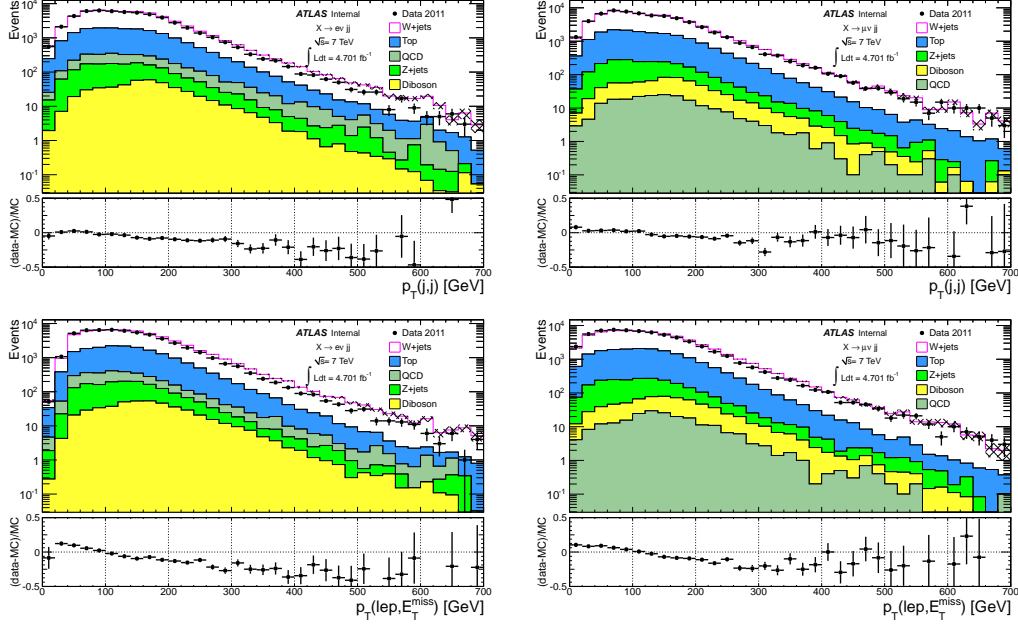


Figure 7.1: Comparison of data and background after $\ell\nu jj$ preselections. The dijet p_T (top) and lep+ E_T^{miss} p_T (bottom) in both the electron (left) and muon (right) channels are shown.

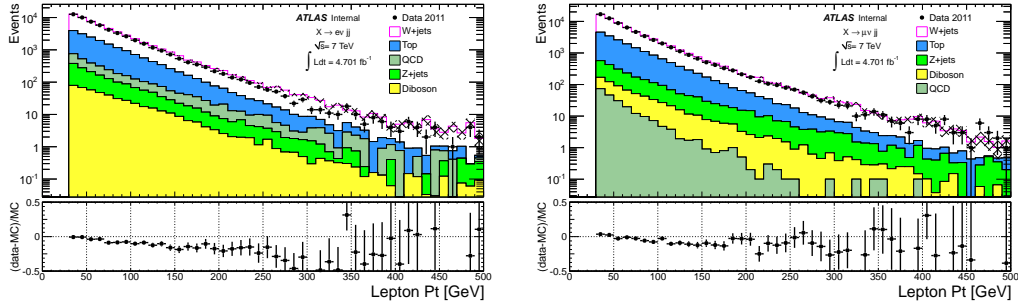


Figure 7.2: Comparison of data and background after $\ell\nu jj$ preselections. The electron p_T (left) and muon p_T (right) are shown.

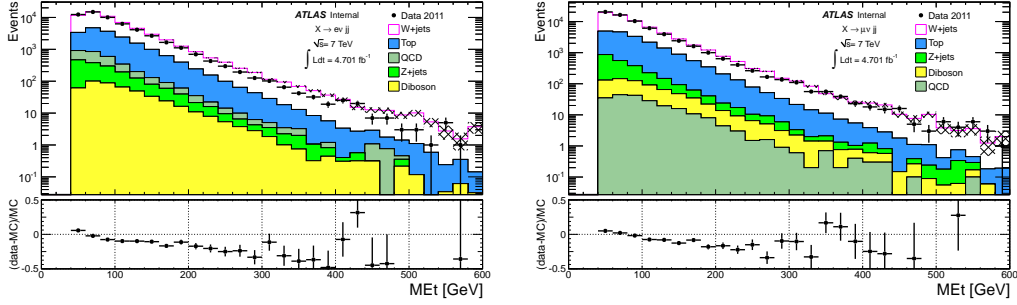


Figure 7.3: Comparison of data and background after $\ell\nu jj$ preselections. The missing transverse momentum for the electron (left) and muon (right) channel is shown.

This shape is attributed to the ALPGEN W/Z +jets MC sample overestimating the W/Z +jets cross section with increasing values of W/Z pt. This behavior has been observed and documented in both the $WZ \rightarrow \ell\ell jj$ exotic diboson resonance analysis [59] as well as the single lepton with jets and missing transverse momentum SUSY analysis [157]. In this analysis, the same re-weighting procedure as employed by the SUSY single-lepton analysis has been followed to correct for the observed discrepancies.

It has been observed that SHERPA W/Z +jets MC backgrounds match the data better than the ALPGEN samples in the high transverse momentum regions. Shown in Figures 7.4 to 7.6 are comparison plots with ALPGEN and SHERPA W/Z +jets backgrounds on the same axis. It is clear that although the data/MC agreement is better using the SHERPA samples, they lack statistics at higher values of transverse momentum, which is the area of interest for this analysis. Additionally, limitations on available ATLAS computing resources prohibited regeneration of SHERPA samples with necessary number of generated events. For these reasons, by re-weighting the generator level W p_T distribution of the ALPGEN sample to match that of the SHERPA sample, it is possible to benefit from both the statistics of the ALPGEN sample and the shape-agreement of the SHERPA sample.

To understand the observed discrepancies, a generator level comparison was carried out by the previously mentioned SUSY analysis. Figure 7.7, from this study, shows a comparison of the true transverse momentum of the W boson in the electron

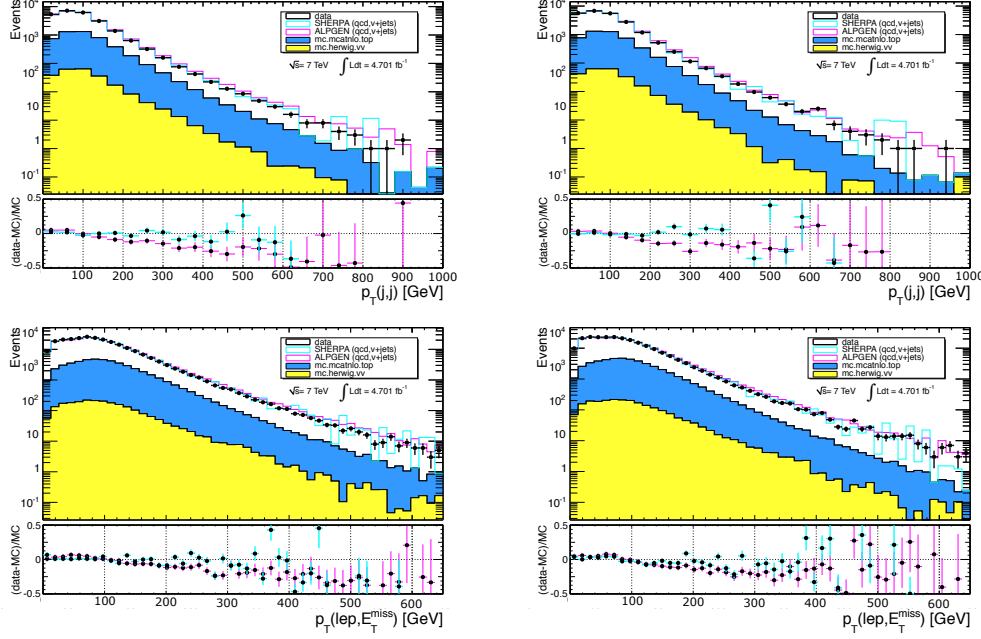


Figure 7.4: Comparison of data with both ALPGEN and SHERPA W/Z +jets MC samples after $\ell\nu jj$ preselections. The dijet p_T (top) and lep+ E_T^{miss} p_T (bottom) in both the electron (left) and muon (right) channels are shown.

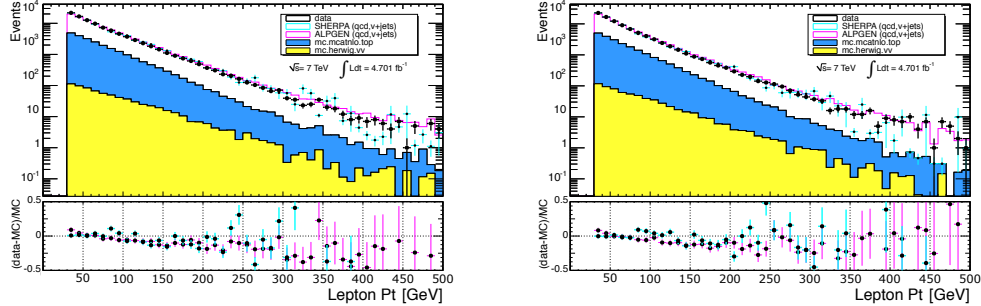


Figure 7.5: Comparison of data with both ALPGEN and SHERPA W/Z +jets MC samples after $\ell\nu jj$ preselections. The electron p_T (left) and muon p_T (right) are shown.

and muon channel. A similar slope in the data/MC ratio is observed comparing generator level objects as is observed comparing reconstructed ALPGEN variables with data. Comparable shapes are observed in the lepton p_T distribution and E_T^{miss} dis-

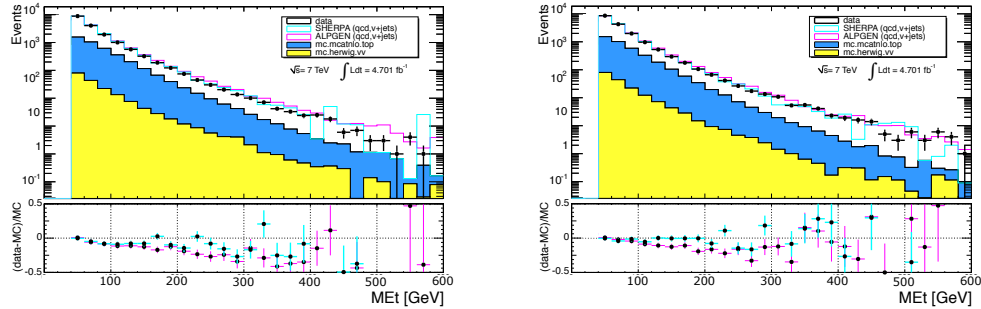


Figure 7.6: Comparison of data with both ALPGEN and SHERPA W/Z +jets MC samples after $\ell\nu jj$ preselections. The missing transverse momentum for the electron (left) and muon (right) channel is shown.

tributions shown in Figure 7.8 and Figure 7.9 respectively.

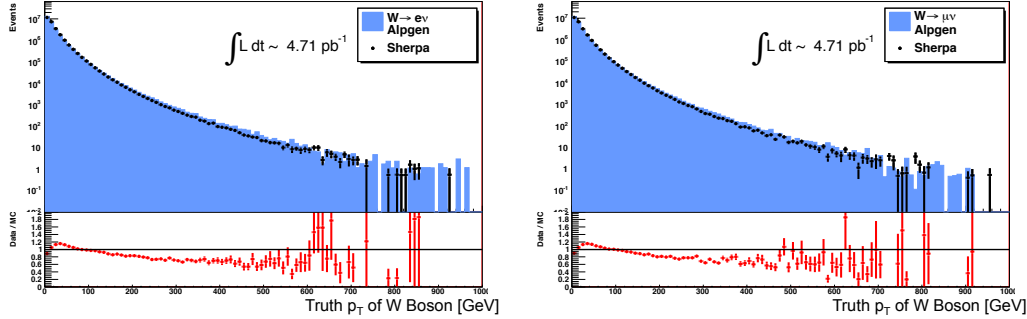


Figure 7.7: Comparison of data with both ALPGEN and SHERPA W/Z +jets MC samples after $\ell\nu jj$ preselections. The truth W boson p_T for the electron (left) and muon (right) channel is shown.

As seen in Figure 7.4, the transverse momentum distribution of the W boson is better simulated by the SHERPA W/Z +jets samples than by the ALPGEN samples. In addition to this, the clear difference in the truth W boson p_T distributions suggests it is possible to apply a re-weighting based on the difference of this variable between ALPGEN and SHERPA. The following weights were derived in reference [157], using no preselection cuts on the generator level W boson (in the muon channel) and are thus directly applicable in this analysis.

- $p_T(W) \leq 10 \text{ GeV} \rightarrow \text{Weight: 0.90}$

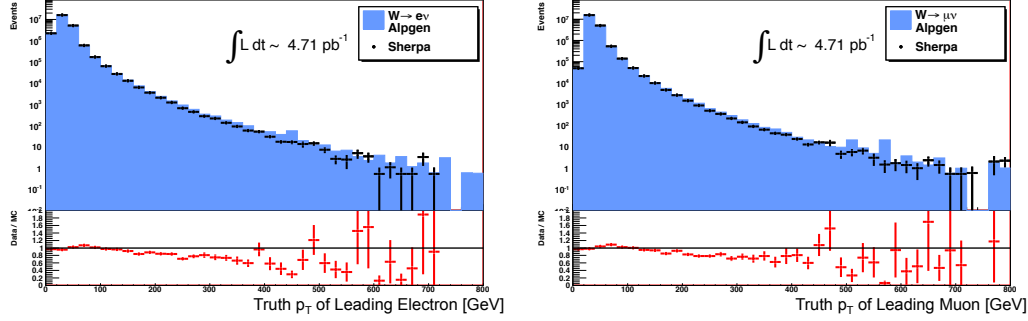


Figure 7.8: Comparison of ALPGEN and SHERPA $W/Z + \text{jets}$ MC samples. The truth lepton p_T for the electron (left) and muon (right) channel is shown.

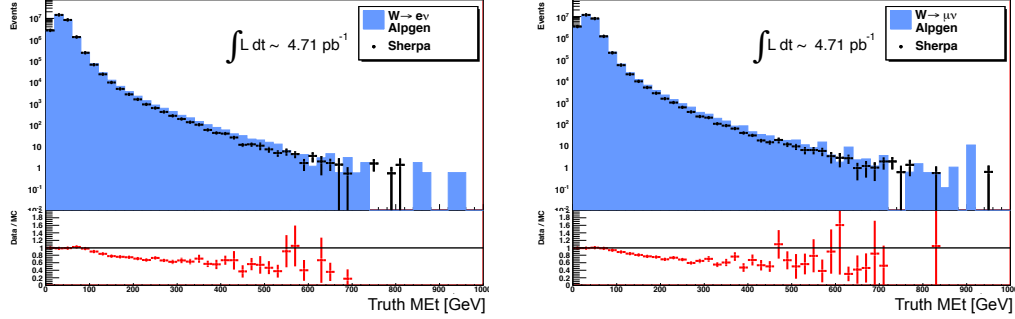


Figure 7.9: Comparison of ALPGEN and SHERPA $W/Z + \text{jets}$ MC samples. The truth E_T^{miss} for the electron (left) and muon (right) channel is shown.

- $10 \text{ GeV} < p_T(W) \leq 20 \text{ GeV} \rightarrow \text{Weight: } 1.05$
- $20 \text{ GeV} < p_T(W) \leq 30 \text{ GeV} \rightarrow \text{Weight: } 1.13$
- $30 \text{ GeV} < p_T(W) \leq 40 \text{ GeV} \rightarrow \text{Weight: } 1.15$
- $40 \text{ GeV} < p_T(W) \leq 250 \text{ GeV} \rightarrow \text{Weight: } \exp\{0.2165 - 0.0022075 \times p_T(W)\}$
- $p_T(W) > 250 \text{ GeV} \rightarrow \text{Weight: } 0.72$

Figures 7.10 to 7.12 show the data/MC comparison plots using ALPGEN $W/Z + \text{jets}$ samples after the application of the above weights. It is clear that this procedure has corrected the previous overestimation of W/Z cross-section in high p_T regions. These weights are then applied to all ALPGEN $W/Z + \text{jets}$ Monte-Carlo samples in this analysis by default.

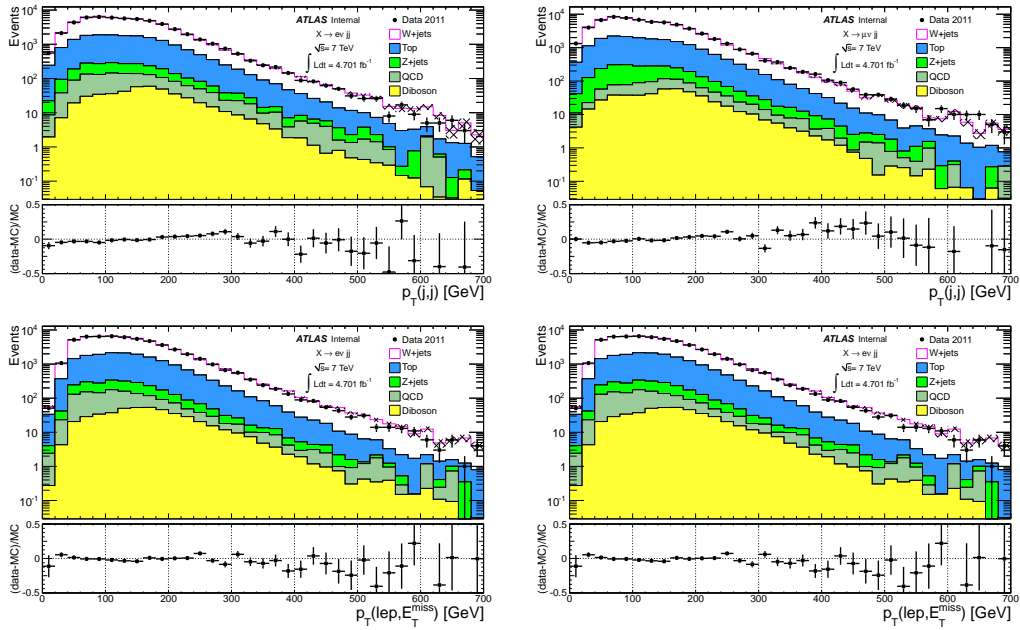


Figure 7.10: Comparison of data and background after $\ell\nu jj$ preselections and ALPGEN reweighting. The dijet p_T (top) and lep+ E_T^{miss} p_T (bottom) in both the electron (left) and muon (right) channels are shown.

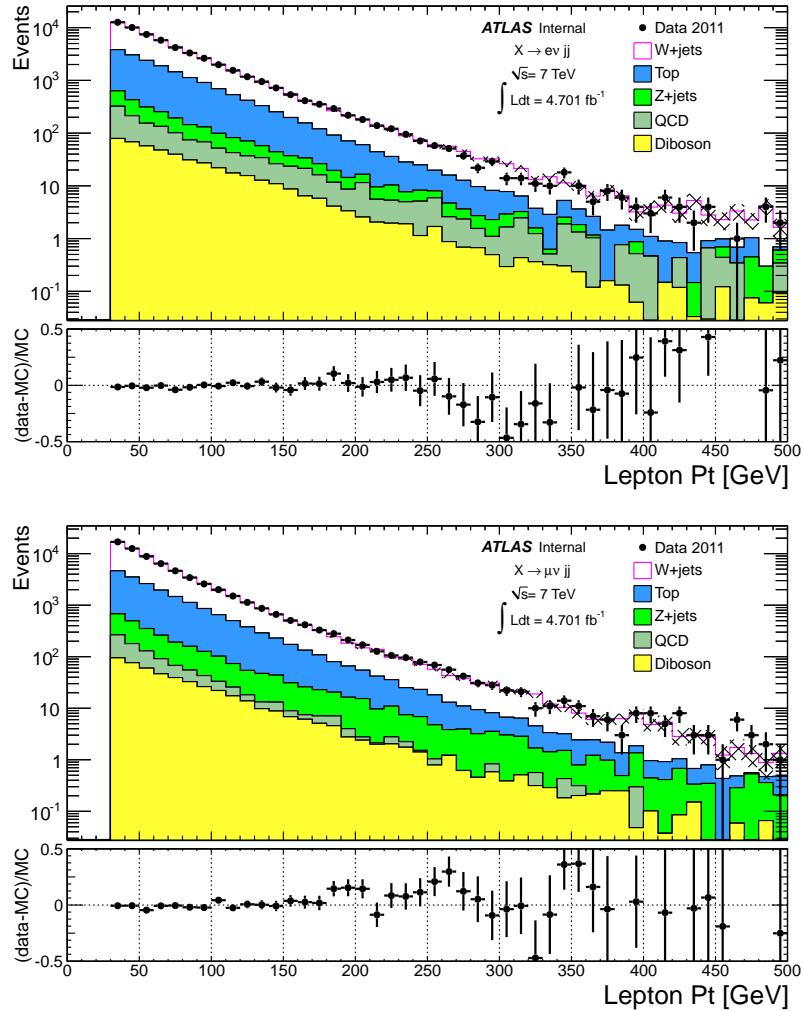


Figure 7.11: Comparison of data and background after $\ell\nu jj$ preselections and ALP-GEN reweighting. The electron p_T (top) and muon p_T (bottom) are shown.

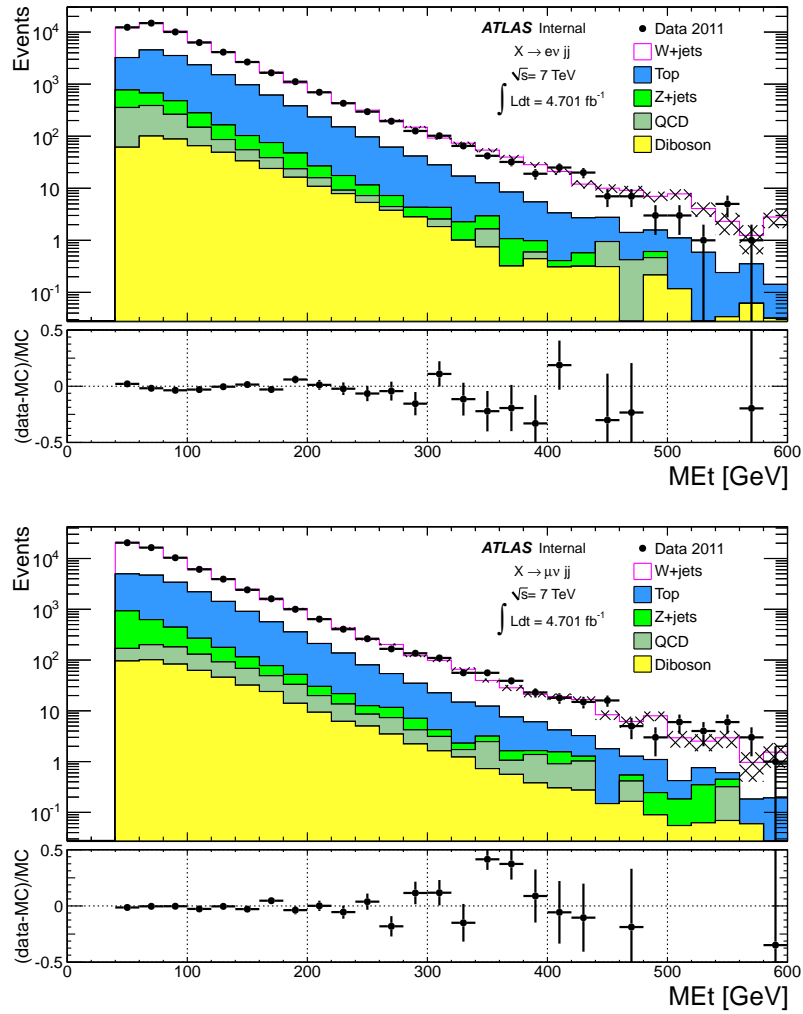


Figure 7.12: Comparison of data and background after $\ell\nu jj$ preselections and ALPGEN reweighting. The missing transverse momentum for the electron (top) and muon (bottom) channel is shown.

7.2 QCD Multijet Modeling and Normalization

To properly estimate the QCD background that enters our signal region, the multijet background is modeled using a data-driven method. In the electron channel, one quality requirement from our electron object definition is inverted. Specifically, it is required that a `tight++` electron fail the calorimeter isolation requirement (see Section 4.1.2), namely: $\text{Et_cone30} > 6 \text{ GeV}$. In the muon channel, events that pass all selection criteria except the requirement on the impact parameter significance of the muon are used to model the multijet background. These “non-pointing” muons must have: $|d_0 \text{ w.r.t PV}|/\sigma(d_0 \text{ w.r.t. PV}) > 3$. These object selections, referred to as ‘anti-lepton’ selections, provide events dominated by QCD multi-jet events.

An additional step is taken to estimate and correct for the amount of events with real leptons from $W+\text{jets}$ background that are present in the QCD template after applying the above QCD criteria. This is done by applying the same ‘anti-lepton’ cuts to $W+\text{jets}$ Monte-Carlo to produce a template of $W+\text{jets}$ events that look like QCD events. This is referred to as the $W+\text{jets}$ contamination template. From this, it is estimated that real $W+\text{jets}$ events account for $\sim 18\%$ of the events in the ‘anti-lepton’ QCD templates in the electron channel and $\sim 7\%$ in the muon channel. For this reason, the $W+\text{jets}$ QCD contamination template is subtracted from the QCD template yielding a more pure estimation of the amount of multijet events passing our selection cuts. Figure 7.13 shows the QCD ‘anti-lepton’ template with the $W+\text{jets}$ contamination template for both electron and muon channels. The real $W+\text{jets}$ component of the data-driven QCD estimation can be clearly seen in the bump around 80 GeV in the falling distribution. Figure 7.14 shows the un-modified QCD ‘anti-lepton’ template along with the QCD template with the $W+\text{jets}$ MC contamination estimation subtracted.

These corrected samples are then combined with the Monte-Carlo backgrounds and scaled to match the data. Both channels normalize this background through a fit to the lepton- E_T^{miss} transverse mass distribution. The $W/Z+\text{jets}$ overall normalisation is allowed to float during these fits, thus a scale factor for these distributions is provided as well. The $M_T(\ell, E_T^{\text{miss}})$ distributions for the $e\nu jj$ and $\mu\nu jj$ chan-

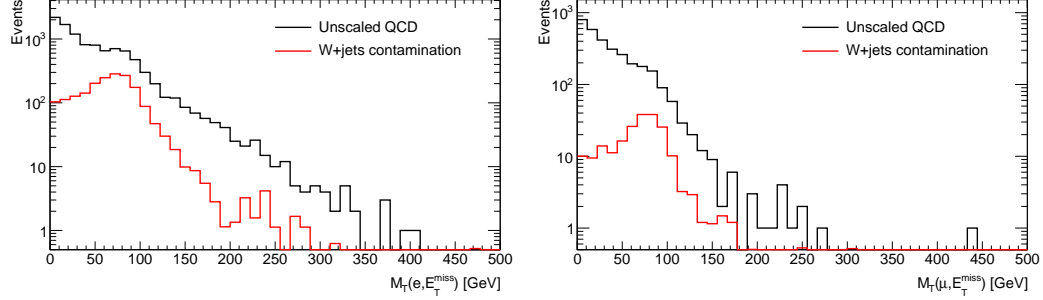


Figure 7.13: $M_T(\ell, E_T^{\text{miss}})$ distributions for QCD ‘anti-lepton’ template (black) with $W+\text{jets}$ contamination estimation (red) for the $e\nu jj$ (left) and $\mu\nu jj$ (right) channel.

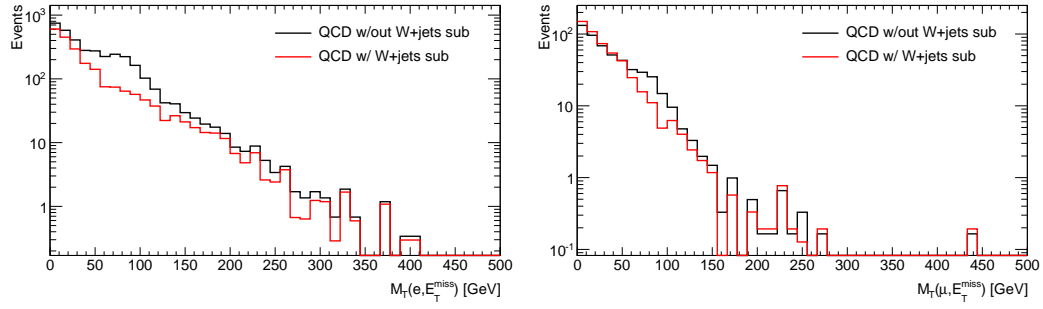


Figure 7.14: $M_T(\ell, E_T^{\text{miss}})$ distributions for QCD ‘anti-lepton’ templates before (black) and after (red) subtraction of $W+\text{jets}$ MC contamination estimation.

nels before and after the multijet/ W/Z -inclusive rescaling are shown in Figure 7.15. The amount by which each multijet event must be scaled such that the sum of event weights agrees with the fit results is presented in Table 7.1. The derived QCD scale factors as well as the $W/Z+\text{jets}$ scale factors are used as the normalisation for distributions throughout the analysis.

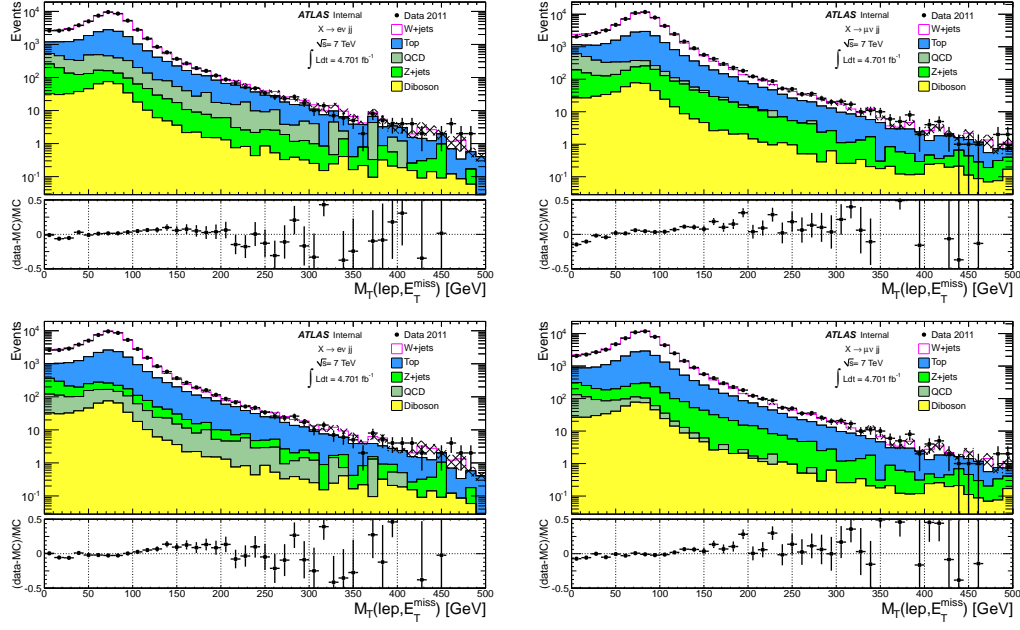


Figure 7.15: Comparison of the data with the background prediction before multijet background estimation (top row) and after multijet background estimation (bottom row) for events in the $e\nu jj$ (left column) and $\mu\nu jj$ (right column) channels.

Scale Factors	Electron Channel	Muon Channel
QCD	0.30 ± 0.05	0.22 ± 0.08
$W/Z+\text{jets}$	1.10 ± 0.01	1.09 ± 0.01

Table 7.1: The scaling factor applied to the multijet background sample such that the sum of event weights agrees with the yield returned from the fit to the M_T distribution.

7.3 Preselection Yields and Distributions

This section presents a comparison of the data with the background prediction after applying the ALPGEN generator level $W p_T$ reweighting as described in Section 7.1, as well as scaling the $W/Z+\text{jets}$ background by the $W/Z+\text{jets}$ inclusive scale factor described in Section 7.2. Table 7.2 shows the estimated yield for each background after the basic selection cuts as well as the observed number of data events and the

predicted signal yield. For both channels, the sum of predicted backgrounds agree with the given data at the 1% level. Only statistical uncertainties are shown in the tables. Figures 7.16 and 7.17 show a comparison of the data and the background prediction for several key observables in the electron channel and muon channels, respectively. Additional distributions after preselection cuts can be found in Appendix B.

A cut-flow for the RS1 and bulk RS $G^* \rightarrow WW$ signals are shown in Tables 7.3 and 7.4 for $M(G^*)=1$ TeV. For the RS1 $G^* \rightarrow WW$ sample at this mass, $(13.0 \pm 0.1)\%$ of Monte Carlo events satisfy the $e\nu jj$ cut requirements and $(10.8 \pm 0.1)\%$ of events satisfy the $\mu\nu jj$ requirements. Similarly, $(9.9 \pm 0.1)\%$ of bulk RS events satisfy the $e\nu jj$ cut requirements while $(8.4 \pm 0.1)\%$ of events satisfy the $\mu\nu jj$ requirements. Similar cut-flows are presented for resonance masses of 500 and 1500 GeV in Appendix A.

Process	$e\nu jj$ channel	$\mu\nu jj$ channel
$W+jets$	37965 ± 153	45469 ± 170
$Z+jets$	1256 ± 16	1798 ± 17
Top	14938 ± 30	16248 ± 31
Diboson	467 ± 4	485 ± 4
QCD	799 ± 37	385 ± 14
Total Bkgd	55444 ± 161	64385 ± 174
Data	54791	63777

Table 7.2: The estimated background yields, the number of data events and the number of predicted signal events after applying the preselection cuts. All uncertainties are statistical only.

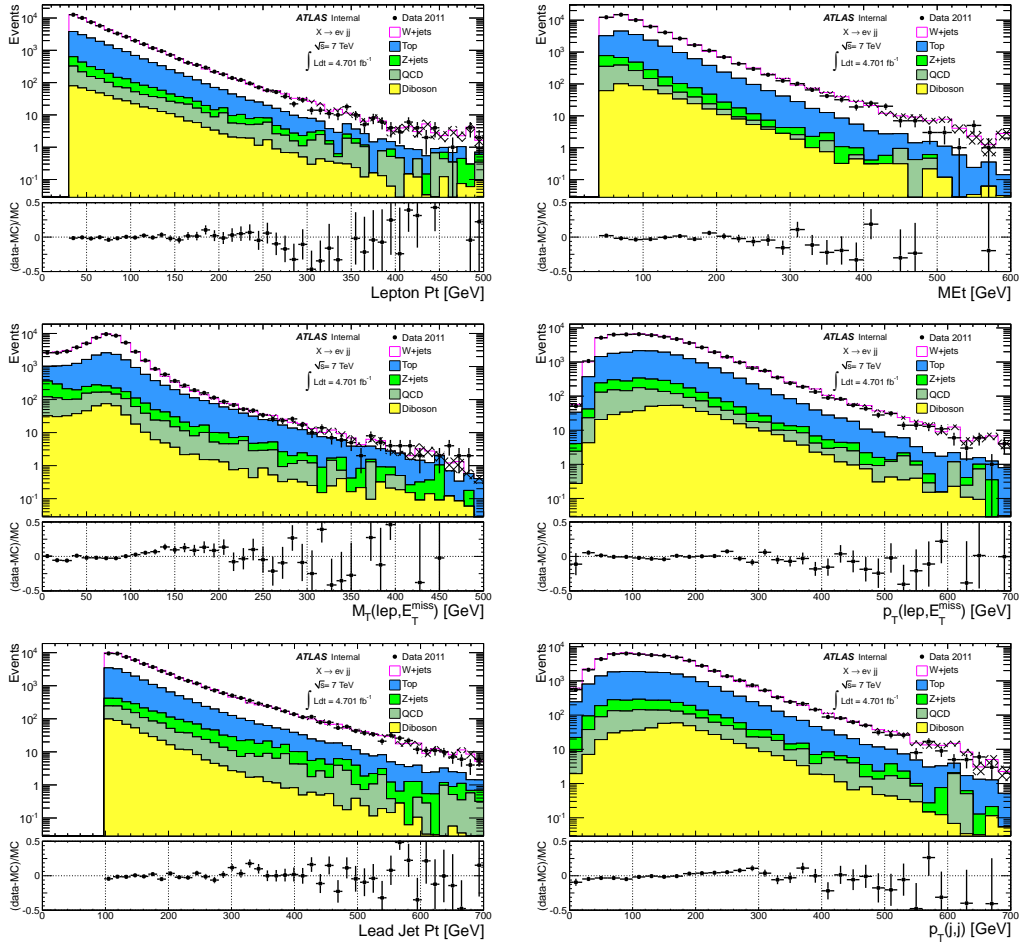


Figure 7.16: Comparison of the data with the background prediction for the $e\nu jj$ channel. The leading electron p_T (top left), E_T^{miss} (top right), lepton- E_T^{miss} transverse mass (middle left), lepton- E_T^{miss} p_T (middle right), leading jet p_T (bottom left), and dijet p_T (bottom right) in events with one electron, large E_T^{miss} , and at least two jets.

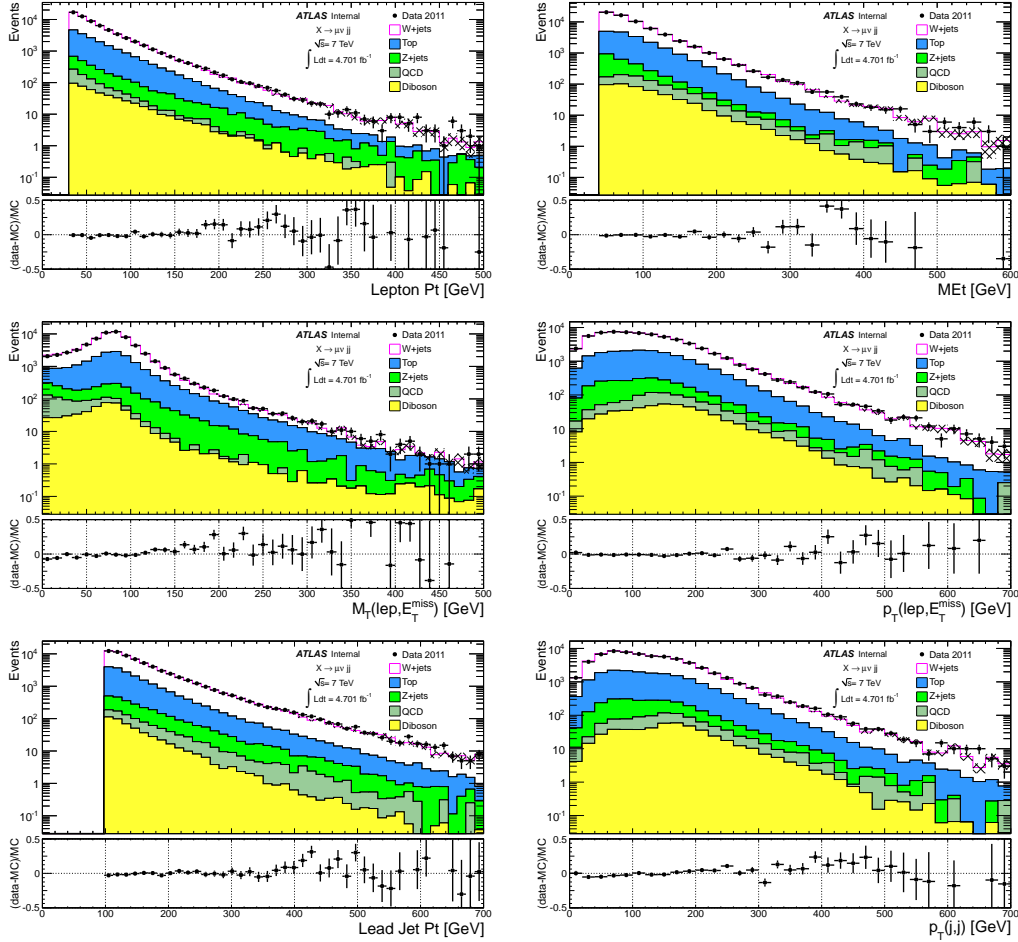


Figure 7.17: Comparison of the data with the background prediction for the $\mu\nu jj$ channel. The leading muon p_T (top left), E_T^{miss} (top right), lepton- E_T^{miss} transverse mass (middle left), lepton- E_T^{miss} p_T (middle right), leading jet p_T (bottom left), and dijet p_T (bottom right) in events with one muon, large E_T^{miss} , and at least two jets.

Cut	RS1 G^*	bulk RS G^*
All Events	30000	15000
Triggered Events	9329	6211
Good Vertex Events	9329	6211
One Good electron	5431	3104
No 2 nd medium++ electron	5428	3099
Good E_T^{miss}	5168	3051
Two or more Good jets	4333	1945
Triangle cut region veto	4051	1886
Leading jet $p_T > 100$ GeV.	3911	1832
Satisfies preselection cuts	3911	1832
Filter Efficiency	1	0.81
Acceptance	(13.0 ± 0.1)%	(9.9 ± 0.1)%

Table 7.3: The number of RS1 and bulk RS G^* with $M(G^*)=1000$ GeV Monte Carlo events remaining after each of the $e\nu jj$ -channel cuts listed in the first column is applied. The signal acceptance after all cuts is shown at the bottom of the table with statistical uncertainty only.

Cut	RS1 G^*	bulk RS G^*
All Events	30000	15000
Triggered Events	7674	5152
Good Vertex Events	7674	5121
One Good muon	4812	4516
No 2 nd muon	4801	4504
Good E_T^{miss}	4665	4398
Two or more Good jets	3782	3657
Triangle cut region veto	3536	3419
Leading jet $p_T > 100$ GeV.	3229	1559
Satisfies preselection cuts	3229	1559
Filter Efficiency	1	0.81
Acceptance	(10.8 ± 0.1)%	(8.4 ± 0.1)%

Table 7.4: The number of RS1 and bulk RS G^* with $M(G^*)=1000$ GeV Monte Carlo events remaining after each of the $\mu\nu jj$ -channel cuts listed in the first column is applied. The signal acceptance after all cuts is shown at the bottom of the table with statistical uncertainty only.

7.4 $t\bar{t}$ Modeling and Control Region

To ensure that the $t\bar{t}$ background is modeled properly, a relatively pure sample of $t\bar{t}$ events is selected out of the events satisfying the preselection criteria described in Section 6.2. The following criteria are required:

- At least two jets with $p_T > 40$ GeV, with the leading jet $p_T > 100$ GeV, and at least two of the jets in the event b -tagged¹. The b -tagged scale factors are applied to the event as recommended by the official ATLAS flavor tagging group. This requirement removes many of the $W/Z+jets$ and diboson events without heavy flavor. Additional ALPGEN $W+c$, $W+c\bar{c}$, and $W+b\bar{b}$ heavy flavor samples are employed in this region to improve the statistics for the $W+jets$ background estimate. Since the nominal ALPGEN $W+jets$ contain heavy flavor jets they must be removed to avoid double counting. This is accomplished through an event flag which marks the event for removal if it is heavy flavor in the inclusive $W+jets$ samples or light flavor in the $W+heavy$ flavor samples.
- Require dijet $p_T > 200$ GeV to stay consistent with the signal selection requirements.
- Remove events with a dijet mass between 65 and 115 GeV. This requirement effectively rejects any remaining possible signal content in the sample.

Four distributions are shown in Figure 7.18: lepton (electron or muon) p_T , E_T^{miss} , $M_T(\ell, E_T^{\text{miss}})$, and H_T , where H_T is the scalar sum of all the jet transverse momenta in the event. Events from the electron and muon channels are combined to maximize statistics in the control region. The plots shown below the larger distributions in these figures are no longer the data/MC ratio as was included in the preselection section. These distributions show the bin-by-bin statistical significance of the

¹ “ b -tagging” is a method by which the distance of the jet vertex from the primary event vertex is used to identify jets originating from bottom quarks. This is possible due to the fact that hadrons containing bottom quarks have sufficient lifetime that they travel some distance before decaying.

deviation observed in the data under the background only assumption. In other words, the statistical significance shown is the calculated z -value from a normal distribution given a specific p -value (the probability that the data has fluctuated to its value under the assumption of no signal) from the data [158]. This definition of significance will be used to quantify the agreement between the measured data and theoretical expectation throughout the rest of this thesis.

The data are consistent at the 1σ -level (statistical uncertainty only) with the sum of the dominant $t\bar{t}$ background and the remaining SM backgrounds. Table 7.5 presents the data and the $t\bar{t}$ and non- $t\bar{t}$ backgrounds for events in the electron, muon, and combined channels.

Process	$e\nu jj$ channel	$\mu\nu jj$ channel
top	295 ± 17	279 ± 16
non-top	23 ± 4	19 ± 4
Data	301 ± 17	301 ± 17
p -value (MC stat + lumi)	0.26	0.48
RS1 G^* ($M_{G^*} = 1$ TeV)	0 ± 0	0 ± 0

Table 7.5: The data, $t\bar{t}$ and non- $t\bar{t}$ yields in the electron, and muon $t\bar{t}$ control regions. Only statistical uncertainties are presented.

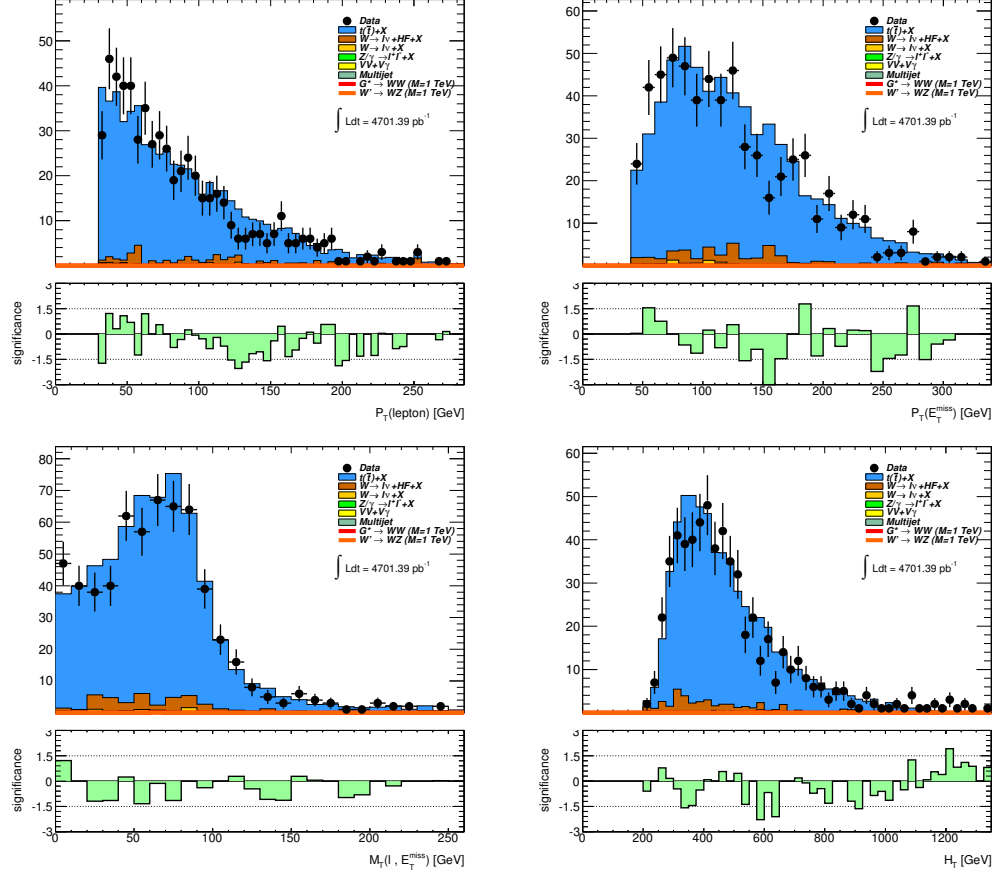


Figure 7.18: Comparison of the data with the background prediction in the $t\bar{t}$ control sample. The following distributions are shown: lepton p_T (top left), E_T^{miss} (top right), $M_T(\ell, E_T^{\text{miss}})$ (bottom left), and $H_T \equiv \sum_{\text{jets}} p_T^j$ (bottom right).

7.5 Signal Control Region and $W/Z+\text{jets}$ Normalization

Because the next-to-leading-order (NLO) corrections to the W/Z cross section grow with increasing W/Z p_T [159] it is expected that the data and $W/Z+\text{jets}$ background will not agree in both the preselection and signal regions. To determine the level with which the $W/Z+\text{jets}$ background must be corrected to agree with the data at very high p_T , a high p_T $W/Z+\text{jets}$ control region (“signal control region”) is created.

In this region the dijet mass window surrounding the W and Z bosons is removed leaving behind two sidebands: one with $M(jj) < 65$ GeV and one with

$M(jj) > 115$ GeV. The complete definition of the control region containing the two $M(jj)$ sidebands is therefore:

- **Signal control region:**

- $p_T(jj) \geq 200$ GeV
- $p_T(\ell\nu) \geq 200$ GeV
- $65 < M(jj) \text{ or } M(jj) > 115$ GeV

The $M(jj)$ distributions in the signal control region are shown for data in Figure 7.19. Here, the $M(jj)$ requirement is loosened for background Monte-Carlo as well as a signal sample, thus showing the predicted background and signal distribution shapes in the signal region (within the $M(jj)$ window).

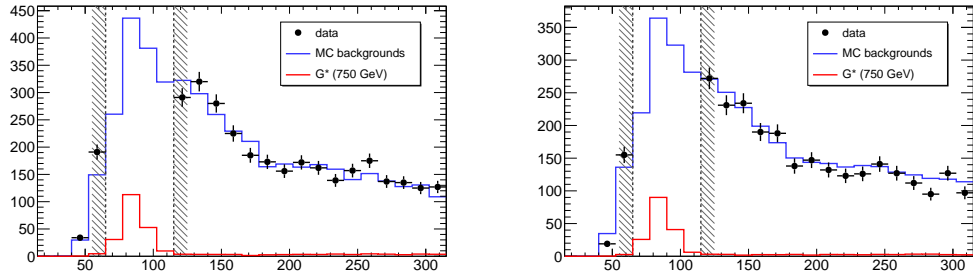


Figure 7.19: $M(jj)$ distribution after $p_T(\ell\nu) \geq 200$ GeV and $p_T(jj) \geq 200$ GeV requirements. An additional requirement of $M(jj) < 65$ GeV or $M(jj) > 115$ GeV is imposed on the data, thus defining the signal control region. The background Monte-Carlo (blue) and an RS1 G^* sample with $M(G^*) = 750$ GeV are shown without the $M(jj)$ window cut imposed. Events in the $e\nu jj$ channel are shown on the left and in the $\mu\nu jj$ channel on the right.

A scale factor for the $W/Z+jets$ background is determined in each sideband, with the $e\nu jj$ and $\mu\nu jj$ channels combined, using Eq. 7.1. The scale factor for the $W/Z+jets$ within the dijet mass (i.e. $65 \leq M(jj) \leq 115$) is computed as the weighted average of the low and high dijet mass sideband scale factors as shown in Eq. 7.2. The values of the scale factors in both sidebands as well as the weighted

average is shown in Table 7.6.

$$SF_{\text{sideband}}^{W/Z+\text{jets}} = \frac{N^{\text{data}} - N^{\text{top}} - N^{\text{dibosons}} - N^{\text{multijet}}}{N^{W+\text{jets}} + N^{Z+\text{jets}}} \quad (7.1)$$

$$SF_{M(jj) \text{ window}}^{W/Z+\text{jets}} = \frac{N_{\text{low } M(jj)}^{\text{data}} \times SF_{\text{low } M(jj)}^{W/Z+\text{jets}} + N_{\text{high } M(jj)}^{\text{data}} \times SF_{\text{high } M(jj)}^{W/Z+\text{jets}}}{N_{\text{low } M(jj)}^{\text{data}} + N_{\text{high } M(jj)}^{\text{data}}} \quad (7.2)$$

Sideband	Scale factor
$M(jj) < 65$	1.17 ± 0.03
$M(jj) > 115$	1.02 ± 0.01
Weighted avg.	1.02 ± 0.03

Table 7.6: The scaling factors derived from the low and high $M(jj)$ sidebands ($e\nu jj$ and $\mu\nu jj$ channels combined). Errors shown for sideband scale factors are statistical only, systematic uncertainties are discussed further in Section 9.9.

The systematic uncertainty on this scale factor is parametrized by the difference between the weighted average and the two sideband scale factors, this is discussed further in Section 9.9. The dijet mass sidebands are shown in Figure 7.20 for the electron and muon channels separately. The diboson invariant mass distribution in each sideband before this scaling is shown in Figure 7.21 for the combined electron and muon channels. Similarly, the diboson invariant mass distribution in the signal control region before and after the weighted average scale factor is applied is shown in Figure 7.22.

A selection of distributions, after applying the $W/Z+\text{jets}$ scale factor, are shown in Figures 7.23 to 7.26. The data agrees with the Monte-Carlo predictions to the level of $\sim 1\sigma$ in both the $e\nu jj$ and the $\mu\nu jj$ channels. This provides confidence that the background estimation in the high- p_T , signal control region is reliable.

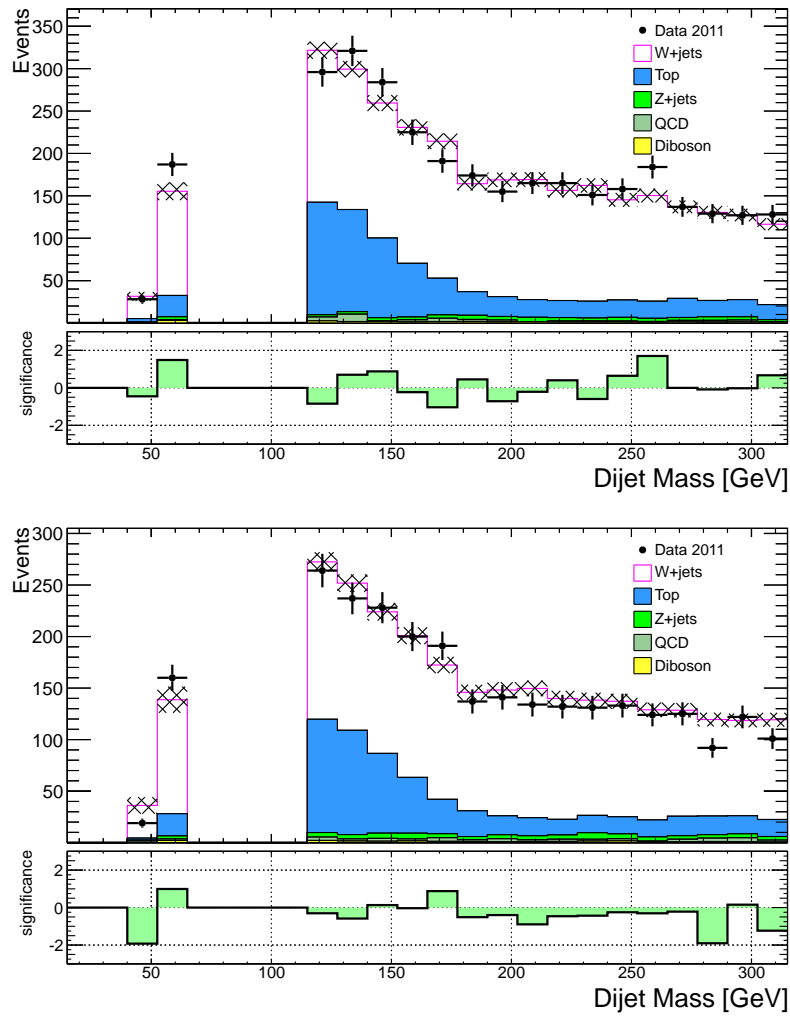


Figure 7.20: Comparison of the data and backgrounds in the signal control region as a function of the dijet mass, $M(jj)$, for electron (top) and muon (bottom) channel events.

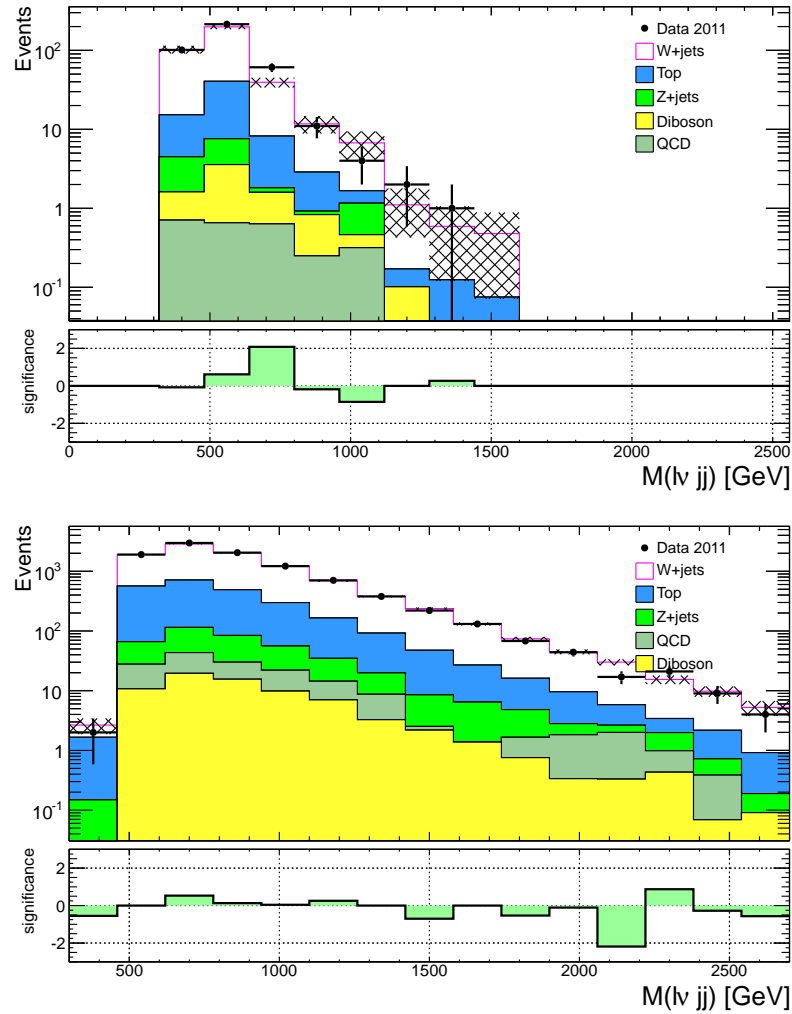


Figure 7.21: Comparison of the data and backgrounds as a function of the diboson invariant mass ($M(\ell\nu jj)$) for the low $M(jj)$ (top) and high $M(jj)$ (bottom) sidebands. These distributions contain both electron and muon channel events.

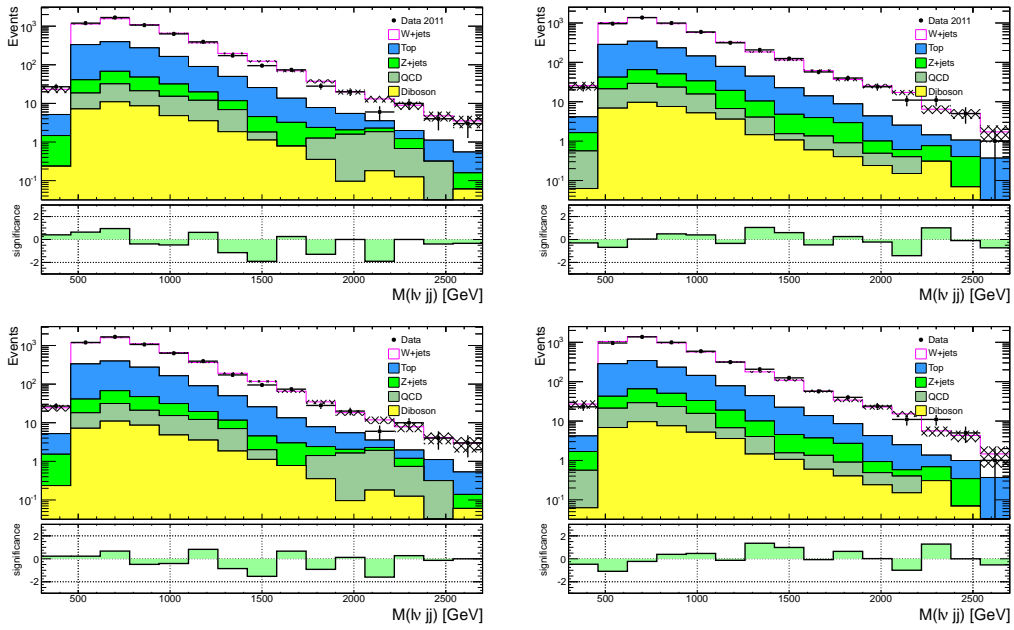


Figure 7.22: Comparison of the data and backgrounds as a function of the diboson invariant mass ($M(\ell\nu jj)$) before (top) and after (bottom) applying the $W/Z+jets$ scale factor derived from the dijet mass sidebands for the electron (left) and muon (right) channels. The $W/Z+jets$ distributions after the $W/Z+jets$ reweighting include the systematic uncertainty from the weighting, as discussed in Section 9.9.

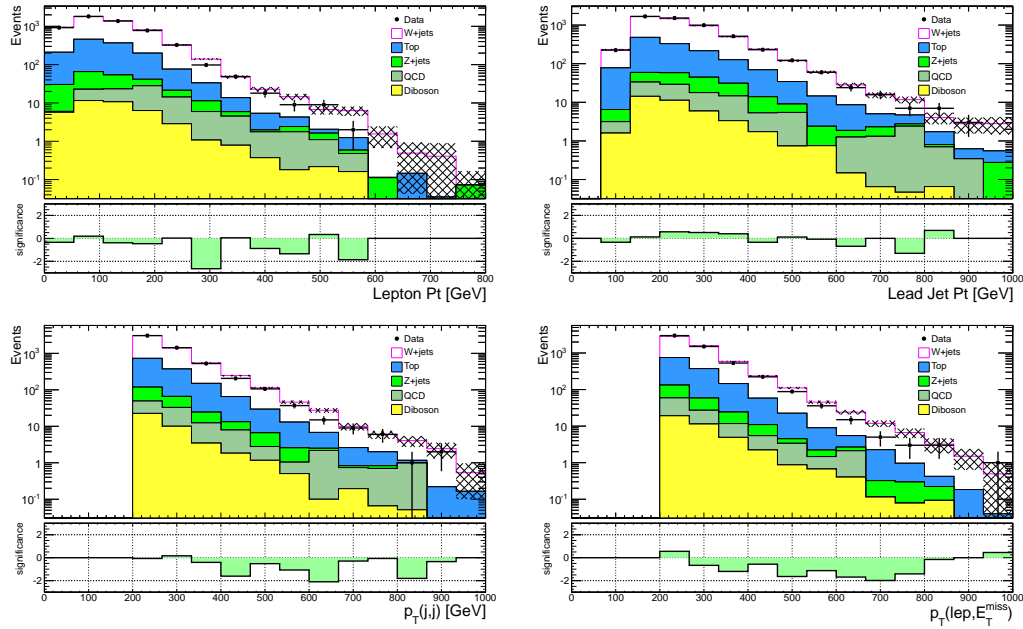


Figure 7.23: Comparison of data and background transverse momenta distributions for $e\nu jj$ events in the signal control region after applying the $W/Z+jets$ scale factor. The distributions of the electron p_T (left) and the leading jet p_T (right) are shown on the top row, while the dijet p_T (left) and electron- E_T^{miss} (right) is below.

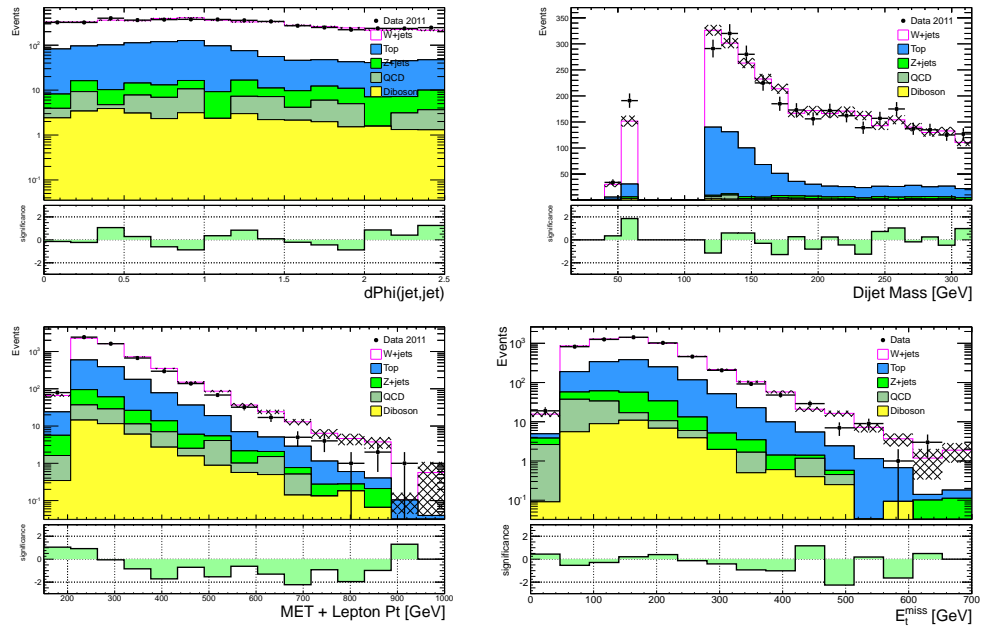


Figure 7.24: Additional comparisons of data and background distributions $e\nu jj$ events in the signal control region after applying the $W/Z+jets$ scale factor. Dijet separation in the ϕ coordinate (left) is shown with the dijet invariant mass (right) on the upper row. On the bottom row is shown the scalar sum of the electron p_T with E_T^{miss} , referred to as L_T , (left) and the recorded missing E_T in the event (right).

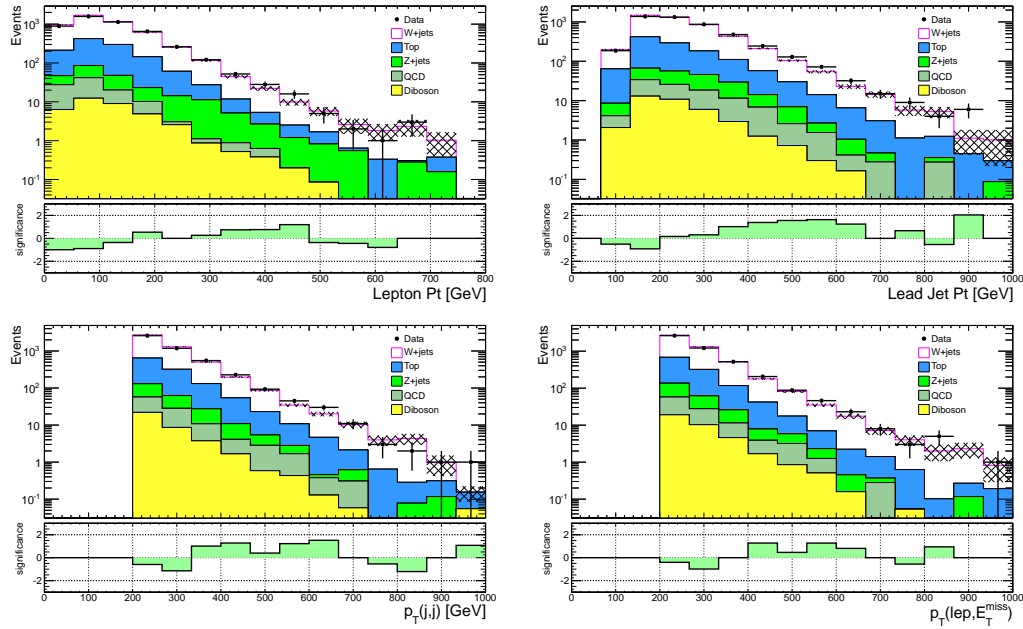


Figure 7.25: Comparison of data and background transverse momenta distributions for $\mu\nu jj$ events in the signal control region after applying the $W/Z+jets$ scale factor. The distributions of muon p_T (left) and the leading jet p_T (right) are shown on the top row, while the dijet p_T (left) and muon- E_T^{miss} (right) is below.

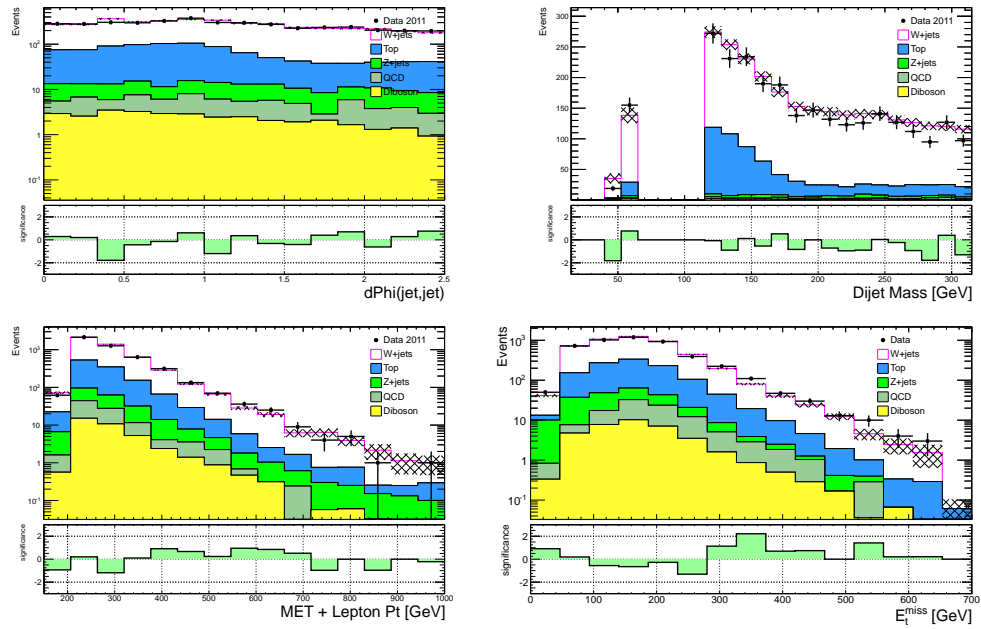


Figure 7.26: Additional comparisons of data and background distributions $\mu\nu jj$ events in the signal control region after applying the $W/Z+jets$ scale factor. Dijet separation in the ϕ coordinate (left) is shown with the dijet invariant mass (right) on the upper row. On the bottom row is shown the scalar sum of muon p_T with E_T^{miss} , referred to as L_T , (left) and the recorded missing E_T in the event (right).

Chapter 8

Signal Selection

In Chapter 7 the theoretical background prediction was validated by comparing Monte Carlo yields and distributions to those of data in regions constructed to have low signal-to-background ratios. The next step is to evaluate the data in the signal region, as defined in Section 6.3, which has been designed specifically to isolate events with final states kinematically similar to heavy diboson resonances, therefore yielding a high signal-to-background ratio. The signal region event yields and distributions after the signal selection cuts are presented in Section 8.1.

8.1 Signal Region Yields and Distributions

This section shows a comparison of the data with the background prediction after the signal selection cuts are applied. As previously described in the Section 6.3, the signal region is defined by the following cuts:

- $p_T(\ell\nu) \geq 200$ GeV
- $p_T(jj) \geq 200$ GeV
- $65 \leq M(jj) \leq 115$ GeV

Table 8.1 shows the predicted background yields, the expected signal contribution for a range of G^* resonance, and the number of data events after the signal selection cuts.

Process	$e\nu jj$ channel		$\mu\nu jj$ channel	
	Yield	Accept. (%)	Yield	Accept. (%)
$W + \text{jets}$	698 ± 20	4.2×10^{-2}	594 ± 21	3.6×10^{-2}
$Z + \text{jets}$	14 ± 2	3.4×10^{-3}	15 ± 2	4.8×10^{-3}
Top	614 ± 6	1.0×10^{-1}	516 ± 5	9.3×10^{-2}
Diboson	76 ± 2	6.6×10^{-2}	63 ± 1	5.6×10^{-2}
QCD	18 ± 6	-	16 ± 2	-
Total Bkgd	1420 ± 22	5.2×10^{-4}	1204 ± 22	4.6×10^{-4}
Data	1452	7.2×10^{-4}	1318	6.5×10^{-4}
Bulk G^* (800 GeV)	44 ± 1	15.5	35 ± 1	12.9
Bulk G^* (1000 GeV)	4 ± 0	6.1	4 ± 0	5.8
Bulk G^* (1200 GeV)	1 ± 0	3.0	0	0
RS1 G^* (750 GeV)	208 ± 4	8.6	163 ± 4	7.4
RS1 G^* (1000 GeV)	22 ± 1	5.2	18 ± 1	4.8
RS1 G^* (1250 GeV)	3 ± 0	3.1	3 ± 0	3.1

Table 8.1: The signal region yields and total acceptances for the estimated background, data and signal events. All uncertainties are statistical only.

The dijet mass distribution within the dijet mass signal region window ($65 < M(jj) < 115$ GeV) is shown in Figure 8.1. Additionally, Figure 8.2 shows the data and Monte Carlo agreement as a function of the invariant mass of the $\ell\nu jj$ system in the signal region. This distribution is to be used as input (discriminating variable) to the statistical analysis, described in Chapter 10. This procedure is used to quantify the agreement between data and Monte Carlo shown in the plots in this section and to set the most stringent exclusion limits to date on RS Graviton production in the diboson decay channel. Additional signal region plots can be found in Appendix C.

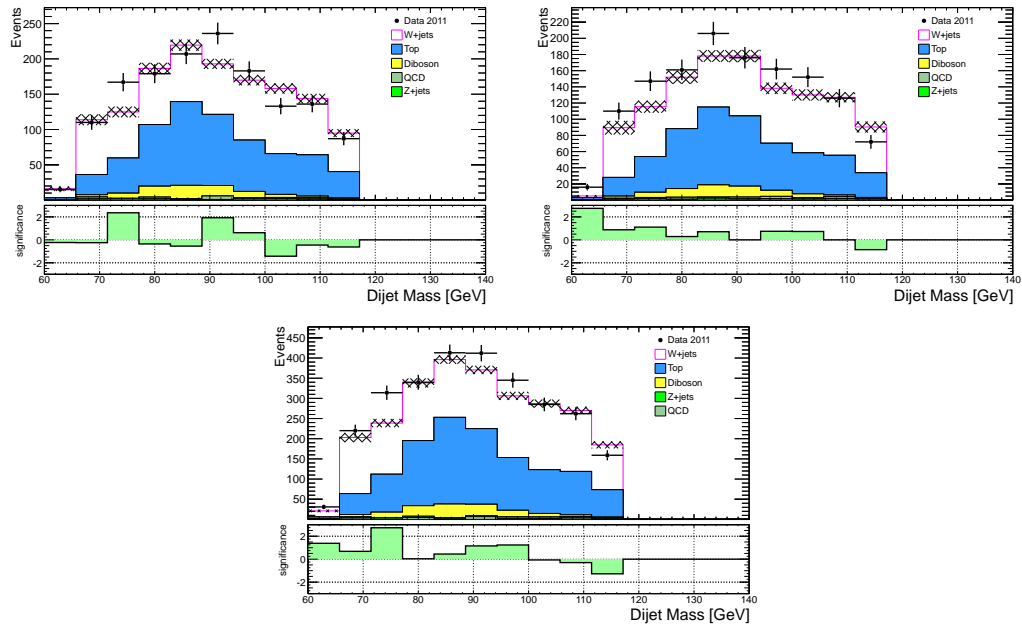


Figure 8.1: Comparison of the data and backgrounds as a function of the dijet mass ($M(jj)$) in the signal region for the electron (top left) and muon (top right) channels and the two channels combined (bottom). The hatched region is the luminosity and statistical uncertainty only.

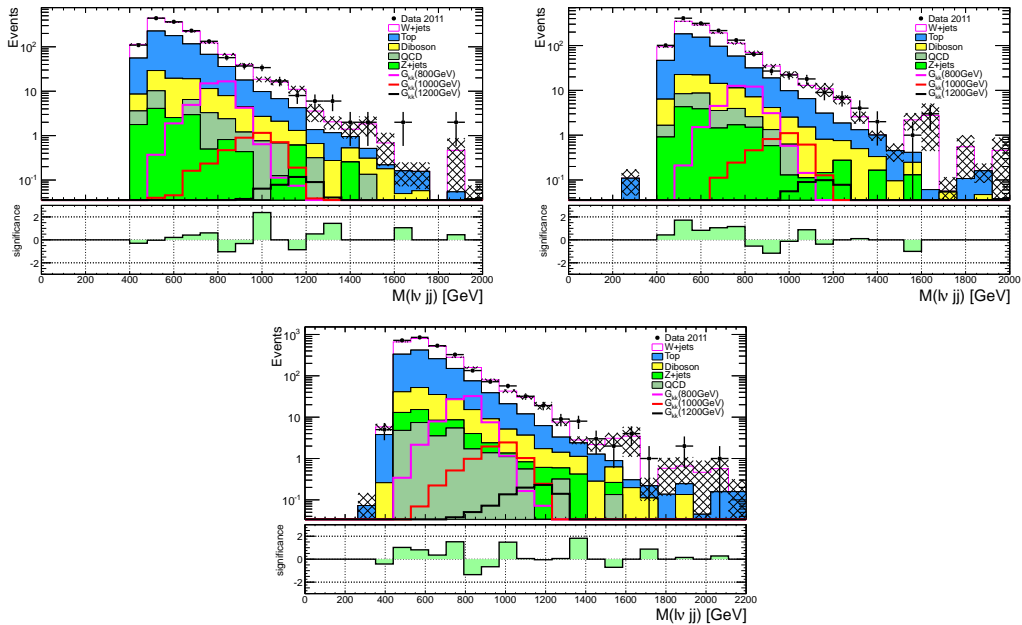


Figure 8.2: Comparison of the data and backgrounds as a function of the diboson invariant mass ($M(\ell\nu jj)$) in the signal region for the electron (top left) and muon (top right) channels and the two channels combined (bottom). The hatched region is the luminosity and statistical uncertainty only.

Chapter 9

Sources of Systematic Uncertainty

Systematic uncertainties result from limited knowledge of the many sources that alter the differential distributions of the final state objects or the global normalization of a source. The following sources of systematic uncertainty are described in this section:

- Trigger Efficiency (Section 9.1)
- Electron Energy Resolution (Section 9.2)
- Electron Energy Scale (Section 9.2)
- Electron Reconstruction Efficiency (Section 9.2)
- Muon p_T Resolution (Section 9.3)
- Muon Reconstruction Efficiency (Section 9.3)
- Jet Energy Resolution (Section 9.4)
- Jet Energy Scale (Section 9.4)
- Missing E_T Resolution (Section 9.5)

- Multijet Normalization (Section 9.6)
- LAr Hole (Section 9.7)
- ALPGEN W +jets re-weighting (Section 9.8)
- W/Z +jets Normalisation and Shape (Section 9.9)
- Luminosity (Section 9.10)
- PDF (signal only) (Section 9.12)
- ISR/FSR (signal only) (Section 9.13)
- $t\bar{t}$ Modeling (Section 9.14)
- Cross Section Normalization (Section 9.15)

The largest systematic uncertainties affecting the signal samples in this analysis are the jet energy scale, initial/final state radiation (ISR/FSR) and the luminosity uncertainty. Many of the uncertainties listed in this chapter depend on the kinematics of the quantity in question and therefore can affect the shape of the diboson invariant mass. Any shape distortion of this distribution is accounted for in the statistical analysis of the data as described in Chapter 10. The diboson invariant mass distribution in the signal region is shown for all systematics that affect the shape. If there is no shape dependence, a single systematic factor is presented. The final values of the estimated systematic uncertainties are presented for all backgrounds and two signal samples in Table 9.7 and Table 9.8.

9.1 Trigger Efficiency

The electron and muon triggers used to collect the data are simulated in the Monte Carlo and a correction factor is determined using $Z \rightarrow \ell\ell$ events in data. The trigger efficiency scale factor is calculated using the trigger signature group recommendation by applying an event-by-event scale factor,

$$SF = \frac{1 - \epsilon_{data}(\ell)}{1 - \epsilon_{MC}(\ell)}, \quad (9.1)$$

where ϵ_{data} and ϵ_{MC} are lepton efficiencies obtained from data and MC samples, respectively. The lepton used to calculate the trigger efficiency scale factor satisfies the object selection criteria outlined in Chapter 4. The correction factor for the relevant trigger is measured in bins of $\eta\text{-}\phi$ separately for the barrel and endcap detectors. The recommended 1 – 2% systematic uncertainty is propagated to the global event weight uncertainty.

9.2 Electron Energy Scale, Energy Resolution and Reconstruction Efficiency

The electron energy resolution and scale corrections are determined from the 2011 dataset and electrons in the Monte Carlo are smeared and scaled accordingly as described in Section 4.1.3. The uncertainties on these corrections were derived in $Z \rightarrow ee$ and $J/\psi \rightarrow ee$ studies and provided in bins of η . The associated systematic uncertainty on the signal acceptance is found by scaling/smearing the electrons by $\pm 1\sigma$ of the central values and observing the change in final acceptance. In this way, systematic uncertainty due to electron energy resolution and scale uncertainty was found to be less than 2%.

As previously discussed, the electron reconstruction efficiency scale factors are determined using W and Z tag and probe measurements. The differences observed in the reconstruction efficiencies between the data and MC are taken into account by weighting the simulation with these scale factors. The systematic uncertainties are then determined by varying the scale factors within their uncertainties. The scale factors and uncertainties are provided by a dedicated ATLAS working group in bins of η , E_T , and electron algorithm (`loose++`, `medium++`, `tight++`). These values are propagated to the global event weight uncertainty to obtain the associated systematic uncertainty on the signal acceptance which was found to be less than 1% in this analysis.

Figures 9.1 and 9.2 show the change in the signal and background $M(\ell\nu jj)$ distribution in the $\ell\nu jj$ channel when varying the electron energy resolution and energy

scale by its $\pm 1\sigma$ uncertainty, respectively. Figure 9.3 shows the effect of varying the electron reconstruction scale factor with its $\pm 1\sigma$ uncertainty for the same distributions. As expected, very little change in the normalization or shape of the distributions is observed.

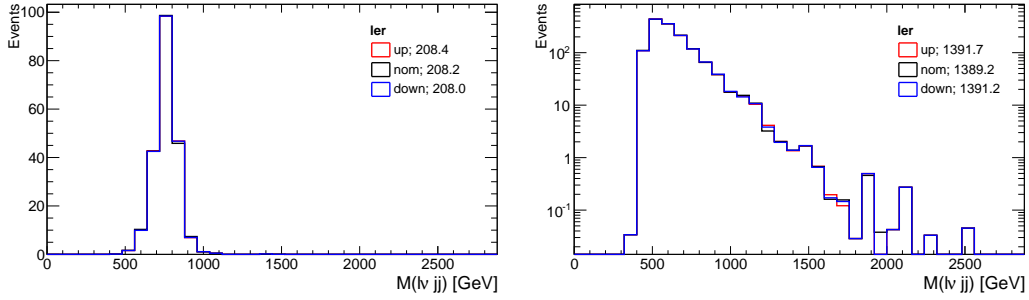


Figure 9.1: The effect of smearing the electron energy by its resolution for the signal $M(G^*) = 750$ GeV (left column) and sum of background (right column). Only single electron events are shown.

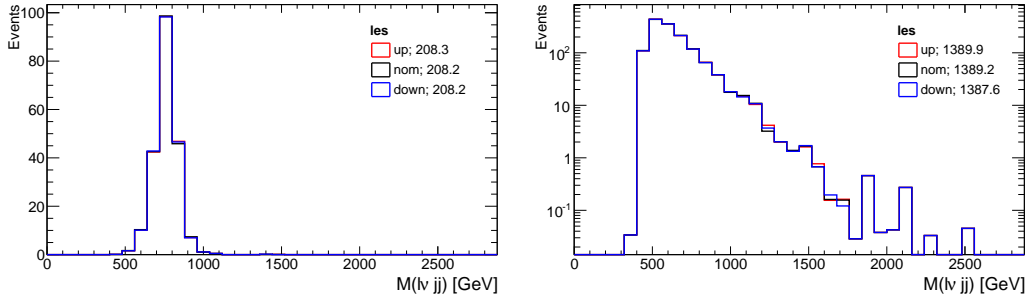


Figure 9.2: The effect of varying the electron energy scale by its $\pm 1\sigma$ uncertainty for the signal $M(G^*) = 750$ GeV (left column) and sum of background (right column). Only single electron events are shown.

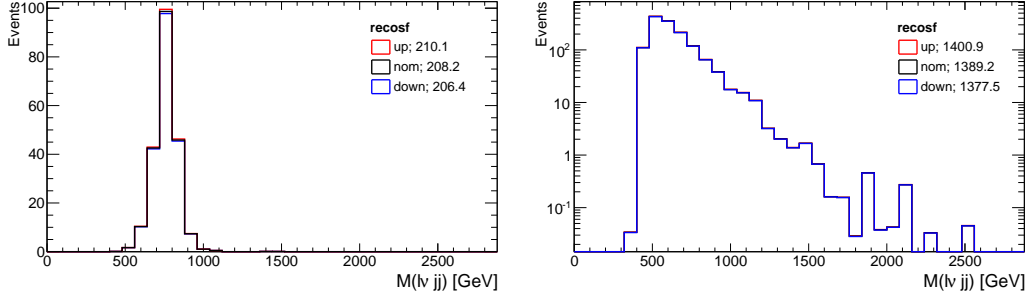


Figure 9.3: The effect of varying the electron reconstruction efficiency scale factor uncertainty by its $\pm 1\sigma$ uncertainty for the signal $M(G^*) = 750$ GeV (left column) and sum of background (right column). Only single electron events are shown.

9.3 Muon Momentum Resolution and Reconstruction Efficiency

As discussed in Section 4.2.1, the muon transverse momentum resolution correction is determined using $Z \rightarrow \mu\mu$ events independently for tracks in the inner detector (ID) and the muon spectrometer (MS). The uncertainty on the resolution smearing procedure requires unsmeared and resmeared the muon p_T using the $\pm 1\sigma$ smearing parameters once for the MS and once for the ID. The total uncertainty is taken as the maximum variation of these two uncertainties. From this prescription, the systematic uncertainty on the acceptance is found to be less than 1% for most samples.

The muon reconstruction efficiency is also determined using $Z \rightarrow \mu\mu$ events and a correction factor is applied to all muons reconstructed in the Monte Carlo. Similar to the electron reconstruction efficiency uncertainty, this muon uncertainty is propagated to the global event weight uncertainty which results in a total systematic uncertainty of less than 1%.

Figure 9.4 shows the change in the signal and background $M(\ell\nu jj)$ distribution in the $\ell\nu jj$ channel when varying the muon ID and MS p_T resolution by its $\pm 1\sigma$ uncertainty. Figure 9.5 shows the effect of varying the muon reconstruction scale factor with its $\pm 1\sigma$ uncertainty for the same distribution. As would be ex-

pected from the small effect on the overall signal acceptance, there is very little change in the normalization and shape from the uncertainty modulations.

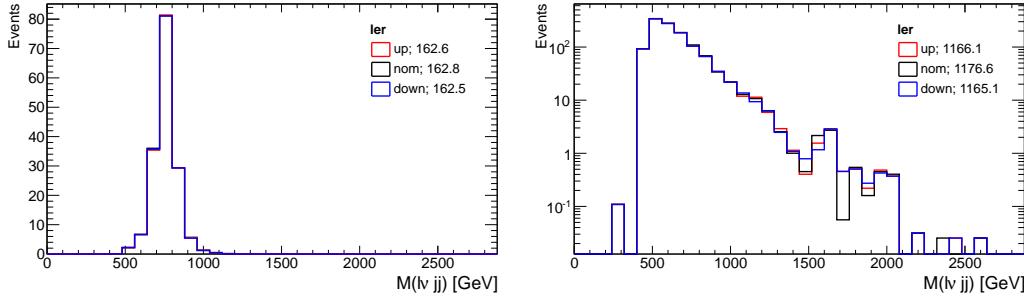


Figure 9.4: The effect of smearing the muon momentum by its resolution (ID and MS) for the signal $M(G^*) = 750$ GeV (left column) and sum of background (right column). Only single muon events are shown.

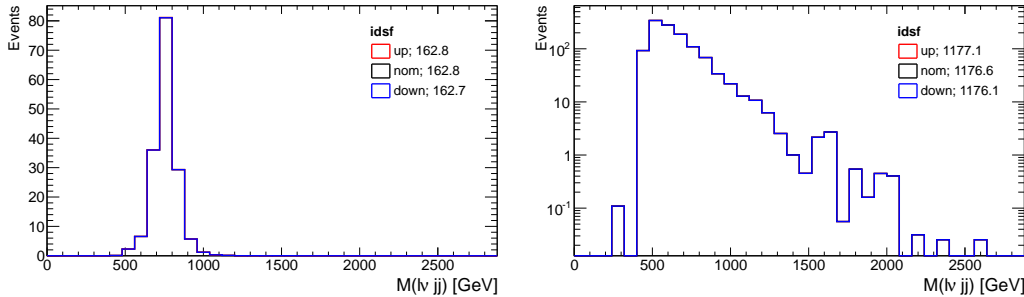


Figure 9.5: The effect of varying the muon reconstruction efficiency scale factor uncertainty by its $\pm 1\sigma$ uncertainty for the signal $M(G^*) = 750$ GeV (left column) and sum of background (right column). Only single muon events are shown.

9.4 Jet Energy Scale and Energy Resolution

The uncertainty on the jet energy scale (JES) calibration is derived using a combination of single hadron response measured in-situ with pp collision data as well as in test-beams, MC simulations with different detector conditions and in-situ dijet balance measurement for the detector η uniformity. In addition to these, the effects due to jet flavor composition and the presence of close-by jets are taken into account

using MC simulations and in-situ validation. The total JES uncertainty (including the flavor composition, close-by jets and pile-up uncertainties added in quadrature) as a function of the jet p_T is shown in Figure 9.6 for four (out of the 26 total) different η regions. This uncertainty is applied to all selected jets assuming a full correlation and propagated to the global event weight uncertainty. The JES systematic uncertainty is the largest uncertainty in this analysis producing changes in acceptance between 4–35% across signal and background MC. The resulting change in the diboson transverse mass distribution for the signal and sum of backgrounds is shown in Figure 9.7.

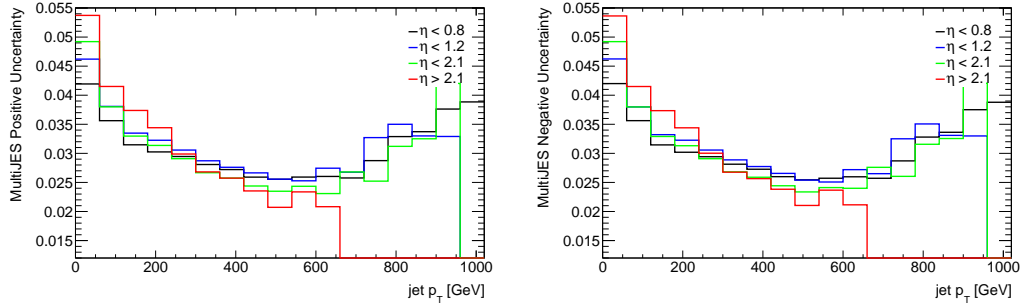


Figure 9.6: The $+1\sigma$ (left) and -1σ (right) fractional uncertainties on the jet energy scale as a function of the jet p_T .

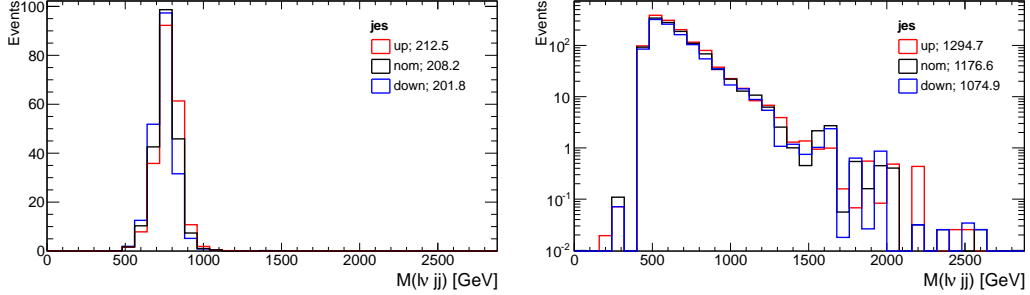


Figure 9.7: The effect of varying the jet energy scale by its $\pm 1\sigma$ uncertainty for the signal $M(G^*) = 500$ GeV (left) and sum of background (right). Only single muon events are shown.

The jet energy resolution (JER) is determined in-situ with two different meth-

ods: the dijet p_T balance and bisector technique. The dijet p_T balance technique uses energy imbalance measured in events with only two jets under the assumption of momentum conservation in the transverse plane. The bisector technique also uses dijet events, however studying energy imbalance along the direction given by the transverse projection of the vector sum of the two leading jets in the event. Both methods have been shown to give consistent results [160]. The JER systematic uncertainty is estimated from systematic uncertainties associated with the two methods.

The fractional jet energy resolution and its absolute uncertainty as a function of the jet p_T are shown in Figure 9.8. These uncertainties lead to overall systematic uncertainties on the order of 1 – 6% for both background and signal MC. The resulting change in the diboson transverse mass distribution for the signal and sum of backgrounds is shown in Figure 9.9.

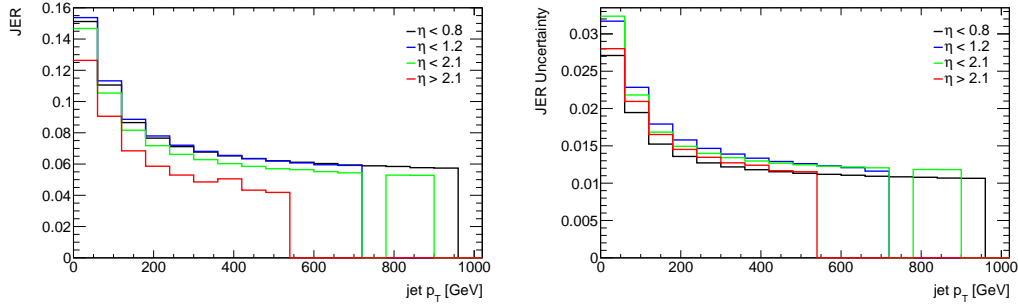


Figure 9.8: The fractional jet energy resolution and its absolute uncertainty as a function of the jet p_T .

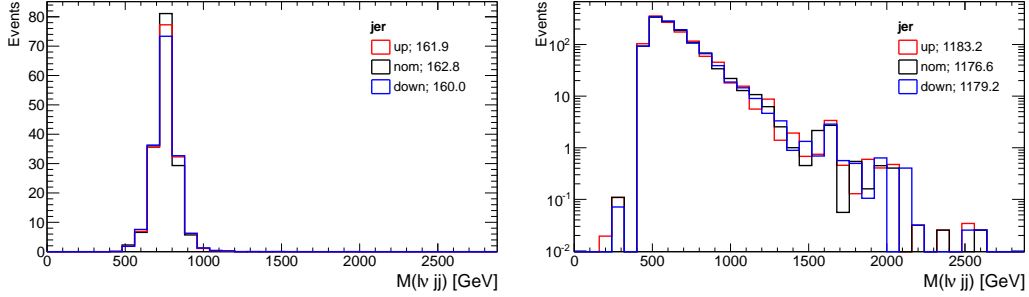


Figure 9.9: The effect of varying the jet energy resolution by its $\pm 1\sigma$ uncertainty for the signal $M(G^*) = 500$ GeV (left) and sum of background (right). Only single muon events are shown.

9.5 E_T^{miss} Uncertainties from Pile-Up and Low- p_T Jets

The measurement of the transverse missing energy is based on the `MET_RefFinal` algorithm. As previously discussed in Section 4.4, the algorithm associates calorimeter energy deposits with high p_T objects such as electrons, photons, muons and jets. The transverse energy of the associated object then replaces the original cell energy, preferable since the objects have a more accurate calibration than the bare calorimeter cells. Therefore, the scale and resolution uncertainties of electrons, muons and jets have a direct impact on the `MET_RefFinal` value. For this reason, when evaluating the systematics on these objects, the event E_T^{miss} is recalculated with the object systematic uncertainties taken into account.

Two systematics are evaluated that are not accounted for by propagating higher level physics object uncertainties into the calculation. These are the uncertainties introduced into the E_T^{miss} due to pile-up and from the calibration of low- p_T jets and low- p_T topo-clusters not associated with any physics objects. The pile-up uncertainties are estimated to be 6.6% from studies of the dependence of ΣE_T on the number of pile-up interactions. The uncertainties from the low- p_T jets and topo-clusters are provided by the dedicated ATLAS jet/ E_T^{miss} group. The effect of both of these uncertainties on the overall systematic uncertainty was observed to be $\sim 1\%$ for all signal and background MC.

9.6 Multijet Background

To assess the systematic uncertainty on the data-driven QCD estimation, we fit the ‘anti-lepton’ template to the data using various template distributions and compare the QCD yield in the signal region. Nominally, the template variable used is the transverse mass of the lepton + E_T^{miss} ($M_T(\ell, E_T^{\text{miss}})$). In addition to this, we perform the multi-jet background estimation using the E_T^{miss} , the sum of the lepton p_T and the E_T^{miss} (referred to as L_T), as well as the transverse mass of the lepton + E_T^{miss} in events having either exactly two jets, or greater than two jets. After each fit was done the maximum resulting change in acceptance yield of multijet events in the signal region was calculated. The results are shown in Table 9.1 with the fractional signal acceptances relative to the nominal fit using $M_T(\ell, E_T^{\text{miss}})$ as the template variable. From these acceptances, we assign a systematic uncertainty of 80% to the $e\nu jj$ channel and 100% to the $\mu\nu jj$ channel using the maximum fractional change in acceptances (see bold numbers in table). Although large, the final QCD yields in the signal region are the smallest of all the background thus these uncertainties have little effect on the overall cross-section limits or mass exclusion reach.

Variable	$SF_{e\nu jj}^{MJ}$	$ \frac{\Delta A_{e\nu jj}^{\text{signal}}}{A_{\text{nominal}}} $	$SF_{\mu\nu jj}^{MJ}$	$ \frac{\Delta A_{\mu\nu jj}^{\text{signal}}}{A_{\text{nominal}}} $
$M_T(\ell, E_T^{\text{miss}})$	0.30	-	0.19	-
$M_T(\ell, E_T^{\text{miss}})(= 2 \text{ jets})$	0.38	0.27	0.33	0.71
$M_T(\ell, E_T^{\text{miss}})(> 2 \text{ jets})$	0.21	0.26	0.12	0.38
L_T	0.52	0.75	0.41	1.05
E_T^{miss}	0.40	0.68	0.35	0.82

Table 9.1: QCD scale factors from fits with various template variables. Fractional change in signal region acceptance also shown.

9.7 Jet p_T Threshold in LAr Hole Removal

As mentioned in Chapter 4, between run 180614 and 185352, a failure of a crate controller in the LAr electromagnetic calorimeter led to six unresponsive Front End Boards (FEBs) creating an inactive region ($-0.1 < \eta < 1.5$ and $-0.9 < \phi < -0.5$) of the calorimeter. To account for this ‘‘LAr hole’’, a simple strategy of vetoing events with a calorimeter jet, with $p_T > 40$ GeV, within the vicinity of the LAr hole is used.

To determine the systematic uncertainty of this strategy, the dedicated Jet/ E_T^{miss} group recommended varying the nominal jet p_T threshold of 40 GeV by 20% and measuring the change in acceptance. A detailed study of this systematic is found in [59], whose final state is very similar to the $\ell\nu jj$ final state of this analysis, and the effect is no larger than 1%. Adopting this result, a 1% uncertainty on the signal and background samples due to this systematic is assigned.

9.8 ALPGEN W +jets re-weighting

To assess the systematic uncertainty from the ALPGEN W +jets re-weighting procedure outlined in Section 7.1, the analysis is run with and without applying the re-weighting and the signal region yields for the W/Z +jets samples are compared. The W/Z +jets signal control region scale factors derived from samples with and without the ALPGEN re-weighting are shown in Table 9.2. The respective signal region yields are shown in Table 9.3.

	$M(jj) < 65$ GeV	$M(jj) > 115$ GeV	Weighted Avg.
With re-weighting	1.159 ± 0.02	1.006 ± 0.01	1.012 ± 0.02
Without re-weighting	0.949 ± 0.04	0.793 ± 0.01	0.799 ± 0.04

Table 9.2: W/Z +jets scale factors derived from distributions with and without applying W +jets re-weighting at preselection.

	$evjj$	$uvjj$
With re-weighting	669 ± 22	587 ± 21
Without re-weighting	682 ± 22	593 ± 21
% change	2%	1%

Table 9.3: Signal region yields from $W/Z+\text{jets}$ MC samples with and without applying $W+\text{jets}$ re-weighting at preselection.

Due to the fact that the signal region yields with and without applying the $W+\text{jets}$ re-weighting agree within statistical uncertainty, no systematic uncertainty is assigned.

9.9 $W/Z+\text{jets}$ Normalisation and Shape

As previously mentioned in Section 7.5, a systematic from the normalization of $W/Z+\text{jets}$ samples in the signal control region is assigned, via the weighted average of the low/high dijet mass sidebands. To estimate a systematic uncertainty on this scale factor, the low and high dijet mass sideband scale factors are plotted and fit as a function of the $\ell\nu jj$ invariant mass. The low dijet mass sideband is fit with a functional form of $\text{SF}_{M(jj)<65}(x) = p_0 \log x + p_1$ while the high dijet mass sideband is fit with a single order polynomial $\text{SF}_{M(jj)>115}(x) = p_0 x + p_1$. These fits along with the average $W/Z+\text{jets}$ scale factor are shown in Figure 9.10. The low/high dijet mass sideband fits are used as envelopes of uncertainty. The nominal value of the averaged scale factor is modulated either ‘up’ by the low dijet mass sideband uncertainty envelope or ‘down’ by the high dijet mass sideband uncertainty envelope, and applied to the $W/Z+\text{jets}$ control and signal regions. Figure 9.11 shows the invariant mass distributions in the $W+\text{jets}$ and $Z+\text{jets}$ samples with these modulations applied.

An additional effect of this method is that by scaling the $W/Z+\text{jets}$ Monte Carlo samples to data in the signal control region, the overall normalization effects of other systematics on these samples are absorbed into the uncertainty assigned

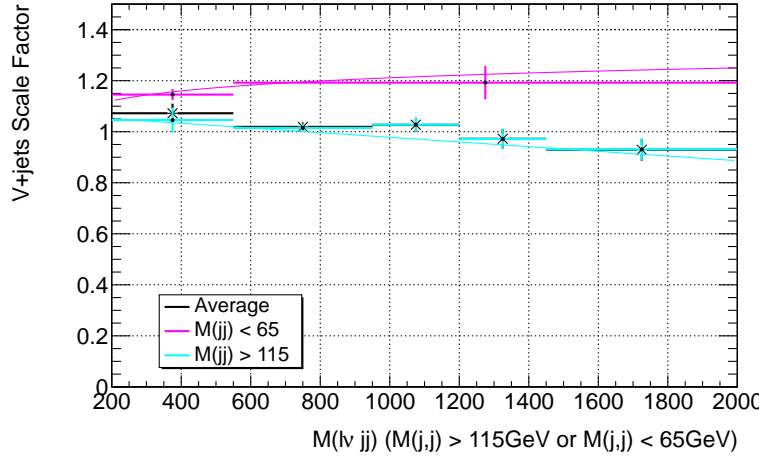


Figure 9.10: W/Z +jets scale factor as function of $M(\ell\nu jj)$. $e\nu jj$ and $\mu\nu jj$ channels combined

to the scaling procedure. Any residual systematic from shape distortion, however, still contributes and is manifested in the statistical analysis of the data described in Chapter 10.

The systematic uncertainty is quoted as the fractional change in the signal region yield from that of the W/Z +jets samples after scaling by the nominal scale factor. Through this procedure, the shape dependence, as a function of $\ell\nu jj$ invariant mass, as well the overall normalization uncertainty are accounted for in the derived systematic. Table 9.4 shows the resulting systematic uncertainties from this scaling.

Sample	$e\nu jj$	$\mu\nu jj$
W +jets	8.8%	9.0%
Z +jets	8.9%	9.1%

Table 9.4: Percent change in signal region acceptance due to uncertainty on W/Z +jets scale factor

Scaling the W/Z +jets MC to match the data, as described, absorbs all systematic uncertainties on the W/Z +jets samples that impact the samples' normalization. This scaling effectively constrains these uncertainties on the W/Z +jets events due

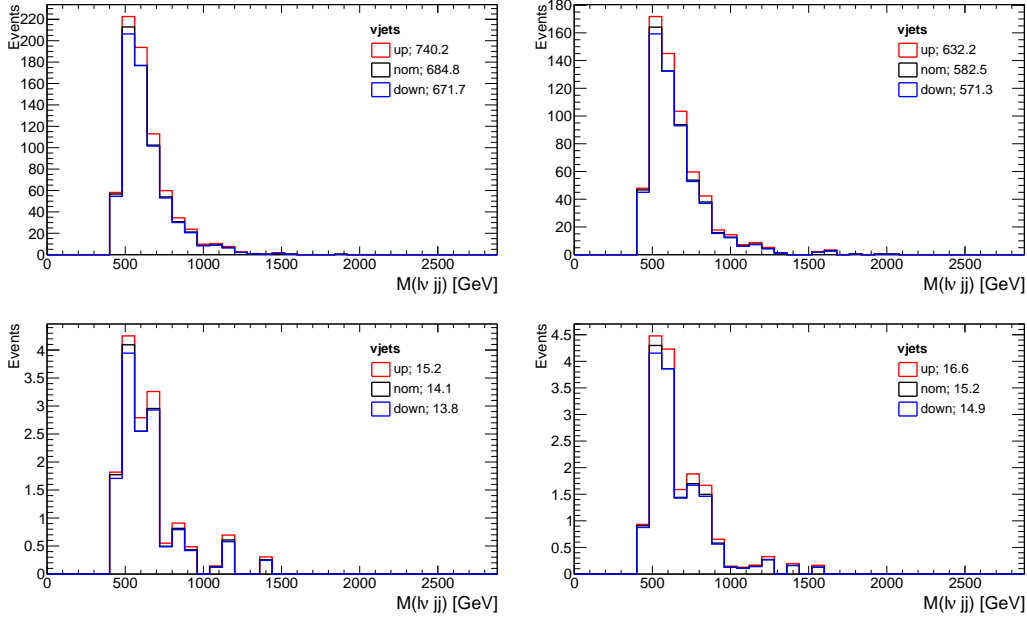


Figure 9.11: The effect of varying the $W/Z + \text{jets}$ normalization scale factor within the envelope scale factor fits to the low and high dijet mass sidebands (see Figure 9.10). The $M(\ell\nu jj)$ distribution in the signal region is shown for both the electron (left) and muon (right) channels and the $W + \text{jets}$ (top) and $Z + \text{jets}$ (bottom) samples.

to the fact that any normalization uncertainties resulting from another source (e.g. jet energy scale, jet energy resolution, etc.) will be ‘normalized away’ when scaling to the data. Additionally, residual shape uncertainties from other sources are much smaller than the assigned scaling uncertainty and negligible; this is illustrated through Figure 9.12 and Figure 9.13. In Figure 9.12, the fractional change in the dijet-mass distribution is shown after modulating the jet energy scale within $\pm 1\sigma$ of its uncertainty. Figure 9.13 shows the same ratio after modulating the jet resolution uncertainty. The events shown have the signal region cuts applied, up to the dijet mass cut. The resulting distributions are flat across the three areas of interest: the low-dijet mass sideband ($M(jj) < 65$ GeV), the high-dijet mass sideband ($M(jj) > 115$ GeV) and the signal region ($65 < M(jj) < 115$ GeV). This illustrates that the largest systematic shape uncertainties (jet energy scale/resolution),

after the $W/Z + \text{jets}$ systematic uncertainty, do not effect the shape of the dijet mass distribution and therefore are negligible and can be absorbed within the $W/Z + \text{jets}$ systematic uncertainty.

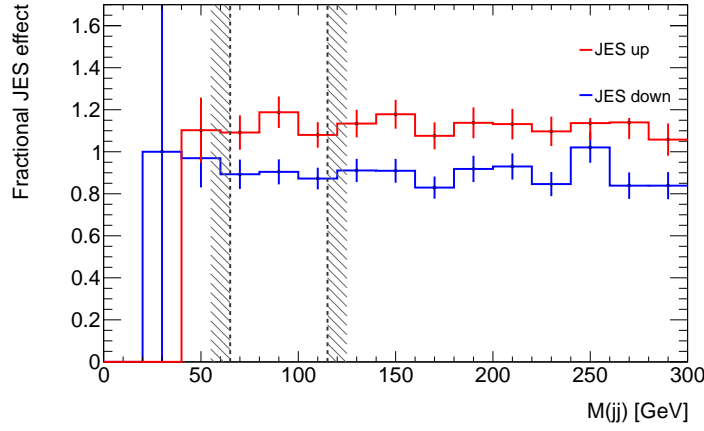


Figure 9.12: The fractional change in the dijet mass distribution after modulating the jet energy scale within $\pm 1\sigma$ of its uncertainty. Events shown have signal region cuts applied up to the dijet mass window cut.

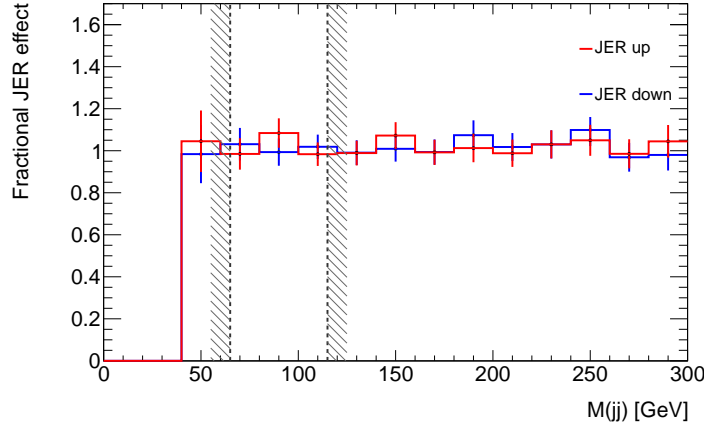


Figure 9.13: The fractional change in the dijet mass distribution after modulating the jet energy resolution within $\pm 1\sigma$ of its uncertainty. Events shown have signal region cuts applied up to the dijet mass window cut.

9.10 Luminosity Uncertainty

The relative luminosity is monitored by the LUCID [161] detector, sampling the number of charged particles per bunch crossing, and the Minimum Bias Trigger Scintillators (MBTS) [162] which trigger on pp events with minimal activity. The global luminosity uncertainty on the 2011 data from these measurements is assigned to be 3.9% [76].

9.11 Selection Check Using the Debug Stream

If the processing of an RDO output of an event extends past the buffer time allowed, the data is dumped into a special “debug” stream. These potentially interesting, however problematic, events are therefore not available in the regular data output stream. It is important for any analysis searching for new physics to check event yields running over this debug stream.

This cross-check was carried out and it was observed that in the electron channel, one event passes the preselection and no events are selected in the signal region. In the muon channel, no events pass either the preselection or signal region requirements. No systematic uncertainty is assigned as a result of this check.

9.12 PDF Signal Uncertainty

The calculation of the total cross-section takes into account the fiducial acceptance due to phase-space requirement of the MC simulations. The central value of the signal acceptance is calculated based on PYTHIA generated with MRST2007lo* [163] parton distribution function (PDF) and the corresponding ATLAS MC10 [164] tune. The systematic uncertainties on the acceptances due to the limited knowledge of the proton PDFs come from the error matrices in CTEQ6.6 [165], a parton distribution function FORTRAN library, and the differences in the central values of the acceptance between CTEQ6.6 and MSTW2008 NLO [166], as recommended by the PDF4LHC group [167]. The calculation of the acceptance uncertainties is itemized below:

- The uncertainty within the CTEQ 6.6 PDF set is obtained by using the master formula provided by the PDF groups. For CTEQ6.6 PDF, there are 22 independent parameters, and the central values for these parameters are determined from the global PDF fits to experimental data. The 44 PDF errors sets are determined by varying one parameter by $\pm 1\sigma$ while fixing other 21 parameters to their central values.

$$\Delta A = \frac{1}{2} \sqrt{\sum_{i=1}^{22} (A_i^+ - A_i^-)^2} \quad (9.2)$$

where $A_i^{+(-)}$ is the acceptance calculated for $\pm 1\sigma$ variation of PDF set i ($i = 1, 2, \dots, 22$).

- The uncertainty between different PDF sets is estimated by comparing CTEQ6.6 to the MSTW2008 NLO 68% PDF set.

The PDF uncertainties on the signal acceptance in both the electron and muon channels is below 1%.

A comparison of 25k $G^* \rightarrow WW$ events generated with CTEQ6L LO and MSTW LO* PDFs is shown in Figures 9.14 and 9.15 for four values of $M(G^*)$. It is clear from these distributions that the choice of PDF for signal generation does not impact the lepton p_T or η by more than 5% for any $M(G^*)$, therefore this is assigned as the systematic uncertainty on the bin-to-bin acceptance for the signal.

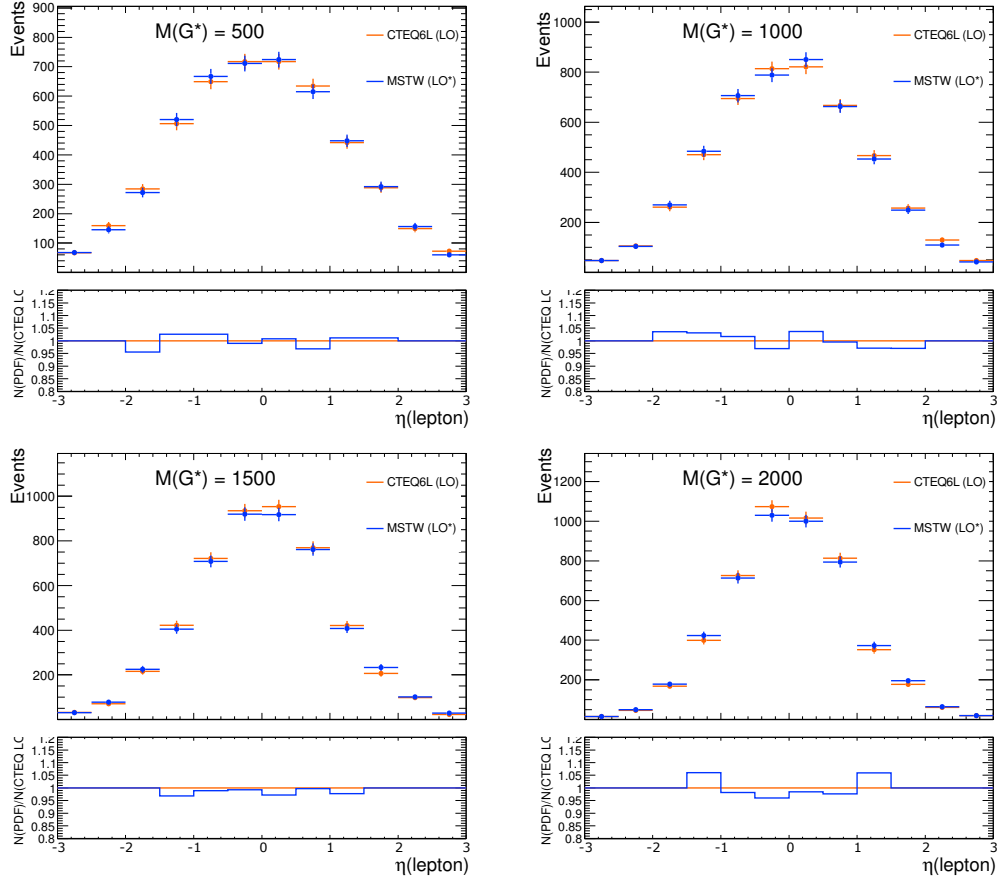


Figure 9.14: Lepton η in $G^* \rightarrow WW$ Events generated with CTEQ6L LO PDFs (orange) and MSTW LO* PDFs (blue). The ratio of the two is only shown for bins containing more than 5% of the sample size.

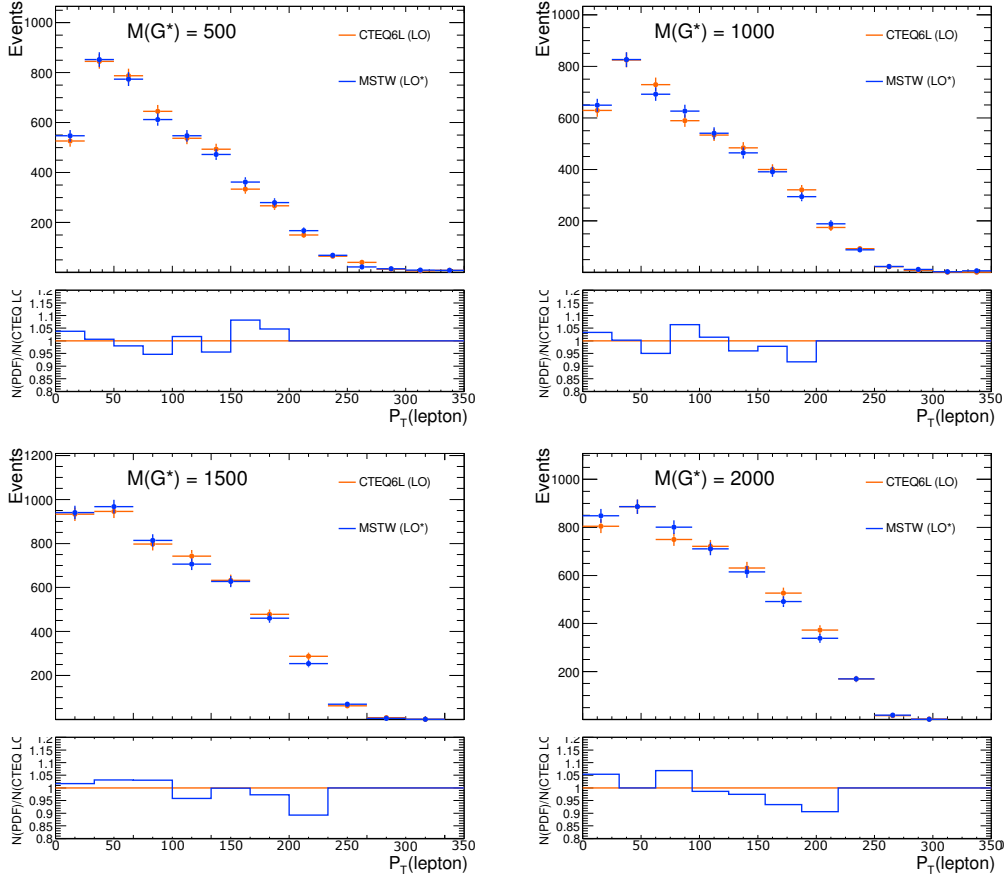


Figure 9.15: Lepton p_T in $G^* \rightarrow WW$ Events generated with CTEQ6L LO PDFs (orange) and MSTW LO* PDFs (blue). The ratio of the two is only shown for bins containing more than 5% of the sample size.

9.13 Initial and Final State Radiation Signal Uncertainty

In any process that contains colored or charged objects in the initial or final state, the radiation from these accelerated partons (quarks or gluons) may give large corrections to the overall topology of events. In effect, these corrections can change final state of a basic $2 \rightarrow 2$ process into $2 \rightarrow 3$ or $2 \rightarrow 4$ final-state topologies. When the radiation is emitted by an incoming parton, this phenomenon is referred to as Initial-State Radiation (ISR), when it is emitted by an outgoing parton it is called Final-State Radiation (FSR).

The effect of ISR/FSR in this analysis is studied by varying the PYTHIA parameters governing the amount of ISR and FSR by a factor of 2, as recommended by the dedicated ATLAS top working group [168], above and below the nominal value. The signal acceptance is found to vary by 5% relative to the central value, which is determined using the ATLAS Monte Carlo events. Additional details of this procedure are found in [169].

9.14 $t\bar{t}$ Modeling

The following sources of uncertainty on the $t\bar{t}$ differential distributions are investigated:

- Top quark mass. This is measured in MC@NLO Monte Carlo events generated with $m_t = 170$ and $m_t = 175$ GeV. The difference in acceptance from using the nominal $m_t = 172.5$ GeV is assigned as the uncertainty and is evaluated to be 3%. The variation between these samples is seen in Figure 9.16.
- Initial and final state radiation (ISR/FSR). The procedure to determine this variation is identical to the procedure used for the corresponding signal systematic uncertainty. Three samples of ACER [170] Monte Carlo events are generated to study this effect. The first sample has the nominal ISR/FSR settings and the second and third samples have the ISR/FSR parameters varied

by the parameters shown in Table 9.5. The difference between the ISR/FSR “up” and ISR/FSR “down” samples is found to be 5% and is assigned as the uncertainty. The variation between these samples is seen in Figure 9.16.

- Generator. Events are generated with POWHEG and the difference in acceptance from the nominal MC@NLO events, 2.5%, is assigned as the uncertainty. The variation between these samples is seen in Figure 9.17.
- Parton shower model. Events are generated with POWHEG using either HERWIG or PYTHIA for parton showering and hadronization. Because the nominal MC@NLO samples are generated with HERWIG, only the difference between the two POWHEG samples is assigned as the uncertainty. This uncertainty is 5.0% for the signal selection. The variation between these samples is seen in Figure 9.17.

These four contributions are combined in quadrature and a total systematic uncertainty for $t\bar{t}$ modeling of 8% is assigned.

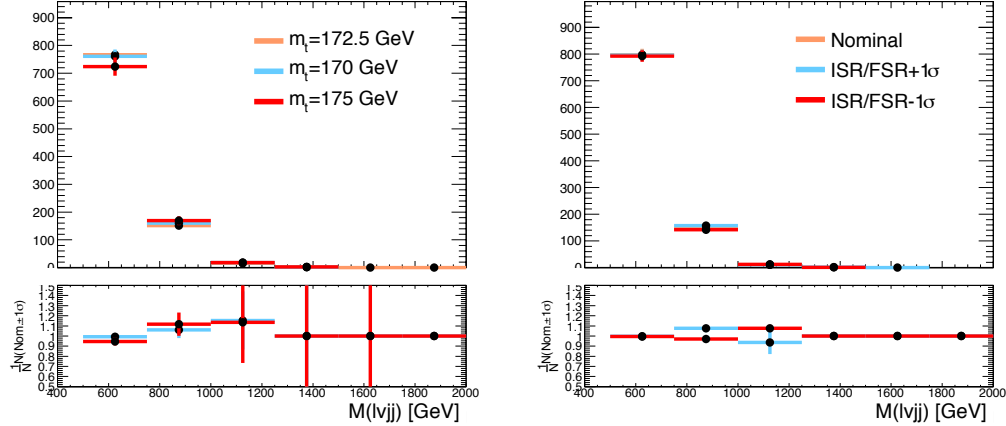


Figure 9.16: The effect of the varying the top mass by ± 2.5 GeV around 172.5 GeV (left) and the PYTHIA ISR/FSR parameters shown in Table 9.5 in the MC@NLO $t\bar{t}$ samples (right) after all selection cuts are applied.

Parameter	PARP(67)	PARP(64)	PARP(72)	PARJ(82)
Nominal	4.0	1.0	0.192	1.0
ISR/FSR up	6.0	0.25	0.384	0.5
ISR/FSR down	0.5	4.0	0.096	2.0

Table 9.5: PYTHIA parameter settings used in the ISR/FSR varied samples for the signal acceptance uncertainty. These parameters are as suggested from the dedicated ATLAS top working group [168].

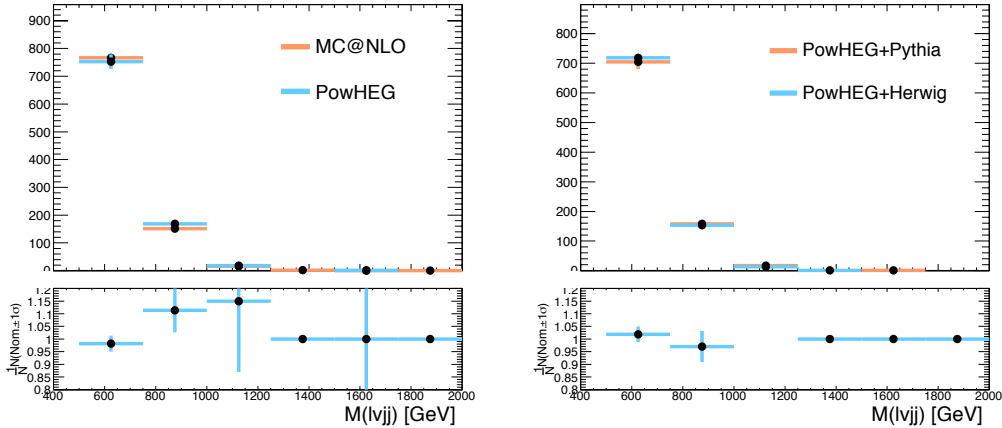


Figure 9.17: The effect of changing the $t\bar{t}$ event generator from MC@NLO to POWHEG (left) and changing the hadronization and parton shower model from PYTHIA to HERWIG (right) after all selection cuts are applied.

9.15 Theoretical Cross Section Uncertainty

Uncertainties on the theoretical cross sections used for the Standard Model backgrounds in this analysis are combined with the appropriate weights to give a contribution to the systematic uncertainty on the total background. The uncertainty on the W and Z boson production cross section is estimated using FEWZ [171]. Although not directly applied due to the theoretical scale uncertainties absorbed by the $W/Z+jets$ scaling uncertainty, as described in Section 9.9, it is presented below. This uncertainty is calculated as the sum in quadrature of contributions from

the MSTW2008NNLO eigenvector PDF sets, from varying the factorization and renormalization scales by two and one half respectively, and from varying $\alpha_s(M_Z)$ by $\pm 1\sigma$. Uncertainties on the other cross sections, which are applied, are given by the sum in quadrature of contributions from the relevant eigenvector PDF sets and, when possible, from varying the factorization and renormalization scales by two and one half respectively. The effects of the uncertainties inherent in the theoretical cross sections used in this analysis are summarized in Table 9.6.

Process	Cross Section	Systematic Uncertainty	Reference
$t\bar{t}$	$164.57^{+11.45}_{-15.78}$ pb	$+7.0\%$ -9.6%	[145]
tb	$4.63^{+0.29}_{-0.27}$ pb	$+6.3\%$ -5.8%	[145]
tqb	$64.57^{+3.32}_{-2.62}$ pb	$+5.1\%$ -4.1%	[146]
tW	$15.74^{+1.34}_{-1.36}$ pb	$+8.5\%$ -8.6%	[146]
WW	44.9 ± 2.2 pb	$\pm 5\%$	[149]
WZ	18.5 ± 1.3 pb	$\pm 7\%$	[150]
ZZ	5.96 ± 0.30 pb	$\pm 5\%$	[151]
$W+\text{jets}$	10.46 ± 0.52 nb	$\pm 5\%$	[152]
$Z+\text{jets}$	1.070 ± 0.054 nb	$\pm 5\%$	[152]

Table 9.6: Effects of theoretical cross section uncertainties of background samples

9.16 Summary of Systematic Uncertainties

9.16.1 Systematic Uncertainties for the $WW \rightarrow \ell\nu jj$ Analysis

Table 9.7 shows the fractional uncertainty for each source of systematic uncertainty for all of the backgrounds and one signal sample in the $WW/WZ \rightarrow e\nu jj$ analysis. Table 9.8 shows the same information for the $WW/WZ \rightarrow \mu\nu jj$ analysis. All numbers presented in this table are computed using Eq. 9.3 thus convolving the

shape of the systematic uncertainty with the shape of the signal or background.

$$\overline{\text{systematic}} = \left| \frac{\int M' + \frac{1}{2} (|\delta M'_{+1\sigma}| + |\delta M'_{-1\sigma}|) dM'}{\int M' dM'} - 1 \right| \quad (9.3)$$

Systematic	WW	WZ	ZZ	$t\bar{t}$	single-top	$W+\text{jets}$	$Z+\text{jets}$	Multijet	$G_{RSI}^* \rightarrow WW (M = 750)$
Electron:									
Trigger	< 0.01	< 0.01	< 0.01	< 0.01	< 0.01	(< 0.01)	(< 0.01)	-	< 0.01
E Resolution	0.02	0.02	0.02	< 0.01	< 0.01	(< 0.01)	(0.02)	-	< 0.01
E Scale	0.02	0.01	0.01	< 0.01	0.01	(< 0.01)	(< 0.01)	-	< 0.01
Reconstruction SF	< 0.01	< 0.01	< 0.01	< 0.01	< 0.01	(< 0.01)	(< 0.01)	-	< 0.01
Jet:									
E Scale	0.09	0.07	0.14	0.05	0.05	(0.11)	(0.18)	-	0.03
E Resolution	< 0.01	0.02	0.07	< 0.01	0.01	(0.01)	(0.07)	-	0.01
Missing E_T :									
All Clusters:	0.01	0.01	0.01	0.01	0.01	(0.01)	(0.01)	-	0.01
Pile-up	0.01	0.01	0.01	0.01	0.01	(< 0.01)	(0.04)	-	< 0.01
Global:									
Luminosity	0.039	0.039	0.039	0.039	0.039	(0.039)	(0.039)	-	0.039
LAr Hole	0.01	0.01	0.01	0.01	0.01	(0.01)	(0.01)	-	< 0.01
Theoretical:									
$WW/WZ/ZZ (\sigma)$	0.05	0.07	0.05	-	-	-	-	-	-
$t\bar{t} (\sigma)$	-	-	-	$+0.07$ -0.096	-	-	-	-	-
$t\bar{t}$ (shape)	-	-	-	0.08	-	-	-	-	-
$tb + tqb + tW (\sigma)$	-	-	-	-	0.08	-	-	-	-
$W/Z+\text{jets}$	-	-	-	-	-	0.09	0.09	-	-
PDF	-	-	-	-	-	-	-	-	0.05
ISR/FSR	-	-	-	-	-	-	-	-	0.05
Multijet:									
Normalization	-	-	-	-	-	-	-	-	0.80

Table 9.7: The fractional systematic uncertainty for all sources of uncertainty for all backgrounds and one signal sample near the expected sensitivity for the $WW/WZ \rightarrow evjj$ analysis. A ‘-’ denotes that this systematic does not apply to a particular background. A systematic surrounded by parenthesis denotes that this systematic has been absorbed into a related systematic and is not directly applied to the limit setting procedure to avoid double counting.

Systematic	WW	WZ	ZZ	$t\bar{t}$	single-top	$W+\text{jets}$	$Z+\text{jets}$	Multijet	$G_{RSI}^* \rightarrow WW (M = 750)$
Muon:									
Trigger	0.02	0.02	0.02	0.02	0.02	(0.02)	(0.02)	-	0.02
p_T Resolution	< 0.01	< 0.01	< 0.01	< 0.01	< 0.01	(< 0.01)	(0.04)	-	< 0.01
p_T Scale	< 0.01	< 0.01	< 0.01	< 0.01	< 0.01	(< 0.01)	(0.01)	-	< 0.01
Reconstruction SF	< 0.01	< 0.01	< 0.01	< 0.01	< 0.01	(< 0.01)	(< 0.01)	-	< 0.01
Jet:									
E Scale	0.12	0.09	0.11	0.07	0.09	(0.11)	(0.09)	-	0.03
E Resolution	0.01	0.01	0.15	0.01	0.02	(0.01)	(0.08)	-	0.01
Missing E_T :									
All Clusters:	0.01	0.01	0.01	< 0.01	< 0.01	(0.01)	(0.03)	-	< 0.01
Pile-up	0.01	0.01	0.01	< 0.01	0.01	(0.01)	(0.03)	-	< 0.01
Global:									
Luminosity	0.039	0.039	0.039	0.039	0.039	(0.039)	(0.039)	-	0.039
LAr Hole	0.01	0.01	0.01	0.01	0.01	(0.01)	(0.01)	-	< 0.01
Theoretical:									
$WW/WZ/ZZ (\sigma)$	0.05	0.07	0.05	-	-	-	-	-	-
$t\bar{t} (\sigma)$	-	-	-	$+0.07$ -0.096	-	-	-	-	-
$t\bar{t}$ (shape)	-	-	-	0.08	-	-	-	-	-
$tb + tqb + tW (\sigma)$	-	-	-	-	0.08	-	-	-	-
$W/Z+\text{jets}$	-	-	-	-	-	0.09	0.09	-	-
PDF	-	-	-	-	-	-	-	-	0.05
ISR/FSR	-	-	-	-	-	-	-	-	0.05
Multijet:									
Normalization	-	-	-	-	-	-	-	-	1.00

Table 9.8: The fractional systematic uncertainty for all sources of uncertainty for all backgrounds and one signal sample near the expected sensitivity for the $WW/WZ \rightarrow \mu\nu jj$ analysis. A ‘-’ denotes that this systematic does not apply to a particular background. A systematic surrounded by parenthesis denotes that this systematic has been absorbed into a related systematic and is not directly applied to the limit setting procedure to avoid double counting.

Chapter 10

Signal Significance Calculation

An analysis of search results is a formal definition of the procedure which quantifies the degree to which the hypotheses are favored or excluded by an experimental observation. The ultimate goal of this statistical analysis is to be able to state whether or not a statistically significant observation of the signal has been made. The following chapter describes the tools used to compute the statistical significance of the data observed in this search. After the selection of an experimental observable (e.g. number of events, invariant mass, etc.), there are three main steps toward this goal:

- Define a test-statistic which optimizes the separation between the signal+background hypothesis (H_1) and the background-only hypothesis (H_0) (Section 10.1).
- Run an appropriate number of pseudo-experiments for both hypotheses, incorporating all signal and background nuisance parameters (systematics) in a coherent way (Section 10.2).
- Specify the range of values (rules) of the test-statistic in which observations will be considered exclusions or discoveries. (Section 10.3).

10.1 Log Likelihood Ratio

A negative Poisson log-likelihood ratio is chosen as the test-statistic and the general form of the likelihood ratio is shown in Eq. 10.1. This functional form has been shown to be the optimal choice of test-statistic in searches for a new physics signal above the SM background [172; 173].

$$\Lambda(\mathbf{x}) = \frac{\mathcal{L}(s + b|\mathbf{x})}{\mathcal{L}(b|\mathbf{x})} \quad (10.1)$$

In this equation, \mathcal{L} is the likelihood function which, for this application, is a Poisson probability distribution function. $\mathcal{L}(s + b|\mathbf{x})$ is the likelihood function for the signal+background hypothesis (H1) and $\mathcal{L}(b|\mathbf{x})$ is the likelihood function for the background-only hypothesis (H0). The fully expanded likelihood ratio test statistic is therefore:

$$\Lambda(\mathbf{x}) = \frac{(s + b)^{\mathbf{x}} e^{-(s+b)}}{\mathbf{x}!} / \frac{(b)^{\mathbf{x}} e^{-(b)}}{\mathbf{x}!} = \frac{(s + b)^{\mathbf{x}} e^{-(s+b)}}{(b)^{\mathbf{x}} e^{-(b)}} \quad (10.2)$$

where \mathbf{x} represents the data, b is the estimated background yield, and s is the predicted signal yield.

It is often necessary to combine the likelihood ratios for multiple, orthogonal, analysis channels (e.g. $e\nu jj$ and $\mu\nu jj$) as well as likelihood ratios from bins within a binned discriminating variable (e.g. $M(\ell\nu jj)$). This test-statistic facilitates such combinations as likelihoods are combined through the product of the subdivided likelihoods ($\mathcal{L} = \prod_i \mathcal{L}_i$). The likelihood ratio statistic, with all analysis channels and discrimination variable bins combined can then be written as,

$$\Lambda(\mathbf{x}) = \prod_i \prod_j^{\text{channels bins}} \frac{(s_{ij} + b_{ij})^{\mathbf{x}_{ij}} e^{-(s_{ij} + b_{ij})}}{\mathbf{x}_{ij}!} / \frac{(b_{ij})^{\mathbf{x}_{ij}} e^{-(b_{ij})}}{\mathbf{x}_{ij}!}. \quad (10.3)$$

The likelihood ratio can be thought of as a generalization of the change in χ^2 for a fit to a distribution including signal+background relative to a fit to a background-only distribution. In the high-statistics limit the distributions of $-2 \log \Lambda$ are expected to converge to $\Delta(\chi^2)$, thus it is more common to use negative two multiplied

by the natural logarithm of Λ as shown in Eq. 10.4.

$$\text{NLLR}(\mathbf{x}) = -2 \ln(\Lambda(\mathbf{x})) = -2 \sum_i^{\text{channels}} \sum_j^{\text{bins}} \left[s_{ij} - \mathbf{x}_{ij} \ln \left(1 + \frac{s_{ij}}{b_{ij}} \right) \right] \quad (10.4)$$

Expressing the test-statistic in this form also makes the calculation simpler when using multiple bins and channels.

10.2 Pseudo Experiments

The significance calculation proceeds in a method that is often referred to as ‘Frequentist-as-possible’. The NLLR is evaluated for the data and designated as $\text{NLLR}(\mathbf{x} = D)$. The basic Frequentist assumption is that the value of the observed data, $\text{NLLR}(\mathbf{x} = D)$, is one outcome of an infinite number of possible outcomes. Other possible outcomes for both the signal+background hypothesis and the background only hypothesis are generated by running pseudo-experiments. In this way, it is possible to compare the measured data NLLR with probability density functions describing the outcomes under the assumptions of either hypothesis.

To generate the background distribution for each pseudo-experiment, a new yield is produced using the following formula: $B_j^m = B_j^{0,m}(1 + \sum_i^N g_i)$. Here, j indicates a background process, m corresponds to a specific bin in the discriminating variable distribution (when using a multi-bin NLLR), and g_i represents the contribution of systematic i to the given process and bin. $B_j^{0,m}$, the nominal background yield, is taken randomly from a Poisson distribution with the mean value given by the expected background yield. In this way, statistical fluctuations are taken into account and propagated into the pseudo-experiment yields.

To calculate the systematic terms in the sum, $\sum_i^N g_i$, each systematic yield (e.g. JES, luminosity, etc.) is produced from a random number taken from a normalized Gaussian distribution with its width (σ) set as the magnitude of the systematic as estimated in Chapter 9. In the case where the $+1\sigma$ uncertainty does not equal the -1σ uncertainty a bifurcated Gaussian is used. This Bayesian approach to incorporating the systematic uncertainties is the reason for the ‘as-possible’ when

referring to this method as ‘Frequentist-as-possible’ (it is also referred to as ‘semi-Frequentist’).

If the systematic uncertainty does not depend on the histogrammed variable (e.g. luminosity uncertainty), then the same g_i is used for each bin. If the systematic uncertainty varies with the histogrammed variable, then g_i is scaled in each bin by the relative systematic uncertainty in that bin to the total systematic uncertainty that was used to generate g_i . In this way the “shape” of the systematic uncertainty is incorporated into the new background prediction.

The same steps are followed to produce pseudo-experiment yields for each signal k : $S_k^m = S_k^{0,m}(1 + \sum_i^N g_i)$. Again, m is the bin index and $S_k^{0,m}$ is the nominal k signal yield in the given bin m .

These two yields, B_j^m and S_k^m , are then combined to form two pseudo-data yields corresponding to the two hypothesis: the H0 background-only hypothesis and the H1 signal+background hypothesis. The H0 pseudo-data yield is computed as

$$\begin{aligned} D_b &= \sum_j^{N_b} \sum_m^{N_{bins}} B_j^m \\ &\equiv \sum_j^{N_b} \sum_m^{N_{bins}} B_j^{0,m} \left(1 + \sum_i^{N^{\text{bkgd}}} g_i\right), \end{aligned} \quad (10.5)$$

while the H1 pseudo-data yield is given as

$$\begin{aligned} D_{s+b} &= \sum_m^{N_{bins}} \left(\sum_j^{N_b} B_j^m + \sum_k^{N_s} S_k^m \right) \\ &\equiv \sum_m^{N_{bins}} \left(\sum_j^{N_b} B_j^{0,m} \left(1 + \sum_i^{N^{\text{bkgd}}} g_i\right) + \sum_k^{N_b} S_k^{0,m} \left(1 + \sum_i^{N^{\text{sig}}} g_i\right) \right). \end{aligned} \quad (10.6)$$

The final step is determining the NLLR value for D_b and D_{s+b} , designated $\text{NLLR}(\mathbf{x}=D_b)$ and $\text{NLLR}(\mathbf{x}=D_{s+b})$, for each pseudo-experiment generated. Once enough pseudo-experiments have been performed to produce smooth distributions of $\text{NLLR}(\mathbf{x}=D_b)$ and $\text{NLLR}(\mathbf{x}=D_{s+b})$, each distribution is normalized to unity, thereby forming probability densities $\mathcal{P}(\mathbf{x} = D_b)$ and $\mathcal{P}(\mathbf{x} = D_{s+b})$. The degree to which these distributions are separated from one another is a measure of the

ability to distinguish the signal+background hypothesis from the Standard Model background-only hypothesis.

Examples of NLLR distributions, each generated by 20,000 pseudo-experiments, are shown in Figures 10.1(a), 10.1(b) and 10.1(c). Here, H_0 is the NLLR test-statistic from pseudo-experiments generated under the assumption of the background-only hypothesis. H_1 are similar distributions generated under the signal+background hypothesis. It is clear that as the signal+background hypothesis becomes less distinguishable from the background-only hypothesis or, as in this example, when the signal mass increases and the signal acceptance drops, the corresponding test-statistics similarly become less distinguishable. When the NLLR value of the data is plotted on the same axis, the location of $\mathcal{P}(\mathbf{x} = D)$ with respect to $\mathcal{P}(\mathbf{x} = D_b)$ and $\mathcal{P}(\mathbf{x} = D_{s+b})$ is used to quantify the significance of the search results.

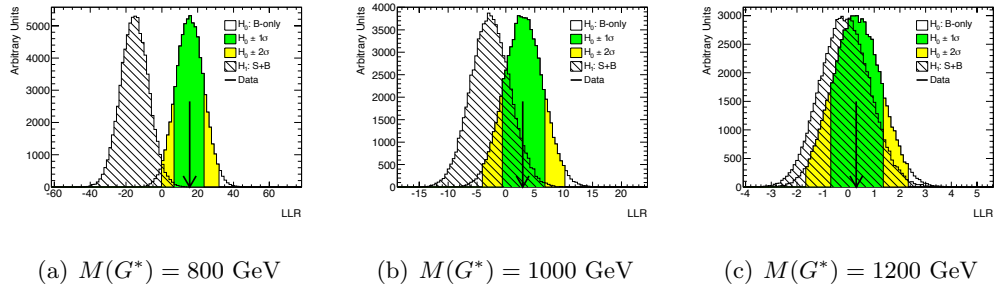


Figure 10.1: NLLR distributions for background only and signal+background hypotheses for three RS1 G^* samples. The solid black arrow shows the median for the background-only hypothesis; the expected NLLR. The green (yellow) band encloses 68% (95%) of background-only pseudo-experiments. The NLLR value given by the data ($\mathcal{P}(\mathbf{x} = D)$) is not shown on these plots.

10.3 Confidence Level Determination

Confidence levels are defined as the fraction of outcomes predicted to fall outside of the specified confidence interval (range of a model parameter). The NLLR test-statistic decreases monotonically for increasingly signal-like (decreasingly background-like) experiments. Therefore, it is possible to define a confidence level which excludes

the possibility of the signal+background (H1) hypothesis as,

$$CL_{s+b} = P_{s+b}(X \geq X_{obs}) \quad (10.7)$$

This is the probability that, assuming the presence of both signal and background at their hypothesized levels, the test statistic (NLLR) would be greater than or equal to the observed data. In other words, the probability of observing data, in the strictly Frequentist sense, that is less signal-like than was observed or, more simply, the probability that the data is the result of the H1 hypothesis. In this way, low values of CL_{s+b} can be used to exclude the signal+background hypothesis.

Specifically, the confidence level of the signal plus background hypothesis (CL_{s+b}) is defined as the integral of $\mathcal{P}(\mathbf{x} = D_{s+b})$ from $+\infty$ down to NLLR($\mathbf{x}=D$) as shown in Eq. 10.8,

$$CL_{s+b} = \int_{\text{NLLR}(\mathbf{x}=D)}^{\infty} \mathcal{P}(\mathbf{x} = D_{s+b}) d\mathcal{P}. \quad (10.8)$$

Similarly, the confidence level for the background alone, CL_b , can be expressed as:

$$CL_b = P_B(X \geq X_{obs}), \quad (10.9)$$

where the probability assumes the background-only (H0) hypothesis. CL_b is the fraction of pseudo-experiment NLLR outcomes that are greater than that observed in data. This represents the probability of observing data that is more background-like than was measured, or the probability, under the background only hypothesis, of the background to fluctuate to at least the value of the data. Therefore, a high CL_b (or low $1 - CL_b$) suggests the data is unlikely to be strictly background-like. Expressed in terms of the probability as computed from the NLLR test statistic, CL_b is written,

$$CL_b = \int_{\text{NLLR}(\mathbf{x}=D)}^{\infty} \mathcal{P}(\mathbf{x} = D_b) d\mathcal{P}. \quad (10.10)$$

In the event of a signal-like excess, CL_b can quantify the confidence of a potential discovery, as it expresses the compatibility with the background-only hypothesis.

A complication arises, however, when using CL_{s+b} to quantify separation between the H0 and H1 hypotheses. That is, this confidence level is inherently dependent on the background model description. If the background is overestimated, or if an experimental result appears consistent with little or no signal together with a downward fluctuation of the background, then $(1 - CL_{s+b})$ may be used to quote exclusion limits that exclude any signal, even with the background itself at high confidence levels.

10.3.1 CL_s Method

The signal plus background confidence level, while a powerful statistical tool, is known to be unstable if the background model dramatically disagrees with the data. A solution to this problem is given by normalizing the signal+background only hypothesis, CL_{s+b} with the background only hypothesis CL_b . This method is referred to as the Modified Frequentist confidence level CL_s [174; 175], shown in Eq. 10.11. In addition to removing the background model dependency of an exclusion, it also leads to more conservative limits as well as a lower false-exclusion rate (type II error) than the nominal value of 1-CL. Thus with the application of CL_s , it is possible to obtain sensible exclusion limits on the signal even when the observed rate is so low that the background hypothesis is called into question.

$$CL_s = \frac{CL_{s+b}}{CL_b} \quad (10.11)$$

It is therefore possible to define a 95% confidence level of signal exclusion when $CL_s \leq 0.05$ ($1 - CL_s > 0.95$).

If an excess of data above the background is observed then the statistical significance is computed from either CL_s or CL_b . Typically the statistical significance of the data is quoted as the degree to which the background-only hypothesis is rejected, which is given by the quantity $1 - CL_b$. This quantity indicates the probability (*p*-value) that the background could have fluctuated to produce a distribution of candidates at least as signal-like as those observed in data. A 3σ evidence of new physics corresponds to $1 - CL_b = 2.7 \times 10^{-3}$ and a 5σ discovery of new physics corresponds to $1 - CL_b = 4.3 \times 10^{-7}$.

In the next chapter, the statistical analysis described above is applied to the search for excited gravitons from warped extra dimensions as presented in this thesis.

Chapter 11

Results

The conclusion of an experimental search for a new particle is a statistical statement, namely whether a statistically significant observation of the signal has been made. If so, a measurement of the cross section can be calculated, if not an upper-bound on the production cross section can be determined [176].

In this chapter, the results of the diboson resonance search are presented for two baseline models: the spin-2 bulk RS $G^* \rightarrow WW$ and the spin-2 RS1 $G^* \rightarrow WW$. The signal acceptance for each model is used to determine a limit on the cross sections (σ) multiplied by the branching ratio (B). A limit on the bulk RS and the RS1 graviton mass is also presented. These mass limits allow a comparison with previous searches at the LHC and the Tevatron as well as set a well understood benchmark for future searches.

11.1 Limits on Excited Gravitons

The discriminating variable used for the statistical analysis is the invariant mass, $M(\ell\nu jj)$, after applying the signal region selection criteria to the backgrounds, both $G^* \rightarrow WW$ signals, and the data. These distributions are shown in Figure 8.2 and again below in Figure 11.1. Table 11.1 shows the event yield for the signal region, similar to Table 8.1, however with full statistical and systematic uncertainties included in the yield errors.

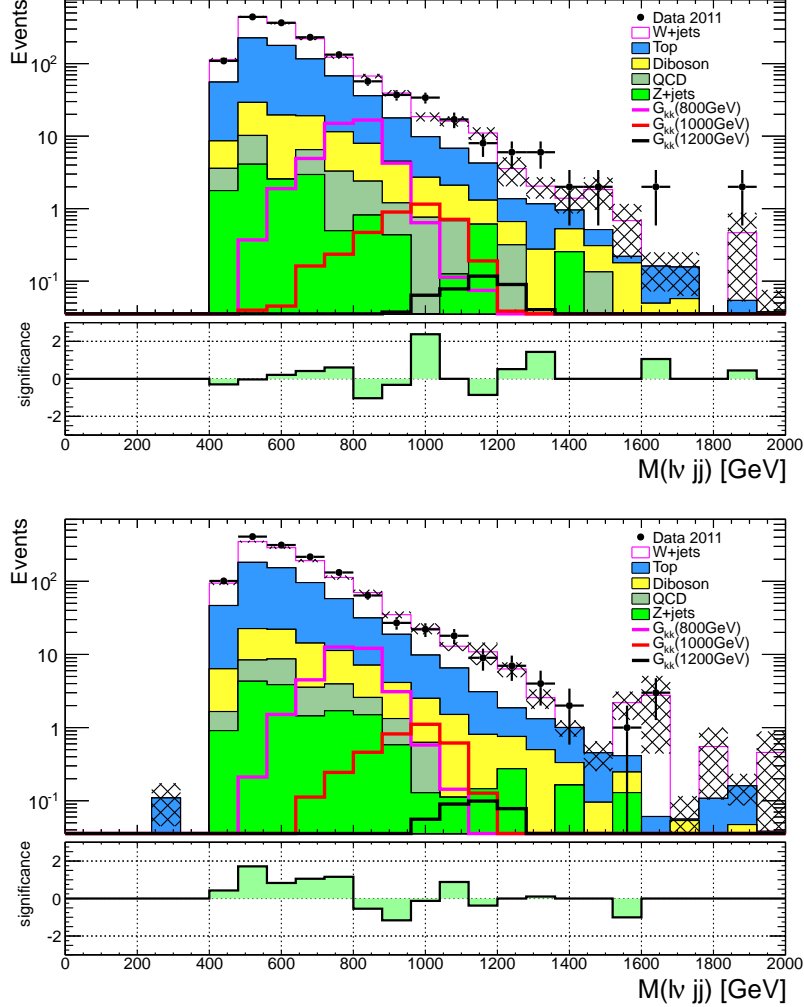


Figure 11.1: Comparison of the data and backgrounds as a function of the diboson invariant mass ($M(\ell\nu jj)$) in the signal region for the $e\nu jj$ (top) and $\mu\nu jj$ (bottom) channels.

Limits are set on the production cross section multiplied by the branching ratio for the two signals as a function of the resonance mass. Figures 11.2 and 11.3 show the cross section multiplied by the branching ratio limits as well as the mass limits for the bulk RS and RS1 gravitons. These limits were derived with complete systematic uncertainty estimations applied and using the signal templates derived with the method described in Section 5.2.2. The $e\nu jj$ and $\mu\nu jj$ channels are orthogonal

Process	$e\nu jj$ channel	$\mu\nu jj$ channel
$W + \text{jets}$	698 ± 64	594 ± 57
$Z + \text{jets}$	14 ± 2	15 ± 2
Top	614^{+59}_{-86}	518^{+50}_{-73}
Diboson	76 ± 9	63 ± 8
QCD	18 ± 24	16 ± 11
Total backgrounds	1420^{+91}_{-110}	1206^{+77}_{-94}
Data	1452	1318
Bulk G^* ($m_{G^*} = 800$ GeV)	44 ± 2	35 ± 2
Bulk G^* ($m_{G^*} = 1000$ GeV)	4 ± 0	4 ± 0
Bulk G^* ($m_{G^*} = 1200$ GeV)	1 ± 0	0
RS1 G^* ($m_{G^*} = 750$ GeV)	208 ± 9	163 ± 8
RS1 G^* ($m_{G^*} = 1000$ GeV)	22 ± 1	18 ± 1
RS1 G^* ($m_{G^*} = 1250$ GeV)	3 ± 0	3 ± 0

Table 11.1: The signal region yields for the estimated background, data and signal events. Errors given are statistical combined with full systematic uncertainties.

and therefore combined using the same statistical treatment as for each individual channel. The lower limit on the resonance mass is derived from the intersection of the central excluded limit line and the production cross section. All resonance masses are excluded if the production cross section for that mass is greater than or equal to the excluded cross section. It is found that the bulk RS graviton is (expected to be) excluded at a 95% CL for masses below **714** (749) GeV, and that the RS1 graviton is (expected to be) excluded at a 95% CL for masses below **936** (952) GeV for the combined $e\nu jj$ and $\mu\nu jj$ channels.

The mass for which the production cross section equals the excluded cross section is presented in Table 11.2 for both final states and all signals. The same information using the fully simulated signal events instead of the signal templates is presented in Table 11.3. In each table the mass limits are presented for the scenario when no

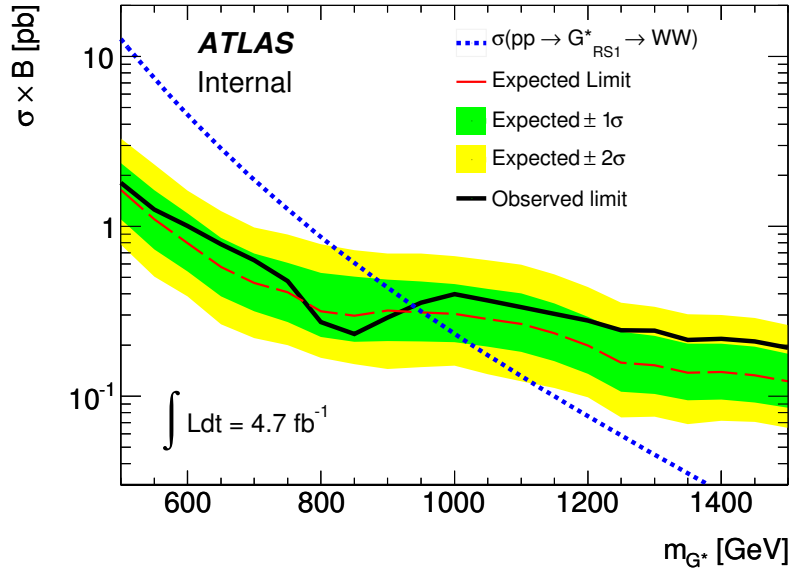


Figure 11.2: The expected excluded production cross section limit multiplied by the branching fraction for the $e\nu jj + \mu\nu jj$ final state assuming the original RS1 graviton $G^* \rightarrow WW$ signal.

systematic uncertainties are included in the limit calculation and the nominal case of full systematic uncertainties. Additionally, Table 11.4 shows the p -values ($1-\text{CL}_b$) calculated for all mass points. The p -value is the probability that the background has fluctuated to or above the data, under the assumption of the background-only hypothesis.

Signal	$e\nu jj$	$e\nu jj$	$\mu\nu jj$	$\mu\nu jj$	Combined	Combined
	w/o sys	w/ sys	w/o sys	w/ sys	w/o sys	w/ sys
RS1 G^* (expected)	1017	966	982	907	1065	952
RS1 G^* (observed)	928	915	982	934	973	936
Bulk RS G^* (expected)	814	728	795	693	838	749
Bulk RS G^* (observed)	818	727	738	631	849	714

Table 11.2: Expected and observed lower mass limits for the RS1 graviton and the ‘bulk’ RS graviton in the $e\nu jj$, $\mu\nu jj$, and combined $e\nu jj + \mu\nu jj$ channels using the template signal histograms to set limits.

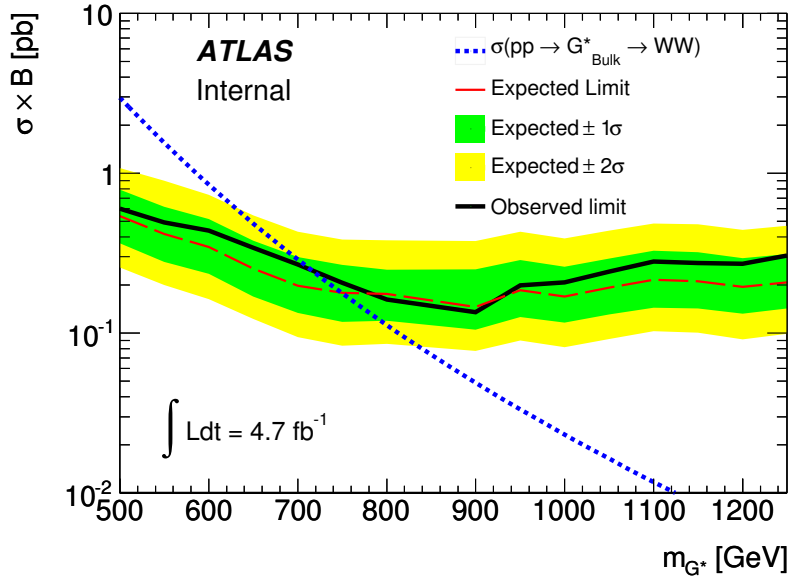


Figure 11.3: The expected excluded production cross section limit multiplied by the branching fraction for the $e\nu jj + \mu\nu jj$ final state assuming the bulk RS $G^* \rightarrow WW$ signal.

Signal	$e\nu jj$	$e\nu jj$	$\mu\nu jj$	$\mu\nu jj$	Combined	Combined
	w/o sys	w/ sys	w/o sys	w/ sys	w/o sys	w/ sys
RS1 G^* (expected)	1008	917	955	845	1044	915
RS1 G^* (observed)	928	915	982	934	973	936
Bulk RS G^* (expected)	814	731	795	690	837	752
Bulk RS G^* (observed)	812	723	750	623	834	710

Table 11.3: Expected and observed lower mass limits for the RS1 graviton and ‘bulk’ RS graviton in the $e\nu jj$, $\mu\nu jj$, and combined $e\nu jj + \mu\nu jj$ channels using the full-sim signal histograms to set limits.

Mass	$e\nu jj$	$\mu\nu jj$	Combined
500	0.60	0.17	0.38
550	0.49	0.22	0.35
600	0.37	0.21	0.27
650	0.32	0.15	0.22
700	0.37	0.12	0.22
750	0.51	0.19	0.34
800	0.69	0.39	0.56
850	0.66	0.64	0.68
900	0.45	0.71	0.61
950	0.21	0.61	0.40
1000	0.14	0.45	0.27
1050	0.18	0.35	0.27
1100	0.21	0.33	0.28
1150	0.18	0.33	0.27
1200	0.11	0.28	0.20
1250	0.07	0.22	0.13
1300	0.07	0.19	0.16
1350	0.08	0.23	0.13
1450	0.02	0.43	0.17
1500	0.01	0.53	0.11

Table 11.4: The probabilities, or p -value $\equiv 1 - \text{CL}_b$, that the background fluctuates to or above the data in each channel. Systematic uncertainties are included in this calculation.

11.2 Summary and Conclusions

A search for resonant diboson production in the $\ell\nu jj$ decay channel with 4.7 fb^{-1} of 2011 ATLAS data at $\sqrt{s} = 7 \text{ TeV}$ has been presented. The observed spectrum agrees with predictions based on Standard Model background processes. Thus, lacking evidence for resonant diboson production, limits on anomalous WW/WZ gauge boson production are set over the mass range of 500 GeV to 1.5 TeV. Specifically,

limits on the cross section times branching ratio of two Randall-Sundrum extra-dimensional excited graviton models have been set which substantially improve on previous searches. These cross section limits are interpreted as limits on the mass of the graviton in the two models. In this way, this analysis has excluded an excited spin-2 RS1 graviton at 95% CL for $M(G_{RS1}^*) < 936$ GeV and an excited spin-2 bulk RS graviton at 95% CL for $M(G_{\text{Bulk}}^*) < 714$ GeV. These results represent the most sensitive exclusion limits for these signals, in these decay channels, to date.

Looking ahead, both ATLAS and CMS continue to record data into 2012, however the center-of-mass energy at the LHC has been increased from 7 to 8 TeV. This will have the effect of extending the LHC's exclusion (or discovery) reach dramatically and provides exciting prospects for diboson resonance searches. At the same time, the higher energy, in association with higher instantaneous luminosities, will result in many challenges to future analyzers due to the substantially increased backgrounds.

As was observed in this thesis, the large W +jets background and its systematics proved a limiting factor in the search sensitivity. One promising way to cut back on such background is the use of the jet mass variable. As the diboson resonances reaches higher masses, the boson decay products reach higher transverse momenta and become more collinear. In the case of a hadronic boson decay, at higher transverse momenta, it becomes more likely for the two jets to be reconstructed as one. This has the result of a distinctive signal signature in the leading jet mass spectrum of a resonance at the W boson mass, not observed in any background. This technique was explored for the analysis presented here, although at the current energy and luminosity, no substantial improvement was observed. It is expected, however, that for next generation diboson analyses, working with 8 TeV collisions, using the jet mass variable will be imperative to cut down on the large backgrounds and extend the discovery sensitivity.

Chapter 12

Appendices

Appendix A

Comparison of Signal Monte Carlo Events

The bulk RS G^* events undergo jet merging at a higher rate compared to the RS1 G^* and SSM+EGM W' events¹. This is seen in Figures A.1, A.2, and A.3 which show the leading jet p_T and jet mass for the three signals for three resonance masses: 500, 1000, and 1500 GeV. At low resonance mass (i.e. 500 GeV) there are essentially no merged jets and the leading jet mass peaks at 10-20 GeV for all samples. For $M = 1000$ GeV, the bulk RS samples show a distinct peak at the W boson mass, whereas the other two samples show a bimodal structure. For $M = 1500$ GeV, all samples peak at the W or Z boson mass, however the bulk RS sample still has a higher fraction of events with a large jet mass, which is a clear indication of jet merging.

¹The SSM+EGM W' model, or Sequential Standard Model Extended Gauge Model W' [177], is an additional benchmark signal explored in the full analysis [156] however not included in this thesis. The decay simulated is $W' \rightarrow WZ \rightarrow \ell\nu jj$

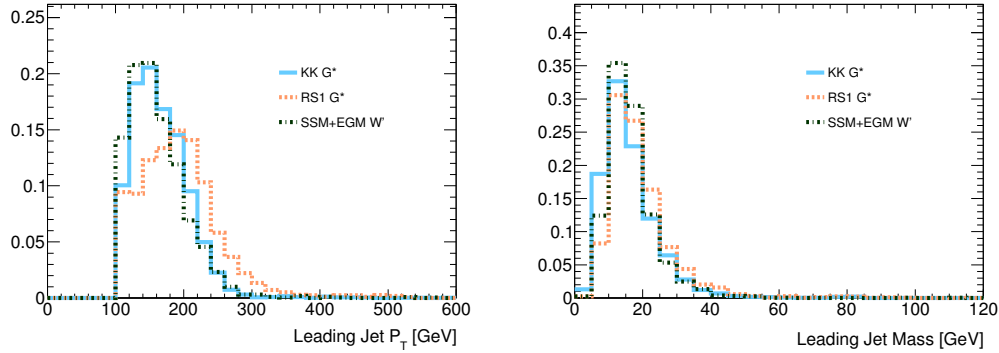


Figure A.1: Comparison of the leading jet p_T (left) and jet mass (right) for the three signal samples considered in this analysis all with resonance mass equal to 500 GeV. The effect of jet merging occurs for lower G^* masses in the bulk RS events compared to the RS1 G^* and SSM+EGM W' .

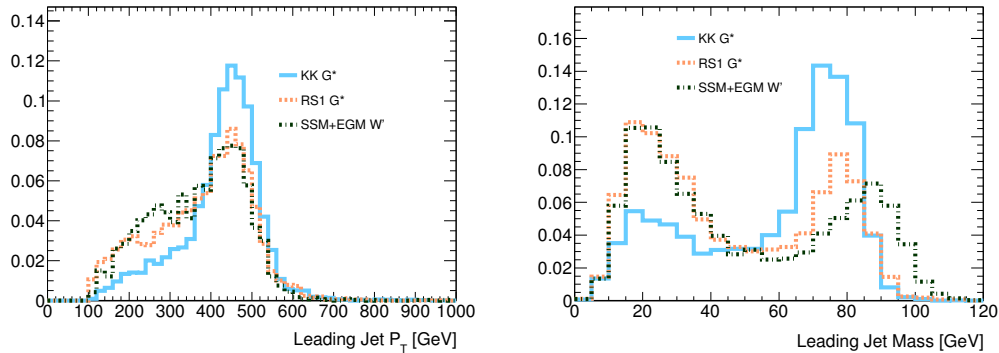


Figure A.2: Comparison of the leading jet p_T (left) and jet mass (right) for the three signal samples considered in this analysis all with resonance mass equal to 1000 GeV. The effect of jet merging occurs for lower G^* masses in the bulk RS events compared to the RS1 G^* and SSM+EGM W' .

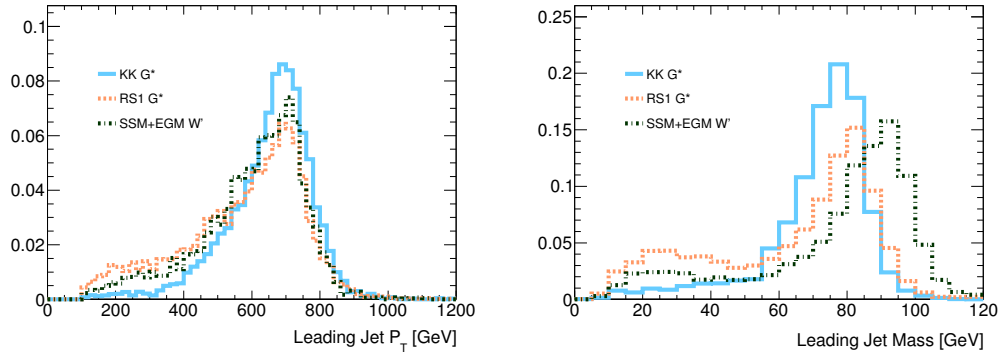


Figure A.3: Comparison of the leading jet p_T (left) and jet mass (right) for the three signal samples considered in this analysis all with resonance mass equal to 1500 GeV. The effect of jet merging occurs for lower G^* masses in the bulk RS events compared to the RS1 G^* and SSM+EGM W' .

The event-level cut flows for signal masses equal to 500 and 1500 GeV for both the $e\nu jj$ and $\mu\nu jj$ channels are shown in Tables A.1 to A.4. The effect of jet merging can be seen in the higher signal mass cut flow at the ‘Two or more Good jets’ cut. Here the cut efficiency is $\sim 30\%$ for the bulk RS graviton sample while for the RS graviton and W' samples the efficiencies are $\sim 55\%$ and $\sim 40\%$, respectively. For the 500 GeV signal mass cut flow, the efficiencies of the same cut for all three signal samples are $\sim 75\%$.

Cut	RS1 G^*	SSM+EGM W'	bulk RS G^*
All Events	30000 (1)	10000 (1)	15000 (1)
Triggered Events	8621 (0.29)	4210 (0.42)	5887 (0.39)
Good Vertex Events	8621 (1)	4210 (1)	5887 (1)
One Good electron	6521 (0.76)	3305 (0.79)	4710 (0.8)
No 2 nd medium++ electron	6516 (1)	3301 (1)	4709 (1)
No good muons	6473 (0.99)	3271 (0.99)	4687 (1)
Two or more Good jets	4701 (0.73)	2473 (0.76)	3596 (0.77)
Good E_T^{miss}	3871 (0.82)	2163 (0.87)	3229 (0.9)
Triangle cut region veto	3415 (0.88)	1956 (0.9)	2919 (0.9)
Leading jet $p_T > 100$ GeV.	3131 (0.92)	1776 (0.91)	2751 (0.94)
Satisfies preselection cuts	3131	1776	2751
Filter Efficiency	1	1	0.81
Acceptance	10.4 ± 0.1	17.8 ± 0.1	14.9 ± 0.1

Table A.1: The number of RS1, W' , and bulk RS G^* with $M(G^*)=500$ GeV Monte Carlo events remaining after each of the $e\nu jj$ -channel cuts listed in the first column is applied. The relative efficiency of each cut is shown in parentheses after the number of surviving events. The signal acceptance after all cuts is shown at the bottom of the table with statistical uncertainty only.

Cut	RS1 G^*	SSM+EGM W'	bulk RS G^*
All Events	30000 (1)	10000 (1)	15000 (1)
Triggered Events	7414 (0.25)	3555 (0.36)	5121 (0.34)
Good Vertex Events	7414 (1)	3555 (1)	5121 (1)
One Good muon	5828 (0.79)	2988 (0.84)	4340 (0.85)
No 2 nd medium++ electron	5825 (1)	2986 (1)	4338 (1)
No good muons	5779 (0.99)	2948 (0.99)	4308 (0.99)
Two or more Good jets	4217 (0.73)	2217 (0.75)	3207 (0.74)
Good E_T^{miss}	3376 (0.8)	1894 (0.85)	2807 (0.88)
Triangle cut region veto	3047 (0.9)	1690 (0.89)	2527 (0.9)
Leading jet $p_T > 100$ GeV.	2758 (0.91)	1524 (0.9)	2363 (0.94)
Satisfies preselection cuts	2758	1524	2363
Filter Efficiency	1	1	0.81
Acceptance	9.2 ± 0.1	15.2 ± 0.1	12.8 ± 0.1

Table A.2: The number of RS1, W' , and bulk RS G^* with $M(G^*)=500$ GeV Monte Carlo events remaining after each of the $\mu\nu jj$ -channel cuts listed in the first column is applied. The relative efficiency of each cut is shown in parentheses after the number of surviving events. The signal acceptance after all cuts is shown at the bottom of the table with statistical uncertainty only.

Cut	RS1 G^*	SSM+EGM W'	bulk RS G^*
All Events	30000 (1)	10000 (1)	15000 (1)
Triggered Events	9849 (0.33)	4525 (0.45)	6544 (0.44)
Good Vertex Events	9849 (1)	4525 (1)	6544 (1)
One Good electron	7548 (0.77)	3796 (0.84)	5582 (0.85)
No 2 nd medium++ electron	7536 (1)	3789 (1)	5581 (1)
No good muons	7453 (0.99)	3724 (0.98)	5514 (0.99)
Two or more Good jets	3915 (0.53)	1539 (0.41)	1581 (0.29)
Good E_T^{miss}	3715 (0.95)	1499 (0.97)	1557 (0.98)
Triangle cut region veto	3555 (0.96)	1455 (0.97)	1530 (0.98)
Leading jet $p_T > 100$ GeV.	3539 (1)	1452 (1)	1529 (1)
Satisfies preselection cuts	3539	1452	1529
Filter Efficiency	1	1	0.81
Acceptance	11.8 ± 0.06	14.5 ± 0.07	8.3 ± 0.06

Table A.3: The number of RS1, W' , and bulk RS G^* with $M(G^*)=1500$ GeV Monte Carlo events remaining after each of the $e\nu jj$ -channel cuts listed in the first column is applied. The relative efficiency of each cut is shown in parentheses after the number of surviving events. The signal acceptance after all cuts is shown at the bottom of the table with statistical uncertainty only.

Cut	RS1 G^*	SSM+EGM W'	bulk RS G^*
All Events	30000 (1)	10000 (1)	15000 (1)
Triggered Events	8275 (0.28)	3746 (0.37)	5166 (0.34)
Good Vertex Events	8275 (1)	3746 (1)	5166 (1)
One Good muon	6407 (0.77)	3097 (0.83)	4334 (0.84)
No 2 nd medium++ electron	6399 (1)	3096 (1)	4334 (1)
No good muons	6299 (0.98)	3021 (0.98)	4265 (0.98)
Two or more Good jets	3482 (0.55)	1275 (0.42)	1227 (0.29)
Good E_T^{miss}	3256 (0.94)	1241 (0.97)	1195 (0.97)
Triangle cut region veto	3163 (0.97)	1219 (0.98)	1166 (0.98)
Leading jet $p_T > 100$ GeV.	3149 (1)	1219 (1)	1166 (1)
Satisfies preselection cuts	3149	1219	1166
Filter Efficiency	1	1	0.81
Acceptance	10.5 ± 0.06	12.2 ± 0.07	6.3 ± 0.06

Table A.4: The number of RS1, W' , and bulk RS G^* with $M(G^*)=1500$ GeV Monte Carlo events remaining after each of the $\mu\nu jj$ -channel cuts listed in the first column is applied. The relative efficiency of each cut is shown in parentheses after the number of surviving events. The signal acceptance after all cuts is shown at the bottom of the table with statistical uncertainty only.

Appendix B

Additional Preselection Plots

B.1 Electron Channel

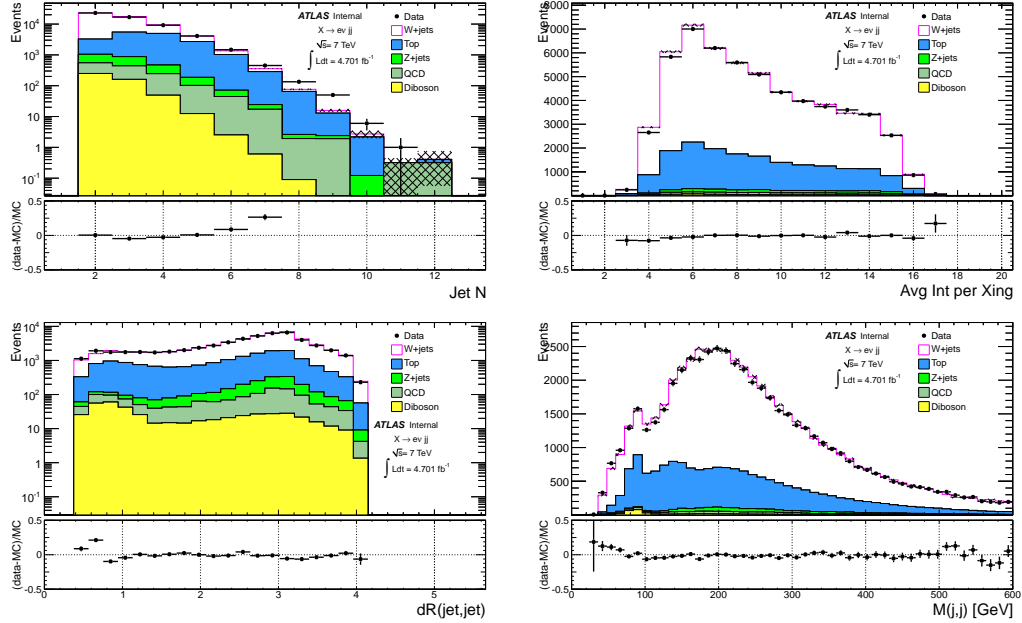


Figure B.1: Comparison of the data with the background prediction after $evjj$ pre-selection.

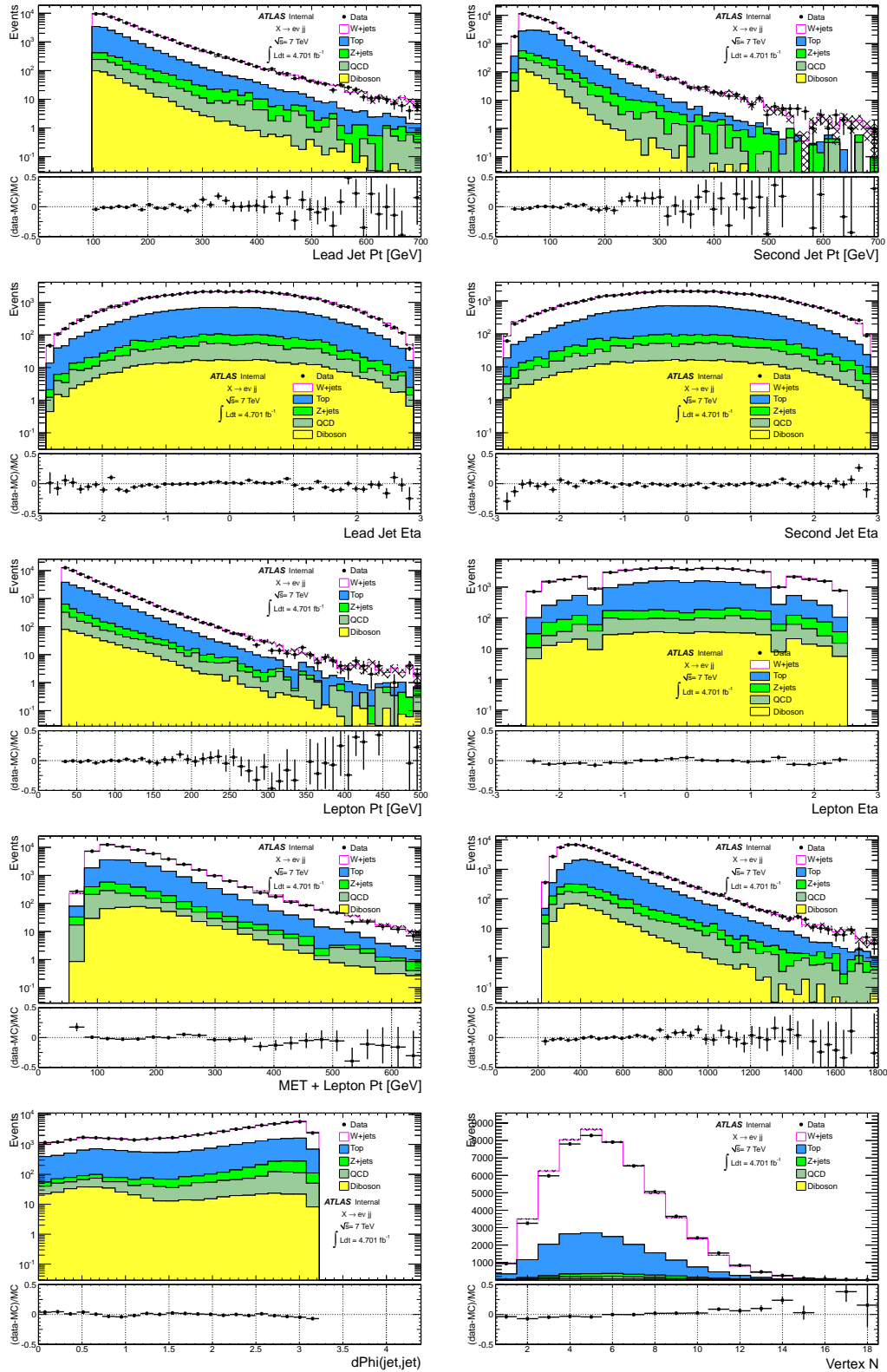


Figure B.2: Comparison of the data with the background prediction after $evjj$ pre-selection.

B.2 Muon Channel

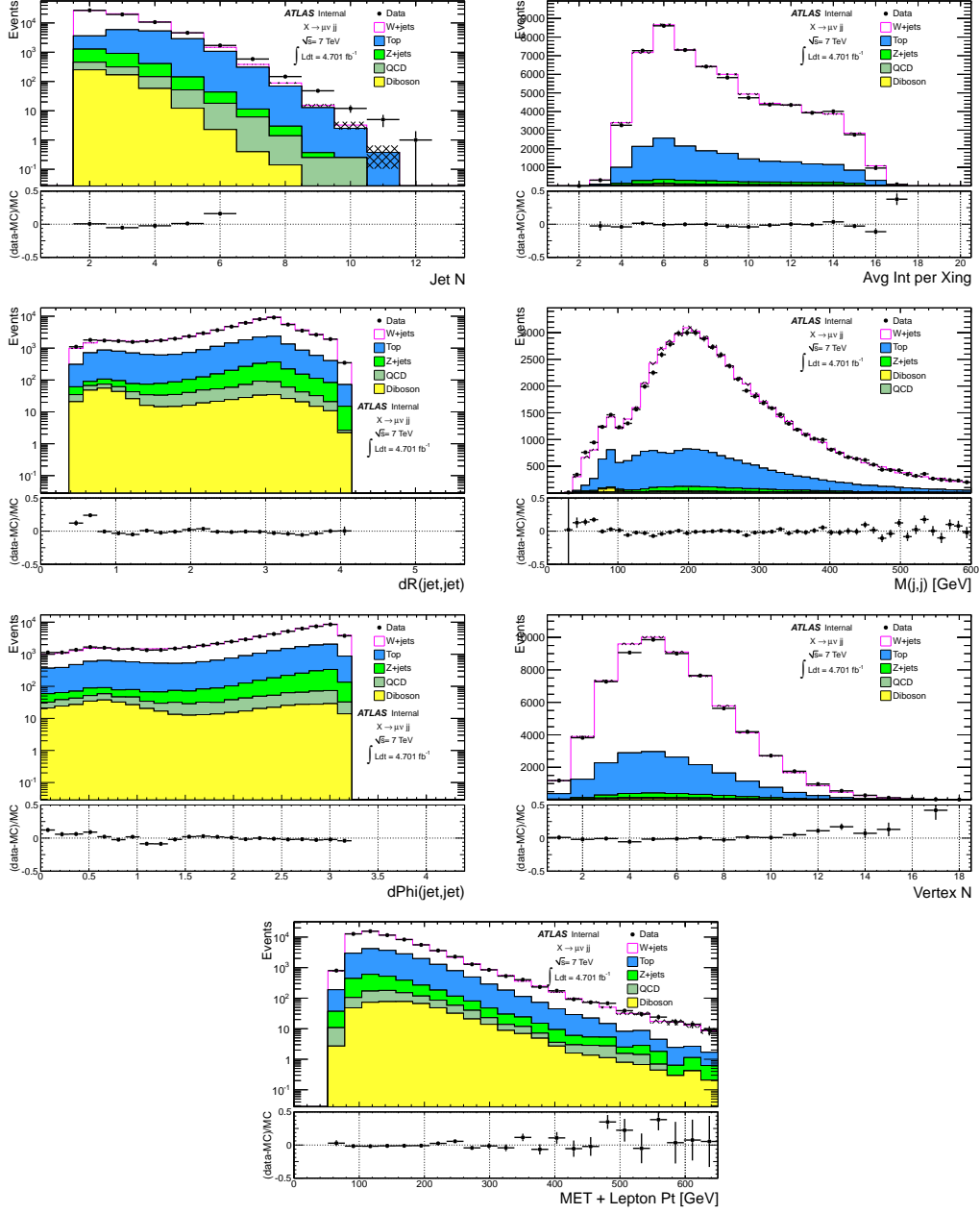


Figure B.3: Comparison of the data with the background prediction after $\mu\nu jj$ pre-selection.

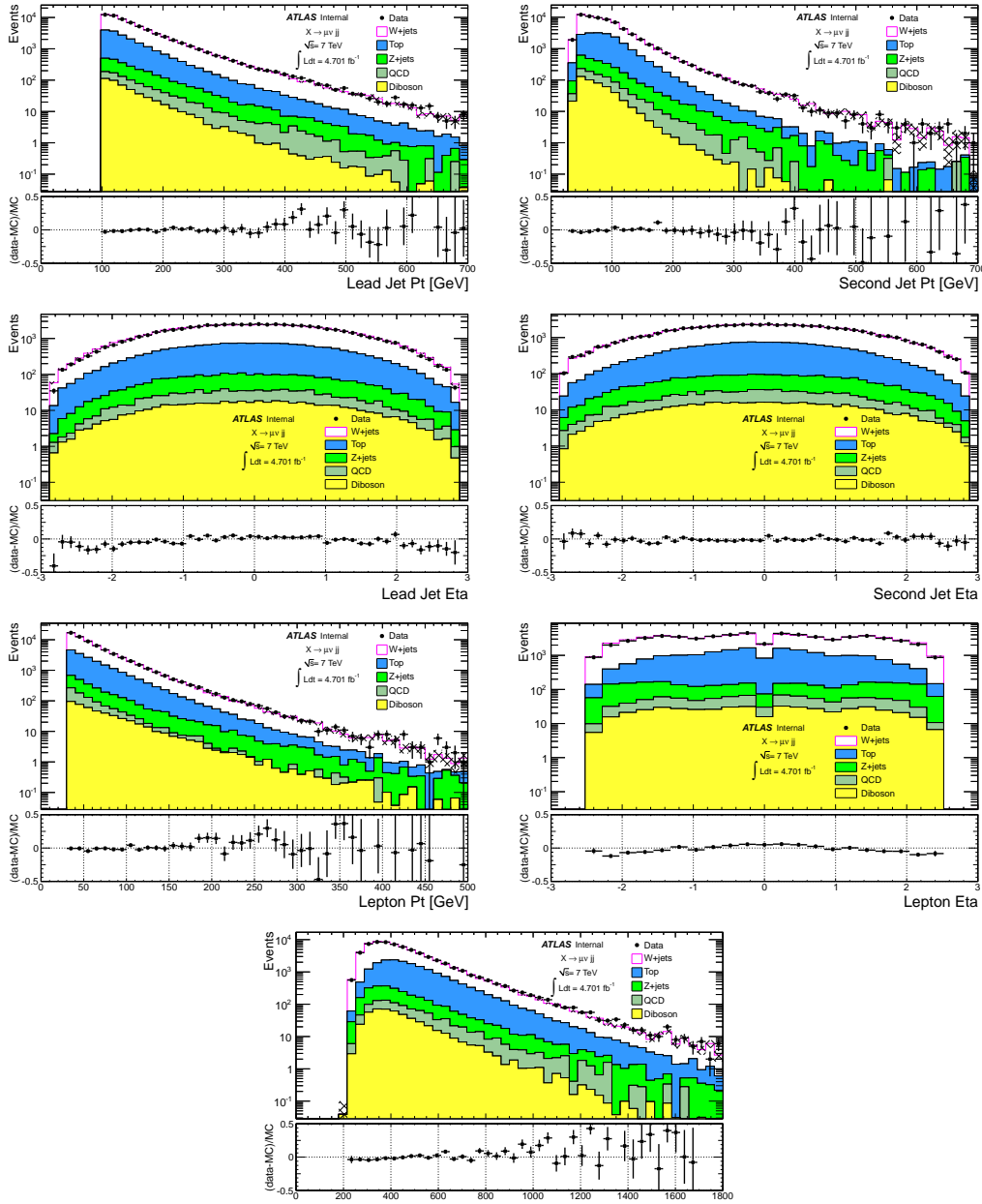


Figure B.4: Comparison of the data with the background prediction after $\mu\nu jj$ pre-selection.

Appendix C

Additional Signal Region Plots

C.1 Electron Channel

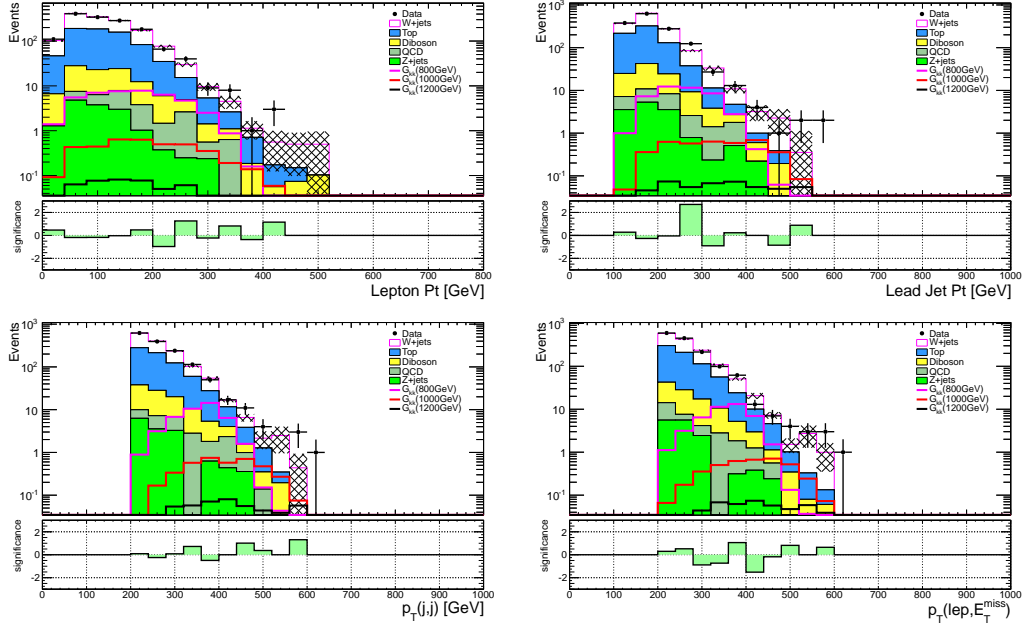


Figure C.1: Comparison of the data with the background prediction after $e\nu jj$ signal region selection.

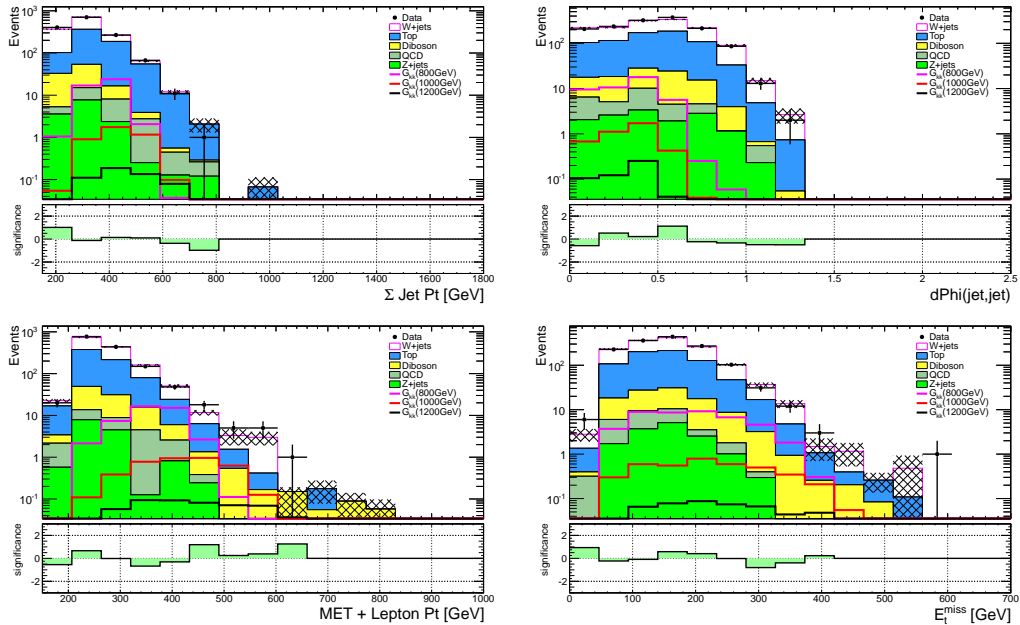


Figure C.2: Comparison of the data with the background prediction after $e\nu jj$ signal region selection.

C.2 Muon Channel

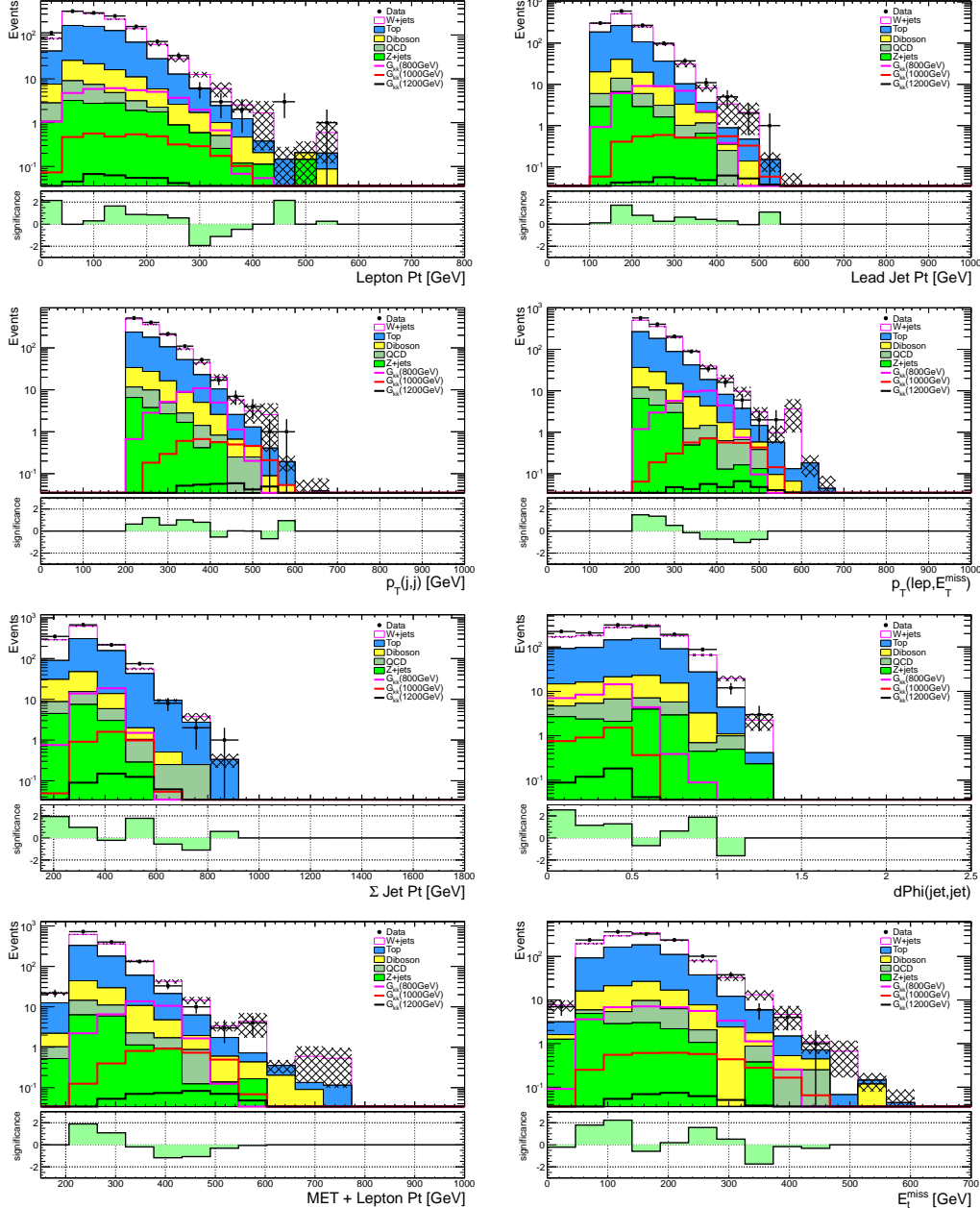


Figure C.3: Comparison of the data with the background prediction after $\mu\nu jj$ signal region selection.

Bibliography

- [1] S. Glashow, “Partial Symmetries of Weak Interactions,” *Nucl. Phys.* **22** (1961) 579–588.
- [2] S. Weinberg, “A Model of Leptons,” *Phys. Rev. Lett.* **19** (1967) 1264–1266.
- [3] F. Halzen and A. D. Martin, *Quarks and Leptons: An Introductory Course in Modern Particle Physics*. Wiley, New York, NY, 1984.
- [4] **Particle Data Group** Collaboration, K. Nakamura *et al.*, “Review of particle physics,” *J. Phys.* **G37** (2010) 075021.
- [5] E. Noether, “Invariant Variation Problems,” *Gott. Nachr.* **1918** (1918) 235–257, [arXiv:physics/0503066 \[physics\]](https://arxiv.org/abs/physics/0503066).
- [6] M. E. Peskin and D. V. Schroeder, *An Introduction to Quantum Field Theory*. Westview, 1995.
- [7] B. Martin and G. Shaw, *Particle Physics*. Wiley, 1997.
- [8] Q. Ho-Kim and X. Pham, *Elementary Particles and their Interactions*. Springer, 1998.
- [9] M. Herrero, “The Standard Model,” [arXiv:hep-ph/9812242 \[hep-ph\]](https://arxiv.org/abs/hep-ph/9812242).
- [10] F. Englert and R. Brout, “Broken Symmetry and the Mass of Gauge Vector Mesons,” *Phys. Rev. Lett.* **13** (1964) 321–323.
- [11] P. W. Higgs, “Broken symmetries, massless particles and gauge fields,” *Phys. Lett.* **12** (1964) 132–133.

- [12] G. Guralnik, C. Hagen, and T. Kibble, “Global Conservation Laws and Massless Particles,” *Phys. Rev. Lett.* **13** (1964) 585–587.
- [13] A. Djouadi, “The Anatomy of Electroweak Symmetry Breaking. I: The Higgs Boson in the Standard Model,” *Phys. Rept.* **457** (2008) 1–216, [arXiv:hep-ph/0503172 \[hep-ph\]](https://arxiv.org/abs/hep-ph/0503172).
- [14] M. Baak, M. Goebel, J. Haller, A. Hoecker, D. Ludwig, *et al.*, “Updated Status of the Global Electroweak Fit and Constraints on New Physics,” [arXiv:1107.0975 \[hep-ph\]](https://arxiv.org/abs/1107.0975).
- [15] **ALEPH Collaboration, CDF Collaboration, D0 Collaboration, DELPHI Collaboration, L3 Collaboration, OPAL Collaboration, SLD Collaboration, LEP Electroweak Working Group, Tevatron Electroweak Working Group, SLD Electroweak and Heavy Flavour Groups** Collaboration, “Precision Electroweak Measurements and Constraints on the Standard Model,” [arXiv:1012.2367 \[hep-ex\]](https://arxiv.org/abs/1012.2367).
- [16] L. Susskind, “Dynamics of spontaneous symmetry breaking in the Weinberg-Salam theory,” *Phys. Rev.* **D20** (1979) 2619–2625.
- [17] A. A. Geraci, S. J. Smullin, D. M. Weld, J. Chiaverini, and A. Kapitulnik, “Improved Constraints on Non-Newtonian Forces at 10 Microns,” *Phys. Rev.* **D78** (2008) 022002, [arXiv:0802.2350 \[hep-ex\]](https://arxiv.org/abs/0802.2350).
- [18] C. Hoyle, D. Kapner, B. R. Heckel, E. Adelberger, J. Gundlach, *et al.*, “Sub-Millimeter Tests of the Gravitational Inverse-Square Law,” *Phys. Rev.* **D70** (2004) 042004, [arXiv:hep-ph/0405262 \[hep-ph\]](https://arxiv.org/abs/hep-ph/0405262).
- [19] S. J. Smullin, A. A. Geraci, D. M. Weld, A. Kapitulnik, and J. Chiaverini, “Testing gravity at short distances.”. Talk given at 32nd SLAC Summer Institute on Particle Physics (SSI 2004): Natures Greatest Puzzles, Menlo Park, California, 2-13 Aug 2004.

- [20] N. Arkani-Hamed, S. Dimopoulos, and G. Dvali, “The Hierarchy Problem and New Dimensions at a Millimeter,” *Phys. Lett.* **B429** (1998) 263–272, [arXiv:hep-ph/9803315 \[hep-ph\]](https://arxiv.org/abs/hep-ph/9803315).
- [21] G. F. Giudice, R. Rattazzi, and J. D. Wells, “Quantum Gravity and Extra Dimensions at High-Energy Colliders,” *Nucl. Phys.* **B544** (1999) 3–38, [arXiv:hep-ph/9811291 \[hep-ph\]](https://arxiv.org/abs/hep-ph/9811291).
- [22] T. Han, J. D. Lykken, and R.-J. Zhang, “Kaluza-Klein states from large extra dimensions,” *Phys. Rev.* **D59** (1999) 105006.
- [23] L. Randall and R. Sundrum, “A large mass hierarchy from a small extra dimension,” *Phys. Rev. Lett.* **83** (1999) 3370–3373, [arXiv:hep-ph/9905221](https://arxiv.org/abs/hep-ph/9905221).
- [24] L. Randall, “Extra dimensions and warped geometries,” *Science* **296** (2002) 1422–1427.
- [25] E. Witten, “Anti-de Sitter space and holography,” *Adv. Theor. Math. Phys.* **2** (1998) 253–291, [arXiv:hep-th/9802150 \[hep-th\]](https://arxiv.org/abs/hep-th/9802150).
- [26] H. Davoudiasl, J. Hewett, and T. Rizzo, “Phenomenology of the Randall-Sundrum Gauge Hierarchy Model,” *Phys. Rev. Lett.* **84** (2000) 2080, [arXiv:hep-ph/9909255 \[hep-ph\]](https://arxiv.org/abs/hep-ph/9909255).
- [27] A. Pomarol, “Gauge bosons in a five-dimensional theory with localized gravity,” *Phys. Lett.* **B486** (2000) 153–157, [arXiv:hep-ph/9911294 \[hep-ph\]](https://arxiv.org/abs/hep-ph/9911294).
- [28] **Particle Data Group** Collaboration, C. Amsler *et al.*, “Review of Particle Physics,” *Phys. Lett.* **B667** (2008) 1–1340.
- [29] W. D. Goldberger and M. B. Wise, “Modulus stabilization with bulk fields,” *Phys. Rev. Lett.* **83** (1999) 4922–4925, [arXiv:hep-ph/9907447 \[hep-ph\]](https://arxiv.org/abs/hep-ph/9907447).
- [30] W. D. Goldberger and M. B. Wise, “Bulk fields in the Randall-Sundrum compactification scenario,” *Phys. Rev.* **D60** (1999) 107505, [arXiv:hep-ph/9907218 \[hep-ph\]](https://arxiv.org/abs/hep-ph/9907218).

- [31] K. M. Cheung, “Phenomenology of radion in Randall-Sundrum scenario,” *Phys. Rev.* **D63** (2001) 056007, [arXiv:hep-ph/0009232 \[hep-ph\]](https://arxiv.org/abs/hep-ph/0009232).
- [32] L. Randall and M. D. Schwartz, “Unification and Hierarchy from 5D Anti-de Sitter Space,” *Phys. Rev. Lett.* **88** (2002) 081801.
- [33] L. Randall and M. D. Schwartz, “Quantum field theory and unification in AdS,” *JHEP* **0111** (2001) 003, [arXiv:hep-th/0108114 \[hep-th\]](https://arxiv.org/abs/hep-th/0108114).
- [34] S. J. Huber and Q. Shafi, “Fermion masses, mixings and proton decay in a Randall-Sundrum model,” *Phys. Lett.* **B498** (2001) 256–262, [arXiv:hep-ph/0010195 \[hep-ph\]](https://arxiv.org/abs/hep-ph/0010195).
- [35] M. S. Carena, E. Ponton, T. M. Tait, and C. Wagner, “Opaque branes in warped backgrounds,” *Phys. Rev.* **D67** (2003) 096006, [arXiv:hep-ph/0212307 \[hep-ph\]](https://arxiv.org/abs/hep-ph/0212307).
- [36] H. Davoudiasl, J. Hewett, and T. Rizzo, “Brane localized kinetic terms in the Randall-Sundrum model,” *Phys. Rev.* **D68** (2003) 045002, [arXiv:hep-ph/0212279 \[hep-ph\]](https://arxiv.org/abs/hep-ph/0212279).
- [37] T. Gherghetta, “Les Houches lectures on warped models and holography,” [arXiv:hep-ph/0601213 \[hep-ph\]](https://arxiv.org/abs/hep-ph/0601213).
- [38] D. Kazakov, S. Lavignac, and J. Dalibard in *Particle Physics Beyond the Standard Model*, vol. 84 of *Les Houches*. Elsevier, 2006.
- [39] R. Kitano, “Lepton flavor violation in the Randall-Sundrum model with bulk neutrinos,” *Phys. Lett.* **B481** (2000) 39–44, [arXiv:hep-ph/0002279 \[hep-ph\]](https://arxiv.org/abs/hep-ph/0002279).
- [40] S. Chang, J. Hisano, H. Nakano, N. Okada, and M. Yamaguchi, “Bulk standard model in the Randall-Sundrum background,” *Phys. Rev.* **D62** (2000) 084025, [arXiv:hep-ph/9912498 \[hep-ph\]](https://arxiv.org/abs/hep-ph/9912498).
- [41] T. Gherghetta and A. Pomarol, “Bulk fields and supersymmetry in a slice of AdS,” *Nucl. Phys.* **B586** (2000) 141–162, [arXiv:hep-ph/0003129 \[hep-ph\]](https://arxiv.org/abs/hep-ph/0003129).

- [42] H. Davoudiasl, J. Hewett, and T. Rizzo, “Bulk gauge fields in the Randall-Sundrum model,” *Phys. Lett.* **B473** (2000) 43–49, [arXiv:hep-ph/9911262 \[hep-ph\]](https://arxiv.org/abs/hep-ph/9911262).
- [43] J. D. Lykken and L. Randall, “The Shape of Gravity,” *JHEP* **0006** (2000) 014, [arXiv:hep-th/9908076 \[hep-th\]](https://arxiv.org/abs/hep-th/9908076).
- [44] T. G. Rizzo, “Testing the nature of Kaluza-Klein excitations at future lepton colliders,” *Phys. Rev.* **D61** (2000) 055005.
- [45] J. D. Lykken, “Weak scale superstrings,” *Phys. Rev.* **D54** (1996) R3693–R3697.
- [46] I. Antoniadis, “A possible new dimension at a few TeV,” *Physics Letters B* **246** (1990) 377 – 384.
- [47] H. Davoudiasl, J. Hewett, and T. Rizzo, “Experimental probes of localized gravity: On and off the wall,” *Phys. Rev.* **D63** (2001) 075004, [arXiv:hep-ph/0006041 \[hep-ph\]](https://arxiv.org/abs/hep-ph/0006041).
- [48] H. Davoudiasl, S. Gopalakrishna, E. Ponton, and J. Santiago, “Warped 5-Dimensional Models: Phenomenological Status and Experimental Prospects,” *New J. Phys.* **12** (2010) 075011, [arXiv:0908.1968 \[hep-ph\]](https://arxiv.org/abs/0908.1968).
- [49] K. Agashe, A. Belyaev, T. Krupovnickas, G. Perez, and J. Virzi, “LHC Signals from Warped Extra Dimensions,” *Phys. Rev.* **D77** (2008) 015003, [arXiv:hep-ph/0612015 \[hep-ph\]](https://arxiv.org/abs/hep-ph/0612015).
- [50] A. L. Fitzpatrick, J. Kaplan, L. Randall, and L.-T. Wang, “Searching for the Kaluza-Klein Graviton in Bulk RS Models,” *JHEP* **0709** (2007) 013, [arXiv:hep-ph/0701150 \[hep-ph\]](https://arxiv.org/abs/hep-ph/0701150).
- [51] B. Lillie, L. Randall, and L.-T. Wang, “The Bulk RS KK-gluon at the LHC,” *JHEP* **0709** (2007) 074, [arXiv:hep-ph/0701166 \[hep-ph\]](https://arxiv.org/abs/hep-ph/0701166).

- [52] K. Agashe, H. Davoudiasl, G. Perez, and A. Soni, “Warped Gravitons at the LHC and Beyond,” *Phys. Rev.* **D76** (2007) 036006, [arXiv:hep-ph/0701186 \[hep-ph\]](https://arxiv.org/abs/hep-ph/0701186).
- [53] K. Agashe, H. Davoudiasl, S. Gopalakrishna, T. Han, G.-Y. Huang, *et al.*, “LHC Signals for Warped Electroweak Neutral Gauge Bosons,” *Phys. Rev.* **D76** (2007) 115015, [arXiv:0709.0007 \[hep-ph\]](https://arxiv.org/abs/0709.0007).
- [54] O. Antipin, D. Atwood, and A. Soni, “Search for RS gravitons via $W_L W_L$ decays,” *Phys. Lett.* **B666** (2008) 155–161, [arXiv:0711.3175 \[hep-ph\]](https://arxiv.org/abs/0711.3175).
- [55] **ATLAS** Collaboration, “Search for high-mass dilepton resonances with 5 fb^{-1} of $p\bar{p}$ collisions at $\sqrt{s} = 7 \text{ TeV}$ with the ATLAS experiment,” Tech. Rep. ATLAS-CONF-2012-007, CERN, Geneva, 2012.
- [56] **CMS** Collaboration, “Search for Signatures of Extra Dimensions in the Diphoton Mass Spectrum at the Large Hadron Collider,” *Phys. Rev. Lett.* **108** (2012) 111801.
- [57] **D0** Collaboration, V. M. Abazov *et al.*, “Search for resonant WW and WZ production in $p\bar{p}$ collisions at $\sqrt{s} = 1.96 \text{ TeV}$,” *Phys. Rev. Lett.* **107** (2011) 011801, [arXiv:1011.6278 \[hep-ex\]](https://arxiv.org/abs/1011.6278).
- [58] **D0 Collaboration** Collaboration, A. et al., “Search for a Resonance Decaying into WZ Boson Pairs in $p\bar{p}$ Collisions,” *Phys. Rev. Lett.* **104** (2010) 061801.
- [59] **ATLAS** Collaboration, G. Aad *et al.*, “Search for new particles decaying to ZZ using final states with leptons and jets with the ATLAS detector in $\sqrt{s} = 7 \text{ TeV}$ proton-proton collisions,” [arXiv:1203.0718 \[hep-ex\]](https://arxiv.org/abs/1203.0718).
- [60] O. S. Brüning, P. Collier, P. Lebrun, S. Myers, R. Ostojic, J. Poole, and P. Proudlock, *LHC Design Report*. CERN, Geneva, 2004.
- [61] L. Evans and P. Bryant, “LHC Machine,” *JINST* **3** (2008) S08001.

- [62] **ATLAS** Collaboration, G. Aad *et al.*, “The ATLAS Experiment at the CERN Large Hadron Collider,” *JINST* **3** (2008) S08003.
- [63] **CMS** Collaboration, R. Adolphi *et al.*, “The CMS experiment at the CERN LHC,” *JINST* **3** (2008) S08004.
- [64] **LHCb** Collaboration, J. Alves, A. Augusto *et al.*, “The LHCb Detector at the LHC,” *JINST* **3** (2008) S08005.
- [65] **ALICE** Collaboration, K. Aamodt *et al.*, “The ALICE experiment at the CERN LHC,” *JINST* **3** (2008) S08002.
- [66] CERN, LEP Design Report: Vol. 2. The LEP Main Ring. Geneva, 1984.
- [67] A. Team, “Diagram of an LHC dipole magnet. Schéma d'un aimant dipôle du LHC.” 1999.
- [68] K. H. Reich, “The CERN proton synchrotron booster,” in *3rd IEEE Particle Accelerator Conference*, pp. 959–961. Washington, DC, USA, 1969.
- [69] G. Plass, “The CERN proton synchrotron: 50 years of reliable operation and continued development,” *Eur. Phys. J.* **H36** (2012) 439–454.
- [70] S. Geer, “Physics Results from the CERN Super Proton Synchrotron Proton-Antiproton Collider,” *Conf. Proc.* **C8506091** (1985) 649.
- [71] C. Lefevre, “The CERN accelerator complex. Complexe des accélérateurs du CERN.” 2008.
- [72] M. Brice, “The Linac 2 Pre-Injector.” 2008.
- [73] **ATLAS** Collaboration, “Luminosity Determination Using the ATLAS Detector,” Tech. Rep. ATLAS-CONF-2010-060, CERN, Geneva, 2010.
- [74] G. Adrian, D. Allen, *et al.*, “Probing intensity limits of LHC-Type bunches in CERN SPS with nominal optics,” Tech. Rep. CERN-ATS-2011-176, CERN, Geneva, 2011.

- [75] W. Holfe, D. Valuch, R. Assmann, S. Redaelli, R. Schmidt, D. Wollmann, and M. Zerlauth, “Emittance blow-up and loss maps in the LHC using the transverse damper as exciter,” <https://cdsweb.cern.ch/record/1433367>.
- [76] **ATLAS** Collaboration, “Luminosity Determination in pp Collisions at $\sqrt{s} = 7$ TeV using the ATLAS Detector in 2011,” Tech. Rep. ATLAS-CONF-2011-116, CERN, Geneva, 2011.
- [77] **ATLAS** Collaboration, G. Aad *et al.*, “Luminosity Determination in pp Collisions at $\sqrt{s} = 7$ TeV Using the ATLAS Detector at the LHC,” *Eur. Phys. J.* **C71** (2011) 1630, [arXiv:1101.2185 \[hep-ex\]](https://arxiv.org/abs/1101.2185).
- [78] **ATLAS** Collaboration, *ATLAS detector and physics performance: Technical Design Report, 1.* Technical Design Report ATLAS. CERN, Geneva, 1999.
- [79] **ATLAS** Collaboration, *ATLAS detector and physics performance: Technical Design Report, 2.* Technical Design Report ATLAS. CERN, Geneva, 1999.
- [80] **ATLAS** Collaboration, “The ATLAS Experiment at the CERN Large Hadron Collider,” *J. Instrum.* **3** (2008) S08003.
- [81] **ATLAS** Collaboration, *Expected performance of the ATLAS experiment: detector, trigger and physics.* CERN, Geneva, 2009. [arXiv:0901.0512](https://arxiv.org/abs/0901.0512). CERN-OPEN-2008-020.
- [82] **Particle Data Group** Collaboration, S. Eidelman *et al.*, “Review of particle physics,” *Phys. Lett.* **B592** (2004) 1.
- [83] **ATLAS** Collaboration, G. Aad *et al.*, “Readiness of the ATLAS Tile Calorimeter for LHC collisions,” *Eur. Phys. J.* **C70** (2010) 1193–1236, [arXiv:1007.5423 \[physics.ins-det\]](https://arxiv.org/abs/1007.5423).
- [84] **ATLAS** Collaboration, *ATLAS Tile Calorimeter: Technical Design Report.* Technical Design Report ATLAS. CERN, Geneva, 1996.

- [85] T. Barillari, E. Bergeaas Kuutmann, *et al.*, “Local Hadronic Calibration,” Tech. Rep. ATL-LARG-PUB-2009-001-2. ATL-LARG-PUB-2009-001, CERN, Geneva, 2009.
- [86] **ATLAS Pixel** Collaboration, A. Andreazza, “Test beam performance of the ATLAS Pixel Detector modules,” *Nucl. Instrum. Meth.* **A565** (2006) 23–29.
- [87] **ATLAS** Collaboration, *ATLAS Muon Spectrometer: Technical Design Report*. Technical Design Report ATLAS. CERN, Geneva, 1997.
- [88] **ATLAS** Collaboration, “Monitored Drift Tubes Chambers for Muon Spectroscopy in ATLAS,” Tech. Rep. ATL-MUON-94-044. ATL-M-PN-44, CERN, Geneva, 1994.
- [89] T. Argyropoulos, K. Assamagan, *et al.*, “Cathode strip chambers in ATLAS : Installation, commissioning and in situ performance,” in *Nuclear Science Symposium Conference Record, 2008. NSS '08. IEEE*, pp. 2819 –2824. 2008.
- [90] G. Cattani, “Performance of the ATLAS Resistive Plate Chambers,” Tech. Rep. ATL-MUON-PROC-2010-001, CERN, Geneva, 2010.
- [91] E. Etzion, Y. Benhammou, J. Ginzburg, M. Ishino, L. Levinson, G. Mikenberg, N. Panikashvili, D. Primor, V. P. Smakhtin, and S. Tarem, “The Certification of ATLAS Thin Gap Chambers Produced in Israel and China,” Tech. Rep. physics/0411136. ATL-COM-MUON-2004-019. TAUP-2787, CERN, Geneva, 2004.
- [92] **ATLAS** Collaboration, *ATLAS Level-1 Trigger: Technical Design Report*. Technical Design Report ATLAS. CERN, Geneva, 1998.
- [93] W. Lampl, S. Laplace, D. Lelas, P. Loch, H. Ma, S. Menke, S. Rajagopalan, D. Rousseau, S. Snyder, and G. Unal, “Calorimeter Clustering Algorithms: Description and Performance,” Tech. Rep. ATL-LARG-PUB-2008-002. ATL-COM-LARG-2008-003, CERN, Geneva, 2008.

- [94] **ATLAS** Collaboration, “Expected Electron Performance in the ATLAS Experiment,” Tech. Rep. ATL-PHYS-PUB-2011-006, CERN, Geneva, 2011.
- [95] **ATLAS** Collaboration, “Electron and Photon Reconstruction and Identification in ATLAS: Expected Performance at High Energy and Results at 900 GeV,” Tech. Rep. ATLAS-CONF-2010-005, CERN, Geneva, 2010.
- [96] **ATLAS** Collaboration, G. Aad *et al.*, “Electron performance measurements with the ATLAS detector using the 2010 LHC proton-proton collision data,” [arXiv:1110.3174 \[hep-ex\]](https://arxiv.org/abs/1110.3174).
- [97] M. Aharrouche *et al.*, “Measurement of the response of the ATLAS liquid argon barrel calorimeter to electrons at the 2004 combined test-beam,” *Nucl. Instrum. Methods Phys. Res.* **A614** (2010) 400–432.
- [98] M. Aharrouche *et al.*, “Response uniformity of the atlas liquid argon electromagnetic calorimeter,” *Nucl. Instrum. Methods Phys. Res.* **A582** no. arXiv:0709.1094. 2, (2007) 429–455.
- [99] S. Hassani *et al.*, “A muon identification and combined reconstruction procedure for the ATLAS detector at the LHC using the (MUONBOY, STACO, MuTag) reconstruction packages,” *Nucl. Instrum. Meth.* **A572** (2007) 77–79.
- [100] V. Boisvert, P. Calafiura, S. George, G. Polesello, S. Rajagopalan, and D. Rousseau, “Final Report of the ATLAS Reconstruction Task Force,” Tech. Rep. ATL-SOFT-2003-010, CERN, Geneva, 2003.
<http://atlas-proj-rtf.web.cern.ch/>.
- [101] **ATLAS** Collaboration, *ATLAS Muon identification and measurements: Technical Design Report*. Technical Design Report ATLAS. CERN, Geneva, 1999.
- [102] A. Salvucci, “Measurement of Muon Momentum Resolution of the ATLAS Detector,” Tech. Rep. ATL-PHYS-PROC-2012-013, CERN, Geneva, 2012.

- [103] **ATLAS** Collaboration, “Muon Momentum Resolution in First Pass Reconstruction of pp Collision Data Recorded by ATLAS in 2010,” Tech. Rep. ATLAS-CONF-2011-046, CERN, Geneva, 2011.
- [104] N. Orlando, “Muon reconstruction efficiency measurement in the ATLAS experiment,” Tech. Rep. ATL-PHYS-PROC-2012-011, CERN, Geneva, 2012.
- [105] S. Ellis, J. Huston, K. Hatakeyama, P. Loch, and M. Tonnesmann, “Jets in hadron-hadron collisions,” *Prog. Part. Nucl. Phys.* **60** (2008) 484–551, [arXiv:0712.2447 \[hep-ph\]](https://arxiv.org/abs/0712.2447).
- [106] G. Sterman and S. Weinberg, “Jets from Quantum Chromodynamics,” *Phys. Rev. Lett.* **39** (1977) 1436–1439.
- [107] M. Cacciari, G. P. Salam, and G. Soyez, “The Anti-k(t) jet clustering algorithm,” *JHEP* **0804** (2008) 063, [arXiv:0802.1189 \[hep-ph\]](https://arxiv.org/abs/0802.1189).
- [108] S. D. Ellis and D. E. Soper, “Successive combination jet algorithm for hadron collisions,” *Phys. Rev.* **D48** (1993) 3160–3166, [arXiv:hep-ph/9305266 \[hep-ph\]](https://arxiv.org/abs/hep-ph/9305266).
- [109] M. Cacciari and G. P. Salam, “Pileup subtraction using jet areas,” *Phys. Lett.* **B659** (2008) 119–126, [arXiv:0707.1378 \[hep-ph\]](https://arxiv.org/abs/0707.1378).
- [110] P. Adragna, C. Alexa, K. Anderson, A. Antonaki, A. Arabidze, *et al.*, “Testbeam studies of production modules of the ATLAS tile calorimeter,” *Nucl. Instrum. Meth.* **A606** (2009) 362–394.
- [111] **ATLAS** Collaboration, “Jet Energy Measurement with the ATLAS Detector in proton-proton Collisions at $\sqrt{s} = 7$ TeV,” [arXiv:1112.6426 \[hep-ex\]](https://arxiv.org/abs/1112.6426).
- [112] **ATLAS** Collaboration, “Update on the jet energy scale systematic uncertainty for jets produced in proton-proton collisions at $\sqrt{s} = 7$ TeV measured with the ATLAS detector,” Tech. Rep. ATLAS-CONF-2011-007, CERN, Geneva, 2011.

- [113] P. Loch, J. A. Backus Mayes, G. Zevi Della Porta, C. Sandoval, S. Menke, F. Vives, A. Schwartzman, and P. Manning, “Pile-up corrections for jets from proton-proton collisions at $\sqrt{s} = 7$ TeV in ATLAS in 2011,” Tech. Rep. ATL-COM-PHYS-2012-349, CERN, Geneva, 2012.
- [114] **ATLAS** Collaboration, G. Aad *et al.*, “Measurement of Inclusive Jet and Dijet Cross Sections in Proton-Proton Collisions at 7 TeV Centre-of-Mass Energy with the ATLAS Detector,” *Eur. Phys. J.* **C71** (2011) 1512, [arXiv:1009.5908 \[hep-ex\]](https://arxiv.org/abs/1009.5908).
- [115] J. Sauvan and J. Grivaz, “Probing the measurement of jet energies with the ATLAS detector using Z+jet events from proton-proton collisions at $\sqrt{s} = 7$ TeV,” Tech. Rep. ATLAS-COM-CONF-2012-015, CERN, Geneva, 2012.
- [116] T. Carli, G. Choudalakis, D. Gingrich, C. Issever, L. Kogan, J. Kvita, M. Relich, T. Spreitzer, A. Tanasijczuk, M. Vetterli, and F. Vives, “Probing the measurement of jet energies with the ATLAS detector using photon+jet events in proton-proton collisions at $\sqrt{s} = 7$ TeV,” Tech. Rep. ATL-COM-PHYS-2012-237, CERN, Geneva, 2012.
- [117] D. W. Miller, A. Schwartzman, and D. Su, “Jet-vertex association algorithm,” Tech. Rep. ATL-COM-PHYS-2008-008, CERN, Geneva, 2008.
- [118] D. W. Miller, A. Schwartzman, and D. Su, “Pile-up jet energy scale corrections using the jet-vertex fraction method,” Tech. Rep. ATL-COM-PHYS-2009-180, CERN, Geneva, 2009.
- [119] **ATLAS** Collaboration, “Data-Quality Requirements and Event Cleaning for Jets and Missing Transverse Energy Reconstruction with the ATLAS Detector in Proton-Proton Collisions at a Center-of-Mass Energy of $\sqrt{s} = 7$ TeV,” Tech. Rep. ATLAS-CONF-2010-038, CERN, Geneva, 2010.
- [120] **ATLAS** Collaboration, “Performance of the Missing Transverse Energy Reconstruction and Calibration in Proton-Proton Collisions at a

- Center-of-Mass Energy of 7 TeV with the ATLAS Detector,” Tech. Rep. ATLAS-CONF-2010-057, CERN, Geneva, 2010.
- [121] **ATLAS** Collaboration, G. Aad *et al.*, “Performance of Missing Transverse Momentum Reconstruction in Proton-Proton Collisions at 7 TeV with ATLAS,” [arXiv:1108.5602 \[hep-ex\]](https://arxiv.org/abs/1108.5602).
- [122] **ATLAS** Collaboration, *ATLAS Jet, E_T^{miss} , and mass reconstruction: Technical Design Report*. Technical Design Report ATLAS. CERN, Geneva, 1999.
- [123] **ATLAS** Collaboration, G. Aad *et al.*, “Measurement of the $W \rightarrow l\nu$ and $Z/\gamma \rightarrow ll$ production cross sections in proton-proton collisions at $\sqrt{s} = 7$ TeV with the ATLAS detector,” *JHEP* **1012** (2010) 060, [arXiv:1010.2130 \[hep-ex\]](https://arxiv.org/abs/1010.2130).
- [124] **ATLAS Liquid Argon Calorimeter** Collaboration, P. Giovannini, “Local hadron calibration with ATLAS,” *J. Phys. Conf. Ser.* **293** (2011) 012057.
- [125] **ATLAS** Collaboration, “Tau Reconstruction and Identification Performance in ATLAS,” Tech. Rep. ATLAS-CONF-2010-086, CERN, Geneva, 2010. [arXiv:1009.6135 \[hep-ex\]](https://arxiv.org/abs/1009.6135).
- [126] **ATLAS** Collaboration, “Updated Luminosity Determination in pp Collisions at $\sqrt{s} = 7$ TeV using the ATLAS Detector,” Tech. Rep. ATLAS-CONF-2011-011, CERN, Geneva, 2011.
- [127] M. A. Dobbs *et al.*, “Les Houches Guidebook to Monte Carlo Generators for Hadron Collider Physics,” [arXiv:hep-ph/0403045](https://arxiv.org/abs/hep-ph/0403045).
- [128] M. L. Mangano, M. Moretti, F. Piccinini, R. Pittau, and A. D. Polosa, “ALPGEN, a Generator for Hard Multiparton Processes in Hadronic Collisions,” *JHEP* **0307** (2003) 001, [arXiv:hep-ph/0206293 \[hep-ph\]](https://arxiv.org/abs/hep-ph/0206293).
- [129] T. Sjostrand, S. Mrenna, and P. Z. Skands, “PYTHIA 6.4 Physics and Manual,” *JHEP* **0605** (2006) 026, [arXiv:hep-ph/0603175 \[hep-ph\]](https://arxiv.org/abs/hep-ph/0603175).

- [130] M. Bahr, S. Gieseke, M. Gigg, D. Grellscheid, K. Hamilton, *et al.*, “Herwig++ Physics and Manual,” *Eur. Phys. J.* **C58** (2008) 639–707, [arXiv:0803.0883 \[hep-ph\]](https://arxiv.org/abs/0803.0883).
- [131] S. Frixione and B. R. Webber, “Matching NLO QCD computations and parton shower simulations,” *JHEP* **0206** (2002) 029, [arXiv:hep-ph/0204244 \[hep-ph\]](https://arxiv.org/abs/hep-ph/0204244).
- [132] G. Corcella, I. Knowles, G. Marchesini, S. Moretti, K. Odagiri, *et al.*, “HERWIG 6: An Event generator for hadron emission reactions with interfering gluons (including supersymmetric processes),” *JHEP* **0101** (2001) 010, [arXiv:hep-ph/0011363 \[hep-ph\]](https://arxiv.org/abs/hep-ph/0011363).
- [133] J. Butterworth, J. R. Forshaw, and M. Seymour, “Multiparton interactions in photoproduction at HERA,” *Z. Phys.* **C72** (1996) 637–646, [arXiv:hep-ph/9601371 \[hep-ph\]](https://arxiv.org/abs/hep-ph/9601371).
- [134] T. Gleisberg, S. Hoeche, F. Krauss, M. Schonherr, S. Schumann, *et al.*, “Event generation with SHERPA 1.1,” *JHEP* **0902** (2009) 007, [arXiv:0811.4622 \[hep-ph\]](https://arxiv.org/abs/0811.4622).
- [135] B. Cooper, J. Katzy, M. Mangano, A. Messina, L. Mijovic, *et al.*, “Monte Carlo tuning in the presence of Matching,” [arXiv:1109.5295 \[hep-ph\]](https://arxiv.org/abs/1109.5295).
- [136] S. Hoeche, F. Krauss, N. Lavesson, L. Lonnblad, M. Mangano, *et al.*, “Matching parton showers and matrix elements,” [arXiv:hep-ph/0602031 \[hep-ph\]](https://arxiv.org/abs/hep-ph/0602031).
- [137] S. Catani, F. Krauss, R. Kuhn, and B. Webber, “QCD matrix elements + parton showers,” *JHEP* **0111** (2001) 063, [arXiv:hep-ph/0109231 \[hep-ph\]](https://arxiv.org/abs/hep-ph/0109231).
- [138] F. Krauss, “Matrix elements and parton showers in hadronic interactions,” *JHEP* **0208** (2002) 015, [arXiv:hep-ph/0205283 \[hep-ph\]](https://arxiv.org/abs/hep-ph/0205283).

- [139] A. Pukhov, E. Boos, M. Dubinin, V. Edneral, V. Ilyin, *et al.*, “CompHEP: A Package for evaluation of Feynman diagrams and integration over multiparticle phase space,” [arXiv:hep-ph/9908288 \[hep-ph\]](https://arxiv.org/abs/hep-ph/9908288).
- [140] A. Pukhov, “CalcHEP 2.3: MSSM, structure functions, event generation, batchs, and generation of matrix elements for other packages,” [arXiv:hep-ph/0412191 \[hep-ph\]](https://arxiv.org/abs/hep-ph/0412191).
- [141] A. Datta, K. Kong, and K. T. Matchev, “Minimal Universal Extra Dimensions in CalcHEP/CompHEP,” *New J. Phys.* **12** (2010) 075017, [arXiv:1002.4624 \[hep-ph\]](https://arxiv.org/abs/1002.4624).
- [142] E. Richter-Was, D. Froidevaux, and L. Poggioli, “ATLFAST 2.0 a fast simulation package for ATLAS,” Tech. Rep. ATL-PHYS-98-131, CERN, Geneva, 1998.
- [143] S. Frixione, P. Nason, and B. R. Webber, “Matching NLO QCD and parton showers in heavy flavor production,” *JHEP* **0308** (2003) 007, [arXiv:hep-ph/0305252 \[hep-ph\]](https://arxiv.org/abs/hep-ph/0305252).
- [144] **ATLAS** Collaboration, “Measurement of the $W \rightarrow \ell\nu$ production cross-section and observation of $Z \rightarrow \ell\ell$ production in proton-proton collisions at $\sqrt{s} = 7$ TeV with the ATLAS detector,” Tech. Rep. ATLAS-CONF-2010-051, CERN, Geneva, 2010.
- [145] S. Moch and P. Uwer, “Theoretical status and prospects for top-quark pair production at hadron colliders,” *Phys. Rev.* **D78** (2008) 034003, [arXiv:0804.1476 \[hep-ph\]](https://arxiv.org/abs/0804.1476).
- [146] N. Kidonakis, “Next-to-next-to-leading-order collinear and soft gluon corrections for t-channel single top quark production,” *Phys. Rev.* **D83** (2011) 091503, [arXiv:1103.2792 \[hep-ph\]](https://arxiv.org/abs/1103.2792).
- [147] N. Kidonakis, “NNLL resummation for s-channel single top quark production,” *Phys. Rev.* **D81** (2010) 054028, [arXiv:1001.5034 \[hep-ph\]](https://arxiv.org/abs/1001.5034).

- [148] N. Kidonakis, “Two-loop soft anomalous dimensions for single top quark associated production with a W or H ,” *Phys. Rev.* **D82** (2010) 054018, [arXiv:1005.4451 \[hep-ph\]](https://arxiv.org/abs/1005.4451).
- [149] **ATLAS** Collaboration, G. Aad *et al.*, “Measurement of the WW cross section in $\sqrt{s} = 7$ TeV pp collisions with the ATLAS detector and limits on anomalous gauge couplings,” [arXiv:1203.6232 \[hep-ex\]](https://arxiv.org/abs/1203.6232).
- [150] **ATLAS** Collaboration, G. Aad *et al.*, “Measurement of the WZ production cross section and limits on anomalous triple gauge couplings in proton-proton collisions at $\sqrt{s} = 7$ TeV with the ATLAS detector,” *Phys. Lett.* **B709** (2012) 341–357, [arXiv:1111.5570 \[hep-ex\]](https://arxiv.org/abs/1111.5570).
- [151] **ATLAS** Collaboration, G. Aad *et al.*, “Measurement of the ZZ production cross section and limits on anomalous neutral triple gauge couplings in proton-proton collisions at $\sqrt{s} = 7$ TeV with the ATLAS detector,” *Phys. Rev. Lett.* **108** (2012) 041804, [arXiv:1110.5016 \[hep-ex\]](https://arxiv.org/abs/1110.5016).
- [152] J. Butterworth, E. Dobson, U. Klein, B. Mellado Garcia, T. Nunnemann, J. Qian, D. Rebuzzi, and R. Tanaka, “Single Boson and Diboson Production Cross Sections in pp Collisions at $\sqrt{s} = 7$ TeV,” Tech. Rep. ATL-COM-PHYS-2010-695, CERN, Geneva, 2010.
- [153] L. Randall and R. Sundrum, “An Alternative to Compactification,” *Phys. Rev. Lett.* **83** (1999) 4690–4693.
- [154] J. E. Gaiser and E. Bloom, “Charmonium spectroscopy from inclusive ψ' and J/ψ radiative decays,” *Phys. Rev.* **D34** (1986) 711–721.
- [155] W. Verkerke and D. P. Kirkby, “The RooFit toolkit for data modeling,” [arXiv:physics/0306116 \[physics\]](https://arxiv.org/abs/physics/0306116).
- [156] T. Gadfort and E. Williams, “Search for resonant WW and WZ production using lepton + E_T^{miss} + jets events with the ATLAS detector,” Tech. Rep. ATL-COM-PHYS-2012-385, CERN, Geneva, 2012.

- [157] **ATLAS** Collaboration, G. Aad *et al.*, “Search for supersymmetry with jets, missing transverse momentum and at least one hadronically decaying tau lepton in proton-proton collisions at $\sqrt{s} = 7$ TeV with the ATLAS detector,” [arXiv:1204.3852 \[hep-ex\]](https://arxiv.org/abs/1204.3852).
- [158] G. Choudalakis and D. Casadei, “Plotting the differences between data and expectation,” *European Physical Journal Plus* **127** (2012) 25, [arXiv:1111.2062 \[physics.data-an\]](https://arxiv.org/abs/1111.2062).
- [159] T. Becher, C. Lorentzen, and M. D. Schwartz, “Resummation for W and Z production at large p_T ,” *Phys. Rev. Lett.* **108** (2012) 012001, [arXiv:1106.4310 \[hep-ph\]](https://arxiv.org/abs/1106.4310).
- [160] G. Romeo, A. Schwartzman, R. Piegaia, T. Carli, and R. Teuscher, “Jet energy resolution from in-situ techniques with the atlas detector using proton-proton collisions at a center of mass energy $\sqrt{s} = 7$ tev,” Tech. Rep. ATL-COM-PHYS-2011-240, CERN, Geneva, 2011.
- [161] C. Gabaldon, “Measurement of the luminosity by the atlas experiment,” Tech. Rep. ATL-LUM-PROC-2011-004, CERN, Geneva, Oct, 2011.
- [162] F. Bertolucci, “The ATLAS Tile Calorimeter performance at LHC in pp collisions at 7 TeV,” Tech. Rep. ATL-TILECAL-PROC-2012-001, CERN, Geneva, Jan, 2012.
- [163] A. Sherstnev and R. Thorne, “Parton Distributions for LO Generators,” *Eur. Phys. J.* **C55** (2008) 553–575, [arXiv:0711.2473 \[hep-ph\]](https://arxiv.org/abs/0711.2473).
- [164] **ATLAS** Collaboration, “Charged particle multiplicities in pp interactions at $\sqrt{s} = 0.9$ and 7 TeV in a diffractive limited phase-space measured with the ATLAS detector at the LHC and new PYTHIA6 tune,” Tech. Rep. ATLAS-CONF-2010-031, CERN, Geneva, 2010.

- [165] P. M. Nadolsky, H.-L. Lai, Q.-H. Cao, J. Huston, J. Pumplin, D. Stump, W.-K. Tung, and C.-P. Yuan, “Implications of CTEQ global analysis for collider observables,” *Phys. Rev.* **D78** (2008) 013004.
- [166] G. Watt, “MSTW PDFs and impact of PDFs on cross sections at Tevatron and LHC,” [arXiv:1201.1295 \[hep-ph\]](https://arxiv.org/abs/1201.1295).
- [167] M. Botje, J. Butterworth, A. Cooper-Sarkar, A. de Roeck, J. Feltesse, S. Forte, A. Glazov, J. Huston, R. McNulty, T. Sjostrand, and R. Thorne, “The PDF4LHC Working Group Interim Recommendations,” Tech. Rep. arXiv:1101.0538, 2011.
- [168] **ATLAS** Collaboration, G. Aad *et al.*, “Measurement of $t\bar{t}$ production with a veto on additional central jet activity in pp collisions at $\sqrt{s} = 7$ TeV using the ATLAS detector,” [arXiv:1203.5015 \[hep-ex\]](https://arxiv.org/abs/1203.5015).
- [169] **ATLAS** Collaboration, G. Aad *et al.*, “Search for resonant WZ production in the WZ to $l \nu l' l'$ channel in $\sqrt{s} = 7$ TeV pp collisions with the ATLAS detector,” [arXiv:1204.1648 \[hep-ex\]](https://arxiv.org/abs/1204.1648).
- [170] B. P. Kersevan and E. Richter-Was, “The Monte Carlo Event Generator ACERMC 2.0 with Interfaces to PYTHIA 6.2 and HERWIG 6.5. ACERMC 2.0 program manual,” Tech. Rep. ATL-PHYS-2004-020, CERN, Geneva, 2004.
- [171] K. Melnikov and F. Petriello, “Electroweak gauge boson production at hadron colliders through $O(\alpha(s)^2)$,” *Phys. Rev.* **D74** (2006) 114017, [arXiv:hep-ph/0609070 \[hep-ph\]](https://arxiv.org/abs/hep-ph/0609070).
- [172] J. Neyman and E. S. Pearson, “On the problem of the most efficient tests of statistical hypotheses,” *Phil. Trans. R. Soc. Lon.* **A231** (1933) pp. 289–337.
- [173] S. L. Meyer, *Data analysis for scientists and engineers*. Wiley, New York, NY, 1975.

- [174] A. L. Read, “Modified frequentist analysis of search results (The CL(s) method),” <https://cdsweb.cern.ch/record/451614>.
CERN-OPEN-2000-205.
- [175] T. Junk, “Confidence level computation for combining searches with small statistics,” *Nucl. Instrum. Meth. A* **434** (1999) 435–443,
[arXiv:hep-ex/9902006](https://arxiv.org/abs/hep-ex/9902006) [hep-ex].
- [176] G. Cowan, K. Cranmer, E. Gross, and O. Vitells, “Asymptotic formulae for likelihood-based tests of new physics,” *Eur. Phys. J. C* **71** (2011) 1554,
[arXiv:1007.1727](https://arxiv.org/abs/1007.1727) [physics.data-an].
- [177] G. Altarelli, R. Casalbuoni, S. De Curtis, N. Di Bartolomeo, R. Gatto, *et al.*,
“Extended gauge models and precision electroweak data,” *Phys. Lett. B* **318** (1993) 139–147.